UNIVERSIDAD AUTÓNOMA DE NUEVO LEÓN
FACULTAD DE CIENCIAS FÍSICO MATEMÁTICAS

SYNTHESIS AND CHARACTERIZATION OF PEROVSKITE-INSPIRED ANTIMONY COMPOUNDS FOR PHOTODETECTOR APPLICATIONS

POR:
VARSHIKA PUTHAN VEEDU SASIDHARAN

COMO REQUISITO PARA OBTENER EL GRADO DE
DOCTORADO EN INGENIERÍA FÍSICA

JUNIO, 2025

UNIVERSIDAD AUTÓNOMA DE NUEVO LEÓN
FACULTAD DE CIENCIAS FÍSICO MATEMÁTICAS

SYNTHESIS AND CHARACTERIZATION OF PEROVSKITE-INSPIRED ANTIMONY COMPOUNDS FOR PHOTODETECTOR APPLICATIONS

POR:

VARSHIKA PUTHAN VEEDU SASIDHARAN

COMO REQUISITO PARA OBTENER EL GRADO DE
DOCTORADO EN INGENIERÍA FÍSICA

JUNIO, 2025

Universidad Autónoma de Nuevo León

Facultad de Ciencias Físico Matemáticas

Los miembros del comité de tesis aprueban la tesis realizada por la alumna **Varshika Puthan Veedu Sasidharan**, con matrícula **2125380**, como opción al grado de **Doctorado en Ingeniería Física** (Doctor in Engineering Physics).

El Comité de Tesis

_____

Dr. Manuel García Méndez
Presidente

_____ _____

Dra. Bindu Krishnan
Secretaria

Dr. Carlos Luna Criado
Vocal 1

_____ _____

Dra. Raquel Mendoza Reséndez
Vocal 2

Dra. Nora Elizondo Villarreal
Vocal 3

Vo. Bo.

_____

Dr. Álvaro Eduardo Cordero Franco
Subdirector de Posgrado

San Nicolás de los Garza, Nuevo León, junio 2025

Universidad Autónoma de Nuevo León
Facultad de Ciencias Físico-Matemático
Posgrado en Ingeniería Física Industrial

The members of the Thesis Committee recommend that the thesis «Synthesis and Characterization of Perovskite-Inspired Antimony Compounds for Photodetector Applications», completed by the student VARSHIKA PUTHAN VEEDU SASIDHARAN, with registration number 2125380, be accepted for defense as a partial requirement for obtaining the degree of (DOCTORADO EN INGENERIA FISICA).

The Thesis Committee

Dr. Manuel Garcia Mendez
Advisor

Dr. Bindu Krishnan
Co-advisor

Dr. Carlos Luna Criado
Revisor

Dr. Raquel Mendoza Resendez
Revisor

Dr. Nora Elizondo Villarreal
Revisor

Vo. Bo.

Dr. Álvaro Eduardo Cordero Franco
Subdirector de Estudios de Posgrado

San Nicolás de los Garza, Nuevo León, june 2025

Contents

Dedicated to,

Acha, Amma, Appu and **Anii**

your endless love, strength, and belief in me are the foundation of everything I do.

This work is as much yours as it is mine.

Science

for inspiring curiosity, purpose, and perseverance.

Family and **Friends**

for walking beside me with encouragement and kindness throughout this journey.

Acknowledgement

First and foremost, I would like to express my heartfelt gratitude to **Dr. Manuel García Méndez**, my thesis advisor, for his unwavering guidance, constant encouragement, and invaluable support throughout every stage of my doctoral journey. His expertise, insightful feedback, and patience have been instrumental in shaping both my research and academic growth. I am truly thankful for the opportunity to learn under his mentorship, which greatly contributed to the successful completion of this work.

I am also deeply grateful to my co-advisor, **Dr. Bindu Krishnan**, whose involvement and contributions were instrumental to the completion of this work. Her constant support, insightful feedback, and encouragement helped shape the direction of my research and brought clarity to many challenging moments.

I would like to extend my sincere thanks to **Dr. Lakshmi M** (**Mercy College, Palakkad**) for helping me discover and apply for this research opportunity. Her encouragement played a crucial role in setting me on this path. I also express my deep appreciation to **Dr. Sadasivan Shaji**, a key member of our research group, for his help and guidance throughout my PhD. His support in understanding article writing, research methods, and critical discussions enriched my learning experience immensely.

My gratitude also goes to **Dr. David Avellaneda Avellaneda**, another valued group member, for his help in maintaining equipment and assisting with several characterizations and technical doubts. I am grateful to **Dr. Sanal Kozhiparambil Chandran** and **Dr. Francisco José Solís Pomar** for providing the X-ray diffraction (XRD) equipment and ensuring its proper use, which significantly contributed to the success of this work.

I would also like to acknowledge **FCFM**, **FIME, FCQ, CIIDIT** and **CIMAV (Dr. Isabel Mendivil)** for providing various tools and facilities essential to my research.

I would like to express my heartfelt gratitude to **Dr. Edgar Martínez Guerra** and **Dr. Carlos Luna Criado**, the coordinators of the **Facultad de Ciencias Físico Matemáticas (FCFM)** at UANL, for their exceptional support and guidance throughout my doctoral program. Their administrative and academic assistance was crucial to the successful progression of my thesis,

and their encouragement greatly enhanced my research experience. I am also thankful to **Dr. Atilano Martínez Huerta**, Director of the FCFM, for his invaluable support, as well as to **Dr. Álvaro Eduardo Cordero Franco**, Subdirector de Posgrado, for his continued help. My gratitude extends to the members of my thesis committee — **Dr. Manuel García Méndez**, **Dr. Bindu Krishnan**, **Dr. Carlos Luna Criado**, **Dr. Raquel Mendoza Reséndez**, and **Dr. Nora Elizondo Villarreal** — for their thoughtful feedback and insightful suggestions, which were essential in refining my work.

This work would not have been possible without the financial support I received. I am sincerely grateful to the **Universidad Autónoma de Nuevo León (UANL)** for this academic opportunity, and to the **Secretaría de Ciencia, Humanidades, Tecnología e Innovación (SECIHTI, formerly CONAHCyT), Mexico**, for my scholarship and funding this research through **Project No. CB-2016/284800**. I also acknowledge the support from the **PAICyT-UANL Project No. 245-CE-2022**, and the **Fundación UANL**, which generously funded my travel expenses for the exchange program in Singapore.

I am extremely grateful for the opportunity to participate in a research exchange program at **Nanyang Technological University (NTU), Singapore**, under the mentorship of **Prof. Nripan Mathews**. His generosity in offering me this position and his insightful mentorship have played a significant role in shaping my skills and outlook as a researcher. I am also thankful to **Prof. Cuong Dang** for the collaboration on our work related to radiation detectors, which formed a key component of my research.

During my doctoral journey, I had the privilege of mentoring two students from FIME: **Marco Uriel Rodríguez Hernández** (bachelor student) and **Miguel Avilés Cardós** (master student). Assisting them with their research was a rewarding and enriching experience for me.

I would also like to thank my fellow research group members: **Diana Maria, Dr. Aiswarya, Dr. Akshana, Dr. Sebin, Joseph, Dr. Paulosutty, Dr. Albert, Katia, Pooja, Wilfred, Jithin, Shilpa, Indhu, Daniel lopez, Angel, Angela, Valeria, Shalvin, Sreepriya**, and professors **Dr. Arturo Juarez, Dr. Edgar Garcia, Dr. Ana Maria Guzman, Dr. Azael Martinez**, as well as friends **Dr. Sreed Sharma, Dr. Denis Ariel, Aleena, Gopi, Sreerag, Madhu, Amritha, and Catalina** at FIME, for their companionship and contributions to a collaborative research environment.

I also acknowledge the support of students and professors at FCFM, UANL — including **Dr. Omar, Adolfo, Karen, Cesar, Rodolfo, Dr. Karan Singh, Dr. Claudia Rosa, Dr. Daniel,**

Alecia, Jithin, Shambu, Vimal, Omar, Issac, Juan, Ramon, Alma, and **Dr. Alfredo Tlahuice Flores, Dr. Diego Gerardo Gomez, Dr. Miguel Angel, Dr. Hector Manuel, Dr. Francisco Vicente, Dr. Sergio Alberto** — for fostering a vibrant academic atmosphere.

I am truly grateful to the administrative staff — **Briseida, Romy, Karla, Adriana, Mauricio, Luica, Gabriel, Alajendra**, **Rosy Sanchez** and others — for their indispensable assistance throughout my time at UANL.

On a personal note, I am eternally grateful to my parents, **Mr. P. Sasidharan** and **Mrs. Pushpalatha Sasidharan**, for their unwavering love, prayers, encouragement, and support throughout my life. I owe my deepest thanks to my brother, **Vishvak P.S**, for always being there for me, and to my beloved companion, **Dr. Anil Prasad**, for his constant love, care, encouragement, and understanding, especially during the most demanding phases of my research. I am also thankful to my aunty, **Maalika Girish Panicker**, for kindly providing me accommodation during my stay in Singapore.

I would like to sincerely thank **Dr. Priyanka Kajal** and **Dr. Francesco Maddalena**, the postdoctoral researchers (NTU) who assisted me closely throughout my exchange program journey. Their support, technical insights, and motivation have made a profound difference in both my research and personal growth.

I sincerely thank the NTU students — **Paul Erinjeri Jogi**, **Darrell Jun Jie Tay**, **Wu Qinjie**, and **Chengyuan Xiao** — for their dedicated help and collaboration in executing my research projects. I am also thankful to **Dr. Vipinraj Sugathan, Dr. Thambidurai Mariyappan, Emhe, Ryan, Dr. Shubam, Ankit Jaiswal, Saumiya, Abhishek Nambiar, Aakash Sharma, Wang yanju, Hong Kang, Dr. Guibin, Edwin, Dr. Ayan, Dr. Riyas Ahmad, Divyam Sharma, Shibi, Neha, Shyam, Dr. Akhil,** and for their valuable assistance, and I extend my gratitude to all other members of the **NTU research group** for their consistent support and encouragement.

Last but not least, I would like to thank all my **teachers, family, friends, and well-wishers** — including those whose names I may have unintentionally omitted — for their love and support. This thesis would not have been possible without all of you.

Finally, I thank **God** for giving me the strength, patience, and grace to carry this work through to completion.

Abstract

This thesis investigates lead-free perovskite-inspired antimony-based semiconductors for photodetector applications, with an emphasis on developing novel materials to replace toxic lead in optoelectronic devices. While organic-inorganic hybrid perovskite solar cells have achieved impressive efficiencies (~25%), their commercialization is hindered by environmental and toxicity concerns. To address this, the study explores the potential of group VA elements, particularly antimony (Sb), as lead substitutes in halide perovskite structures. This includes materials such as cesium antimony iodide ($Cs_3Sb_2I_9$), silver antimony iodide ($AgSb_2I_7$ and Ag_2SbI_5), copper antimony iodide (Cu_2SbI_5), and mixed-alloy Rudorffites incorporating bismuth ($Ag(Bi,Sb)_2I_7$). The research begins with the synthesis of antimony sulfide (Sb_2S_3) thin films using chemical bath deposition (CBD), followed by modifications to produce a range of antimony-based semiconductors with less explored properties. The primary focus is their photodetection capabilities, particularly their self-powered, broad-band spectral response. Remarkably, these materials exhibit intrinsic ferroelectric properties, enabling self-driven photoconduction without the need for an external power source—an essential advancement for efficient photodetector technologies. To optimize these materials for high-performance applications, the study thoroughly evaluates their structural, morphological, elemental, and optoelectronic properties. Key challenges related to material stability, scalability, and operational efficiency are also addressed, providing valuable insights into the development of lead-free antimony-based photodetectors. This work significantly contributes to the growing field of environmentally friendly, high-performance semiconductors, paving the way for next-generation optoelectronic devices.

Resumen

Esta tesis investiga semiconductores basados en antimonio inspirados en perovskitas libres de plomo para aplicaciones en fotodetectores, con énfasis en el desarrollo de nuevos materiales que reemplacen al tóxico plomo en dispositivos optoelectrónicos. Aunque las celdas solares de perovskita híbrida orgánico-inorgánica han alcanzado eficiencias impresionantes (~25%), su comercialización se ve limitada por preocupaciones medioambientales y de toxicidad. Para abordar este problema, el estudio explora el potencial de elementos del grupo VA, en particular el antimonio (Sb), como sustitutos del plomo en estructuras de perovskitas halogenadas. Entre los materiales estudiados se encuentran el yoduro de antimonio y cesio ($Cs_3Sb_2I_9$), yoduro de antimonio y plata ($AgSb_2I_7$ y Ag_2SbI_5), yoduro de antimonio y cobre (Cu_2SbI_5), y aleaciones mixtas tipo Rudorffita con bismuto ($Ag(Bi,Sb)_2I_7$).

La investigación comienza con la síntesis de películas delgadas de trisulfuro de antimonio (Sb_2S_3) mediante deposición química en baño (CBD), seguida de modificaciones para producir una gama de semiconductores basados en antimonio con propiedades poco exploradas. El enfoque principal es evaluar sus capacidades de fotodetección, particularmente su respuesta espectral de amplio rango sin requerir alimentación externa. Notablemente, estos materiales exhiben propiedades ferroeléctricas intrínsecas, lo que permite una fotoconducción autoinducida, sin necesidad de una fuente de energía externa—un avance esencial para tecnologías de fotodetectores eficientes.

Para optimizar estos materiales en aplicaciones de alto rendimiento, el estudio evalúa exhaustivamente sus propiedades estructurales, morfológicas, elementales y optoelectrónicas. También se abordan los principales desafíos relacionados con la estabilidad del material, la escalabilidad y la eficiencia operativa, aportando información valiosa para el desarrollo de fotodetectores basados en antimonio y libres de plomo. Este trabajo representa una contribución significativa al creciente campo de los semiconductores ecológicos y de alto desempeño, allanando el camino hacia dispositivos optoelectrónicos de próxima generación.

List of Figures

List of Tables

Abbreviations

CBD	:	Chemical Bath Deposition	**α**	:	Absorption coefficient
S	:	Sensitivity	**PV**	:	Photovoltaic
R	:	Responsivity	**FTO**	:	Fluorine-doped tin oxide
EQE	:	External Quantum Efficiency	**ETL**	:	Electron transport layer
D	:	Detectivity	**HTL**	:	Hole transport layer
NEP	:	Noise-Equivalent Power	**SAI**	:	Silver antimony Iodide
VB	:	Valence band	**PAS**	:	Polar-Active Semiconductors
CB	:	Conduction band	**FWHM**	:	Full width at half maximum
VBM	:	Valence band maximum	**NPLs**	:	Nanoplatelets
CBM	:	Conduction band minimum	**NRs**	:	Nanorods
IMA	:	International Mineralogical Association	**E_g**	:	Band gap
CVD	:	Chemical vapor deposition	**E_f**	:	Fermi level
PCEs	:	Power Conversion Efficiencies	**B.E.**	:	Binding energy
DMF	:	Dimethylformamide	**UV–Vis**	:	Ultraviolet–Visible
DMSO	:	Dimethyl sulfoxide	**CsCl**	:	Cesium chloride
XRD	:	X-ray diffraction	**CL**	:	Cathodoluminescence
SEM	:	Scanning Electron Microscopy	**XPS**	:	X-ray Photoelectron Spectroscopy
EDS/EDX	:	Energy Dispersive X-ray Spectroscopy	**BSE**	:	Backscattered electrons
SE	:	Secondary electrons			

Chapter 1: Introduction

This thesis chapter serves as an introductory exploration into the significance of lead-free antimony-based semiconductors, outlining the study's hypothesis and objectives. It provides insight into the research aims and the potential impact of these compounds in photodetector applications. By establishing this foundation, the chapter prepares readers for the detailed exploration of lead-free antimony perovskites and their role in advancing optoelectronic technologies.

1.1 General background on Thin-Film Photodetectors

Have you ever wondered how smartphone cameras capture crisp images or how solar panels convert sunlight into usable electricity? At the core of these technologies are photodetectors—specialized materials that convert light into electrical signals. In recent years, researchers have discovered that when these materials are made exceptionally thin—less than one-thousandth of a millimeter—they exhibit remarkable properties (Figure 1.1) not found in their bulk counterparts [1].

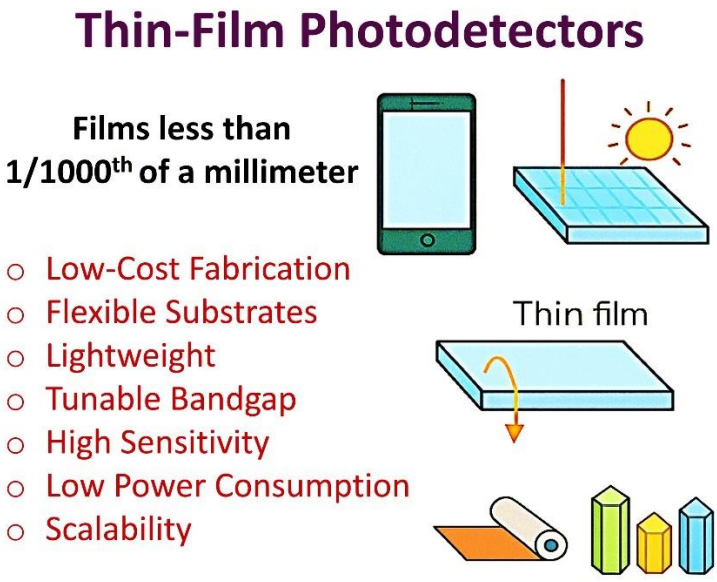

Figure 1.1. Overview of thin-film semiconductors for next-generation photodetection applications.

These ultra-thin materials, known as thin films, offer several advantages. Their reduced thickness allows light to excite electrons more efficiently, enabling faster and more sensitive detection [2]. Furthermore, the spectral response of these films can be precisely tuned by controlling their thickness—an advantage not achievable with thicker materials [3,4]. Thin films also offer mechanical flexibility, which enables their integration into emerging applications such as wearable health monitors and foldable electronic displays [1].

Another compelling aspect of thin films is their ease of fabrication. They can be produced using simple, scalable coating techniques while consuming minimal material, making them both cost-effective and environmentally favorable [5]. Additionally, their versatility allows deposition on a wide range of substrates, including glass, plastic, and even textiles [6].

This thesis investigates the optoelectronic mechanisms and performance optimization of lead-free antimony-based semiconductor thin films for next-generation photodetection applications. Emphasis is placed on emerging material systems such as $Cs_3Sb_2I_9$, $AgSb_2I_7$, Bi-alloyed Sb_2S_3, $Ag(Bi,Sb)_2I_7$, and Cu_2SbI_5, evaluating their potential to enable high-efficiency, solution-processable devices suited for applications ranging from solar energy harvesting to biomedical imaging. Through comprehensive material characterization and device engineering, this work aims to establish foundational design principles for sustainable thin-film photodetectors, with transformative implications for energy, healthcare, and consumer technologies.

1.2 Mechanisms of Photodetection in Thin Films

Thin-film photodetectors operate based on several key physical mechanisms that differ from bulk materials due to their reduced dimensionality and enhanced surface effects [7]. The general photodetection process in thin films involves the following steps as shown in the figure 1.2 below:

1. **Light Absorption in Thin Films**

When light irradiates a thin-film photodetector, the semiconductor material absorbs photons whose energy equals or exceeds the material's bandgap—the energy separation between the valence and conduction bands [8]. This interaction excites electrons from the valence band into the conduction band, generating mobile electron-hole pairs that form the basis of photodetection [9].

In ultrathin films (typically <100 nm), quantum confinement effects become significant. The reduced dimensionality forces charge carriers into a spatially restricted region, resulting in a widened bandgap and altered optical absorption characteristics. This tunability enables spectral sensitivity engineering, allowing materials to be tailored for specific wavelength detection—such as enhancing sensitivity to blue or red light—simply by adjusting film thickness [10].

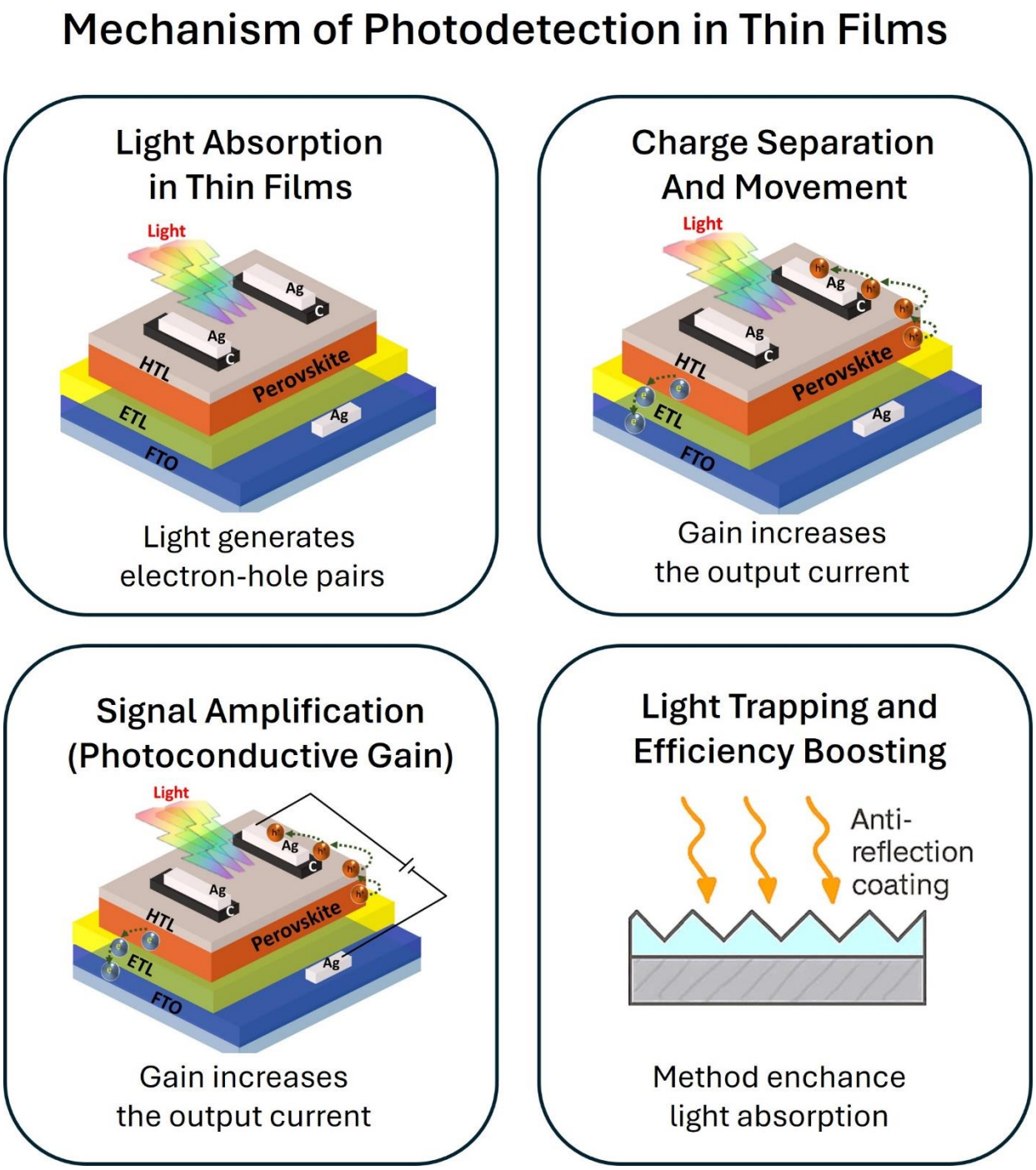

Figure 1.2. Mechanism of photodetection in thin films.

2. **Charge Separation and Transport Mechanisms**

Following photoexcitation, the generated electron-hole pairs must be efficiently separated and transported to the electrodes to yield a measurable electrical signal. Thin-film architectures offer a distinct advantage in this context due to the reduced distance that carriers need to travel, which minimizes recombination losses and enhances response speed.

To facilitate charge separation, internal electric fields are introduced via heterojunctions (e.g., p–n junctions) or Schottky barriers at metal-semiconductor interfaces. These built-in fields drive electrons and holes in opposite directions, preventing premature recombination and supporting efficient current extraction [11,12].

However, the polycrystalline nature of most solution-processed thin films introduces grain boundaries, which can act as charge carrier traps. Depending on the material and device design, these traps may either prolong carrier lifetimes (enhancing sensitivity) or impede carrier transport (reducing speed and efficiency) [13].

3. **Signal Amplification via Photoconductive Gain**

Beyond simple photogeneration, certain thin-film photodetectors exhibit signal amplification, wherein a single absorbed photon induces the flow of multiple charge carriers through the external circuit. This gain arises from two primary operating regimes:

- **Photoconductive Mode (High-Gain Operation):** Under external bias, electrons may traverse the device multiple times before recombination, particularly in materials with trap-rich environments. For example, in Sb_2S_3-based detectors, hole traps extend electron lifetimes, thereby boosting the current beyond the initial photon count [14].
- **Photovoltaic Mode (Self-Powered Detection):** Here, the built-in electric field of a junction separates charges without the need for external power. This mode is especially attractive for applications requiring low energy consumption, such as wearable electronics and autonomous sensors [15].

4. **Light Trapping and Efficiency Enhancement**

Given the limited thickness of ultra-thin films, light absorption can be suboptimal without the incorporation of specialized optical management strategies. To address this, light-trapping techniques are employed to increase the optical path length within the active layer:

- **Anti-reflection coatings** are applied to suppress surface reflections, thereby improving photon entry into the absorber [16].
- **Multilayer interference structures** combine materials with different refractive indices to create constructive interference patterns that enhance light confinement [17].
- **Surface texturing** scatters incident light, increasing the effective optical path and absorption probability by forcing photons to traverse longer, zig-zagging paths within the material [18].

These strategies collectively improve photodetector efficiency while maintaining minimal film thickness.

5. **Surface Effects and Stability Considerations**

Due to their high surface-to-volume ratio, thin films exhibit surface-dominated behavior that significantly influences optoelectronic performance [19]. While surface states can enhance photoresponse by trapping carriers and extending recombination times, they also pose challenges. Unpassivated surfaces are prone to environmental degradation—such as oxidation in halide perovskites—and can lead to increased dark current through defect-assisted carrier generation [20].

To mitigate these effects, encapsulation techniques using barrier layers are employed to protect against moisture and oxygen ingress [21]. Additionally, chemical passivation using organic or inorganic ligands can neutralize surface defects, improving both stability and performance. These surface engineering approaches are essential for realizing durable, low-noise thin-film devices suitable for long-term use in photovoltaics, sensing, and optoelectronics [22].

1.3 Key Performance Parameters of Photodetectors

Several critical parameters are used to evaluate the performance of the photodetector. These parameters quantify the device's sensitivity to light, its efficiency in converting photons into electrical signals, its ability to detect weak optical signals, and its temporal response.

1. Sensitivity (S)

Sensitivity measures the relative change in the photodetector's current when exposed to light compared to its dark (no illumination) state. It is expressed as a percentage and calculated using:

$$S\ (\%) = [(I_l - I_d)/I_d] \times 100 \quad (1.1)$$

- I_l: Current under illumination (photocurrent + dark current) , I_d: Dark current (current flowing in the absence of light).

A high sensitivity indicates that the device exhibits a strong response to light, making it suitable for low-light detection applications.

2. Responsivity (R)

Responsivity quantifies how efficiently a photodetector converts incident optical power into an electrical current. It is defined as the photocurrent generated per unit of incident light power and is given by:

$$R = I_{ph}/(AP) \quad (1.2)$$

- $I_{ph} = (I_l - I_d)$: Net photocurrent (current due to illumination only), A: Effective active area of the device, P: Incident light intensity (power per unit area) [23].

Responsivity is typically measured in A/W. A higher responsivity means the device generates more current for a given light intensity, indicating better performance.

3. External Quantum Efficiency (EQE)

The External Quantum Efficiency (EQE) describes the percentage of incident photons that are converted into collectible charge carriers (electrons or holes). It is a crucial parameter for assessing the photodetector's efficiency and is calculated as:

$$EQE\ (\%) = [(hcR)/q\lambda] \times 100 \quad (1.3)$$

- h: Planck's constant (6.626×10^{-34} J·s), c: Speed of light (3×10^{8} m/s), q: Elementary charge (1.602×10^{-19} C), λ: Wavelength of incident light.

A high EQE (close to 100%) indicates that nearly all incoming photons contribute to the photocurrent, making the device highly efficient [23].

4. Detectivity (D)

Detectivity is a measure of a photodetector's ability to detect weak optical signals, especially in the presence of noise. It combines responsivity and dark current to evaluate signal-to-noise performance:

$$D = (R\sqrt{A})/\sqrt{2qI_d} \quad (1.4)$$

- A: Device area, I_d : Dark current.

Detectivity is expressed in Jones ($cm \cdot Hz^{1/2} \cdot W^{-1}$). A higher detectivity means the device can detect fainter light signals, which is essential for applications like biomedical imaging or night-vision sensors [24].

5. Rise and Decay Times

The rise time is the duration required for the photocurrent to increase from 10% to 90% of its maximum value when light is turned on. Conversely, the decay time is the time taken for the photocurrent to drop from 90% to 10% when the light is turned off. These parameters describe the temporal response of the photodetector.

A fast rise/decay time indicates a quick response to light changes, which is critical for high-speed applications like optical communications.

6. Noise-Equivalent Power (NEP)

The **Noise-Equivalent Power (NEP)** represents the minimum detectable light power at which the signal equals the noise level. It is calculated as:

$$NEP = \frac{\sigma_{I_{dark}}}{R\sqrt{\Delta f}} \quad (1.5)$$

- $\sigma_{I_{dark}}$: Standard deviation of dark current (noise), Δf: Bandwidth (set to 1 Hz for standardization).

NEP is measured in $W/Hz^{1/2}$. A lower NEP indicates better sensitivity to weak light signals, as the device can distinguish smaller signals from noise.

1.4 Fundamental Principles of Semiconductor Materials for Photodetection Applications

Semiconductors exhibit electrical conductivity between that of conductors and insulators, with resistivity values ranging from 10^{-3} to 10^{8} Ω·cm. This behavior arises from their electronic band structure, which governs their optoelectronic applications. The band theory of solids describes allowed energy bands separated by forbidden gaps, defining a material's electrical and optical properties.

The valence band (VB) contains bound electrons at absolute zero temperature, while the conduction band (CB) holds free electrons that move under an applied field. The energy difference between the valence band maximum (VBM) and conduction band minimum (CBM), known as the bandgap (E_g), typically ranges from 0.1 to 3.0 eV in semiconductors. Photons with energy greater than E_g excite electrons from the VB to the CB, generating electron-hole pairs essential for photodetection.

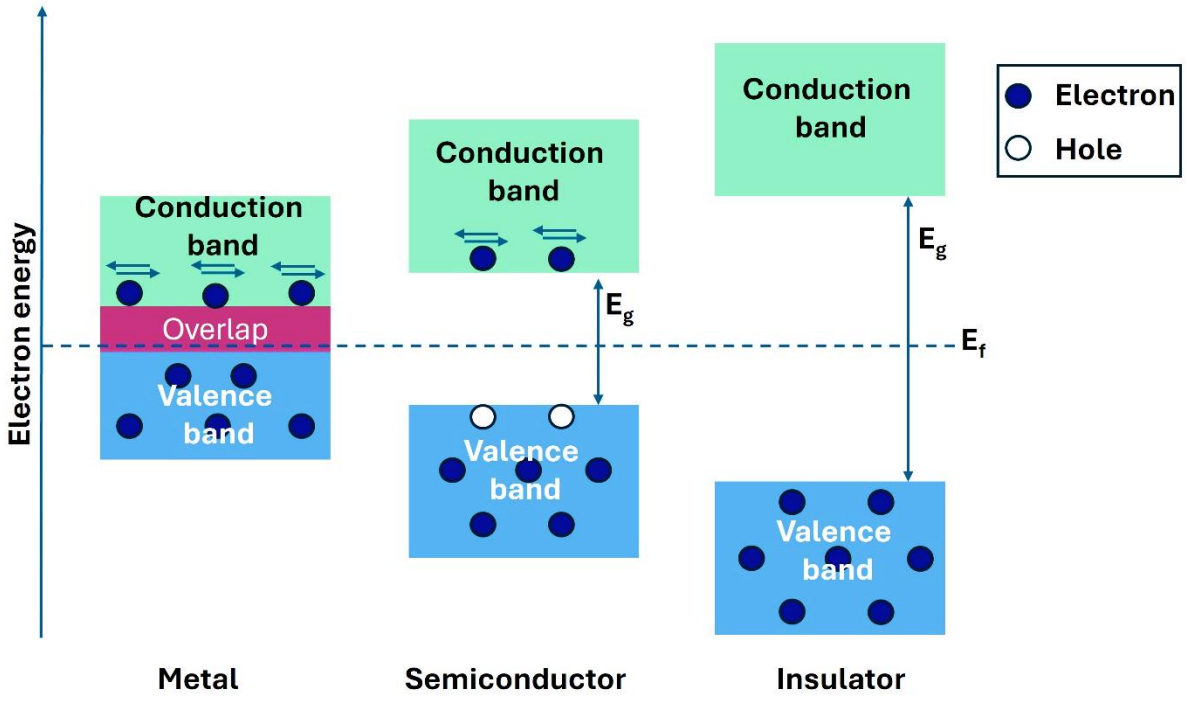

Figure 1.3. Schematic representation of materials based on their position of valence band and conduction band.

Semiconductors can have either a direct or indirect bandgap. In direct bandgap materials (e.g., GaAs, CdTe), the VBM and CBM align in k-space, allowing efficient optical transitions

without phonon assistance. This results in high absorption coefficients (>10^4 cm^{-1}) and strong radiative recombination, making them ideal for optoelectronic applications. In contrast, indirect bandgap semiconductors (e.g., Si, Ge) require phonon participation to satisfy momentum conservation, reducing their optical absorption efficiency [25].

Phonons, the quantized vibrations of the crystal lattice, significantly influence semiconductor behavior by:

- Facilitating momentum conservation in indirect transitions,
- Governing carrier scattering and mobility,
- Contributing to thermal conductivity.

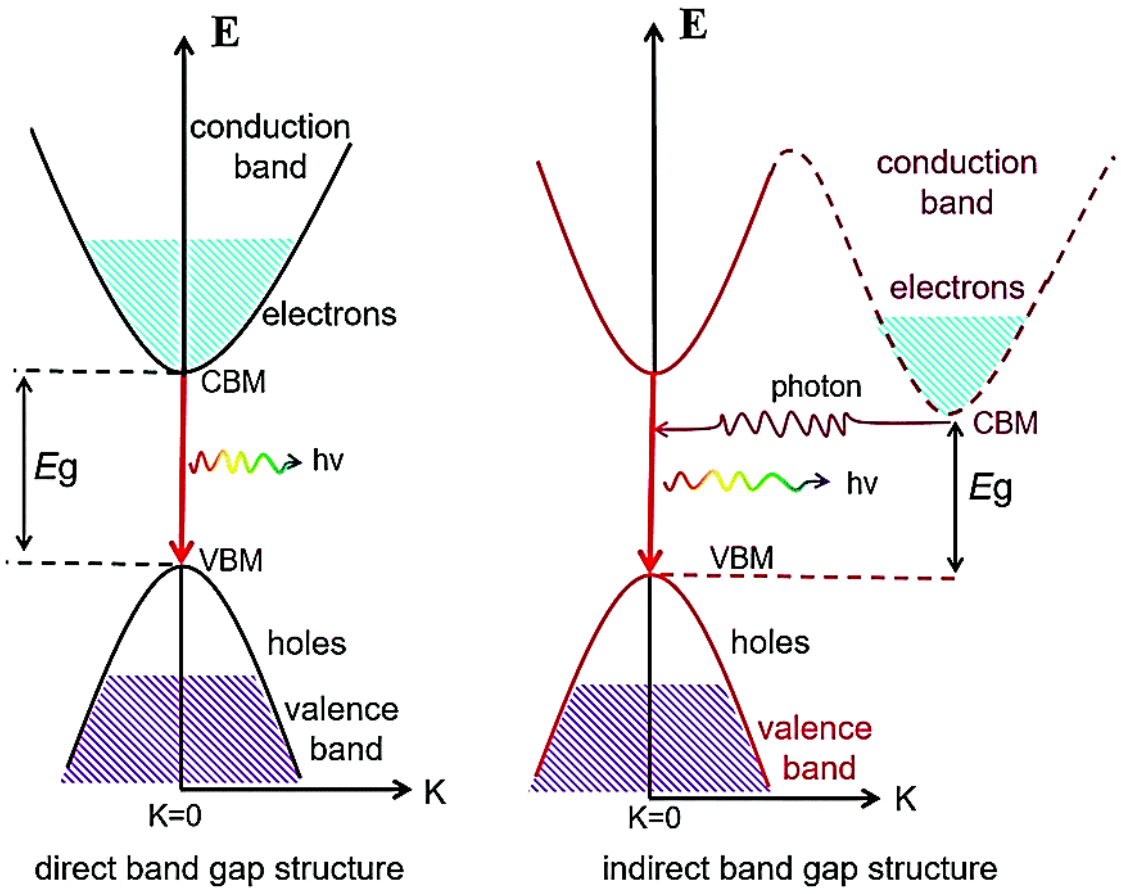

Figure 1.4. For direct bandgap semiconductors, the conduction band minimum andvalence band maximum have the same k-vectors. In contrast, indirect bandgap semiconductors have different k values.

The Fermi level (E_f) represents the electron chemical potential and varies with temperature. In intrinsic semiconductors, E_f lies near mid-gap. Doping shifts E_f, with donor impurities moving

it toward the CB (n-type) and acceptors shifting it toward the VB (p-type). This controlled modulation of E_f enables precise tuning of carrier concentrations and junction properties.

For thin-film photodetectors, semiconductor properties influence:

- **Bandgap engineering** through quantum confinement effects in nanostructured materials, allowing spectral tuning by adjusting thickness [26].
- **Enhanced light-matter interaction** through optical confinement, increasing absorption efficiency [27].
- **Controlled carrier transport** via defect engineering, optimizing electron mobility while minimizing recombination losses [28].
- **Strain modulation** of electronic properties through substrate-induced lattice strain, tailoring electronic behavior [29].

The selection and optimization of semiconductor materials require balancing these interdependent factors to achieve desired photodetector performance, including spectral response, detectivity, response time, and stability. Focusing on lead-free antimony-based semiconductors, materials such as perovskites, rudorffites, and chalcogenides are gaining traction as alternatives to lead-based counterparts, addressing toxicity and environmental concerns. Antimony chalcogenides have demonstrated photovoltaic efficiencies exceeding 10% [30], while perovskite-inspired antimony materials offer improved stability and reduced toxicity [31]. Chalcogenide perovskites, with tunable bandgaps and environmental resilience, are promising candidates for thin-film solar applications [32]. Integrating these lead-free semiconductors into thin-film technologies advances the development of efficient, stable, and sustainable optoelectronic devices.

1.5 The Structural and Compositional Evolution of lead- free perovskites- Inspired Semiconductors

The development of semiconductors began in the early 20th century with studies on the electrical properties of materials like silicon and germanium, leading to the invention of the transistor in 1947, which revolutionized modern electronics. Over time, research expanded into

alternative semiconductors, including chalcogenides, a class of materials containing sulfur, selenium, or tellurium, known for their tunable optical and electronic properties.

Meanwhile, the field of metal-halide perovskites has expanded significantly in recent years, driven by the search for lead-free alternatives that combine structural diversity with promising optoelectronic properties. While the term *perovskite* originally referred to calcium titanate ($CaTiO_3$), named in honor of mineralogist Lev von Perovski, its usage has evolved to encompass a broad range of compounds sharing the same crystallographic framework.

Research in the field of perovskite materials has attracted substantial interest due to their remarkable properties and potential applications in various optoelectronic devices. Of particular interest are metal halide perovskites with the general formula $APbX_3$, where A represents a monovalent cation and X denotes a halide anion.

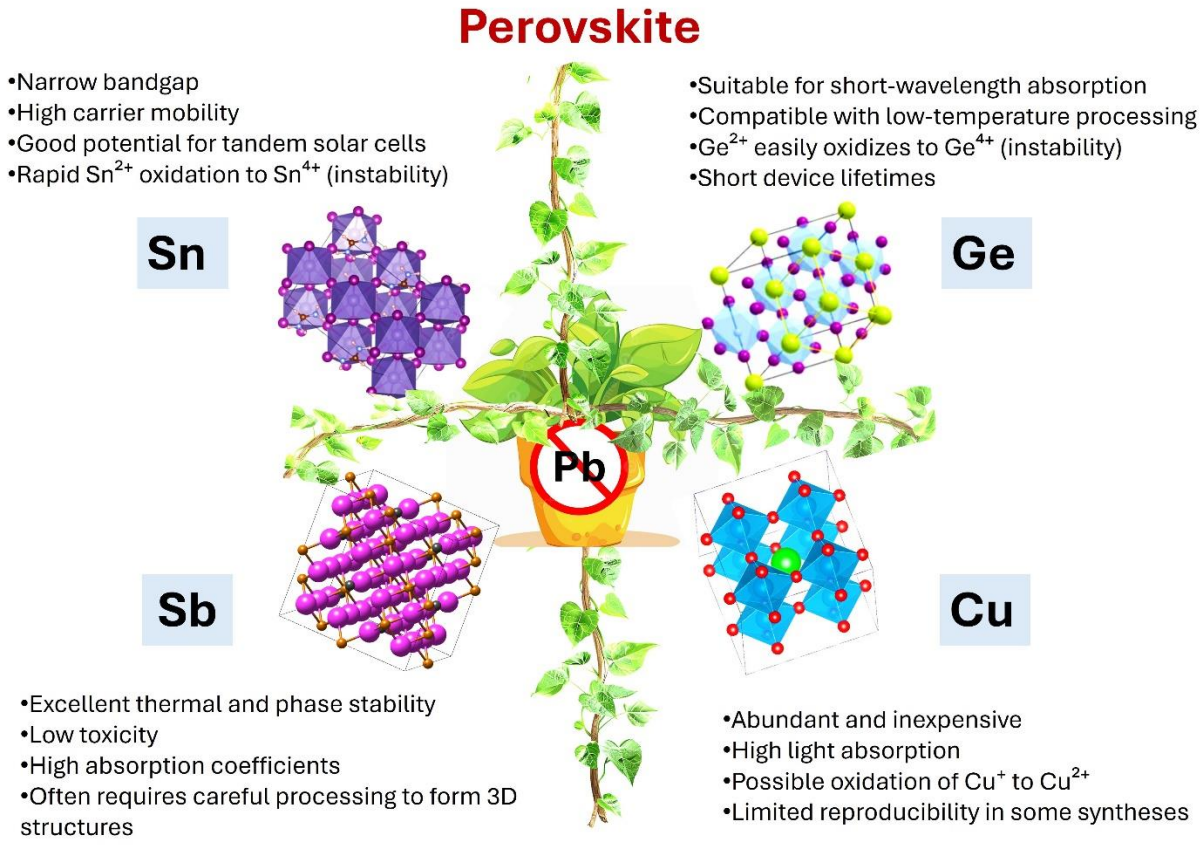

Figure 1.5. A few kinds of common lead-free organic-inorganic hybrid perovskite structures.

Lead-based perovskites, such as methylammonium lead iodide ($MAPbI_3$), have showcased outstanding optoelectronic characteristics, making them promising candidates for

photovoltaic applications. However, concerns regarding the toxicity and environmental impact of lead have prompted researchers to explore alternatives free from lead that offer comparable or superior performance while addressing sustainability challenges. This thesis centres on the development and characterization of lead-free perovskite materials as potential substitutes for lead-based counterparts, with the goal of advancing the field of optoelectronics towards more sustainable and eco-friendly solutions.

Lead-free halide perovskites encompass post-transition metal or metalloid elements. Elements like tin and germanium, belonging to the same group as lead, are deemed indispensable because of their susceptibility to oxidation, which can lead to rapid deterioration of desirable photovoltaic properties. Additionally, tin compounds are known to be toxic, with well-documented adverse effects on human health.

The substitution of lead with environmentally friendly and non-toxic elements has paved the way for the development of lead-free metal halide perovskites. Lead halide-based perovskite materials present limitations such as toxicity, water solubility, bioavailability, carcinogenicity, and instability when exposed to ambient conditions such as air, heat, humidity, and light. As a result, various elements like Sn, Ge, Bi, Sb, and specific transition metals have been investigated as potential substitutes for synthesizing perovskite structures with appealing optoelectronic properties [33].

The replacement of lead in halide perovskites has been explored through several strategic approaches as shown in Figure 1.6. One prominent strategy involves isovalent substitution, where Pb^{2+} is replaced by other divalent cations such as group 14 elements (e.g., Sn^{2+}, Ge^{2+}), alkaline earth metals (e.g., Mg^{2+}, Ca^{2+}, Sr^{2+}, Ba^{2+}), and certain transition metals (e.g., Mn^{2+}, Fe^{2+}, Ni^{2+}, Cu^{2+}, Cd^{2+}) [34,35]. These substitutions aim to retain the ABX_3 perovskite framework, though stability and oxidation issues—especially in Sn^{2+} and Ge^{2+}—remain significant challenges.

A second approach is heterovalent substitution, wherein Pb^{2+} is replaced by a combination of cations with different valence states. This includes aliovalent trivalent cations such as Sb^{3+} and Bi^{3+}, which do not maintain the ABX_3 structure but instead lead to the formation of vacancy-ordered perovskites with the general formula $A_3B_2X_9$, typically adopting 0D or 2D layered structures [36,37]. These materials exhibit high stability and moisture resistance but often suffer from lower carrier mobility due to reduced dimensionality.

Another variant of heterovalent substitution is the mixed-valence strategy, wherein Pb^{2+} is replaced by a combination of monovalent (e.g., Tl^{+}, Ag^{+}) and trivalent (e.g., Bi^{3+}, In^{3+}) cations, forming double perovskites with the general formula $A_2B(I)B(III)X_6$. Notable

examples include $Cs_2AgBiBr_6$ and $Cs_2AgInCl_6$, which exhibit indirect bandgaps and improved environmental stability [38,39].

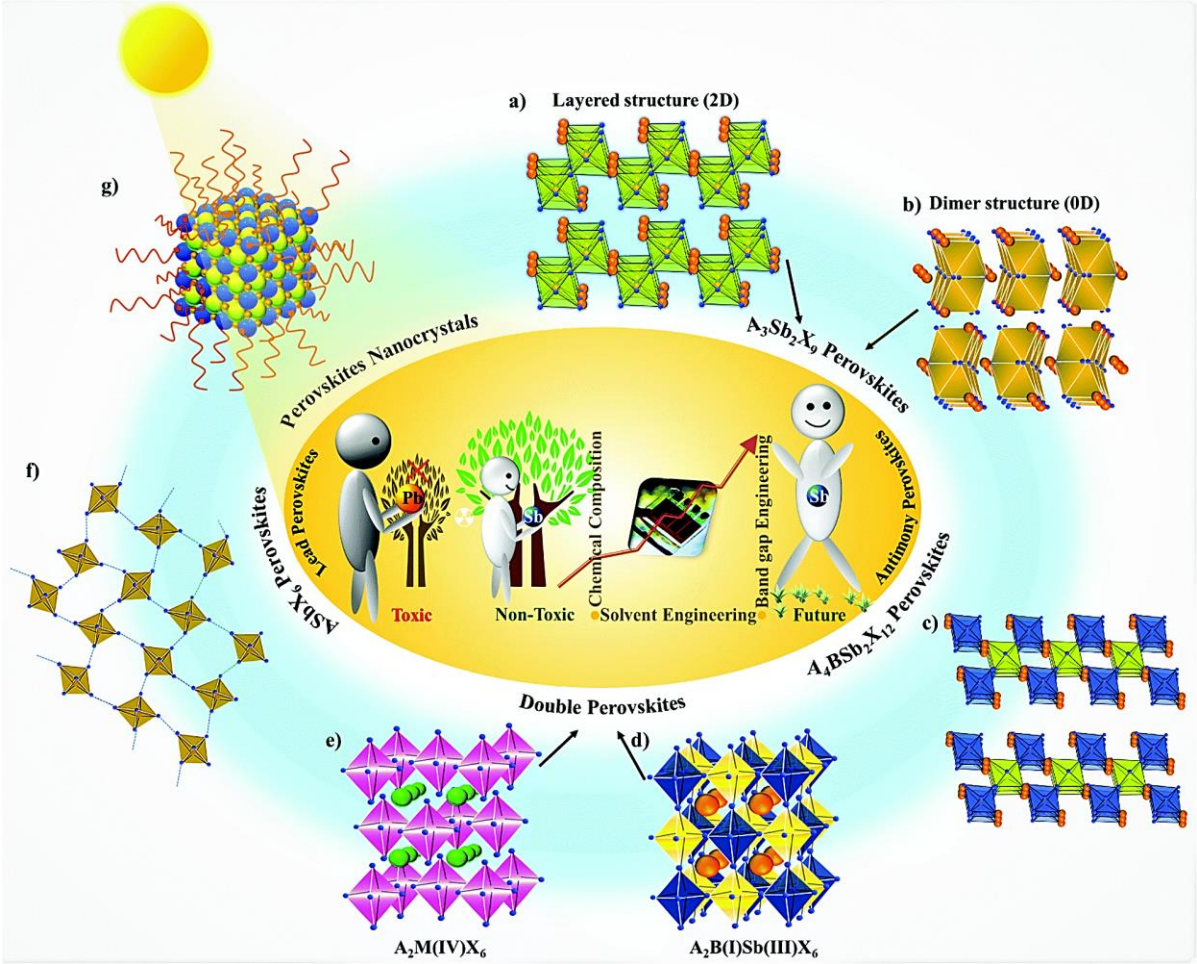

Figure 1.6. Schematic crystal structures of (a) a corner-sharing octahedron layered structure (2D) α-$A_3Sb_2X_9$ perovskite; (b) face-sharing fused bioctahedron dimer structure (0D) $A_3Sb_2X_9$ perovskite; (c) polyhedral model of a mixed metal halide $A_4BSb_2X_{12}$ perovskite; (d) polyhedral model of a mixed metal A_2BSbX_6 double perovskite; (e) perspective view of the $A_2M(IV)X_6$ crystal structure (cubic) with one-half deficient M; (f) antimony(V) halide complex where $[SbX_6]$- octahedra form an integrated 3D framework through halogen interactions (X…X); and (g) illustration of perovskite quantum dot with stabilizing ligands (Figure adapted from reference [40]).

An emerging method is the split-anion approach, where the halide anion (X^-) is partially or fully replaced by chalcogenide anions (e.g., S^{2-}, Se^{2-}). This leads to the formation of chalcogenide-halide perovskites or hybrid materials with enhanced covalent bonding, resulting in improved long-term thermal and chemical stability under ambient conditions [41].

Additionally, oxide-based perovskites have garnered attention for their inherent structural robustness and chemical stability, although their indirect bandgaps and poor charge transport limit their use in high-performance optoelectronic applications [42].

Group VA metals such as bismuth and antimony, known for their trivalent forms, offer high chemical stability and lower toxicity, making them attractive candidates as light absorbers. However, their wide bandgaps, high exciton binding energies, and heavy carrier effective masses pose limitations on their performance. Currently, the power conversion efficiency of VA metal halides trails behind that of lead halides. Improving the performance of VA metal-based halide materials requires a thorough exploration of their film formation mechanisms, structures, and electronic properties to develop materials with appropriate bandgaps and minimal defect characteristics [43].

The Rudorffite Classification and Its Historical Context

In 2017, Turkevych et al. proposed the term *rudorffite* to describe a distinct subset of ternary metal-halide compounds structurally related to $NaVO_2$, a synthetic oxide first characterized by Walter Rüdorff. $NaVO_2$, which crystallizes in a rhombohedral $CdCl_2$-type structure (space group *R3m*), consists of alternating layers of edge-sharing [NaO_6] and [VO_6] octahedra. However, long before this classification, Okada and Keil (1982) had assigned the name *caswellsilverite* to $NaVO_2$, a designation formally accepted by the International Mineralogical Association (IMA). This name paid tribute to geologist Dr. Caswell Silver and linked $NaVO_2$ to $NaCrS_2$, a structurally similar mineral identified in meteorite fragments from Norton County, Kansas, USA [44,45].

Both $NaVO_2$ and $NaCrS_2$ adopt the *R3m* space group, forming a layered rhombohedral network characterized by alternating metal-oxygen (or metal-sulfur) octahedra. Inspired by this structural motif, Turkevych et al. identified a comparable arrangement in ternary silver-bismuth iodides ($Ag_xBi_\gamma I_{x+3\gamma}$). In these halide-based analogs, the extended metal-halide framework comprises edge-sharing [AgI_6] and [BiI_6] octahedra, forming a similar rhombohedral phase. However, a key distinction arises in silver-bismuth iodides: whereas the cationic sublattice in $NaVO_2$ and $NaCrS_2$ is fully occupied, $Ag_xBi_\gamma I_{x+3\gamma}$ intrinsically incorporates cationic vacancies ([ΔI_6]) due to charge neutrality constraints imposed by the oxidation states of Ag^+ and Bi^{3+}. These vacancies significantly influence defect-mediated charge transport and ion migration, crucial factors in the optoelectronic behavior of these materials [44].

Beyond Rhombohedral Symmetry: The Emergence of Defect Spinels

While the *R3m* structure provides one framework for metal-halide compositions, an alternative structural configuration emerges in certain members of the $A_xB_yX_{x+3y}$ family (where $A^+ = Ag^+/Cu^+$, $B^{3+} = Bi^{3+}/Sb^{3+}$, $X^- = I^-/Br^-$). Some ternary silver and copper halides crystallize in a cubic spinel-like structure belonging to the *Fd3m* space group, reminiscent of the mineral spinel ($MgAl_2O_4$) [44][46].

In classical spinel structures, divalent cations (e.g., Mg^{2+}) occupy tetrahedral sites, while trivalent cations (e.g., Al^{3+}) are situated in octahedral coordination. However, in silver-bismuth and silver-antimony halides exhibiting *Fd3m* symmetry, the tetrahedral positions remain vacant, with both Ag^+ and Bi^{3+} (or Sb^{3+}) residing exclusively in octahedral coordination. This vacancy-driven structural adaptation classifies these materials as *defect spinels*, a term that reflects their deviation from conventional spinel configurations. The presence of intrinsic cationic vacancies alters their electronic band structure and ionic conductivity, distinguishing them from other ternary halide systems [44].

Although the atomic arrangements of silver and copper pnictohalides differ from those of caswellsilverite (rudorffite), recent literature has extended the *rudorffite* designation to include cubic defect spinel phases within the $A_xB_yX_{x+3y}$ family. This broad application of the term has led to some ambiguity, as the structural differences between rhombohedral and spinel-like ternary halides are significant. Given this complexity, the term *silver/copper pnictohalides* provides a more precise classification, capturing the diverse structural adaptations these materials exhibit [44].

This nomenclature not only acknowledges their relationship to perovskite-inspired frameworks but also highlights their remarkable compositional and structural versatility. As research advances, a deeper understanding of how these structural variations influence electronic, optical, and defect properties will be essential in optimizing their functionality for next-generation optoelectronic applications.

1.6 Rationale for Material Selection and Identification of Research Gaps

The selected material systems—$Cs_3Sb_2I_9$, $AgSb_2I_7$, $Ag(Bi,Sb)_2I_7$, and Cu_2SbI_5—were chosen

for their ease of their **facile synthesis**, **distinct optoelectronic properties**, and potential to address critical challenges in photodetection, including **self-powered operation**, **spectral tunability**, and **interfacial charge transport efficiency**. Each system offers unique advantages while presenting specific limitations that warrant further investigation.

1.6.1 Literature Survey on Cesium Antimony Iodide

Cesium antimony iodide ($Cs_3Sb_2I_9$) has emerged as a promising lead-free halide perovskite-inspired material for optoelectronic applications, including photovoltaics and photodetection. Its intrinsic non-toxicity, chemical stability, and earth-abundant composition make it a favorable candidate over conventional lead-based perovskites, which suffer from environmental and long-term stability issues [47].

1.6.1.1 Crystal Structure and Dimensionality

Cesium antimony iodide ($Cs_3Sb_2I_9$) crystallizes in two distinct polymorphic forms—zero-dimensional (0D) dimer and two-dimensional (2D) layered structures—each exhibiting markedly different structural and electronic characteristic. The 0D dimer phase adopts a hexagonal structure (space group *P6₃/mmc*, No. 194), composed of isolated $[Sb_2I_9]^{3-}$ bioctahedra formed via face-sharing SbI_6 octahedra. These discrete units, spatially separated by Cs^+ ions, restrict orbital overlap, resulting in poor charge transport and an indirect bandgap of ~2.4 eV (k–Γ). Conversely, the 2D layered phase crystallizes in a trigonal structure (space group *P3m1*, No. 164), where infinite layers of corner-sharing SbI_6 octahedra are stacked and held apart by Cs^+ ions. This structural motif enhances in-plane orbital connectivity and charge delocalization, yielding a direct bandgap of ~2.05 eV (Γ–Γ) and improved charge transport. Due to its excellent thermal stability, reduced toxicity, strong visible light absorption (~10^5 cm^{-1}), and a band structure comparable to lead-halide perovskites, $Cs_3Sb_2I_9$ continues to be explored as a promising lead-free material for optoelectronic applications, including photodetectors and photovoltaics [47–52].

1.6.1.2 Optical and Electronic Properties

The optical and electronic behavior of $Cs_3Sb_2I_9$ is intimately tied to its structural dimensionality. The 0D and 2D polymorphs exhibit bandgaps typically ranging from 1.9 to 2.4 eV, depending on factors such as crystallinity, film orientation, and synthesis approach. The 0D dimer phase, with its spatially confined octahedral units, shows a wider indirect bandgap (~2.4 eV) and weak photoluminescence due to inefficient orbital overlap and high

exciton binding energy. In contrast, the 2D layered phase offers a narrower, direct bandgap (~2.05 eV) with enhanced charge transport, making it more suitable for light-harvesting applications. Despite these advantages, both phases often suffer from low charge carrier mobilities (~10^{-3} to 10^{-2} $cm^2 \cdot V^{-1} \cdot s^{-1}$) attributed to defect states and localized excitons. To overcome these limitations, recent strategies including halide substitution, cation alloying, and dimensional tuning have been proposed to optimize the optoelectronic performance of $Cs_3Sb_2I_9$-based devices [47,50,53–55].

1.6.1.3 Synthesis and Thin-Film Formation

Various solution- and vapor-based approaches have been developed to fabricate phase-pure $Cs_3Sb_2I_9$ thin films:

- **Solution processing** typically involves the co-dissolution of CsI and SbI_3 in high-boiling-point solvents such as DMSO or DMF, followed by spin-coating and thermal annealing. This method offers scalable film formation but can suffer from phase competition and incomplete conversion [53,56].
- **Anti-solvent engineering** enhances film crystallinity and morphology by inducing rapid nucleation during spin coating. A representative method includes the use of isopropanol as an antisolvent after spin-coating a CsI/SbI_3 solution in DMF:HCl, which significantly reduces pinhole formation and promotes the growth of larger grains [56].
- **Vapor-assisted deposition** offers precise control over film uniformity and stoichiometry. For instance, $Cs_3Sb_2I_9$ has been fabricated via co-evaporation of CsI and SbI_3, or by vapor-phase reaction after depositing CsI, followed by annealing in SbI_3 vapor [47]. Similarly, a two-step chemical vapor deposition (CVD) process using CsI and SbI_3 powders followed by thermal treatment has been used to produce microplate structures with high thermal stability and ultrafast photoresponse [57].
- **Colloidal synthesis** and **nanocrystal formation** have also been reported using high-temperature injection of Cs-oleate into an antimony precursor mixture. This method enables control over dimensionality and polymorph selection, with demonstrated success in synthesizing both layered and dimer polymorphs of $Cs_3Sb_2I_9$ [58,59].
- **Vapor-anion exchange methods** have recently been applied to fabricate high-quality layered $Cs_3Sb_2I_9$ films for optoelectronic devices such as LEDs and resistive-

switching memory. In this method, spin-coated films are exposed to SbI_3 vapor in a sealed environment to drive complete conversion and enhance crystallinity [60,61].

Film quality and phase purity in these methods are highly sensitive to factors such as precursor molar ratios, solvent dielectric constants, reaction atmosphere, and post-deposition annealing conditions. Therefore, optimizing each synthesis step is critical to achieving device-grade films.

1.6.1.4 Photovoltaic and Optoelectronic Applications

Solar Cells

Although $Cs_3Sb_2I_9$-based solar cells have not yet achieved the high efficiencies of lead-based perovskites, they have demonstrated power conversion efficiencies (PCEs) in the range of 1.5–3.2%, along with outstanding thermal and environmental stability [53,56,61]. Several strategies have been adopted to improve device performance:

- **Interface engineering**, involving the optimization of electron and hole transport layers, has helped enhance charge extraction and minimize recombination losses [53,61].
- **Halide and cation alloying** (e.g., Cl^-, Br^-, MA^+, Rb^+) has been used to modulate the band structure and reduce defect densities, enabling better film quality and device performance [58,59].
- **Doping and heterostructure formation** have also been explored to improve energy-level alignment and internal electric field strength [60,61].

While PCEs remain modest compared to Pb-based counterparts, the intrinsic stability and non-toxic composition of $Cs_3Sb_2I_9$ make it a strong contender for durable solar technologies.

Photodetectors

In addition to photovoltaics, $Cs_3Sb_2I_9$ is a promising material for photodetector applications due to its moderate bandgap (~1.8–2.2 eV) and ambient-phase stability. Devices fabricated using vapor-deposited $Cs_3Sb_2I_9$ microplates have shown ultrafast photoresponse, low dark current, and robust performance under visible light illumination [57,62].

Moreover, self-powered photodetectors based on this material have been realized by leveraging its internal electric field, enabling operation without external bias [60,61]. These

devices are notable for their high sensitivity and fast response speeds, establishing $Cs_3Sb_2I_9$ as a versatile candidate for optoelectronic applications.

1.6.1.5 Stability and Environmental Advantages

Compared to lead-based perovskites, $Cs_3Sb_2I_9$ demonstrates exceptional thermal and environmental stability. It retains both its structural integrity and optoelectronic performance under extended exposure to moisture, oxygen, and elevated temperatures [56,57,59]. Additionally, being completely lead-free, $Cs_3Sb_2I_9$ aligns well with environmental safety regulations, making it a promising material for green electronics and bio-compatible applications [58,60].

1.6.1.6 Current Challenges and Research Directions

Despite these promising features, $Cs_3Sb_2I_9$ still faces several critical challenges that limit its widespread application:

- **Low carrier mobility** and **high trap-state densities** reduce charge transport and limit device efficiency [58,59].
- **Controlling the dimensionality** between 0D (dimeric) and 2D (layered) polymorphs remains a synthesis-sensitive issue and is difficult to reproduce consistently across large-area devices [56,58].
- The **narrow bandgap tunability** (~1.9–2.2 eV) limits its utility in tandem architectures or devices requiring broadband absorption [59].
- **Optimization of device architecture**, especially **transport layer selection** and **interface passivation**, remains essential to achieving competitive power conversion efficiencies [53,61].

Ongoing research is increasingly focused on addressing the intrinsic limitations of *$Cs_3Sb_2I_9$* by engineering hybrid and heterostructured interfaces, exploring novel synthesis techniques: such as vapor anion exchange and nanocolloid-based methods and tailoring dimensionality and defect chemistry. These approaches aim to enhance charge transport, control polymorphism, and improve overall optoelectronic performance, thereby unlocking the full potential of *$Cs_3Sb_2I_9$* for next-generation device applications[58,60].

1.6.2 Literature Survey on Silver Antimony Iodide and Mixed-Alloy Rudorffite ($Ag(Bi,Sb)_2I_7$)

Silver antimony iodides are emerging lead-free halide materials of interest for optoelectronic devices, photodetectors, and photovoltaics due to their appropriate bandgap values and potential ferroelectric properties [44].

1.6.2.1 Crystal Structure and Composition

The crystal structure and composition of silver–antimony iodides (Ag–Sb–I) closely resemble their bismuth-based counterparts, as both belong to the family of pnictogen-based halides with a general formula of $A_xB_yX_{x+3y}$, where $A^+ = Ag^+$ or Cu^+, $B^{3+} = Sb^{3+}$ or Bi^{3+}, and $X^- = I^-$, Br^-, or Cl^- [44]. These compounds exhibit a variety of structural motifs depending on the A:B ratio. Silver-rich phases ($x > 1$), such as Ag_2SbI_5, tend to crystallize in a layered rhombohedral structure with R3m symmetry, wherein Ag^+ and Sb^{3+} ions are distributed across alternating <111> layers [44]. In contrast, Sb-rich compositions ($y > 1$), including $AgSb_2I_7$ and $AgSbI_4$, often adopt a cubic defect spinel-type structure with Fd3m symmetry, characterized by partially vacant octahedral sites within the cation sublattice [44]. These frameworks consist of edge-sharing $[AgI_6]$ and $[SbI_6]$ octahedra, forming three-dimensional networks similar to those observed in $AgBi_2I_7$ and other bismuth-based analogs [63]. Despite the electronic similarities between Sb^{3+} and Bi^{3+}, their differing ionic radii and electronegativities induce structural variations such as octahedral tilting and distinct bonding environments, which in turn impact lattice stability and electronic structure [64]. This compositional tunability underscores the structural diversity of the Ag–Sb–I system and highlights its adaptability for halide-based semiconductor development [44].

1.6.2.2 Optical Properties and Bandgap

Silver-antimony iodides, such as $AgSbI_4$ and Ag_2SbI_5, exhibit direct bandgaps typically ranging from 1.6 to 2.1 eV, making them promising candidates for visible-light optoelectronic applications including photodetectors and solar cells [44,65]. These materials demonstrate strong absorption coefficients in the visible spectrum, often exceeding 10^5 cm^{-1}, which is comparable to their silver-bismuth analogues. Bandgap estimations obtained through Tauc plot analysis confirm their suitability for efficient light harvesting. Notably, $AgSbI_4$ has shown thermochromic behavior, with its bandgap reducing from 1.68 eV to 1.55 eV upon heating under vacuum, suggesting potential for temperature-dependent optical modulation [65]. The optical characteristics of these materials are largely influenced by their

underlying crystal structures, which vary depending on stoichiometry. For instance, layered structures with R3m symmetry or defect spinel frameworks with Fd3m symmetry arise based on the relative Ag/Sb content, enabling compositional tunability of electronic and optical properties [44,64]. While photoluminescence studies on Ag–Sb–I systems remain limited, preliminary findings point to moderate radiative recombination and carrier lifetimes, highlighting the need for deeper investigation into defect dynamics and excitonic interactions in these compounds [64].

1.6.2.3 Synthesis Methods

- **Anti-solvent-assisted spin coating** has also been employed to synthesize hexagonal Ag_2SbI_5. In this method, AgI and SbI_3 are dissolved in a DMSO/HI solvent system, followed by thermal treatment at 110 °C to promote crystallization and improve film uniformity [66].

- **Solid-state synthesis under vacuum** has been used to obtain phase-pure $AgSbI_4$. This approach involves heating the mixed precursors at elevated temperatures, resulting in thermochromic behavior and a bandgap shift from 1.68 eV to 1.55 eV upon heating, highlighting the material's thermal responsiveness and structural stability [65].

- **Solution-based spin-coating** is a widely used technique for fabricating silver-antimony iodide films. Precursors such as AgI and SbI_3 are dissolved in polar solvents like dimethylformamide (DMF) and dimethyl sulfoxide (DMSO), often in combination with bismuth iodide (BiI_3) to form mixed-halide compounds such as Mixed- alloy Rudorffite ($AgBi_{2-x}Sb_xI_7$). The Sb/Bi ratio significantly influences film morphology and photovoltaic performance, with a 3:1 ratio yielding optimal results [64].

1.6.2.4 Device Applications

Silver-antimony iodides and their mixed-halide alloys, although structurally and electronically similar to silver-bismuth iodides, have seen limited exploration in device integration. However, tuning the Sb/Bi ratio in mixed-halide absorbers such as $AgBi_{2-x}Sb_xI_7$ has demonstrated improvements in grain morphology and photovoltaic performance, highlighting their potential in solar cell applications [64]. Devices fabricated from these materials could benefit from the compositional flexibility afforded by varying Sb and Bi content, which directly influences optoelectronic properties and charge transport

characteristics. Furthermore, the hexagonal Ag_2SbI_5 phase, obtained via anti-solvent-assisted spin coating followed by thermal treatment [66], presents promising structural stability that could be advantageous in device operation. The thermochromic $AgSbI_4$ phase, synthesized through solid-state reaction methods, exhibits a tunable bandgap that may be exploited for temperature-sensitive optoelectronic devices [65]. Although direct device studies remain sparse, these materials hold promise for future integration in photovoltaics and photodetectors due to their favorable bandgap tunability and material stability.

1.6.2.5 Stability and Environmental Impact

Silver-antimony iodides and their mixed-halide derivatives exhibit promising environmental stability compared to lead-based perovskites, addressing critical concerns related to toxicity and long-term device operation [44,64]. The inherent robustness of their crystal structures, particularly in phases like Ag_2SbI_5 and $AgBi_{2-x}Sb_xI_7$, contributes to enhanced moisture and thermal stability, which is crucial for practical optoelectronic applications [66]. Furthermore, the use of non-toxic and earth-abundant elements such as Sb and Ag aligns with the growing demand for environmentally friendly materials in sustainable device fabrication [67,68]. While these compounds demonstrate reduced environmental hazards, ongoing research is required to optimize synthesis protocols that minimize chemical waste and energy consumption during production [65]. The thermochromic behavior observed in $AgSbI_4$ also suggests potential for stable operation under variable thermal conditions, enhancing their suitability for real-world applications [65].

1.6.2.6 Research Gaps and Challenges

Despite the promising optoelectronic properties and improved environmental profile of silver-antimony iodides, several research gaps and challenges remain. Firstly, the synthesis of phase-pure and high-quality silver-antimony iodide thin films with scalable and reproducible methods is still limited, particularly when compared to their bismuth-based analogs [64,66]. Current fabrication techniques often involve complex multi-step processes or require precise control over precursor stoichiometry and processing conditions, which hinders large-scale production [66]. Additionally, the detailed understanding of the relationship between crystal structure, defect chemistry, and charge transport mechanisms in these materials remains incomplete, restricting the optimization of device performance [64].

Moreover, while preliminary studies have demonstrated the potential of mixed Sb/Bi compositions to tune optoelectronic properties, systematic investigations on stability under

operational conditions and long-term device reliability are scarce [64,65]. Another challenge lies in the limited exploration of silver-antimony iodides in functional device architectures beyond photodetectors, such as solar cells or memristive devices, which require further optimization of interfaces and charge extraction layers [65]. Finally, the environmental impact of the synthesis routes, including chemical usage and energy demands, has not been fully assessed, highlighting the need for greener and more sustainable fabrication approaches [67].

1.6.3 Literature Survey on Copper Antimony Iodide

Copper antimony iodides have recently gained attention as environmentally friendly, lead-free semiconductors for optoelectronic applications. Their favorable optoelectronic properties, isoelectronic substitution potential with bismuth-based counterparts, and compatibility with low-temperature synthesis methods make them promising candidates for photovoltaic and photodetector devices [44,48].

1.6.3.1 Crystal Structure

Copper antimony iodides represent an emerging class of lead-free semiconductors with promising structural stability. Jia et al. synthesized Cu_3SbI_6 using a conventional one-step spin-coating method and reported that the material crystallizes in a stable rhombohedral R3m space group, which is isostructural with Cu_2BiI_5 and $CuBiI_4$ variants previously explored in the Cu–Bi–I family [48]. This structural similarity offers a platform for understanding the lattice behavior and defect tolerance of Cu–Sb–I compounds in analogy with their Bi-based counterparts [44,69].

1.6.3.2 Optical Properties and Bandgap

The optical properties of Cu_3SbI_6 suggest it has a suitable bandgap for optoelectronic applications. Jia et al. observed promising optoelectronic features in the *R3m* phase of Cu_3SbI_6, supporting its candidacy for visible-light photodetection and solar cell use [48]. Although specific bandgap values were not elaborated in detail, prior studies on analogous Cu–Bi–I materials show bandgaps typically ranging from 1.7 to 2.0 eV [44,70], implying a comparable range may exist for Cu–Sb–I compounds due to their structural and electronic similarity.

1.6.3.3 Synthesis Methods

The synthesis of copper antimony iodide remains limited in literature, with Jia et al. pioneering the fabrication of Cu_3SbI_6 films through a one-step spin-coating method involving metal halide precursors in polar solvents such as DMSO [48]. In comparison, Cu–Bi–I materials have been synthesized using a variety of methods including solid-state reactions [69], melt-crystallization [44], one-step solution processing [44], and two-step thermal evaporation techniques [71]. The success of spin-coating in producing crystalline Cu_3SbI_6 suggests that low-temperature, scalable methods could be feasible for the Cu–Sb–I family as well.

1.6.3.4 Device Applications

Although the Cu–Bi–I system has been explored for use in photodetectors and photovoltaics, research on the device integration of Cu–Sb–I is at a nascent stage. Jia et al. demonstrated that Cu_3SbI_6 possesses optoelectronic properties suitable for device applications, indicating potential for future implementation in solar cells or photodetectors [48]. In parallel, Cu_2BiI_5 has shown high responsivity (>100 mA/W) in photodetector configurations, and its isoelectronic Sb analogs are anticipated to offer similar, if not enhanced, performance due to favorable band alignment and reduced toxicity [44].

1.6.3.5 Research Gaps and Challenges

Despite structural promise and favorable optical characteristics, copper antimony iodides remain largely unexplored. The lack of systematic studies on phase behavior, defect chemistry, and long-term stability hinders their practical deployment. The influence of stoichiometry on optoelectronic properties is still unclear, and comprehensive characterizations: such as time-resolved photoluminescence, carrier mobility, and environmental stability are missing. Moreover, device integration strategies remain underdeveloped, especially when compared to the broader copper–bismuth–iodide literature [44,48,71].

Hypothesis

Lead-free antimony-based semiconductors synthesized under ambient conditions can enable self-powered photodetection through ferroelectricity-driven charge separation and bandgap tunability.

General objective

To investigate the optoelectronic properties and photodetection performance of lead-free antimony-based semiconductors synthesized under ambient conditions via chemical bath, spin coating, drop casting, thermal evaporation and rapid iodization methodology, with a focus on self-powered operation, spectral tunability, and interfacial engineering for enhanced stability.

1.7 Specific objectives

Synthesize and Characterize Lead-Free Antimony-Based Materials

- To synthesize lead-free antimony-based materials ($Cs_3Sb_2I_9$, $AgSb_2I_7$, $Ag(Bi,Sb)_2I_7$, and Cu_2SbI_5) using facile and ambient condition processing methods.
- Characterize the structural, optical, and electrical properties of these materials using techniques such as X-ray diffraction (XRD), scanning electron microscopy (SEM), UV-Vis spectroscopy, and electrical measurements.

Investigate the Photodetection Performance

- Assess the photodetection capabilities of each material, focusing on spectral response, sensitivity, response time, and dark current.
- Evaluate the potential for self-powered operation through bias-free or low-bias photodetection in the materials, particularly $Cs_3Sb_2I_9$ and $AgSb_2I_7$, leveraging ferroelectric and heterojunction-enhanced charge separation.

Tune Bandgap and Enhance Stability

- Examine the effects of cation and anion alloying ($Ag(Bi,Sb)_2I_7$) on the bandgap and environmental stability of the materials.

Evaluate Low-Bias UV-Visible Detection Performance

- Investigate the performance of Cu_2SbI_5 as a low-bias UV-visible photodetector, focusing on its energy-efficient photodetection at minimal applied voltages.
- Compare the energy efficiency and photodetector performance of Cu_2SbI_5 against other lead-free materials to understand its potential for practical applications.

Develop a Comprehensive Structure-Property-Performance Relationship

- Establish correlations between material composition, structural characteristics, and optoelectronic performance for all five material systems.
- Provide insights into the design principles for future lead-free antimony-based photodetectors with improved efficiency, stability, and practicality in real-world applications.

1.8 Justification

The increasing environmental concerns over the toxicity and sustainability of lead-based semiconductors, particularly in optoelectronic devices like photodetectors, has driven the need for alternative materials that are both environmentally friendly and efficient. Antimony-based semiconductors, specifically lead-free systems, represent a promising solution due to their favorable optoelectronic properties, such as tunable bandgaps, high absorption coefficients, and potential for self-powered operation.

The materials selected for this research—$Cs_3Sb_2I_9$, $AgSb_2I_7$, $Ag(Bi,Sb)_2I_7$, and Cu_2SbI_5—offer distinct advantages, including ferroelectric polarization for bias-free detection, enhanced charge transport through heterojunctions, and improved environmental stability through alloying. These materials are synthesized under ambient conditions using simple, scalable methods, ensuring their practical applicability for large-scale production.

This work aims to fill key research gaps by systematically exploring the synthesis, photodetection performance, and stability of these materials. By addressing challenges such as spectral response limitations, interface recombination, and stability under operational conditions, this research will contribute to the development of cost-effective, efficient, and environmentally friendly photodetectors. Ultimately, the findings will support the transition from lead-based to lead-free alternatives, advancing the field of sustainable optoelectronic devices for applications in radiation detection, environmental monitoring, and other emerging technologies.

Chapter 2: Experimental Methods

This chapter describes experimental techniques to synthesize perovskite thin films. For the fabrication of thin films, we are focusing on chemical bath deposition, spin coating, and thermal evaporation methods. For the structure, morphology, elemental composition, and optoelectronic properties studies X-Ray diffraction (XRD), Raman spectroscopy, scanning electron microscopy (SEM), Energy dispersive X-Ray spectroscopy (EDS), X-Ray photoelectron spectroscopy (XPS), UV-Vis-NIR spectroscopy are used. A detailed discussion about the characterization techniques used is summarized.

2.1 Thin film deposition techniques

2.1.1 Chemical bath deposition (CBD) method

Chemical bath deposition (CBD), also known as chemical solution deposition, is a solution-based technique widely employed for the growth of thin films on various types of substrates, including irregular or large-area surfaces. This method relies on immersing well-cleaned substrates into an aqueous precursor solution containing metal ions and complexing agents (Figure 2.1). The film formation is governed by surface chemistry, where the substrate acts as an active site for heterogeneous nucleation. Ions from the solution adhere to all exposed surfaces of the substrate and initiate crystal growth, enabling the deposition of homogeneous films with uniform thickness and composition [72,73]. The growth typically occurs through two mechanisms: ion-by-ion deposition, where ions react directly at the substrate surface, and cluster-by-cluster deposition, where pre-formed hydroxide or colloidal clusters adsorb and convert into a solid film [74]. The efficiency and quality of the deposition are strongly influenced by parameters such as the bath temperature, which affects reaction kinetics and crystallinity; the pH of the solution, which controls ion speciation and solubility; the molar concentration of precursors, which regulates the ion supply; and the deposition duration, which determines film thickness and morphology [72–74]. Optimizing these parameters is essential for producing high-quality, adherent films suitable for electronic, photovoltaic, and optoelectronic applications.

Figure 2.1. Schematic diagram of chemical bath deposition method under ambient condition.

2.1.2 Spin coating method

Spin coating is a widely used technique for depositing uniform thin films on flat substrates using centrifugal force. In this process, a liquid precursor is dispensed onto the center of a substrate, which is then rotated at high speeds (typically ~3000 rpm). The centrifugal force spreads the fluid radially outward, while solvent evaporation and viscous drag help form a thin, uniform film with thicknesses ranging from nanometers to micrometers [75,76]. The process is governed by fluid dynamics and evaporation kinetics, and film thickness is primarily influenced by parameters such as spin speed, solution viscosity, concentration, surface tension, and spinning time [77].

Spin coating consists of four stages as shown in Figure 2.2: (i) Deposition, where the solution is applied; (ii) Spin-up, where the substrate accelerates and excess fluid is expelled; (iii) Spin off, during which the film thins uniformly due to viscous shear; and (iv) Evaporation, where solvent loss solidifies the film [76]. The final thickness and morphology are largely determined during the stable flow and evaporation stages, where the interplay of centrifugal force, solvent volatility, and fluid properties governs the film formation. Originally introduced for coating paints and photoresists, spin coating is now essential in microelectronics, photovoltaics, and nanomaterial research [75].

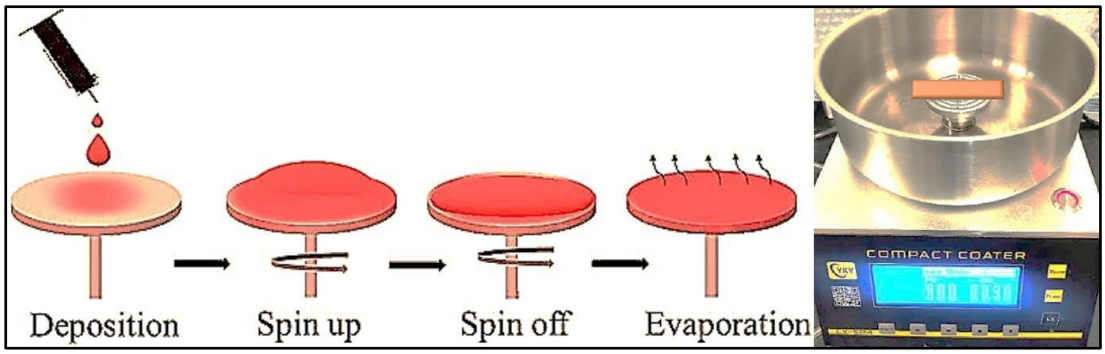

Figure 2.2. Different stages involved in spin coating process.

2.1.3 Thermal evaporation method

Thermal evaporation is a widely used physical vapor deposition (PVD) technique for fabricating thin films from metals, non-metals, or compounds such as oxides and nitrides [78]. In this process, the source material is placed in a resistively heated crucible or filament—commonly referred to as a "boat"—made of high melting point metals like tungsten, molybdenum, or tantalum [79]. The deposition is carried out under high vacuum conditions (~10^{-6} to 10^{-5} Torr) to minimize gas-phase collisions and ensure a clean environment for film growth [78–80].

When heated, the source material evaporates or sublimates, producing a vapor flux that travels in a line-of-sight trajectory toward the substrate. Upon reaching the cooler substrate surface, the vapor condenses and forms a thin film, with thickness controllable from angstroms to micrometers depending on process parameters [80]. The material holder is typically placed at the bottom of the chamber, while the substrate is suspended above it to enable uniform deposition.

Filament or resistive heating evaporation is a simple and cost-effective implementation, where the metal boat heats the material directly through Joule heating [79]. These boats not only facilitate melting and evaporation but also ensure safe operation at low voltages despite high currents. This method enables the deposition of both single and multilayer films with good uniformity and purity [78–80].

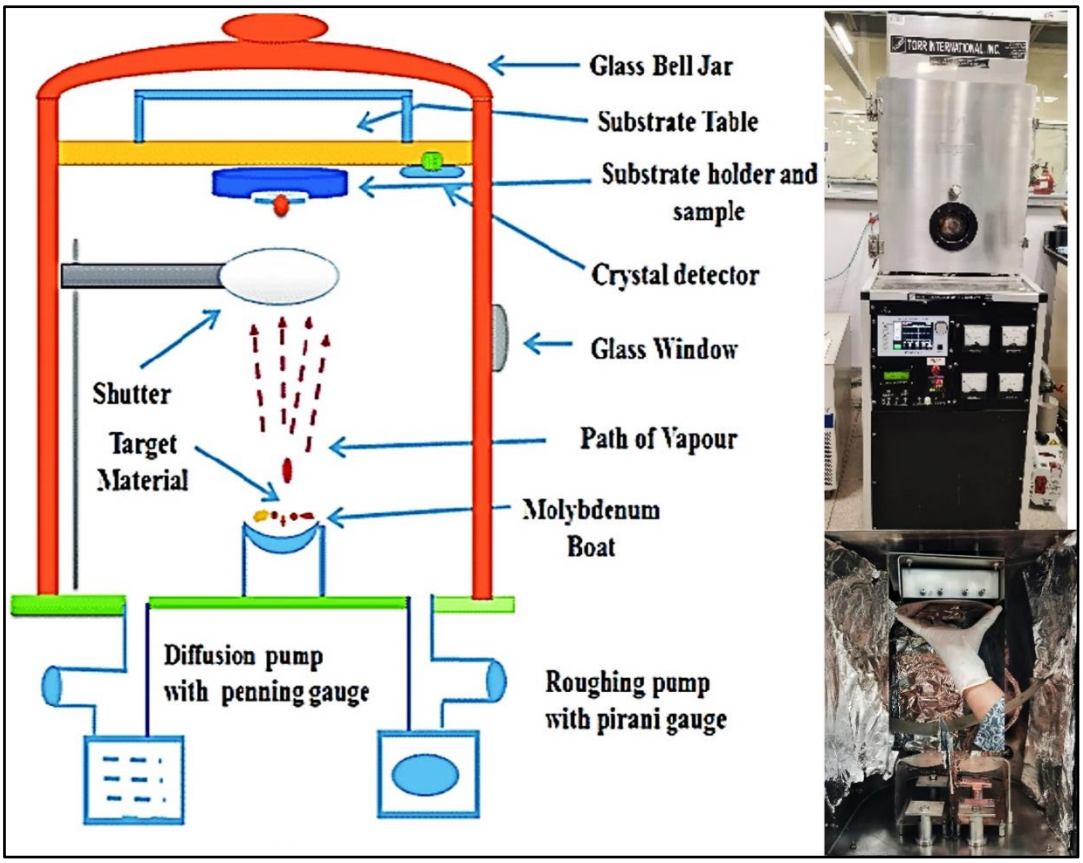

Figure 2.3. Basic schematic of the thermal evaporation process.

2.2 Characterization techniques

2.2.1 X-ray diffraction (XRD)

X-ray diffraction (XRD) is a powerful technique used to investigate the crystallographic structure, phase composition, and other structural parameters of materials. When X-rays, whose wavelengths are on the order of interatomic spacings, interact with a crystalline material, they are scattered by the electrons surrounding the atoms. The atoms within the crystal lattice serve as a periodic array of scattering centers, leading to constructive interference under specific conditions. This phenomenon produces a diffraction pattern that reflects the material's atomic arrangement [81].

The condition for constructive interference is described by Bragg's Law, which is given as:

$$n\lambda = 2d_{hkl}\mathrm{Sin}\theta \qquad (2.1)$$

where λ is the wavelength of the incident X-rays, n is the order of diffraction (typically taken as 1), d_{hkl} is the interplanar spacing for the Miller indices hkl, and θ is the angle of incidence. When the path difference between two reflected rays is an integer multiple of the X-ray wavelength, constructive interference occurs, producing a diffraction peak at a specific angle.

The intensities and positions of these peaks in the XRD pattern are characteristic of the atomic arrangement within the sample. Moreover, the average crystallite size D can be estimated from the peak broadening using the Scherrer equation:

$$D = \frac{0.9\lambda}{\beta \cos\theta} \tag{2.2}$$

where β is the full width at half maximum (FWHM) of the diffraction peak (in radians), λ is the X-ray wavelength, and θ is the Bragg angle [82]. This method is particularly useful for nanocrystalline materials, where line broadening due to small grain size is significant.

For our samples measurements were performed in the standard θ–2θ geometry using a PANalytical Empyrean diffractometer equipped with a Cu-Kα radiation source (λ = 1.54056 Å). The scans were carried out at room temperature to identify phase composition and crystallinity.

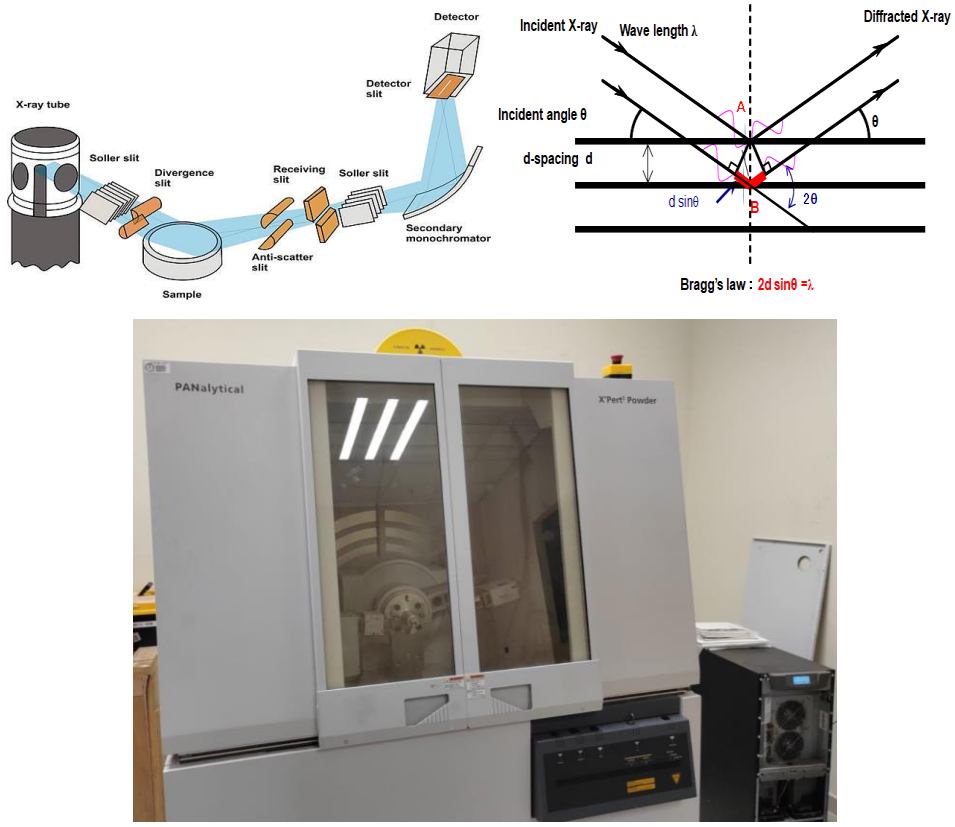

Figure 2.4. Schematic diagram of X-ray diffraction.

2.2.2 Raman spectroscopy

Raman spectroscopy is a non-destructive vibrational spectroscopic technique that provides valuable insights into the structural, chemical, and phase-related properties of materials. It is based on the Raman effect, first observed by C.V. Raman in 1928, which involves the inelastic scattering of monochromatic light, typically from a laser source [83,84]. When incident photons interact with the molecular vibrations or phonons of a material, most are scattered elastically (Rayleigh scattering), retaining their original energy. However, a small fraction undergoes inelastic scattering, resulting in energy shifts corresponding to specific vibrational modes of the molecules—this is known as Raman scattering [85].

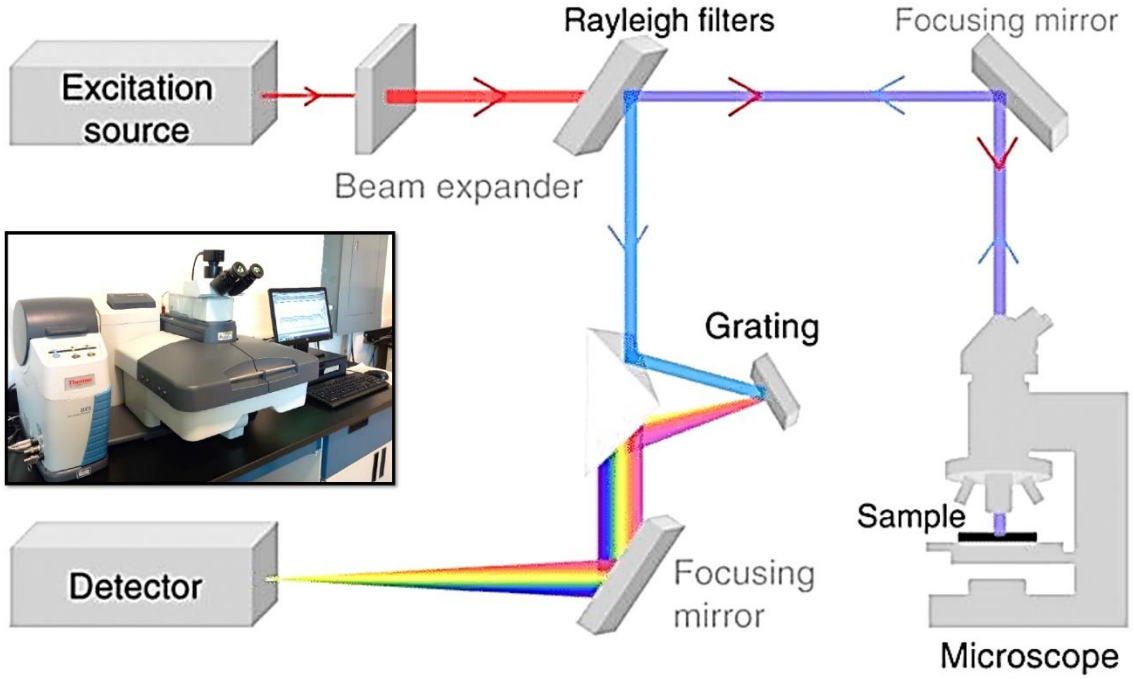

Figure 2.5. Schematic diagram of Raman spectroscopy

The Raman spectrum arises from these energy shifts and provides a molecular fingerprint unique to the vibrational, rotational, and other low-frequency modes of the sample. These spectral features can reveal a wide range of material characteristics, including crystallinity, molecular symmetry, chemical bonding, polymorphism, and phase composition [86]. The observed Stokes (lower energy) and anti-Stokes (higher energy) shifts in the spectrum are plotted as a function of Raman shift (in cm^{-1}), which reflects the difference in energy between the incident and scattered photons.

Due to its sensitivity to local structure and bonding, Raman spectroscopy is particularly

useful for analyzing semiconductors, perovskites, carbon materials, and molecular crystals, offering spatially resolved information when combined with confocal microscopy. This makes it a crucial tool in both fundamental research and materials development [84,85].

For our sample, Raman spectra were recorded using a Thermo Scientific DXR Raman microscope equipped with a 532 nm excitation laser.

2.2.3 Scanning electron microscopy (SEM) and Energy Dispersive X-ray Spectroscopy (EDS)

Scanning Electron Microscopy (SEM) is a powerful imaging technique used to analyze the surface morphology, microstructure, and compositional features of materials. It operates by scanning the surface of a sample with a finely focused beam of high-energy electrons. The interactions between the incident electron beam and the atoms in the sample generate a variety of signals, including secondary electrons (SE), backscattered electrons (BSE), characteristic X-rays, Auger electrons, and other emissions such as cathodoluminescence (CL) and absorbed current [87].

The most used signals in SEM analysis are secondary electrons and backscattered electrons. Secondary electrons, generated from inelastic scattering events near the sample surface, provide high-resolution images that reveal fine topographical details. In contrast, backscattered electrons, which result from elastic interactions between incident electrons and atomic nuclei, provide compositional contrast: heavier elements backscatter electrons more efficiently and appear brighter in BSE images, while lighter elements appear darker [87,88].

In addition to imaging, SEM systems are often coupled with Energy Dispersive X-ray Spectroscopy (EDS) to obtain elemental composition information. EDS detects the characteristic X-rays emitted when incident electrons displace inner-shell electrons from atoms in the sample, and outer-shell electrons transition to fill the vacancy. These X-rays are element-specific and allow for qualitative and semi-quantitative analysis of the elemental distribution within the sample. The spatial resolution of EDS is typically limited by the interaction volume of the electron beam and is suitable for identifying elements with atomic number $Z > 4$ (i.e., above beryllium) [87,89].

The combination of SEM and EDS is widely used in materials science,

nanotechnology, and solid-state chemistry for microstructural and compositional characterization. While SEM provides high-resolution morphological imaging, EDS complements it with localized chemical information, enabling phase identification, contamination analysis, and defect assessment in thin films and bulk materials [87–89].

For our sample, Energy-dispersive X-ray spectroscopy (EDX) analysis was carried out using a Hitachi SU8020 scanning electron microscope, which also provided surface morphology imaging.

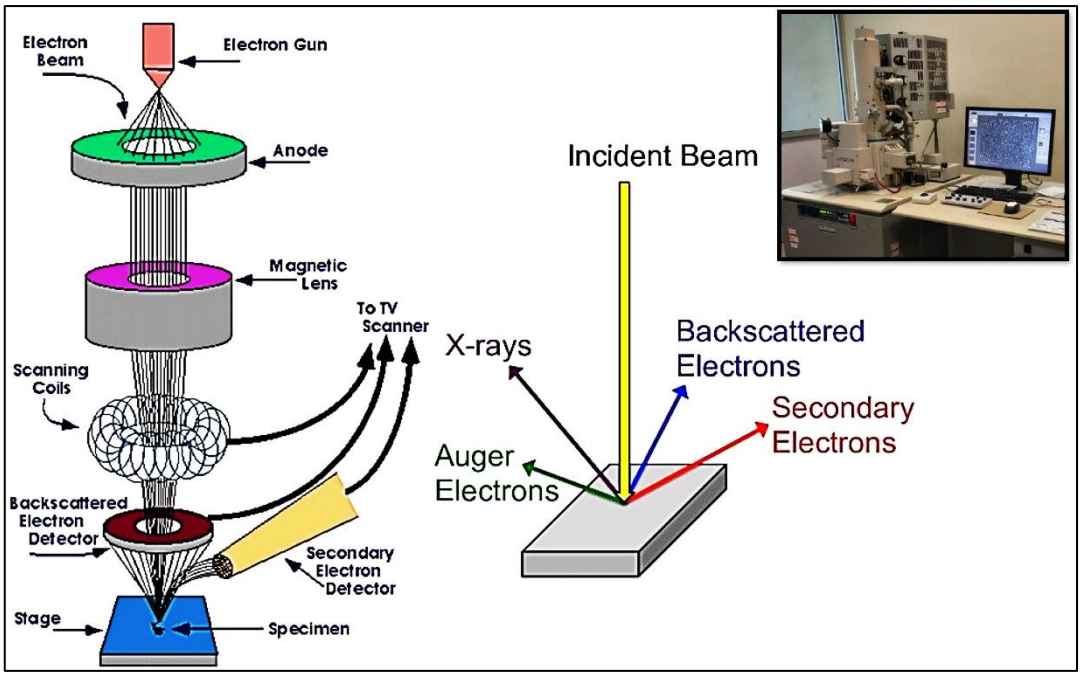

Figure 2.6. Schematic diagram of scanning electron microscopy

2.2.4 X-ray photoelectron spectroscopy (XPS)

X-ray Photoelectron Spectroscopy (XPS) is a powerful surface-sensitive analytical technique employed to investigate the elemental composition, chemical states, and electronic structure of materials within the top ~1–10 nm of the surface. It operates on the fundamental principle of the photoelectric effect, in which core-level electrons are ejected from a material upon irradiation with monochromatic X-rays, typically Al Kα (1486.6 eV) or Mg Kα (1253.6 eV) [90].

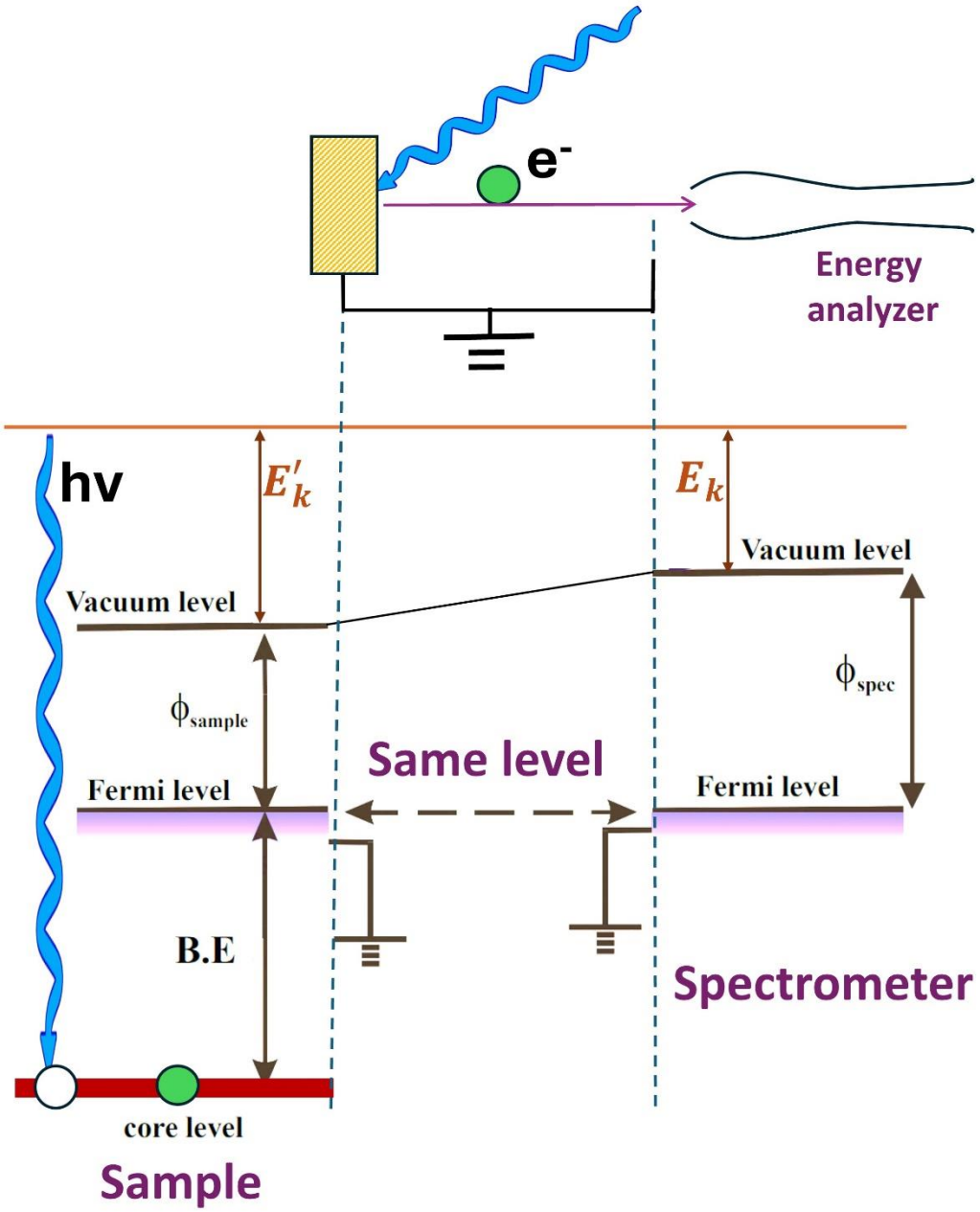

Figure 2.7. Schematic energy level diagram illustrating the photoemission process in X-ray Photoelectron Spectroscopy (XPS).

Figure 2.7 illustrates the energy level diagram involved in the XPS process. When a sample is irradiated with X-ray photons of energy hν, these photons interact with core-level electrons. If the photon energy exceeds the binding energy (B.E.) of the electron and the work function of the sample (ϕ_{sample}), the electron is ejected from the sample surface with an initial kinetic energy denoted as E'_k=hν−B.E.−ϕ_{sample}, which

is referenced to the sample's vacuum level [91].

As the photoelectron travels to the spectrometer, its kinetic energy is re-evaluated relative to the spectrometer's own vacuum level. This measured kinetic energy is represented as E_k, and it is what the detector uses to compute the corresponding binding energy. To enable a consistent energy reference, the Fermi levels of the sample and the spectrometer are aligned during measurement. The relationship between the photon energy, binding energy, spectrometer work function (ϕ_{spec}), and measured kinetic energy is described by the XPS equation:

$$BE = h\nu - E_k - \varphi_{spec} \qquad (2.3)$$

The spectrometer measures the kinetic energy of the emitted electrons and internally calculates the corresponding binding energies by calibrating against a known reference. Typically, the adventitious carbon C 1s peak at 284.6 eV is used for referencing [92].

The resulting XPS spectrum plots photoelectron intensity versus binding energy. Peaks at specific binding energies correspond to core-level electrons from distinct elements. Chemical shifts in these peaks reflect variations in the chemical environment, such as oxidation states or covalency, due to differences in screening, effective nuclear charge, or final-state effects [92–94].

XPS is particularly sensitive to the oxidation state of elements and can resolve multiplet splitting, shake-up satellites, and Auger peaks. Importantly, because only electrons originating from near the surface escape without energy loss, XPS inherently probes the surface region, making it invaluable for surface analysis of thin films, catalysts, and semiconductor interfaces [90,92–94].

In insulating or semiconducting samples, photoemission results in a net positive charge buildup as electrons are emitted. If not compensated, this leads to a uniform shift of all peaks toward higher binding energies—a phenomenon known as "charging." Charge neutralization is typically achieved using a flood gun or low-energy electron source [90,92–94].

Moreover, accurate determination of BE requires proper Fermi level alignment between the sample and the spectrometer. For metals, this alignment is straightforward due to the availability of free electrons. However, in semiconductors and insulators with low density of states at the Fermi level, poor alignment can complicate BE assignment and chemical state interpretation [90,92–94].

For our sample, the chemical composition and the elemental states were determined by a Thermo Scientific K-alpha X-ray photoelectron spectrometer.

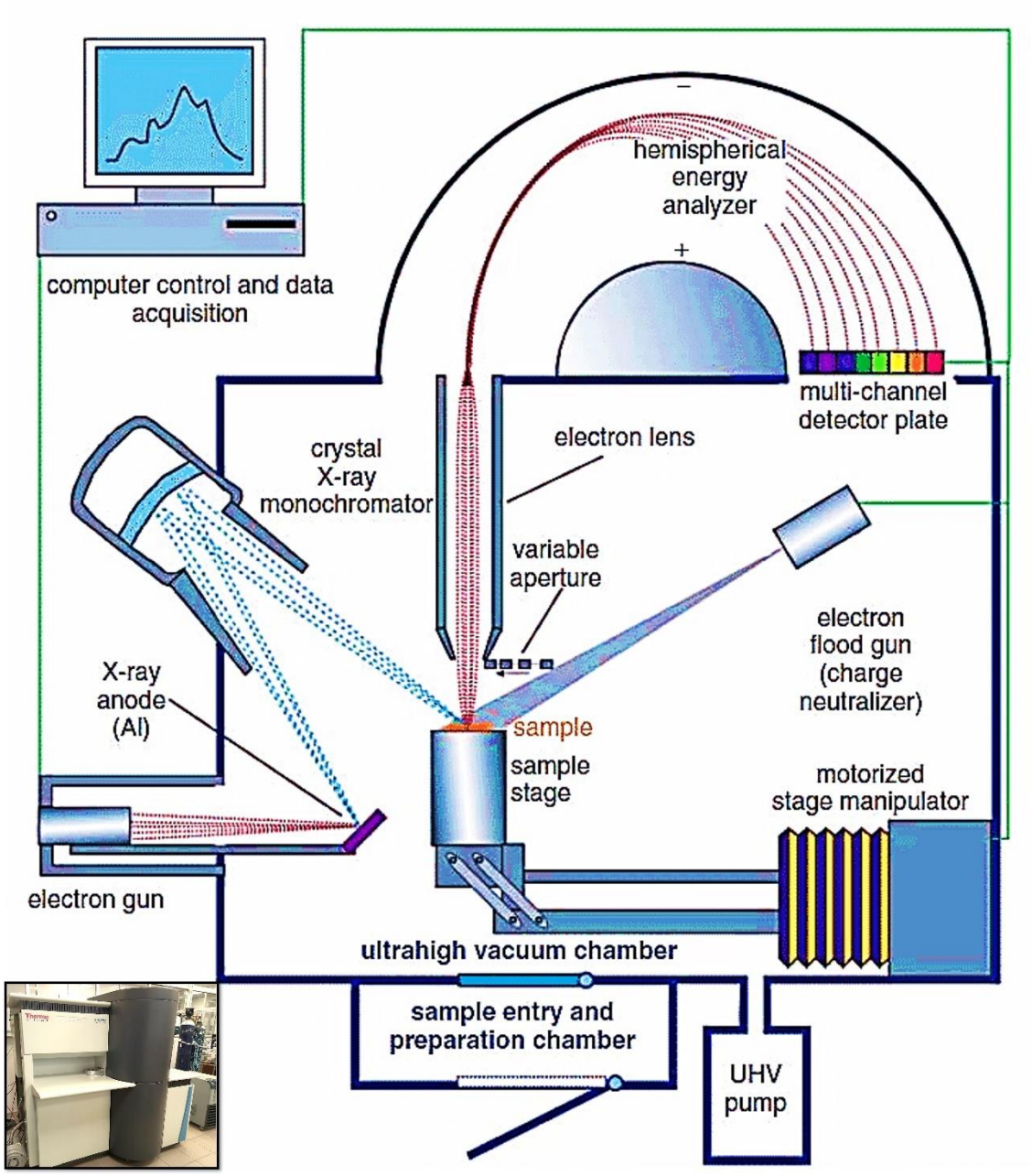

Figure 2.8. Schematic diagram of the XPS instrument showing the X-ray source, sample stage, electron optics, hemispherical energy analyzer, detector system, and vacuum chamber, with an inset image of the actual equipment used.

2.2.5 UV-Vis/NIR spectroscopy

Ultraviolet–Visible (UV–Vis) spectroscopy is a fundamental optical characterization technique widely utilized for the quantitative analysis of the interaction between

electromagnetic radiation and matter, particularly in the ultraviolet (200–400 nm) and visible (400–800 nm) spectral regions. This method provides valuable insights into the electronic structure of materials, including thin films and semiconductors, by enabling the investigation of light absorption processes corresponding to electronic transitions [95–97].

The technique operates by measuring the intensity of light transmitted through a sample in relation to a reference—typically air or an uncoated substrate. From this measurement, the transmittance and absorbance as a function of wavelength are determined, allowing for the construction of an absorption spectrum. This spectrum, typically plotted with absorbance (or optical density) on the y-axis and wavelength on the x-axis, reveals characteristic peaks associated with electronic transitions, such as those from the valence band to the conduction band, or transitions involving localized defect and trap states [95–97].

A crucial parameter extracted from UV–Vis data is the optical bandgap energy (Eg), which can be estimated using the Tauc relation given by:

$$(\alpha h\nu)^n = A(h\nu - E_g) \qquad (2.4)$$

where A is a constant, α is the absorption coefficient, h is Plank's constant, and ν is the frequency of the incident photon. The value of the exponent n depends on the type of optical transition, i.e., $n = 2$ for a direct allowed, $n = ½$ for an indirect allowed and $n = 2/3$ for a forbidden bandgap semiconductor respectively. To determine α, the measured transmittance (T) and reflectance (R) spectra are employed using the relation:

$$\alpha = \frac{1}{d}\ln\left[\frac{(1-R)^2}{T}\right] \qquad (2.5)$$

The thickness of the film (d) was determined using a stylus profilometer or SEM cross section analysis. With the calculated α values and photon energies, the Tauc plot $(\alpha h\nu)^n$ vs. hν allows for the extrapolation of the linear region to the photon energy axis, yielding the optical bandgap. This analysis is essential for evaluating the suitability of the thin film for optoelectronic applications such as photovoltaics, photodetectors, and light-emitting devices. Thus, UV–Vis spectroscopy serves as a pivotal technique in assessing the fundamental optoelectronic behavior of semiconductor materials [95–97].

For our sample, optical transmittance and reflectance spectra were obtained using a Jasco V-770 UV-Vis-NIR spectrophotometer.

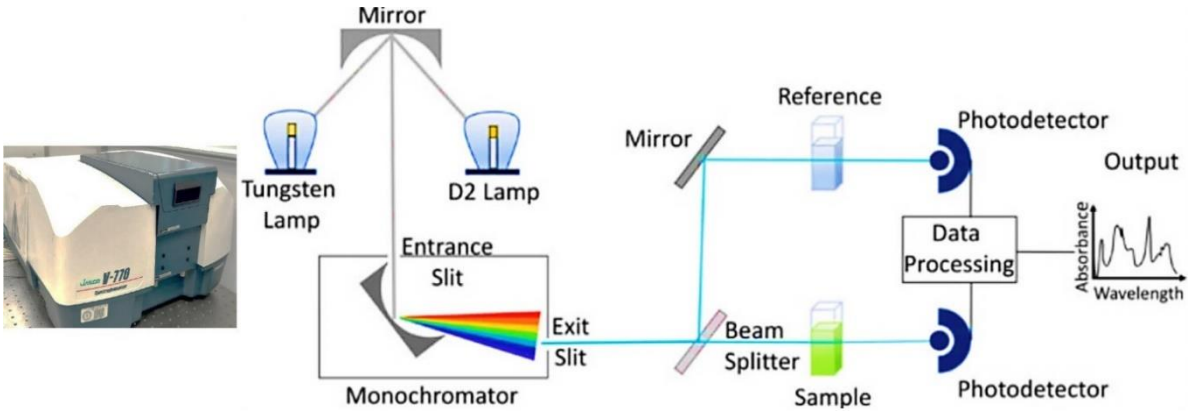

Figure 2.9. Schematic diagram of UV-Vis spectroscopy.

2.2.6 Electrical Measurements

To evaluate the optoelectronic performance of the fabricated thin-film devices, current–voltage (I–V) measurements were conducted using a precision source-measure unit (SMU), specifically the Keithley 6487 Picoammeter/Voltage Source, which offers high sensitivity for low-current detection down to the femtoampere range. This instrument enabled accurate characterization of photocurrent responses under both dark and illuminated conditions, essential for assessing photoconductive and photovoltaic behavior in semiconducting thin films [98,99].

Electrical contacts to the device were established using a flash-dry silver colloidal suspension (SPI Supplies, USA), which provides reliable ohmic contacts due to its high conductivity and compatibility with various substrate materials. The silver paste was applied and dried to form stable electrode interfaces, minimizing contact resistance and ensuring consistent electrical measurements across the sample area [98,99].

Measurements were performed both in the dark and under controlled illumination using a range of light sources, including a halogen lamp (for broadband white-light exposure), monochromatic LEDs, and laser diodes, to simulate different spectral regions of the solar spectrum and evaluate wavelength-dependent photoresponse. The light sources used were calibrated for intensity using a standard power meter, and the incident optical power density for each source was kept consistent across the active device area to

ensure reproducibility.

The specific illumination wavelengths and their corresponding power densities were as follows:

UV (405 nm): 10.0 mW·cm^{-2}

Blue (465 nm): 6.9 mW·cm^{-2}

Green (525 nm): 5.5 mW·cm^{-2}

Yellow (595 nm): 4.5 mW·cm^{-2}

Red (630 nm): 5.1 mW·cm^{-2}

Near-IR (740 nm): 13.4 mW·cm^{-2}

This systematic multi-wavelength illumination approach enabled the detailed assessment of the device's spectral responsivity and facilitated the identification of peak photoresponse regions. Such analysis is critical for establishing a direct correlation between the photophysical properties of the material—such as bandgap alignment and defect-related transitions—and the overall device performance, thereby validating its potential for practical optoelectronic applications [98,99].

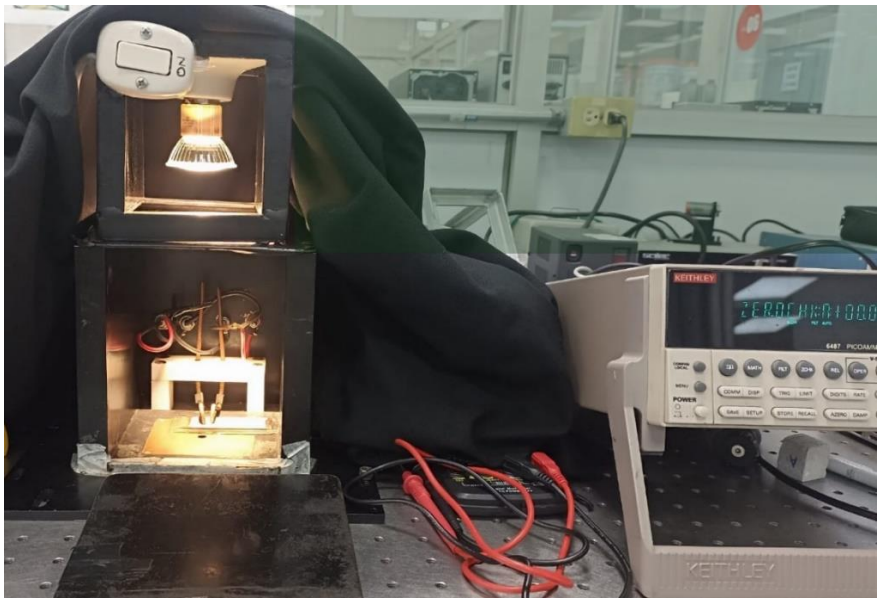

Figure 2.10. Schematic of the electrical measurement setup showing the sample connected to a Keithley source meter and illuminated by a light source for photoresponse characterization

Having laid the groundwork with fundamental methodologies and characterization techniques, the subsequent chapters explore the synthesis, detailed material characterization, and photodetector performance of perovskite-inspired antimony-based compounds.

Chapter 3: Synthesis and characterization of Cesium antimony iodide ($Cs_3Sb_2I_9$) for self-powered photodetector application

3.1 Introduction

The remarkable success of solar cells based on ammonium lead iodide perovskite has initiated a widespread search for lead-free inorganic perovskite materials. This effort aims to address the significant challenges of toxicity and stability inherent to lead-based perovskites [1,2]. In this context, all-inorganic cesium antimony iodide perovskite derivatives have emerged as highly promising alternatives [1,2].

Cesium antimony iodide derivatives are attractive due to the similar ionic radii and isoelectronic nature of antimony (Sb^{3+}) relative to lead (Pb^{2+}). When Sb^{3+} replaces Pb^{2+}, it forms SbI_6^{3-} octahedra through bonding with iodide anions. These octahedra then coordinate with cesium cations to construct the $Cs_3Sb_2I_9$ phase, which exists in two structural forms: a 0-D dimer (space group *$P6_3/mmc$*, No.194) and a 2-D layered structure (space group *$P\bar{3}m1$*, No.164) [3,4,5]. The electronic band structure of these materials reveals a band gap (k-Γ) of 2.4 eV [5,6]for the dimer phase and a direct band gap (Γ-Γ) of 2.05 eV for the layered phase [5,7]. Due to their improved stability, lower toxicity, large absorption coefficient (10^5 cm^{-1}), and electronic structure similar to lead-halide perovskites, $Cs_3Sb_2I_9$ has attracted considerable interest [48].

Despite the growing interest in $Cs_3Sb_2I_9$, only a limited number of studies have investigated its synthesis. Both physical and chemical methods have been employed to produce these materials. For example, a recent study demonstrated the synthesis of layered $Cs_3Sb_2I_9$ microcrystals using a PDMS (polydimethylsiloxane)-assisted physical vapor deposition method for photodetector applications [62]. Additionally, $Cs_3Sb_2I_9$ thin films have been prepared by co-evaporating CsI and SbI_3 [47], and by depositing a CsI layer through evaporation followed by annealing in SbI_3 vapor [47]. Another approach involved a two-step chemical vapor deposition of CsI and SbI_3 powders, followed by annealing at 180°C for 15 minutes in a nitrogen gas-filled tube furnace,

resulting in the fabrication of $Cs_3Sb_2I_9$ microplates [57]. Photoconductive devices made from these microplates exhibited high thermal stability and ultra-fast response times.

Further advancements include the synthesis of $Cs_3Sb_2I_9$ nanocolloids via a chemical method where a Cs-oleate precursor solution at 180°C or 230°C was injected into an antimony precursor obtained by reacting SbI_3 with octanoic acid, oleylamine, and 1-octadecene [58]. This method was also used to synthesize both polymorphs of $Cs_3Sb_2I_9$, and studies on their degradation [59] and photocatalytic properties [102] have been reported.

Other chemical techniques include spin coating and antisolvent engineering. The antisolvent engineering process involved dissolving CsI (0.75 M) and SbI_3 (0.495 M) in a solution mixture of N,N-dimethylformamide and hydrochloride (DMF:HCl, 1:0.03 volume ratio), followed by stirring for three hours and filtering with a 0.22 μm polytetrafluoroethylene (PTFE) filter. Isopropanol (IPA) was then dropped as an antisolvent onto a rotating substrate after 8 to 10 seconds of spin coating (3000 rpm, deposition time-30 s). Finally, the films were annealed at 230°C within a nitrogen-filled glove box [56]. Another technique synthesized a precursor solution by dissolving CsI, SbI_3, CsCl, and $SbCl_3$ in a DMSO:DMF (3:1 volume ratio) mixture, which was then stirred for an extended period at 70°C. Following this, 60 minutes after the introduction of hydriodic acid, the solutions were spin-coated (4000 rpm, 30 s). Finally, annealing was performed on a hotplate for 30 minutes at an annealing temperature of 135°C [53].

Recently, the vapor-anion exchange method has been employed to demonstrate the performance of 2D $Cs_3Sb_2I_9$ emitter-based LEDs and resistive-switching random-access memory devices [60]. In this method, SbI_3 (0.25 M) and CsI (1 M) were combined with dimethyl sulfoxide (DMSO) to create the precursor solution, which was continuously stirred for 6 hours at 70°C and then spin-coated for 40 seconds at 8000 rpm [61]. These spin-coated films were then transferred directly to a glass container, preheated to 200°C, and sealed after being filled with 10 μL of SbI_3 in DMF. The films were then annealed at 200°C for 15 minutes to remove any remaining solvent and produce layer-structured $Cs_3Sb_2I_9$ perovskite.

All these methods for synthesizing $Cs_3Sb_2I_9$ require high concentrations of precursors and involve complexities such as time-consuming intermediate steps or treatments at temperatures around or below 200°C. This has created a need for faster and simpler synthesis processes for $Cs_3Sb_2I_9$ perovskite material that use lower concentrations of heavy metal-containing precursors and avoid tedious intermediary steps.

In the present study, we synthesized $Cs_3Sb_2I_9$ thin films through a straightforward iodization process using Sb_2S_3-CsCl precursors. Sb_2S_3 thin films were first deposited using a chemical bath technique, followed by spin-coating or drop-casting of CsCl. The thin films formed through these methods, with varying CsCl concentrations and iodization times, were analyzed to determine their structure, morphology, composition, and optoelectronic properties. These films demonstrated self-powered photodetection as photoconductors, showing reproducible and steady photo-switching properties under optimal conditions at self-powered states.

3.2 Experimental

Materials

All materials were purchased and used without further purification: $SbCl_3$ (Antimony chloride, Fermont, 99.7%), $(CH_3)_2CO$ (Acetone, Fermont, 99.6%), $Na_2S_2O_3.5H_2O$ (Sodium thiosulphate, Fermont, 99.9%), CsCl (Cesium chloride, Fisher Chemical, 99.9%), and I_2 (Iodine, Fermont).

Synthesis

First, Sb_2S_3 thin films were synthesized using a chemical bath containing freshly prepared $SbCl_3$ and $Na_2S_2O_3$. Subsequently, cesium chloride (CsCl) layers were either drop-casted or spin-coated onto these Sb_2S_3 thin films. Following the deposition of CsCl, the films underwent iodization in iodine vapor. Figure 3.1 illustrates the schematic representation of the entire synthesis process, highlighting the two routes of CsCl application: drop casting and spin coating.

(i) Chemical Bath Deposition of Sb_2S_3 Thin Films

To prepare the chemical bath for Sb_2S_3 thin films, 325 mg of $SbCl_3$ was dissolved in 2.4 ml of acetone ($(CH_3)_2CO$). To achieve a total bath volume of 100 ml, 12.5 ml of 1 M $Na_2S_2O_3.5H_2O$ solution and 65 ml of deionized water were added and stirred thoroughly [19]. Premium glass substrates were meticulously cleaned using a soap solution before being positioned vertically in the bath. The deposition process was carried out for two hours under ambient conditions. Post-deposition, the films were removed, rinsed with deionized water, and dried in warm air.

(ii) Drop Casting of CsCl

Aqueous solutions of cesium chloride (CsCl) with varying molarities (volume: 0.6 ml) were drop casted onto the Sb_2S_3 films, followed by drying at 70°C. The resulting Sb_2S_3-CsCl films, fabricated using different CsCl molarities, were labeled as D0.001 (0.001 M), D0.0025 (0.0025 M), D0.005 (0.005 M), and D0.025 (0.025 M).

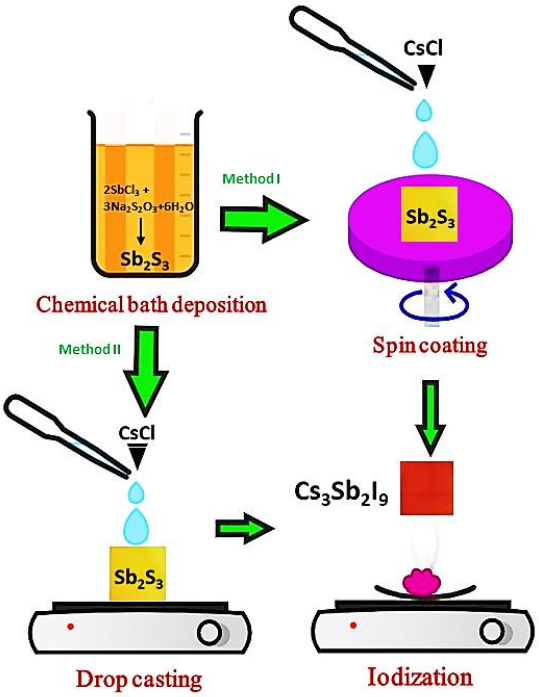

Figure 3.1. Schematic representation for $Cs_3Sb_2I_9$ thin film synthesis (two routes of CsCl by drop casting and spin coating) [50]

(iii) Spin Coating of CsCl

CsCl thin films were deposited on Sb2S3 films by spin coating (using CY Scientific Instruments China, Model CY-SP4). CsCl powder was dissolved in a mixed solvent (water:acetone, 1:1 volume ratio), and a total volume of 2 ml was applied at a spin speed of 500 rpm for 30 seconds. During the deposition, a modest amount of heat was applied to facilitate rapid CsCl deposition on the films. The films produced with different CsCl molarities were labeled as S0.005 (0.005 M), S0.025 (0.025 M), and S0.05 (0.05 M).

(iv) Iodization

The drop-casted and spin-coated films were iodized at different times in a Petri dish at 100°C using 50 mg of iodine powder. For the optimized drop-casted molarity (0.005 M) and spin-coated optimized molarity (0.025 M), the iodization time varied from 30 seconds to 10 minutes

3.3 Crystalline Structure

X-ray Diffraction Analysis

Figure 3.2(a) and (b) present the X-ray diffraction (XRD) patterns of $Cs_3Sb_2I_9$ thin films, which were formed through a 6-minute iodization process using different molarities of CsCl for both drop-casting and spin-coating methods to optimize the CsCl concentration.

Drop-Casting Method:

The diffraction patterns of the drop-casted CsCl samples along with their photos are shown in Figure 3.2(a). When compared with standard data (calculated pattern: ICDD file #01-088-0689), the experimental peaks indexed with the (100), (101), (006), (202), (204), (209), (0012), and (404) planes correspond to the hexagonal structured $Cs_3Sb_2I_9$ perovskite (space group *$P6_3/mmc$*, No.194, a=b=8.349, c=20.916, and α=β=90°, γ=120°). Among the drop-casted films (D0.001, D0.0025, and D0.025), the D0.005 sample exhibited phase purity. The high intensity of the (006) plane indicates a strong preferred orientation perpendicular to the substrate surface. Peaks attributed to CsCl (ICDD #00-001-0936) were observed in the D0.025 film. Decreasing the molarity to D0.0025 and D0.001 results in the appearance of SbI_3 peaks, identified with (113), (116), and (119) planes (ICDD file pattern 00-007-0273), indicating a rhombohedral crystal structure. The as-prepared Sb2S3-CsCl films (DAS and SAS samples) showed CsCl peaks at 21.5°, 30.57°, 43.83°, 49.39°, and 54.4° corresponding to the (100), (110), (200), (210), and (211) planes of a simple cubic structure, as indicated in Figure 3.3.

Spin-Coating Method:

Figure 3.2(b) displays the diffraction patterns of $Cs_3Sb_2I_9$ thin films formed using spin-coated CsCl. Unlike the drop-casting approach, spin-coated samples require higher CsCl molarities to form ternary $Cs_3Sb_2I_9$.

Discreet SbI_3 peaks are dominant at lower CsCl molarities (S0.005), while higher CsCl molarities (S0.05) show dominant CsCl peaks as expected. For the S0.025 sample, no impurity phases are observed, and strong reflections attributed solely to $Cs_3Sb_2I_9$ are present. When the molarity of CsCl is increased to 0.05 M, CsCl peaks become more prominent, consistent with the standard CsCl ICDD #00-001-0936.

The XRD data indicates that the formation of $Cs_3Sb_2I_9$ thin films via spin-coating requires a higher concentration of CsCl compared to drop-casting. The presence of impurity phases such as SbI_3 at lower CsCl molarities confirms the necessity for optimization in CsCl content for achieving pure $Cs_3Sb_2I_9$ phase.

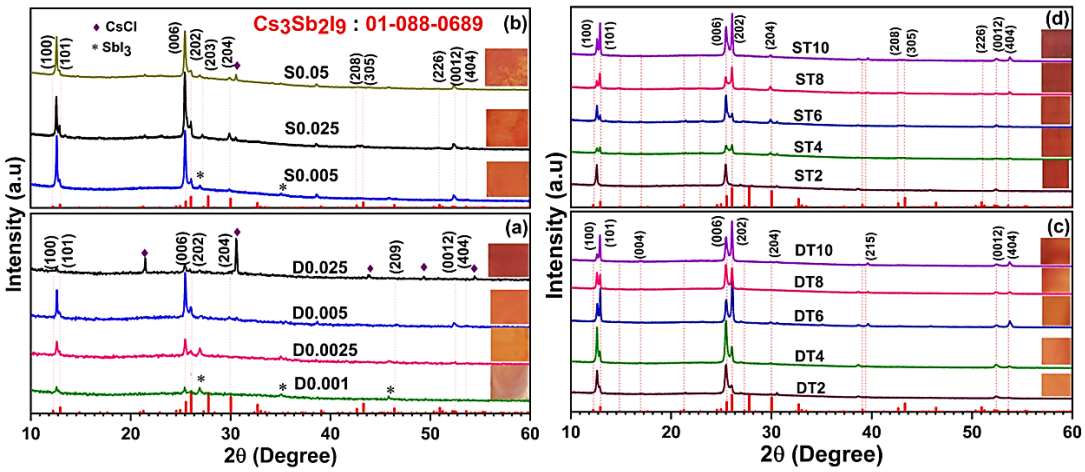

Figure 3.2. X-ray diffraction (XRD) patterns and images of $Cs_3Sb_2I_9$ thin films synthesized by differing molarity through (a) drop-casting and (b) spin-coating methods, as well as by varying iodization times in (c) drop-casting and (d) spin-coating. The standard hexagonal $Cs_3Sb_2I_9$ pattern (ICDD # 01-088-0689) is included for reference. Peaks corresponding to CsCl and SbI_3 are highlighted [50].

Figure 3.2(c) illustrates the XRD patterns of $Cs_3Sb_2I_9$ thin films synthesized by drop casting with varying iodization times at the optimal CsCl molarity of 0.005 M. The

thin films labeled DT4, DT6, DT8, and DT10 correspond to phase-pure $Cs_3Sb_2I_9$. Major peaks are observed at 13°, 25.47°, and 26.07°, with minor peaks at 39°, 53.6°, and 52.5°. Films iodized for 30 seconds and 1 minute were amorphous, as shown in Figure. 3.4. After 2 minutes of iodization, cesium antimony iodide peaks appeared (DT2). Phase-pure $Cs_3Sb_2I_9$ thin films were formed at iodization times of 4 to 10 minutes, indicated by the planes (100), (101), (006), (202), (204), (209), (0012), and (404), corresponding to the hexagonal $Cs_3Sb_2I_9$ perovskite structure.

Figure 3.2(d) shows the XRD patterns of $Cs_3Sb_2I_9$ thin films formed using spin-coated CsCl at the optimal molarity of 0.025 M, with varying iodization times. The ST4, ST6, ST8, and ST10 thin films represent pure phases of $Cs_3Sb_2I_9$ with varying orientations ((100), (101), (006), and (202)), indicating different growth orientations. The relief of residual tensile stress and recrystallization causes modifications in the perovskite film growth direction [103]. For ST2 thin films, unreacted CsCl was detected due to insufficient iodization time. It has been reported that vapor-assisted solution-processed films tend to organize in a dimeric form [51], where SbI^{6-} octahedra fuse into $Sb_2I_9^{3-}$ dimers by sharing their triangular faces. These dimers are formed through a solution processing approach using polar solvents, while layered forms are obtained through a low-temperature solid-state reaction [49]. By removing one layer from every third Sb layer along the <111> direction, the hypothetical perovskite $Cs_3Sb_3I_3$ transforms into the crystal structure of 2D layered $Cs_3Sb_2I_9$ to achieve adequate charge balance [51]. $Cs_3Sb_2I_9$ tends to form isolated dimers of face-sharing octahedra in a 0D structure [51].

Crystalline Size, Lattice Strain, Stress, and Dislocation Density

Table S.1 displays the computed crystallite size, lattice strain, stress, and dislocation density of $Cs_3Sb_2I_9$ thin films. The crystallite size (D) and lattice strain (ε) were calculated using the Williamson-Hall (W-H) plot, defined by the equation:

$$\beta cos\theta = \frac{k\lambda}{D} + 4\varepsilon Sin\theta \tag{3.1}$$

Where k is the shape factor (value 0.9), λ is the X-ray wavelength, β is the full width at half maximum (FWHM) of the prominent peak at 2θ. The W-H plots were obtained by plotting 4sinθ on the x-axis and βcosθ on the y-axis, for drop casted and spin coated samples with varying iodization time (Figure. 3.5, 3.6). From these plots, the

values for lattice strain and crystallite size were derived from the respective slopes and intercepts.

For all the samples, the strain values ranged from 0.003 to 0.004, as shown in Table 3.1. Furthermore, the crystallite size increased with iodization time, ranging from 63 nm to 150 nm. This observation indicates that iodization significantly affects the crystallinity of $Cs_3Sb_2I_9$, with the crystallite size increasing as iodization time extends. Antimony-based perovskite derivatives often feature isolated bioctahedral face-sharing $[Sb_2X_9]^{3-}$ clusters within a zero-dimensional (0D) structure [53].

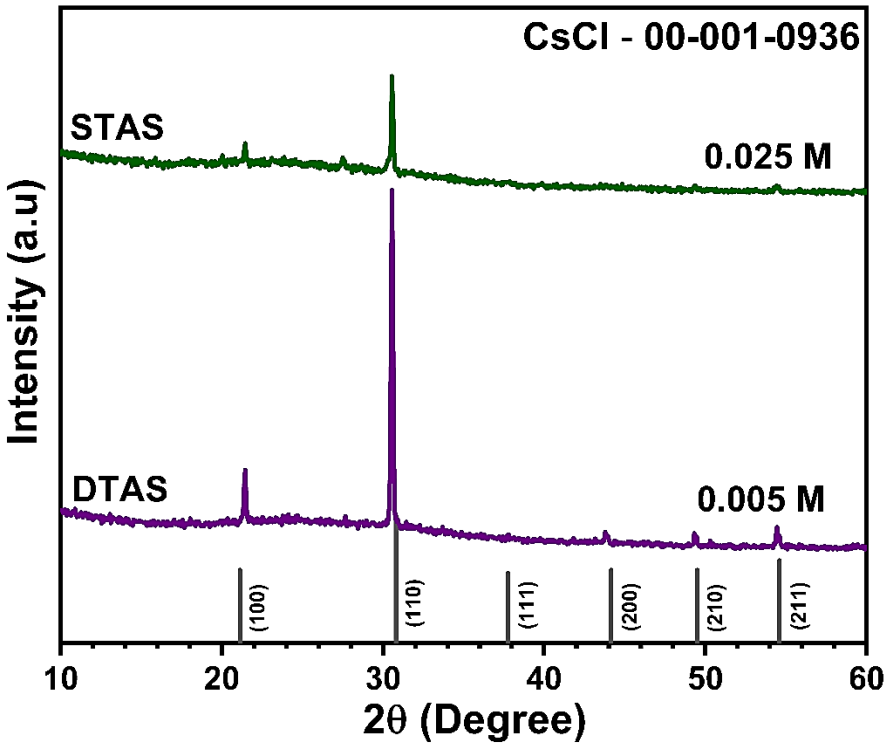

Figure 3.3. XRD pattern of as-prepared drop casted and spin coated thin films [50].

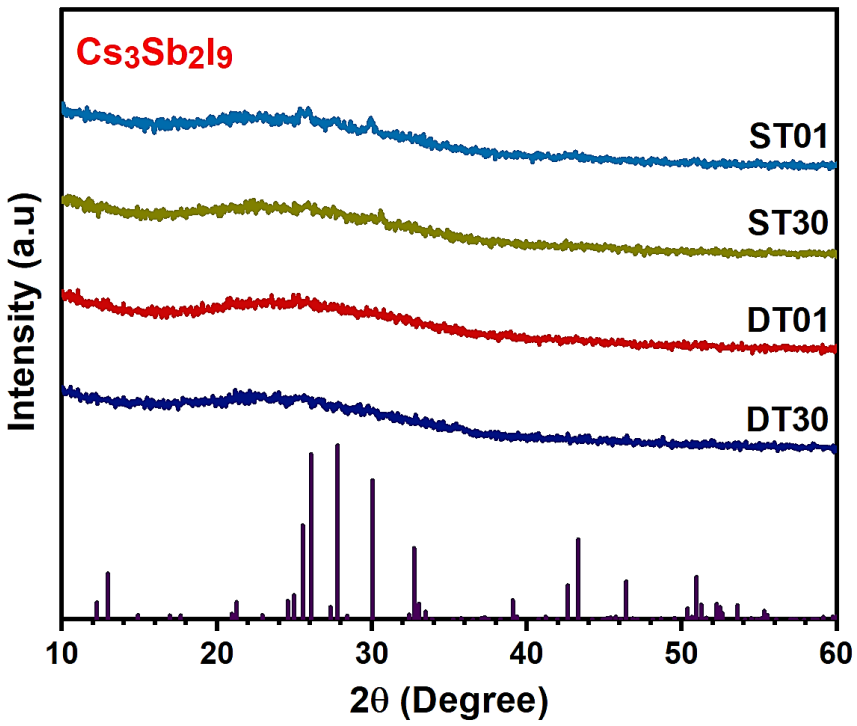

Figure 3.4. 30 s and 1 min iodized drop casted and spin coated films of $Cs_3Sb_2I_9$ [50].

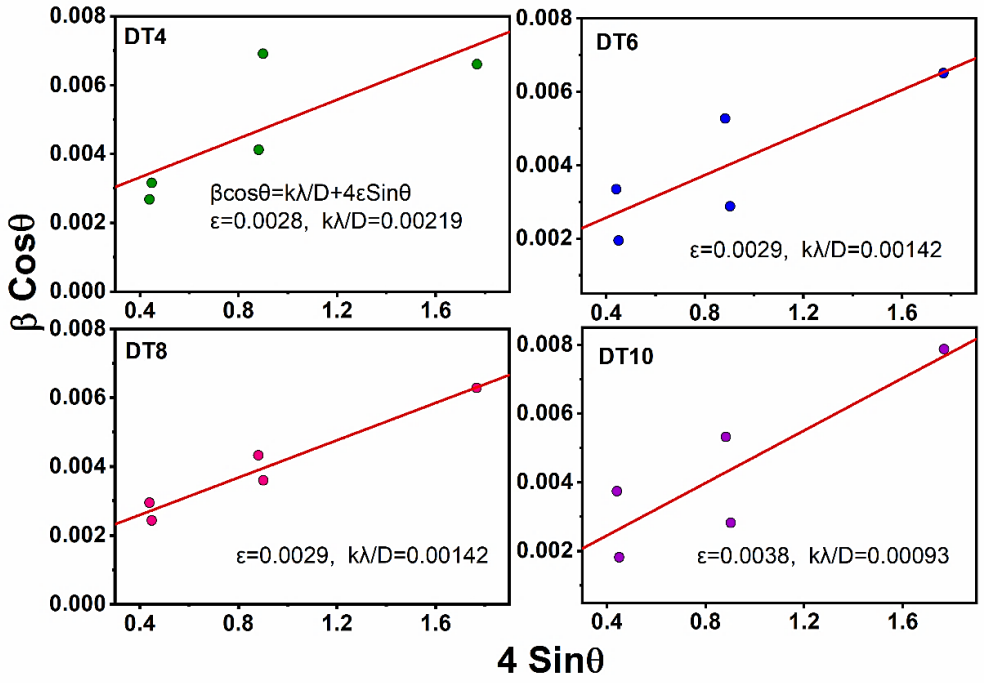

Figure 3.5. W-H plots of drop casted $Cs_3Sb_2I_9$ thin films [50].

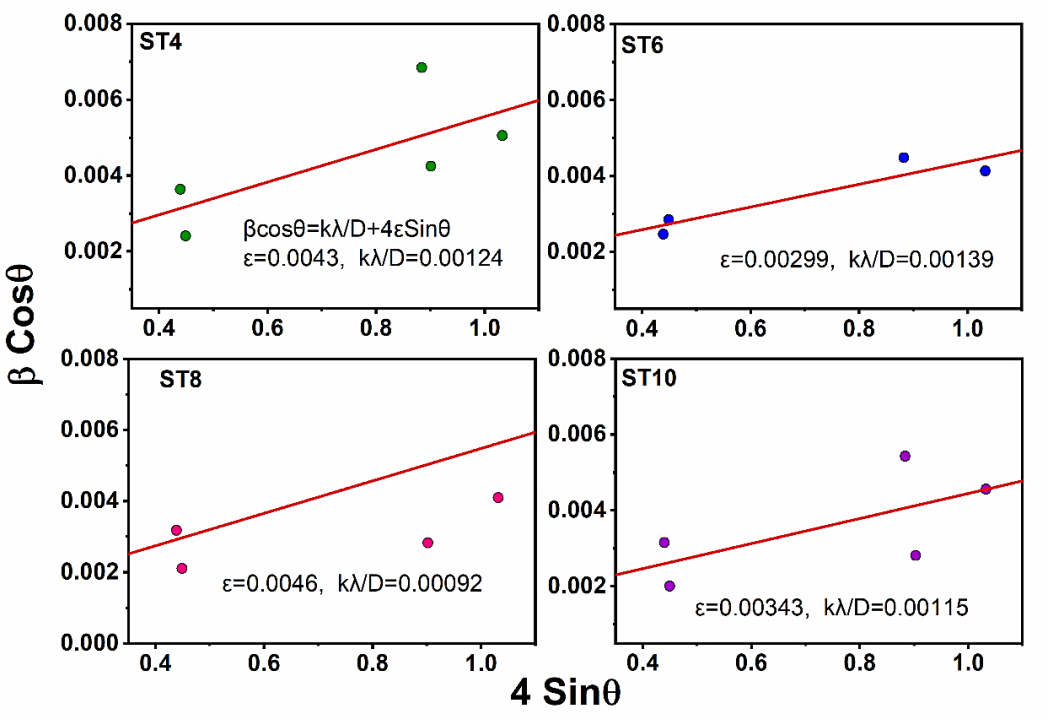

Figure 3.6. W-H plots of spin coated $Cs_3Sb_2I_9$ thin films [50].

Sample	Crystallite size (D) (nm)	Lattice strain (ε) %
DT4	63	0.0028
DT6	98	0.0029
DT8	92	0.0027
DT10	149	0.0038
ST4	112	0.0043
ST6	100	0.003
ST8	150	0.0046
ST10	120	0.0033

Table. 3.1. Crystallite size and lattice strain values of the Cs3Sb2I9 thin films

In general, spin-coated samples demonstrated better crystallinity compared to drop-casted films with the same iodization duration, and the crystallites expanded with increased iodization time for both types of thin films. XRD analysis confirmed the

hexagonal crystal structure of $Cs_3Sb_2I_9$ 0D perovskite (space group: *P6₃/mmc*) in both drop-casted and spin-coated samples.

For further studies, samples formed by varying iodization time at the optimized CsCl concentration were selected.

3.4 Raman Analysis

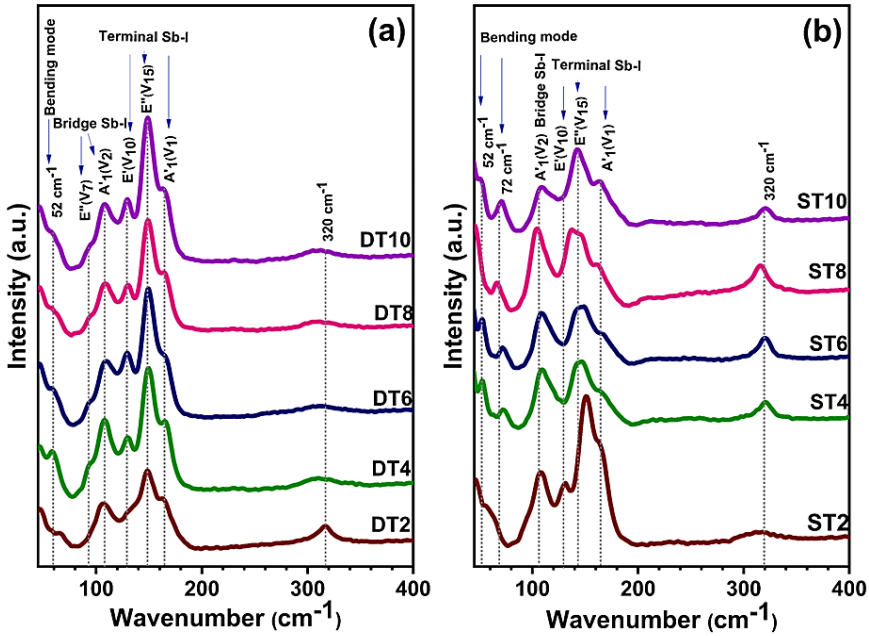

Figure 3.7. Raman spectra of $Cs_3Sb_2I_9$ thin films formed by (a) drop casted CsCl and (b) spin coated CsCl at different iodization times [50].

Figure 3.7**.** illustrates the Raman spectra of $Cs_3Sb_2I_9$ thin films synthesized by CsCl drop-casting and spin-coating at different iodization times. Raman spectroscopy was performed on all phase-pure drop-cast and spin-coated samples with iodization times ranging from 2 to 10 minutes. The characteristic peaks of the ternary $Cs_3Sb_2I_9$ were observed near 52, 72, 93, 108, 129, 145, 165, and 320 cm^{-1}, which are consistent with previously reported peaks for the P63/mmc phase of $Cs_3Sb_2I_9$.

The Raman spectra presented bending modes at 52 and 73 cm^{-1}, bridge Sb-I stretch at 93 cm^{-1} symmetry-E" (vibration-V_7)), and 108 cm^{-1} (A'(V_2)), and terminal Sb-I stretch at 129 (E'(V_{10})), 145 (E" (V_{15})), and 165 cm^{-1} (A'$_1$ (V_1)), respectively. There are no reports detailing the symmetry information for the peak at 320 cm^{-1} in the existing literature. It is known that the dominant vibrational modes of $Cs_3Sb_2I_9$ are associated

with $[Sb_2I_9]^{3-}$ octahedra [104]. Table 3.2 lists the Raman peaks of drop-casted and spin-coated $Cs_3Sb_2I_9$ thin films in accordance with previously reported values [104].

Low-energy bending modes below 80 cm^{-1} result from constraints imposed by covalent connections between octahedra. According to literature [105], the intramolecular Raman spectra of SbI_6 octahedra exhibit five bands, with Sb atoms involved in two of these vibrations: the symmetric Sb-I stretch and the antisymmetric Sb-I planar contraction with perpendicular stretching. The highest-energy modes, arising from Sb-I interactions due to symmetry, correlate with the two major peaks observed in our spectra. Consequently, the peak around 165 cm^{-1} in $Cs_3Sb_2I_9$ can be attributed to the symmetric Sb-I stretch, while the peak near 145 cm^{-1} is assigned to the antisymmetric Sb-I planar contraction [105]. These Raman peaks confirm the hexagonal crystal structure with space group *$P6_3/mmc$*.

For the DT2 and ST2 thin film spectra, different peaks were observed compared to those at other iodization times, indicating the presence of unreacted CsCl. According to previously published results, CsCl exhibits peaks at 77, 127, and 187 cm^{-1} [106]. These specific peaks suggest that DT2 and ST2 samples did not undergo complete conversion to $Cs_3Sb_2I_9$, likely due to insufficient iodization time.

$Cs_3Sb_2I_9$ Raman Peaks (cm^{-1})	Raman peaks Reported[104] (cm^{-1})	Vibration	Symmetry	Assignment
52	52	-	-	Bending modes
72	60.3	-	-	
93	93.5	V_7	E"	Bridge Sb-I stretch
108	108.9	V_2	A'_1	
129	130.7	V_{10}	E'	Terminal Sb-I stretch
145	145.1	V_{15}	E"	
165	169.7	V_1	A'_1	
320	*Not identified*			

Table. 3.2. Raman peaks of drop casted and spin coated $Cs_3Sb_2I_9$ thin films compared to reported values.

3.5 Morphology- Scanning electron microscopy (SEM)

The surface morphology of $Cs_3Sb_2I_9$ thin films was analyzed using scanning electron microscopy (SEM). Figure 3.8 displays SEM images of phase-pure $Cs_3Sb_2I_9$ thin films formed by iodization for 6-10 minutes. The images of films iodized for 2 and 4 minutes are shown in Figure 3.9 The 2-minute iodized drop-cast samples (DT2) Figure 3.9 (a)) typically exhibit flake-like features that are vertically aligned and inclined with respect to the surface. With increased iodization time, the structures in DT4 (Figure 3.9 (b)) become thicker flake-like formations. In the DT6 samples, these flakes transition to rod-like structures composed of small fibers. Moreover, the film iodized for 8 minutes (DT8) consists of tangled and coalesced rod-like structures, while the DT10 sample exhibits a surface covered with thick and faceted flake-like structures.

For spin-coated samples, the morphology evolves similarly with increasing iodization time, transitioning from thin petal-like structures to a compact morphology characterized by mixed bar-petal features (ST2, ST4— Figure 3.9 (c, d), ST6, ST8, and ST10— Figure 3.8 (d, e, f)). Previous studies have reported that $Cs_3Sb_2I_9$ typically exhibits a smooth, pinhole-free surface morphology (0D) [60], with minor voids in its crystal structure (2D) [56].

From this analysis, it is evident that the morphology of $Cs_3Sb_2I_9$ films is influenced by the method of CsCl incorporation and the iodization time. Drop-casted and spin-coated methods result in distinct surface morphologies for $Cs_3Sb_2I_9$. As previously reported, crystallite size increases with higher iodine content [107]. The spin-coated films are observed to be more compact and smoother compared to the drop-casted films.

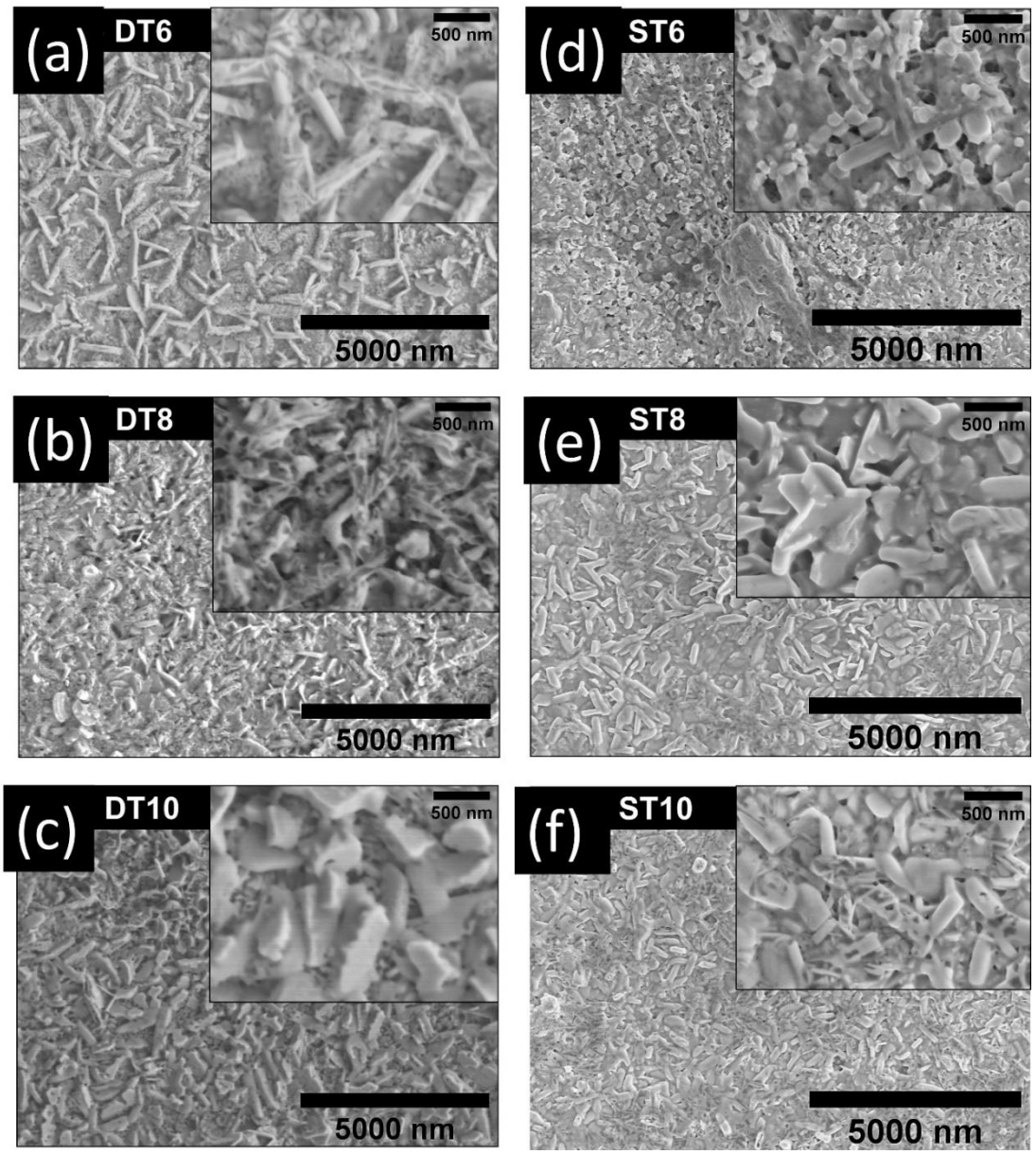

Figure 3.8. SEM images of drop casted and spin coated $Cs_3Sb_2I_9$ thin films a) DT6, b) DT8, c) DT10, d) ST6, e) ST8, and f) ST10 [50].

SEM images of the precursor films (DTAS and STAS) revealed a uniform surface with spherical grains, over which the drop-casted and spin-coated CsCl layers are present (Figure 3.10). Compared to DTAS, the STAS surface is notably smoother, more uniform, and compact. In both instances, the spherical particles in the films correspond to Sb_2S_3 [108], along with dispersed CsCl. Cross-sectional images of the as-prepared (DTAS, STAS) and optimized $Cs_3Sb_2I_9$ thin films are presented in Figure 3.11 and 3.12. From these images, the film thicknesses were estimated and are marked accordingly. The

thicknesses increase from 150 nm to 200 nm for drop-casted samples and from 131 nm to 230 nm for spin-coated samples as the iodization time increases.

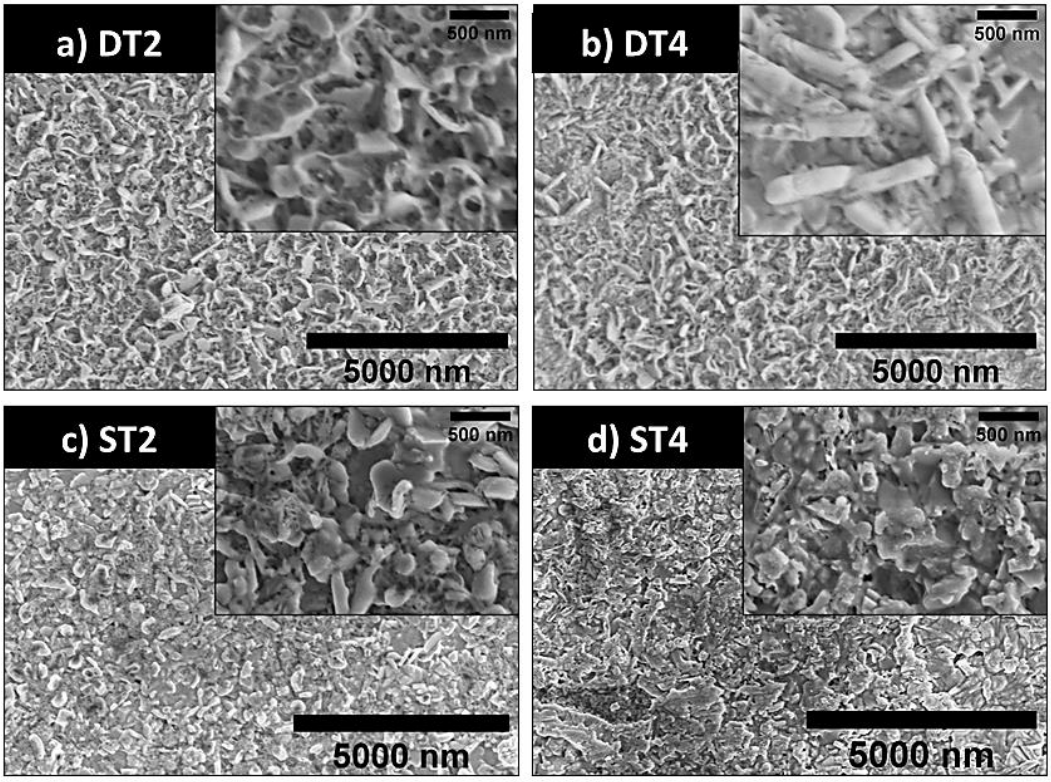

Figure 3.9. SEM images of drop casted and spin coated $Cs_3Sb_2I_9$ thin films a) DT2, b) DT4, c) ST2, and d) ST4 [50].

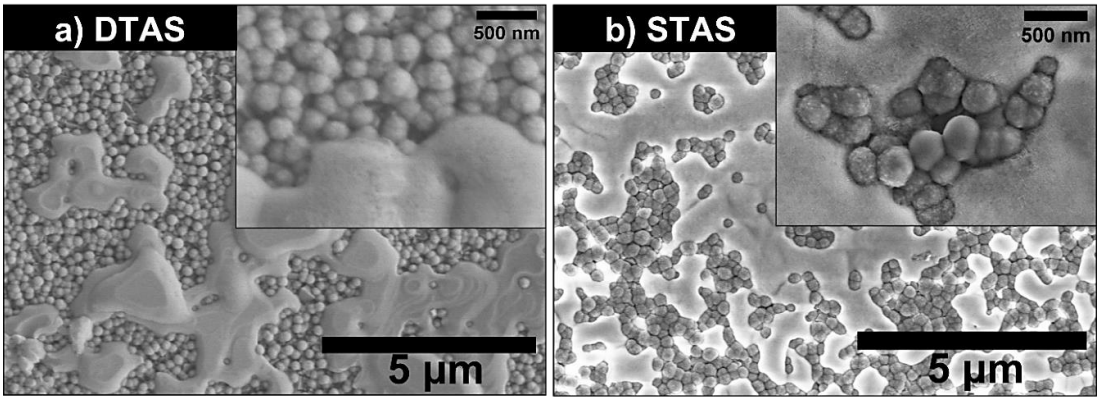

Figure 3.10. SEM images of Sb_2S_3-CsCl precursor (drop casted and spin coated) thin films [50]

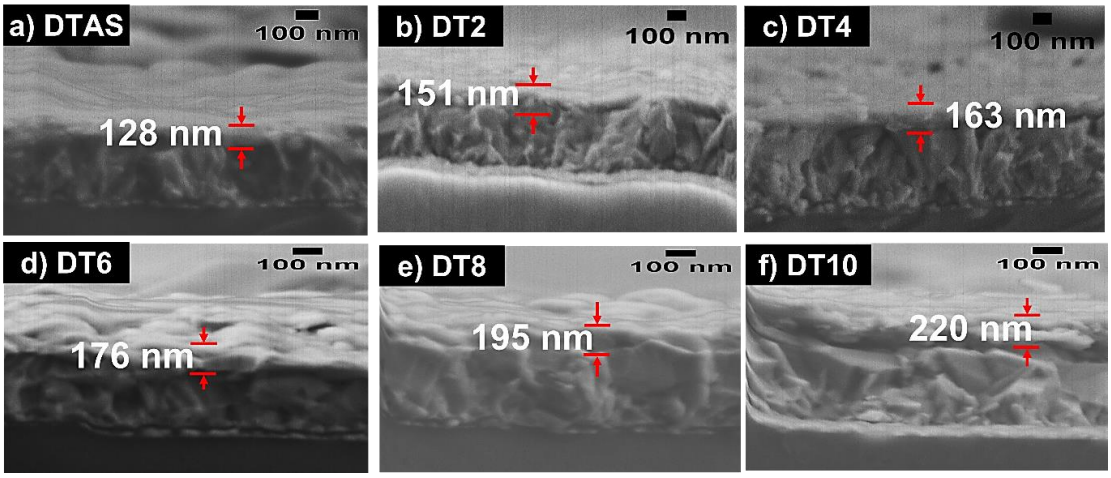

Figure 3.11. Cross-section images of $Cs_3Sb_2I_9$ thin films formed by varying iodization time of drop casted precursor [50]

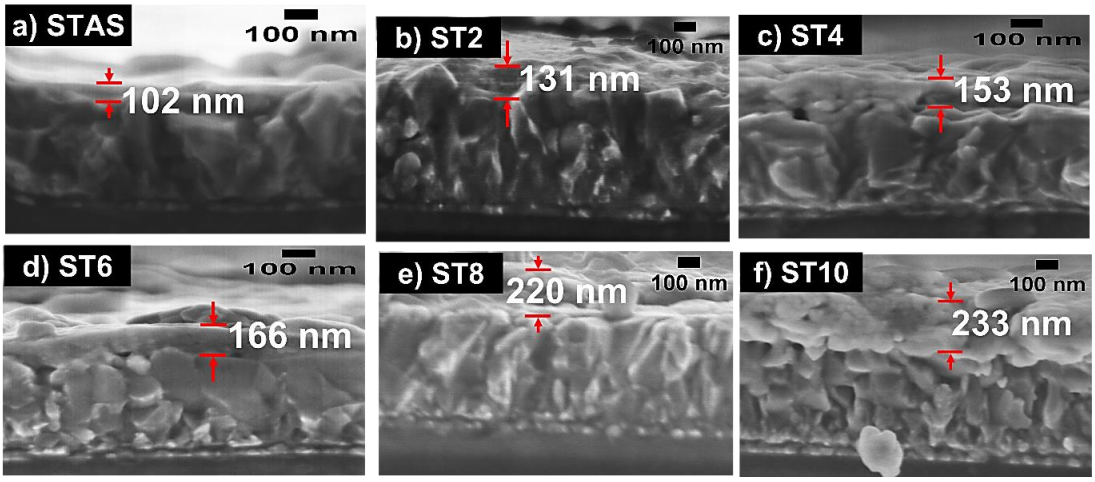

Figure 3.12. Cross section images of $Cs_3Sb_2I_9$ thin formed by varying iodization time of spin coated precursor [50].

It has been reported [9] that as-prepared $Cs_3Sb_2I_9$ thin films formed through antisolvent engineering exhibited a non-uniform morphology with numerous voids. The addition of antisolvents resulted in larger grains and a more favorable crystallization environment. However, films treated with toluene and chlorobenzene as antisolvents still exhibited some holes and non-uniform coverage. Conversely, using IPA as an antisolvent led to the formation of homogeneous, compact, and coarsened crystals [56]. $Cs_3Sb_2I_9$ thin films obtained by vapor halide exchange of CsI-SbI_3 in SbI_3 vapor were more uniform and had a lower density of pinholes compared to those treated with $SbBr_3$ and $SbCl_3$ vapors. The

varied vapor pressures, due to different vaporization temperatures, likely caused these pinholes [61]. Additionally, in the chemical synthesis method, adjusting the reaction temperature allowed tuning of the $Cs_3Sb_2I_9$ nanocrystal morphology into nanoplatelets (NPLs) and nanorods (NRs) [58]. In our study, the iodization of drop-casted or spin-coated CsCl films on Sb_2S_3 results in a homogeneous, pinhole-free compact surface morphology without the need for post-deposition treatments.

3.6 X-ray photoelectron spectroscopy (XPS)

The XPS survey spectrum of a typical $Cs_3Sb_2I_9$ (ST6) thin film, obtained after removing surface contamination through gentle Ar^+ ion etching, is shown in Figure 3.13. This spectrum reveals the presence of Cs, Sb, and I, along with trace amounts of C and O, indicating minimal contamination. The chemical states of these elements were further analyzed through high-resolution core-level spectra, presented in Figure 3.14 (a, b, c). A Shirley type function was used to fit the background, and the peaks were deconvoluted utilizing a Gaussian-Lorentzian sum function. Specifically, the Cs $3d_{5/2}$ and $3d_{3/2}$ peaks are observed at 724.75 eV and 738.68 eV, respectively, with a spin-orbit splitting value (ΔE) of 13.93 eV, confirming the Cs^{+1} oxidation state, as displayed in Figure 3.14(a).

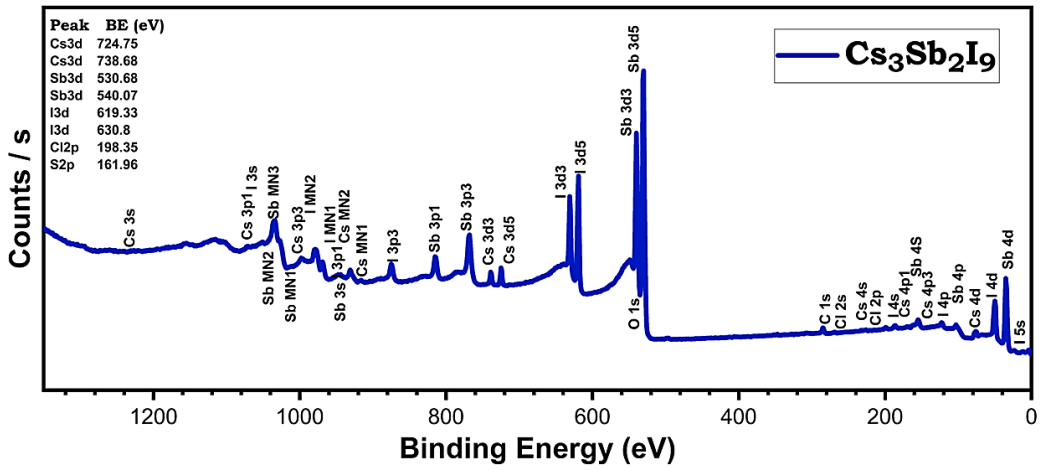

Figure 3.13. XPS survey spectrum of $Cs_3Sb_2I_9$ (ST6) thin film [50].

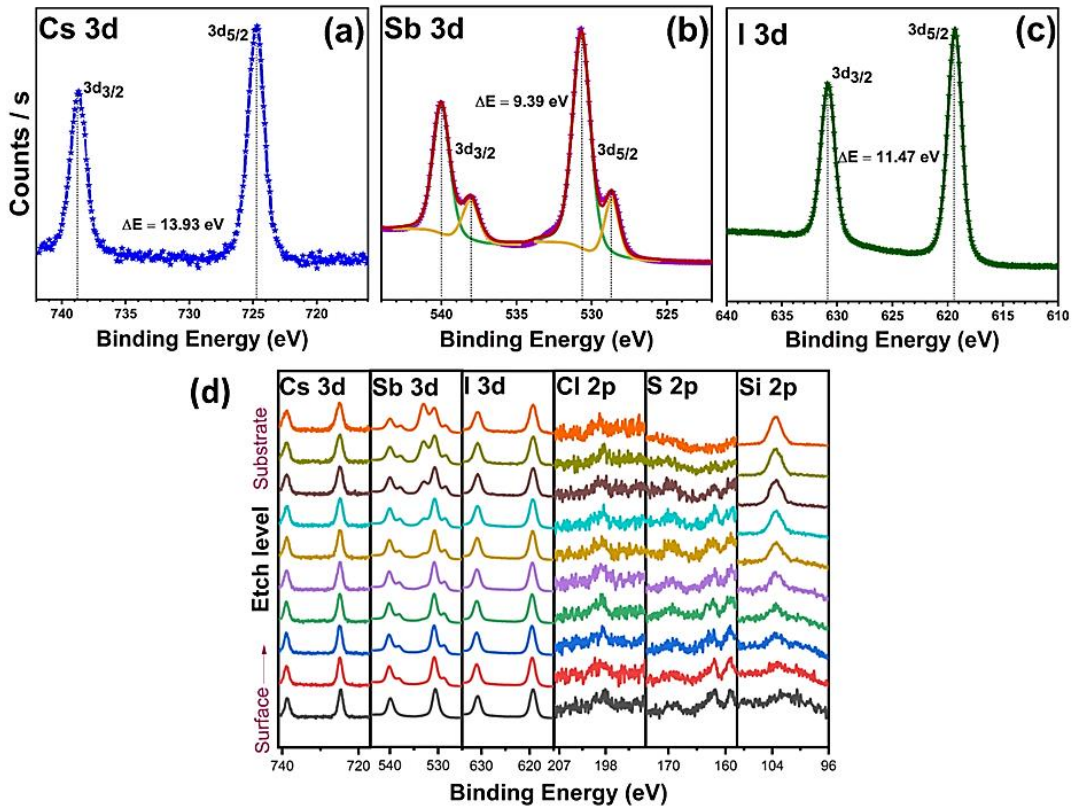

Figure 3.14. High-resolution core-level XPS spectra of $Cs_3Sb_2I_9$ thin film deposited on glass substrate a) Cs 3d b) Sb 3d c) I 3d. The spin-orbit coupled orbitals and the respective energy separations are marked. (d) depth profile analysis of binding energy [50].

In Figure 3.14(b), the Sb 3d peaks are deconvoluted into two doublet pairs. The first doublet, at binding energies of 528.67 eV and 538.06 eV (ΔE=9.39 eV), corresponds to metallic antimony (Sb^0). The second doublet, at binding energies of 530.68 eV and 540 eV, correlates with the Sb^{3+} state in SbI_3. The minor peak associated with metallic antimony (Sb^0) is attributed to the sputter-induced reduction of the Sb^{3+} state within the $Cs_3Sb_2I_9$ matrix during the etching process [100]. This sputter-induced reduction effect has also been observed in XPS analyses of spray-pyrolyzed $Cs_3Bi_2I_9$ [109] and in Sb_2S_3 thin films [100].

Additionally, the I 3d spectra (Figure 3.14(c)) exhibit $3d_{5/2}$ and $3d_{3/2}$ peaks at binding energies of 619.33 eV and 630.8 eV, respectively, with a spin-orbit splitting value (ΔE) of 11.47 eV. These values are consistent with the I^- state [14,5].

Additionally, a depth profile analysis was conducted on the same $Cs_3Sb_2I_9$ (ST6) thin film, as illustrated in Figure 3.14(d). The depth profile demonstrates that the distribution

of Cs, Sb, and I is homogeneous throughout the film. At the interface between the substrate and the film, silicon and oxygen are detected. Notably, no peaks corresponding to Cl 2p and S 2p are observed at any depth, indicating that unreacted Sb_2S_3 and CsCl are not significantly present in the thin film.

Furthermore**,** Figure 3.15 presents energy dispersive X-ray (EDX) mapping and elemental quantification of the optimized $Cs_3Sb_2I_9$ thin film. The EDX mapping image and the corresponding results in the table illustrate the replacement of Cl (from CsCl) and S (from Sb_2S_3) with I to form the $Cs_3Sb_2I_9$ ternary compound. The major elements detected are Cs, Sb, and I, with trace amounts of Cl. The spectrum reveals that the atomic percentages of these elements correspond to their stoichiometric ratios in the compound.

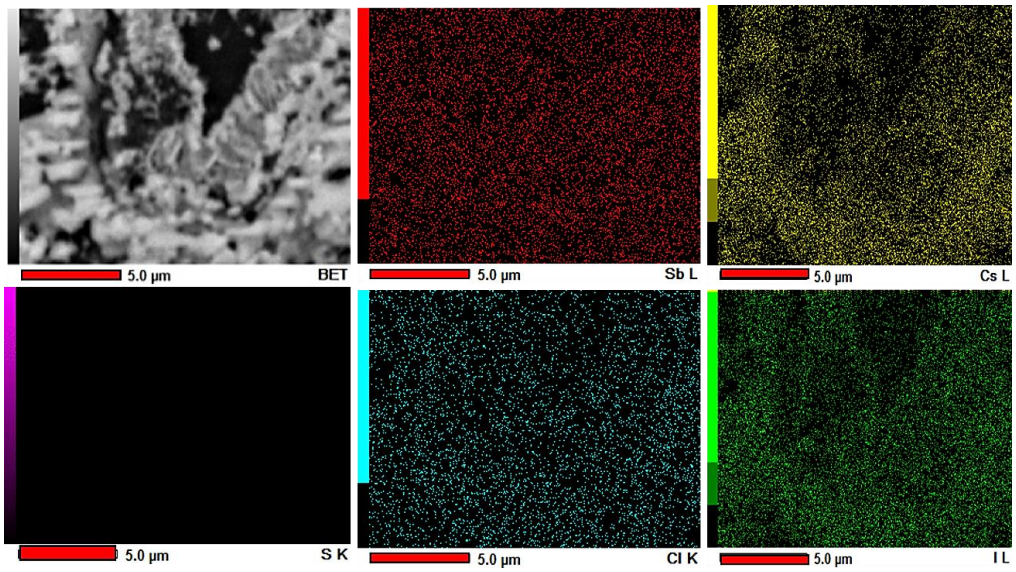

Figure 3.15. EDX mapping of $Cs_3Sb_2I_9$ (ST6) thin film [50].

Element	Atomic%
Sb	7.54
S	0.95
Cs	20.75
Cl	3.61
I	67.14
Total	100.00

Table. 3.3. EDX quantification results of $Cs_3Sb_2I_9$ (ST6) thin film.

3.7 UV-Vis/NIR spectroscopy

The transmittance and reflectance spectra of $Cs_3Sb_2I_9$ thin films in the UV-Vis-NIR region are presented in Figure 3.16 (a, b) for drop-casted and spin-coated samples, respectively. The transmittance of $Cs_3Sb_2I_9$ films remains high within the wavelength range of ~1600 to 2500 nm and then decreases sharply to 10%, indicating strong absorption near 600 nm. Figure 3.17 (a, b) illustrates the absorption spectra for drop-casted (DT) and spin-coated (ST) samples at various iodization times, revealing at least two distinct absorption peaks. The observed excitonic peak near 600 nm (~2.1 eV) marks the onset of absorption, with an additional absorption edge near 470 nm (~2.6 eV).

The band gap (Eg) is determined using a Tauc plot, derived from the equation 2.4 [27]

$$(\alpha h\nu)^n = A\left(h\nu - E_g\right) \tag{2.4}$$

where h is Planck's constant, ν is the photon frequency, and A is a constant. The value of n depends on the type of optical transition, with n=2 indicating a direct allowed transition and n=2/3 for a direct forbidden transition. The absorption coefficient (α) is calculated using equation 2.5 [100]:

$$\alpha = \frac{1}{d}\ln\left[\frac{(1-R)^2}{T}\right] \tag{2.5}$$

where d is the average film thickness (cm), T is the transmittance, and R is the reflectance. The thickness of the films was determined from SEM cross-sectional images, yielding an absorption coefficient on the order of ~10^5 cm^{-1}. Three distinct absorption peaks originating from the same bands are reported for both dimeric and layered forms [110]. Tauc plots for both direct ($(\alpha h\nu)^2$ vs. hν) and indirect ($(\alpha h\nu)^{(1/2)}$ vs. hν) transitions are analyzed, as shown in Figure 3.16 (c, d) and Figure 3.18, respectively, over the energy range of 0.5-2.6 eV. The direct band gaps are approximately 1.7 eV for drop-casted and 1.6 eV for spin-coated $Cs_3Sb_2I_9$ thin films, whereas the indirect band gap value of <0.7 eV does not correspond to the films' color.

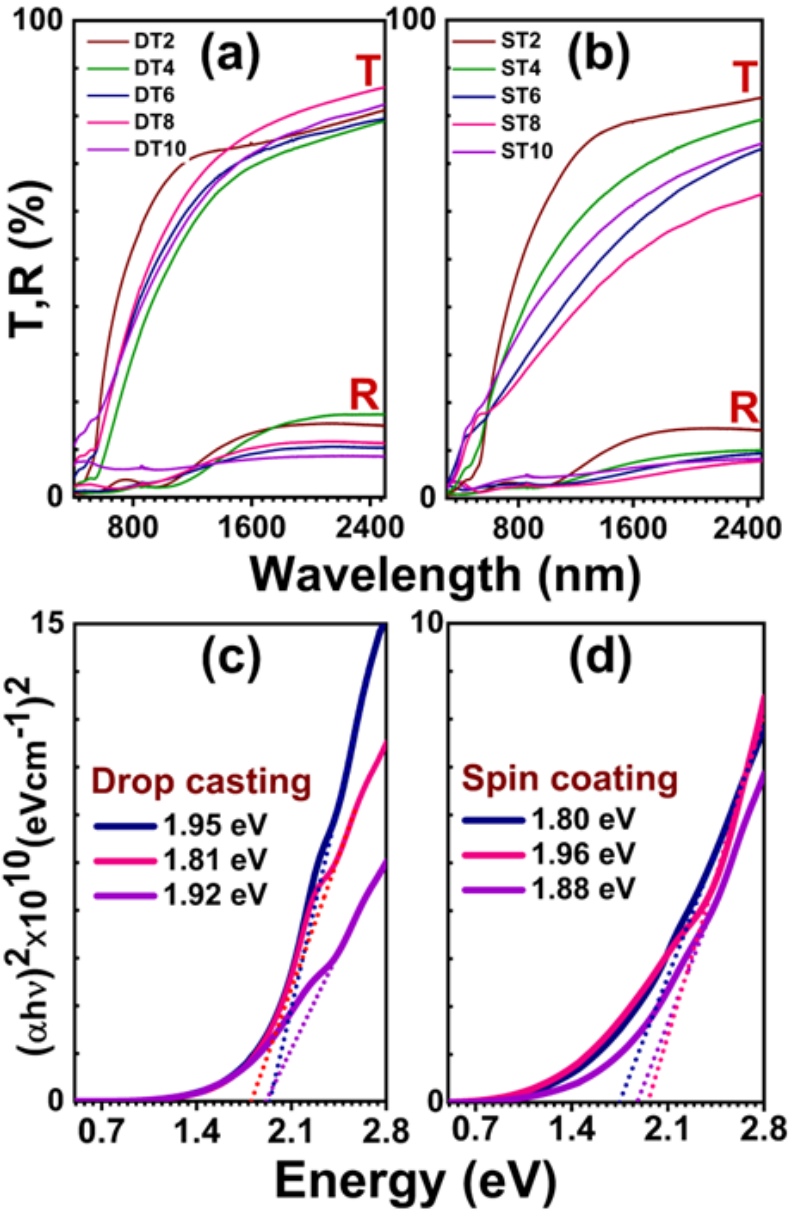

Figure 3.16. UV-Vis-NIR spectral analysis of $Cs_3Sb_2I_9$ thin films: Transmittance, Reflectance (a) drop casted films (b) spin-coated films; Tauc plots (c) drop casted films (d) spin-coated films [50].

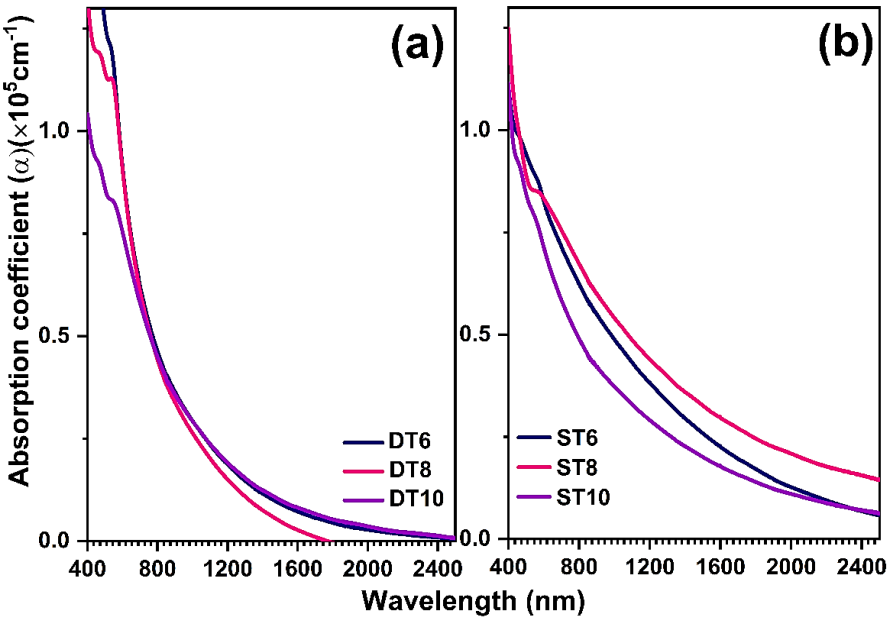

Figure 3.17. Absorption coefficient vs Wavelength spectra of $Cs_3Sb_2I_9$ thin films: a) drop casted, b) spin coated [50].

In this study, $Cs_3Sb_2I_9$ thin films synthesized via drop casting and spin coating through rapid iodization exhibit an increase in absorption onset in the wavelength region below 800 nm, as shown in Fig. S.11. Both methods yield similar bandgap values ranging between 1.6-1.7 eV. According to the literature, an indirect band gap of 2.3-2.5 eV has been reported for dimer-phase $Cs_3Sb_2I_9$ thin films [23,5,6]. The electronic band structure estimates an indirect band gap (k-Γ) of 2.4 and 2.5 eV [5,6] for the dimer phase and a direct band gap (Γ-Γ) of 2.05 eV for the layered phase [5,7]. Previous studies have indicated that $Cs_3Sb_2I_9$ films exhibit a band gap of 1.96 eV after six months of exposure to ambient air, demonstrating only a minor impact on the band gap value due to prolonged air exposure [49]. Notably, only polycrystalline perovskite thin film absorbers with high band gaps (>1.7 eV) have shown power conversion efficiencies (PCE) greater than 20%. Thus, $Cs_3Sb_2I_9$ thin films with a band gap of 1.6-1.7 eV could be viable for creating tandem solar cells. These tandem structures would combine wide-bandgap electronics with low-bandgap photovoltaics to enhance performance in hybrid configurations [111].

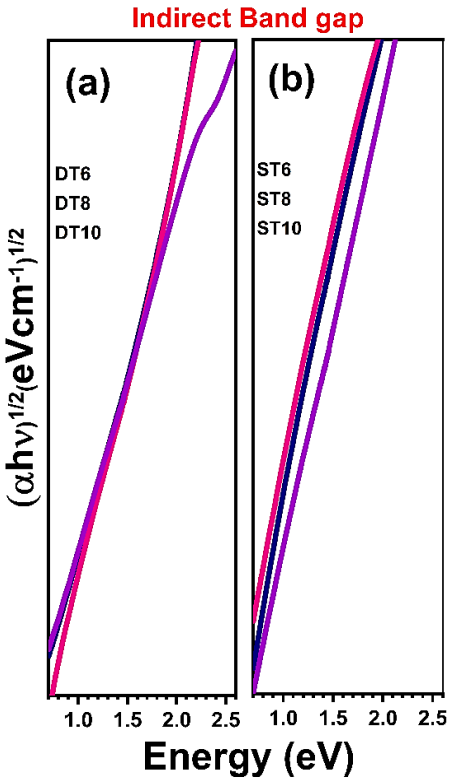

Figure 3.18. Tauc plot of indirect band gap of: a) drop casted, and b) spin coated thin films [50].

3.8 Photocurrent response measurement

The photoresponse of drop-casted (DT6, DT8, and DT10) and spin-coated (ST6, ST8, and ST10) $Cs_3Sb_2I_9$ thin films was investigated at a bias voltage of 10 V under illumination from a 50 W halogen lamp with an intensity of 30 W/cm², as depicted in Figure 3.19. Upon exposure to light, all the samples demonstrated a distinct photoresponse, characterized by an increase in the output current of the photodetector upon illumination. This current reached a peak value and subsequently returned to the baseline dark current once the light source was turned off. Among the samples, DT6 and ST6 were selected for further zero-bias photoresponse studies due to their superior stability under illumination.

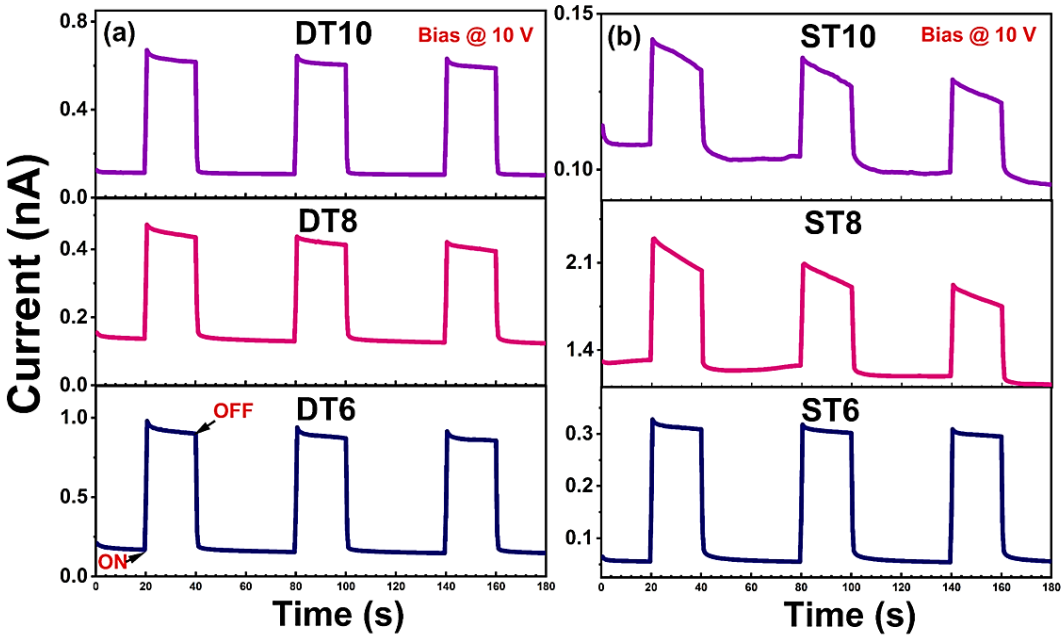

Figure 3.19. Cyclic photocurrent response measurement of $Cs_3Sb_2I_9$ thin films (bias of 10 V) [50]

The electrical resistivity (ρ) of these films was calculated using the sheet resistance (R_s) derived from the I-V characteristics and the film thickness (d) measured by cross-sectional SEM. The resistivity was determined using the following relation [4]:

$$\rho = \frac{V}{I} \times d \qquad (3.2)$$

For DT6 and ST6 samples, the resistivity values were found to be 4×10^4 Ω·cm and 1.4×10^5 Ω·cm, respectively. The performance of these devices, particularly for potential applications, is closely tied to the morphology and surface coverage of the perovskite thin films [60].

The I-V characteristics of the DT6 and ST6 photodetectors are presented in Figure 3.20. Both samples exhibited a stable photo-switching response under zero-bias conditions, which was evaluated over 135 continuous cycles to assess the reproducibility and long-term stability of the self-powered $Cs_3Sb_2I_9$ photodetectors, as shown in Figure 3.21. The on/off ratios for the self-driven photodetectors were calculated to be 15 for DT6 and 3 for ST6.

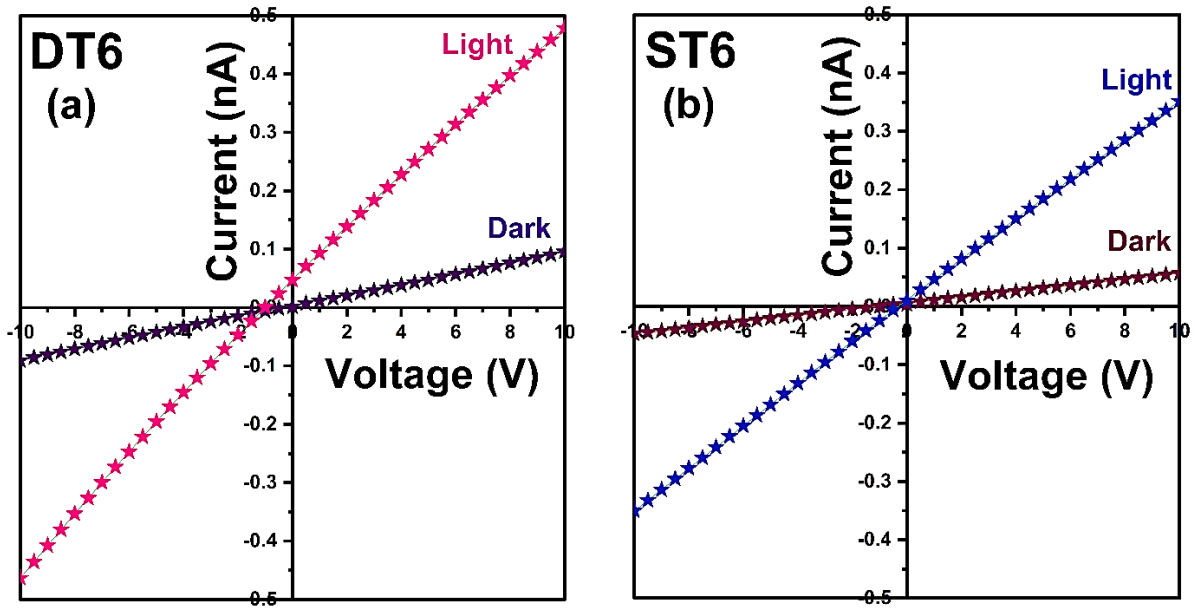

Figure 3.20. IV characteristics of $Cs_3Sb_2I_9$ self-powered photodetector a) DT6 and b) ST6 thin films [50].

Additionally, key performance metrics such as sensitivity, responsivity, and detectivity of the $Cs_3Sb_2I_9$ thin-film-based photoconductors were evaluated under illumination from the 50 W halogen lamp (P = 30 W/cm²). Photosensitivity (S) was determined using the equation (1.1):

$$S\ (\%) = [(I_l - I_d)/I_d] \times 100 \qquad (1.1)$$

where I_l is the current under illumination and I_d is the dark current. Responsivity (R), representing the photocurrent generated per unit of incident light power, was calculated as equation (1.2):

$$R = I_{ph}/(A \times P) \qquad (1.2)$$

The photocurrent I_{ph} is defined as $I_{ph} = (I_l - I_d)$. The responsivity and detectivity (D) were calculated using the following formulas, where A represents the effective area (0.25 cm²) and e is the electron charge:

$$D = R\sqrt{A} / \sqrt{2eI_d} \qquad (1.4)$$

The photosensitivity, responsivity, and detectivity of $Cs_3Sb_2I_9$ thin films, formed by rapid iodization of drop-cast and spin-coated precursors, were found to be 1.4×10^{3}% and 2.2×10^{2}%, 6.2×10^{-10} and 2.4×10^{-10} mA/W, and 9.6×10^{5} and 2.4×10^{5} Jones, respectively [4].

A comparative analysis of the self-powered photodetectors fabricated from $Cs_3Sb_2I_9$ thin films through rapid iodization, alongside other reported $Cs_3Sb_2I_9$ and $Cs_3Bi_2I_9$ photodetectors, is

summarized in Table 3.4. It is observed that the Ag/C/0D $Cs_3Sb_2I_9$/C/Ag photoconductor exhibits relatively lower photodetector characteristics compared to other photodiodes. However, the effective area of these devices is larger. Unlike previously reported devices that operate using 0D or 0D/2D $Cs_3Bi_2I_9$ or $Cs_3Sb_2I_9$ thin films in photovoltaic (PV) structures, our self-driven photodetector utilizes 0D $Cs_3Sb_2I_9$ (dimer – hexagonal structure) thin films in photoconductor mode. This unique architecture, despite its lower performance, offers a simpler synthesis process that merits attention.

Table. 3.4. Comparison of self-powered lead-free Sb and Bi based perovskite photodetectors performance with our work [50].

Architecture	**Synthesis method**	**Sensitivity (%)**	**Area (cm^2)**	**Light source**	**Responsivity (mAW^{-1})**	**Detectivity (Jones)**	**Reference**
Ag/C/ 0D $Cs_3Sb_2I_9$/C/Ag	Drop casting followed by rapid iodization	1.4×10^3	0.25	White light	6.2×10^{-10}	9.6×10^5	This work
Ag/C/ 0D $Cs_3Sb_2I_9$/C/Ag	Spin coating followed by rapid iodization	2.2×10^2	0.25	White light	2.4×10^{-10}	2.4×10^5	This work
FTO/c-/mp-TiO_2/ 0D $Cs_3Sb_2I_9$/ Poly-TPD/Au	Spin coating	-	0.0725	505 nm	10^{-3}-10^2	4.3×10^{12}	[112]
FTO/ 0D $Cs_3Sb_2I_9$/C/Ag	Ultrasonic spray	1.57×10^2	0.25	405 nm	0.0051	5.9×10^8	[113]
FTO/TiO_2/ 2D $Cs_3Bi_2Br_9$/Au	Spin coating	-	0.1	300-550 nm	4.33	1.3×10^{11}	[114]
ITO/PEDOT:PSS/ 2D $Cs_3Bi_2I_6Br_3$/ C60/BCP/Ag	Spin coating	4.1×10^4	0.0314	White light	15	4.6×10^{11}	[115]
ITO/SnO_2/0D/2D $CsBi_3I_{10}$/Au	Spin coating	-	0.004	650 nm	0.2×10^{-3}	1.8×10^{13}	[116]

Typically, photodetectors generate electron-hole pairs under illumination, which are then separated by an electric field created by an externally applied bias. The resultant charge flow is collected as the output current signal. Conversely, self-powered photodetectors generate a measurable current signal in response to incident light without any external bias voltage. Such devices can operate in photovoltaic (PV) mode or as integrated nanopower sources [117]. A

PV effect-based photodetector relies on the built-in electric field across a p-n junction or Schottky junction to separate the photogenerated electron-hole pairs. In systems integrated with nanogenerators, electric fields are generated through triboelectric, piezoelectric, or pyroelectric mechanisms [35,36].

Literature reports on $Cs_3Sb_2I_9$ thin films utilized in self-powered photodetectors typically describe devices operating in PV mode within a FTO/TiO_2/$Cs_3Sb_2I_9$/Poly-TPD/Au heterostructure [112]. However, in our experiments, the $Cs_3Sb_2I_9$-based self-powered photodetector operates in photoconductor mode, where no PV effect is feasible. The symmetrical C/Ag contacts on the $Cs_3Sb_2I_9$ thin film surface eliminate the potential influence of a Schottky junction, as evidenced by the ohmic behavior of the I-V characteristics (Figure 3.20).

Given these observations, the self-driven photoconduction mechanism in $Cs_3Sb_2I_9$ thin films is likely rooted in their ferroelectric properties, which induce electrical polarization within the material [37,30,38]. Ferroelectric polarization can generate an electric field, serving as a driving force for separating photoexcited electron-hole pairs, thereby eliminating the need for an external power source. This ferroelectric behavior may arise from the crystal structure, space group, ion arrangement, and charge distribution in $Cs_3Sb_2I_9$. Specifically, the hexagonal structure of 0D $Cs_3Sb_2I_9$ (*$P6_3/mmc$*) confirmed by XRD analysis suggests potential ferroelectricity, even though this effect is more pronounced in 2D $Cs_3Sb_2I_9$ with trigonal symmetry (*R3m*). The arrangement of Cs^+, Sb^{3+}, and I^- ions within the crystal lattice likely influences this ferroelectric behavior.

During illumination, ion migration, as observed in conventional hybrid perovskites and Bi-based perovskite-inspired compounds [39,40,41,42], could lead to lattice strain and local structural disorder, resulting in broken symmetry and induced polarization within the $Cs_3Sb_2I_9$ thin films. This induced electric field can provide the necessary driving force for separating photogenerated carriers, leading to self-powered photoconduction. The presence of lone pair electrons on Sb^+ ions within the $[Sb_2I_9]^{3+}$ octahedra of the crystal lattice may further contribute to the observed ferroelectricity [125].

Further research is needed to thoroughly understand the self-driven photoconduction mechanism and to optimize the optoelectronic performance of these materials.

Regarding photostability, although there is a reduction in photocurrent over time, the ST6 photodetector tends to stabilize after approximately 3000 s, as indicated by the constant on/off

cycles. This stability is likely due to the uniformity and compact morphology of the ST6 films, which offer more consistent photoresponse compared to the DT6 films. Factors such as crystallinity, surface and bulk defects, light-induced degradation, ion migration, film thickness, phase purity, ambient stability, and thermal and photostability [44,45,46] are crucial in determining the performance and application potential of $Cs_3Sb_2I_9$ devices. Additionally, the crystal structure—whether 0D or 2D—dependent on synthesis techniques, also plays a significant role in device performance. The choice of suitable electron transport and hole transport layers, the nature of interfaces [44,17], and the electrode spacing are critical factors as well. Smaller electrode separation ensures adequate absorption, rapid current response, and low leakage current [129].

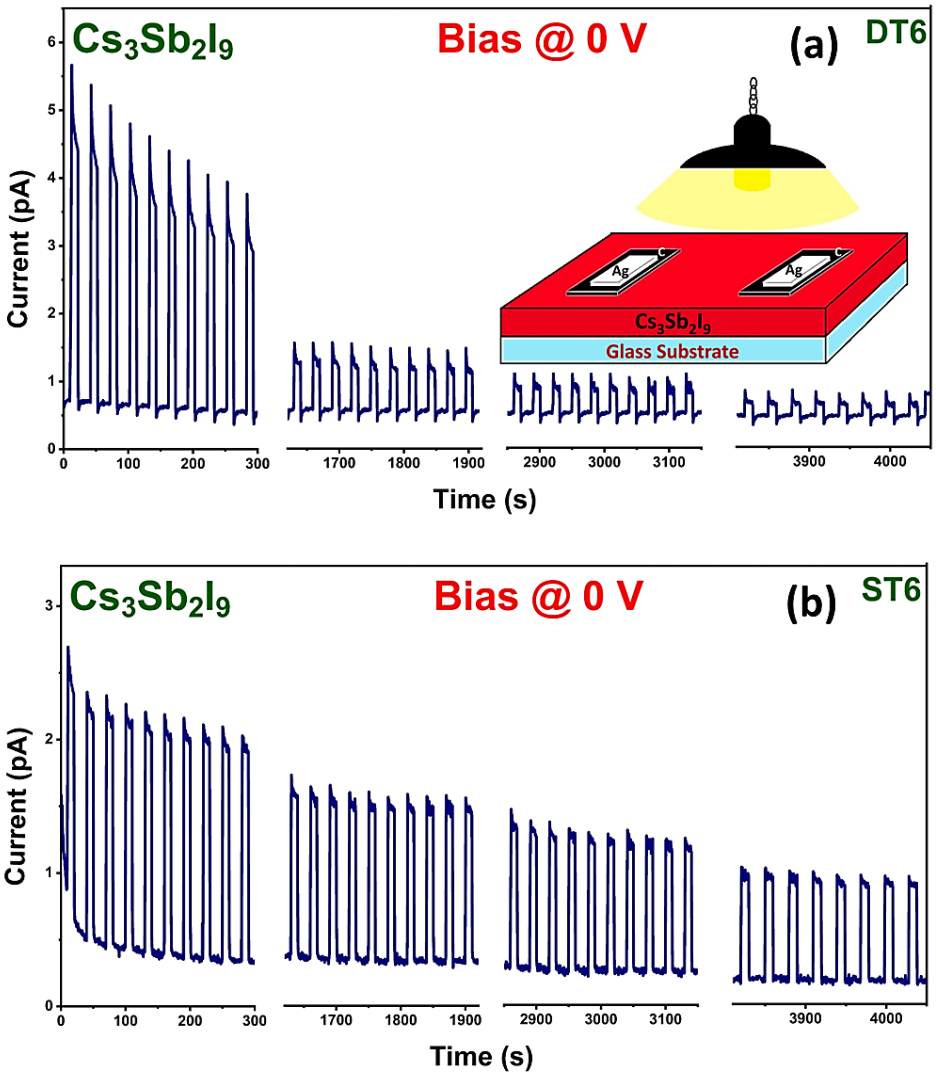

Figure 3.21. Zero-biased photodetection of $Cs_3Sb_2I_9$ perovskite thin film on/off switching response for 135 cycles (4050 s) [50].

To address material instability, surface passivation [48,49,50,51] and proper encapsulation are effective solutions, as demonstrated with other known halide perovskites. Doping the photoactive halide perovskites with sulfur [134] may also enhance stability under light and ambient conditions.

Comparable studies on self-powered $Cs_3Bi_2I_9$ photodetectors synthesized on FTO, which were tested over 2000 s (spanning 2000 consecutive cycles) [135], highlight the exceptional optoelectronic properties and fabrication techniques that enable perovskite-based photodetectors to achieve superior device performance [136]. To ensure compatibility with remote sensing applications, operating these devices in a self-powered mode is highly desirable.

This study focuses on the synthesis of $Cs_3Sb_2I_9$ thin films through the rapid iodization of Sb_2S_3-CsCl precursors, which were deposited using two different fabrication methods: drop casting and spin coating. A comparative analysis conducted at various iodization times reveals the formation of a 0D perovskite hexagonal crystal structure with the space group *$P6_3/mmc$*. The schematic representation of the synthesis mechanism for $Cs_3Sb_2I_9$ thin films is shown in Figure 3.22.

The Sb_2S_3-CsCl precursor was prepared by either drop casting or spin coating CsCl onto a chemically bath-deposited Sb_2S_3 thin film. Previous studies have reported the formation of SbI_3 through the iodization of Sb_2S_3 [67] and SnI_4 from SnS thin films via S^{2-} anion replacement with I^- anions [137]. In our process, during iodization at 100°C, iodine vapor is introduced into the Sb_2S_3-CsCl precursor. This process involves dissociation, anion replacement reactions, and the recrystallization of a new phase. CsCl dissociates (dissociation energy: 439 kJ/mol [138]; enthalpy: -17.183 kJ/mol), and chlorine is replaced by iodine. The anion replacement reaction in Sb_2S_3 during iodization results in sulfur evaporation (Sb-S dissociation energy: 379 kJ/mol [138]) to form SbI_3. The enthalpy of Sb_2S_3 is -141.8 ± 4.1 kJ/mol. This anion replacement mechanism is heavily influenced by surface chemistry, similar to anion exchange reactions in halides [139].

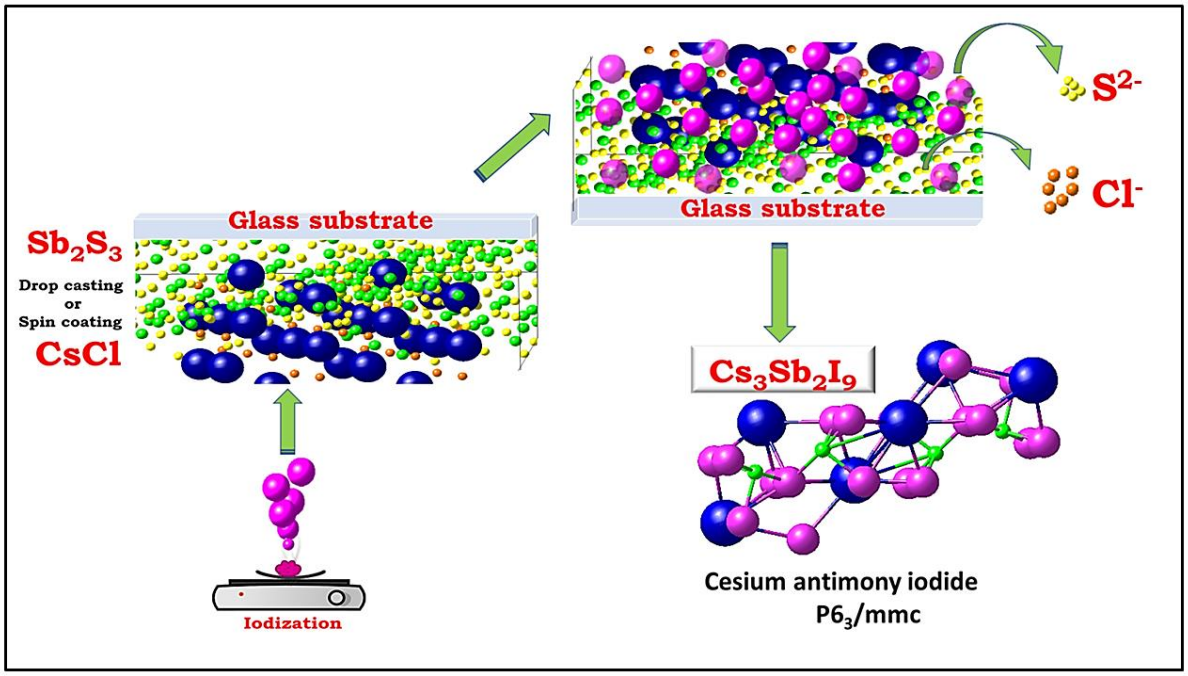

Figure 3.22. Schematic diagram of $Cs_3Sb_2I_9$ synthesis mechanism [50]

The anion replacement reactions occur within 2 minutes, leading to the formation of $Cs_3Sb_2I_9$, and further iodization promotes crystallite growth and reorientation. By correlating the structural and compositional analysis of the films formed under different conditions, we propose a direct anion replacement reaction, as represented in equation (3.3). Additionally, with very low concentrations of CsCl, the formation of SbI_3 is possible, as evidenced by our XRD analysis:

$$2\ Sb_2S_3 + 6\ CsCl + 9\ I_2 \rightarrow 2\ Cs_3Sb_2I_9 + 3\ Cl_2 + 6\ S \qquad (3.3)$$

Considering the formation enthalpy of $Cs_3Sb_2I_9$, calculated with respect to the energies of its constituent atoms, the 0D form is more stable compared to its 2D polymorph [140]. Thus, the 0D $Cs_3Sb_2I_9$ perovskite thin films were successfully synthesized through a facile iodization process of Sb_2S_3-CsCl precursor films.

3.9 Graphene Inco-operation for improved photoresponse

The XRD pattern (Figure 3.23(a)) reveals distinct peaks corresponding to $Cs_3Sb_2I_9$ and graphene, confirming the successful incorporation of graphene into the composite structure. A comparison between pure graphene, graphene + CsCl, and $Cs_3Sb_2I_9$ + graphene indicates

changes in diffraction patterns, suggesting enhanced crystallinity or a modified preferred orientation upon graphene integration. Notably, peaks at typical graphene-related diffraction angles (~26°) further confirm its presence.

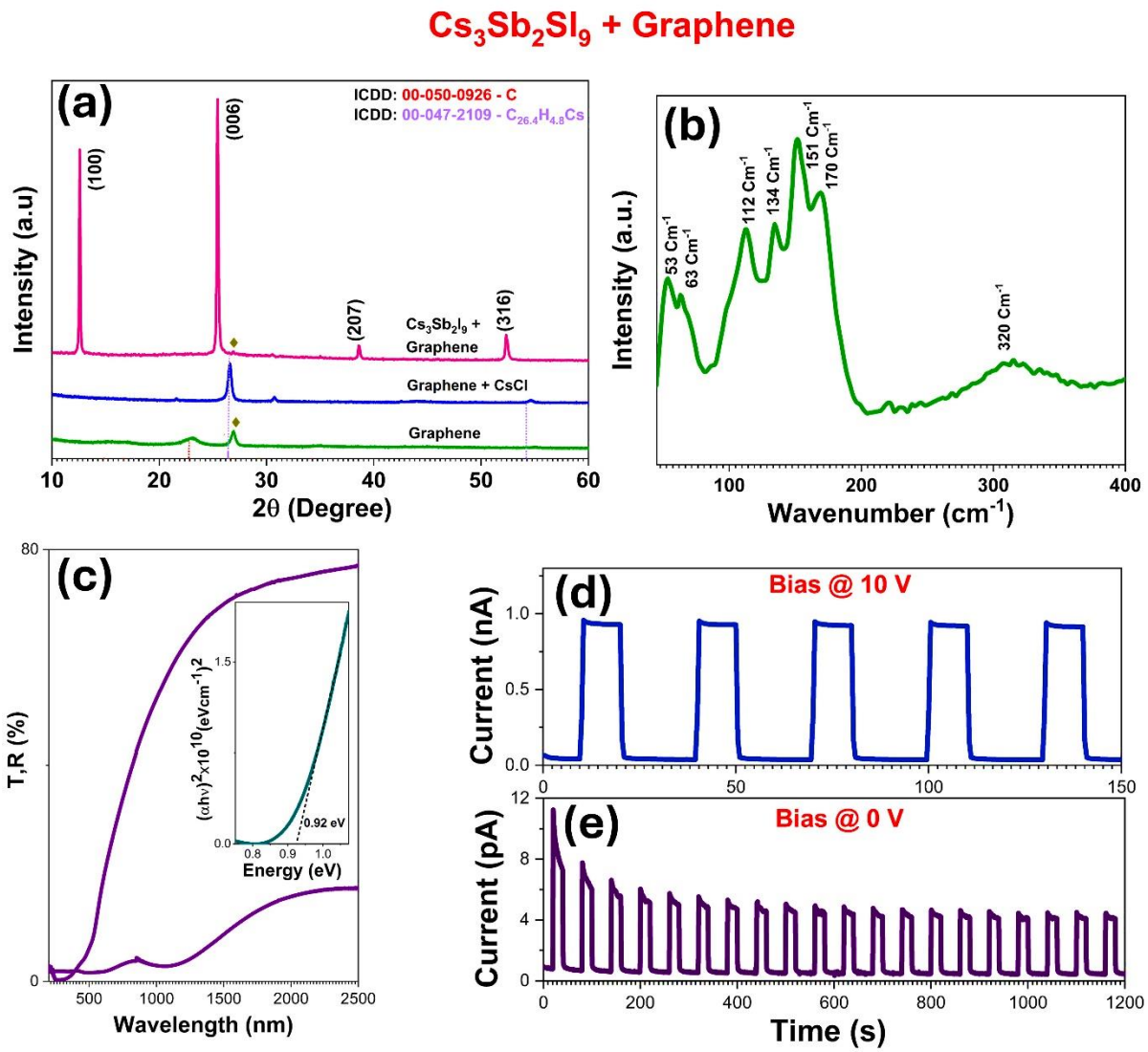

Figure 3.23: Structural, optical, and photodetection analyses of $Cs_3Sb_2I_9$ + graphene composite, highlighting enhanced crystallinity, vibrational modes, optical properties, and photodetection performance.

Raman spectra (Figure 3.23(b)) display characteristic peaks at 63 cm^{-1} and 112 cm^{-1}, attributed to the lattice vibrations of $Cs_3Sb_2I_9$. Additional peaks in the higher wavenumber region further support the structural integrity of the perovskite phase. No clear evidence of graphene's D and G bands (typically around 1350 cm^{-1} and 1580 cm^{-1}) was observed, possibly due to strong interactions with $Cs_3Sb_2I_9$. A slight Raman peak shift suggests graphene's influence on

modulating vibrational modes and contributing to structural stability. The transmittance and reflectance spectra (Figure 3.23(c)) reveal an absorption edge with a corresponding Tauc plot inset, indicating an optical bandgap of 0.92 eV. The incorporation of graphene broadens light absorption and enhances transmittance in the visible to NIR regions. This improvement may be attributed to reduced surface recombination and better charge transport properties facilitated by graphene.

Photodetection under a 10 V bias (Figure 3.23(d)) exhibits stable and periodic current signals, demonstrating effective photodetection. Graphene's high conductivity likely enhances charge collection and improves response speed. The sharp ON/OFF transitions indicate good interfacial contact and efficient charge transfer within the composite. Even at zero bias, photodetection signals were observed (Figure 3.23(e)), confirming self-powered operation. Graphene likely plays a crucial role in facilitating efficient charge separation and transport due to its high carrier mobility. Enhanced signal stability and higher amplitude further suggest that graphene mitigates recombination losses and improves device performance.

3.10 Photoresponse and Stability of ZnO/$Cs_3Sb_2I_9$ Device

Figure 3.24(a) presents the X-ray diffraction (XRD) pattern of the ZnO/$Cs_3Sb_2I_9$ device structure, revealing a clear peak at the (002) orientation, characteristic of the ZnO crystal structure. This confirms the successful deposition of ZnO as the electron transport layer (ETL), oriented to facilitate efficient charge transport and interaction with the $Cs_3Sb_2I_9$ absorber layer.

In Figures 3.24(b) and 3.24(c), the photoresponse of the device is shown at 0V and 2V bias, measured over several days. Initially, the device exhibits a very low current response, but over time, the current increases gradually under illumination. When the device is in the dark, the current decreases slowly. This type of behavior, often referred to as *persistent photoconductivity* (PPC), is commonly observed in materials where charge carriers are trapped in defect states and are gradually released under light exposure. In this case, the increase in current under illumination is likely due to the filling of these trapped states, which improves charge transport. However, the response remains relatively weak, indicating that the overall efficiency is limited.

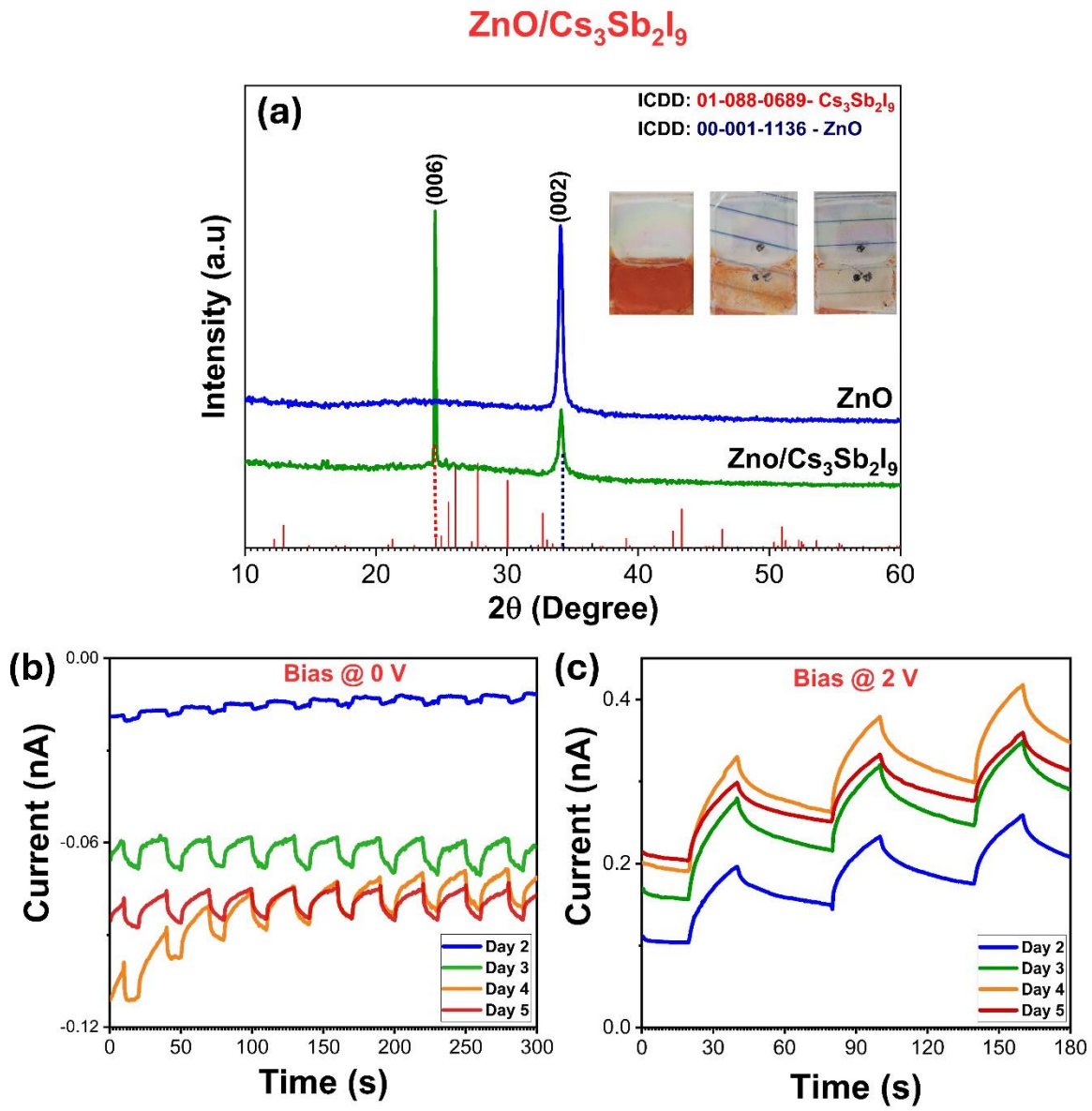

Figure 3.24. (a) XRD pattern showing ZnO (002) orientation, and (b) photoresponse measurements at 0V and (c) at 2V bias, illustrating gradual current increase under illumination and slow decrease in the dark, with degradation observed within one week.

Despite the gradual increase in current under illumination, the device experiences significant degradation within one week, as seen in the decrease in current over time. While $Cs_3Sb_2I_9$ is generally stable, the degradation is primarily attributed to the ZnO layer, which is sensitive to moisture and environmental factors. This sensitivity can lead to a deterioration of the ZnO's electronic properties, negatively affecting the device performance. The slow decrease in current under dark conditions suggests that the charge recombination or trapping is not fully reversed when the device is not illuminated, highlighting the instability caused by the ZnO layer.

This type of current behavior, with slow increases under illumination and gradual decreases in the dark, is characteristic of *hysteresis* observed in devices, often due to charge trapping and release dynamics at the interfaces. To improve the stability of the device, it is crucial to address the degradation of the ZnO layer, possibly through surface passivation or moisture protection, and ensure that the $Cs_3Sb_2I_9$ layer remains stable during prolonged use. Additionally, optimizing the interface between ZnO and $Cs_3Sb_2I_9$ could help reduce charge trapping and improve the overall performance and stability of the device.

3.11 Conclusions

- **Successful Synthesis**: $Cs_3Sb_2I_9$ thin films were successfully synthesized under ambient conditions using a rapid iodization method.
- **Precursor Preparation**: The Sb_2S_3-CsCl precursors were formed by chemical bath deposition of Sb_2S_3, followed by CsCl deposition via drop casting or spin coating.
- **Effect of Deposition Method**: The comparison between drop-casted and spin-coated films showed that the iodization time significantly influenced the crystallite size and surface morphology.
- **Structural Confirmation**: The hexagonal phase of $Cs_3Sb_2I_9$ was confirmed through X-ray diffraction (XRD) and Raman spectroscopy.
- **Morphological Observations**: SEM analysis revealed that both the CsCl deposition technique and iodization duration impacted the film morphology.
- **Optical Properties**: Phase-pure $Cs_3Sb_2I_9$ films exhibited a direct band gap in the range of approximately 1.8–1.96 eV.
- **Photoconductive Behavior**: The films demonstrated photoconductivity and were capable of self-powered visible light detection.

Chapter 4: Synthesis and characterization of silver antimony iodide ($AgSb_2I_7$) for photodetector applications

4.1 Introduction

In recent times, semiconductors derived from antimony (Sb) and bismuth (Bi) have garnered considerable attention due to their potential as non-toxic, eco-friendly materials for optoelectronic applications. These materials, classified as rudorffites or pnictogen-based halides with a general formula of $A_xB_yX_{x+3y}$ (where $A^+ = Ag^+/Cu^+$, $B^{3+} = Sb^{3+}/Bi^{3+}$, and $X = I^-$ or Cl^-, or Br−), are known for their direct bandgaps ranging from 1.6 to 2.8 eV, exceptional light absorption (>10^5 cm^{-1}), efficient charge carrier transport, strong environmental stability, and suitability for low-temperature synthesis routes—attributes that position them as promising candidates for various optoelectronic devices [44,141].

Given the similar electronic configurations and oxidation states (3+ and 5+) of Sb and Bi, silver antimony iodide and silver bismuth iodide display analogous optoelectronic characteristics rooted in their respective crystal lattices [43]. Nevertheless, differences in ionic radius and electronegativity between Sb and Bi cause distinct structural and electronic variations, which can influence their material properties and functional utility [64]. Silver-based iodobismuthates ($Ag_xBi_yI_{x+3y}$) usually consist of a close-packed iodide lattice. Their cation sublattice can exhibit either a layered rhombohedral $CdCl_2$-type framework or a three-dimensional cubic defect spinel arrangement. Silver-rich phases (x > 1) often form layered structures with R3m symmetry, where Ag+ and Bi3+ ions are randomly distributed in alternating <111> layers [44]. In contrast, Bi- or Sb-enriched compositions (y > 1) tend to stabilize in a defect spinel structure with Fd3m symmetry, characterized by vacant octahedral sites within the cation framework [44]. An example is $AgBi_2I_7$, which crystallizes in the Fd3m space group, forming a network of [AgI_6] and [BiI_6] octahedra akin to that seen in $ThZr_2H_7$ [63]. These diverse crystal structures underline the compositional tunability and application-specific versatility of both Ag-Sb-I and Ag-Bi-I systems [141].

Film formation of silver bismuth iodide depends strongly on the method of synthesis. $AgBiI_4$ is typically formed through vapor deposition [142], while hot-casting methods yield Ag_3BiI_6 and Ag_2BiI_5 with uniform grain distribution [143]. Solution-based processes are more

conducive to producing $AgBi_2I_7$ [44]. These materials have demonstrated utility in a range of applications including memristive switching devices [144], chemical sensors [145], and photovoltaic cells [44,64]. Incorporating Sb into Bi-based compositions has been found to enhance solar cell efficiency, with compounds like $AgBi_{0.5}Sb_{1.5}I_7$ outperforming their pure Bi and Sb analogs [68,146–149]. Among the most successful compositions, Ag_2BiI_5, $AgBi_2I_7$, and Ag_3BiI_6 have delivered noteworthy photoresponse, with sulfoiodide variants of Ag-Bi-based materials achieving power conversion efficiencies as high as 5.44% [68,146,147,150]. Despite these promising outcomes, silver-antimony halides remain underexplored, especially in terms of scalable and simplified synthesis protocols that could enhance accessibility and reduce material waste [141].

The motivation for the present study stems from earlier reports demonstrating the rapid transformation of Sb_2S_3 thin films into SbI_3 through a straightforward iodination process [67]. Recent efforts in developing zero-bias photodetectors using compounds such as Cu_2AgBiI_6 [151] and Ag_2BiI_5 [149] have further underscored the relevance of these materials. For example, a self-powered Cu_2AgBiI_6 device achieved a responsivity of 85 mA/W under 405 nm illumination using P3HT as a hole-transporting layer [151], while Ag_2BiI_5 integrated into a mesoporous titania structure maintained consistent responsivity above 100 mA/W across the visible spectrum, making it a compelling material for NIR-blind photodetection [149].

Despite the structural and electronic similarities shared with their Bi-based counterparts, silver-antimony iodides remain relatively uninvestigated, particularly concerning synthesis and functional integration into devices. Mixed-halide absorbers such as $AgBi_{2-x}Sb_xI_7$ ($x = 0.5$ to 2) have been developed using spin-coating methods involving precursors AgI, BiI_3, and SbI_3 dissolved in a DMF/DMSO mixture [64]. Here, tuning the Sb/Bi ratio affected both grain morphology and photovoltaic output, with a 3:1 Sb to Bi ratio yielding optimal performance. Other synthesis approaches include anti-solvent-assisted spin coating to fabricate hexagonal Ag_2SbI_5 using AgI and SbI_3 in DMSO/HI, followed by thermal treatment at 110 °C [66]. Additionally, $AgSbI_4$ was synthesized through solid-state reactions under vacuum at elevated temperatures, resulting in a phase with thermochromic properties and a bandgap reduction from 1.68 eV to 1.55 eV upon heating [65]. While these studies highlight structural stability and bandgap tunability, many lacked direct application in devices, especially photodetectors. This creates an opportunity for further research into simpler, more efficient fabrication strategies tailored for functional optoelectronic integration [141].

The current investigation introduces a novel fabrication route for $AgSb_2I_7$ thin films through the iodization of layered Sb_2S_3/Ag precursors. This process involved thermal evaporation of

Ag onto chemically deposited Sb_2S_3 layers, followed by iodization via both conventional heating and microwave-assisted techniques. Structural and optoelectronic analyses revealed substantial differences between the two iodization methods, notably in terms of crystallographic orientation, surface topography, and overall photoresponse. Furthermore, $AgSb_2I_7$ films were employed in heterojunction photodiodes with configurations such as FTO/n-CdS/i-$AgSb_2I_7$/C/Ag and FTO/n-CdS/i-$AgSb_2I_7$/p-CuI, both demonstrating self-powered photodetection in the visible spectrum. This study represents the first detailed exploration of combining chemical bath deposition, thermal evaporation, and microwave-assisted conversion for synthesizing $AgSb_2I_7$, and thoroughly evaluates its potential for zero-bias photodetector applications.

4.2 Experimental

2.1 Materials

All the materials were purchased and used without further purification. These materials include $SbCl_3$ (Fermont, 99.7%), $Na_2S_2O_3{\cdot}5H_2O$ (Fermont, 99.9%), $(CH_3)_2CO$ (Fermont, 99.6%), silver wire (4N, Alpha Aeser), I_2 (Iodine, Fermont).

2.2 Preparation of Sb_2S_3-Ag thin films

(i) Chemical bath deposition of Sb_2S_3 thin films

To prepare a chemical bath for the Sb_2S_3 thin films, 325 mg of $SbCl_3$ was dissolved in 2.5 ml $(CH_3)_2CO$. Subsequently, the bath, with a final volume of 80 ml, was prepared by adding 12.5 ml of 1 M $Na_2S_2O_3{\cdot}5H_2O$ and 65 ml of deionized water, followed by stirring [108]. Glass substrates (25 × 75 × 1 mm) were thoroughly cleaned and then vertically immersed in the chemical bath kept at room temperature for 2 h. After deposition, the substrates were rinsed with deionized water and dried using warm air.

(ii) Thermal evaporation of Ag layers: A high vacuum thermal evaporation system (Torr International, Model No: THE2-2.5 kW-TP) was used to evaporate silver onto the chemically deposited Sb_2S_3 thin film under a high vacuum of 10^{-6} Torr, with the substrate rotating at 20 rpm and a film deposition rate of 1.2 Å/s. Silver (Ag) layer thicknesses were monitored using a quartz crystal thickness sensor.

2.3 Iodization

Direct heating: Thin films of Ag/Sb_2S_3 were exposed to iodine vapor for 2 to 10 min. In this process, 50 mg of iodine powder in a closed Petri dish was heated on a hotplate at 100 °C, with the samples placed on the top cover.

Microwave heating: The Ag/Sb_2S_3 thin films were treated with iodine in a commercial microwave oven (1100 W) for 2 to 5 minutes. First, iodine powder was preheated in a microwave for one minute. Then, thin films of Ag/Sb_2S_3 were placed above this iodine vapor and microwave-treated for 2 to 5 minutes to form silver antimony iodide (SAI) thin films. Figure 1 illustrates the overall synthesis process.

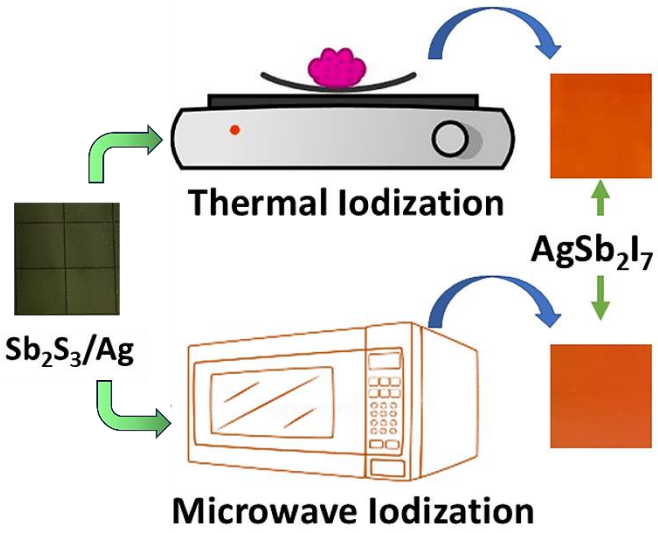

Figure 4.1. Schematic illustration of the synthesis process for silver antimony iodide ($AgSb_2I_7$), depicting the sample preparation stages involved [141].

First Ag thickness was optimized for a given thickness of Sb_2S_3 (~ 400 nm) and iodization time 4 min. Samples of varying Ag were prepared, and the iodized samples were labelled as SAI 100 (100 nm), SAI 70 (70 nm), SAI 50 (50 nm) and SAI 30 (30 nm). Based on the X-ray diffraction studies, Ag thickness of 30 nm was selected for further studies. Hence, Ag of 30 nm was deposited on Sb_2S_3 for the analysis of the SAI film growth as a function of iodization duration for both thermal and microwave processes. The thermally iodized films were labelled as SAI 2N (2 min), SAI 4N (4 min), SAI 6N (6 min), SAI 8N (8 min), and SAI 10N (10 min). The microwave processed films were identified as SAI 2M (2 min), SAI 3M (3 min), SAI 4M (4 min), and SAI 5M (5 min).

2.4 Heterostructures

Heterostructure devices, specifically photodiode configurations of FTO/n-CdS/i-$AgSb_2I_7$/C/Ag and FTO/n-CdS/i-$AgSb_2I_7$/p-CuI, were prepared on commercial FTO coated glass (MSE Supplies LLC, FTO TEC 7100SQ2.2). First, CdS thin films (~ 100 nm) were chemically deposited on a thoroughly cleaned FTO from a bath containing 5 mL of 0.1 M $CdCl_2$, 2.5 mL of 50% v/v $C_6H_{15}NO_3$ (triethanolamine), 5 mL of NH_4OH (15 M), 5 mL of 1 M CH_4N_2S (thiourea), and 32.5 mL of deionized water [152], and post-annealed for 1 h at 400 °C in a furnace (Model 1400, Barnstead Thermolyne). On the CdS-coated FTO substrates, $AgSb_2I_7$ thin films were deposited as described earlier. Following this, carbon and silver electrodes were painted onto the $AgSb_2I_7$ layer to form FTO/n-CdS/i-$AgSb_2I_7$/C/Ag device configuration. In the case of FTO/n-CdS/i-$AgSb_2I_7$/p-CuI devices, Ag (30 nm) and Cu (30 nm) layers were sequentially deposited via thermal evaporation, followed by iodization of the films to achieve the final device structure.

2.5 Characterization

X-ray diffraction (XRD) patterns of the iodized thin films were recorded with a PANalytical Empyrean diffractometer in the normal mode using Cu-Kα radiation (wavelength 1.54056 Å) to analyze the crystal structure. Chemical composition and the elemental states were determined by a Thermo Scientific K-alpha X-ray photoelectron spectrometer (XPS), and energy-dispersive X-ray spectroscopy (EDX) analysis employed with a Hitachi SU 8020 scanning electron microscope by which the surface morphology was examined. Raman spectra were measured by a Thermo Scientific DXR Raman microscope with a 532 nm excitation laser. Optical transmittance and reflectance spectra were measured by a Jasco V-770 UV-Vis-NIR spectrophotometer. Electrical measurements were carried out using a Keithley 6487 picoammeter/voltage source, both in the dark and under illumination from a halogen lamp, LEDs, and lasers, across the electrical contacts made using flash-dry silver colloidal suspension (SPI Supplies).

4.3 Results and discussion

4.4 Crystalline structure

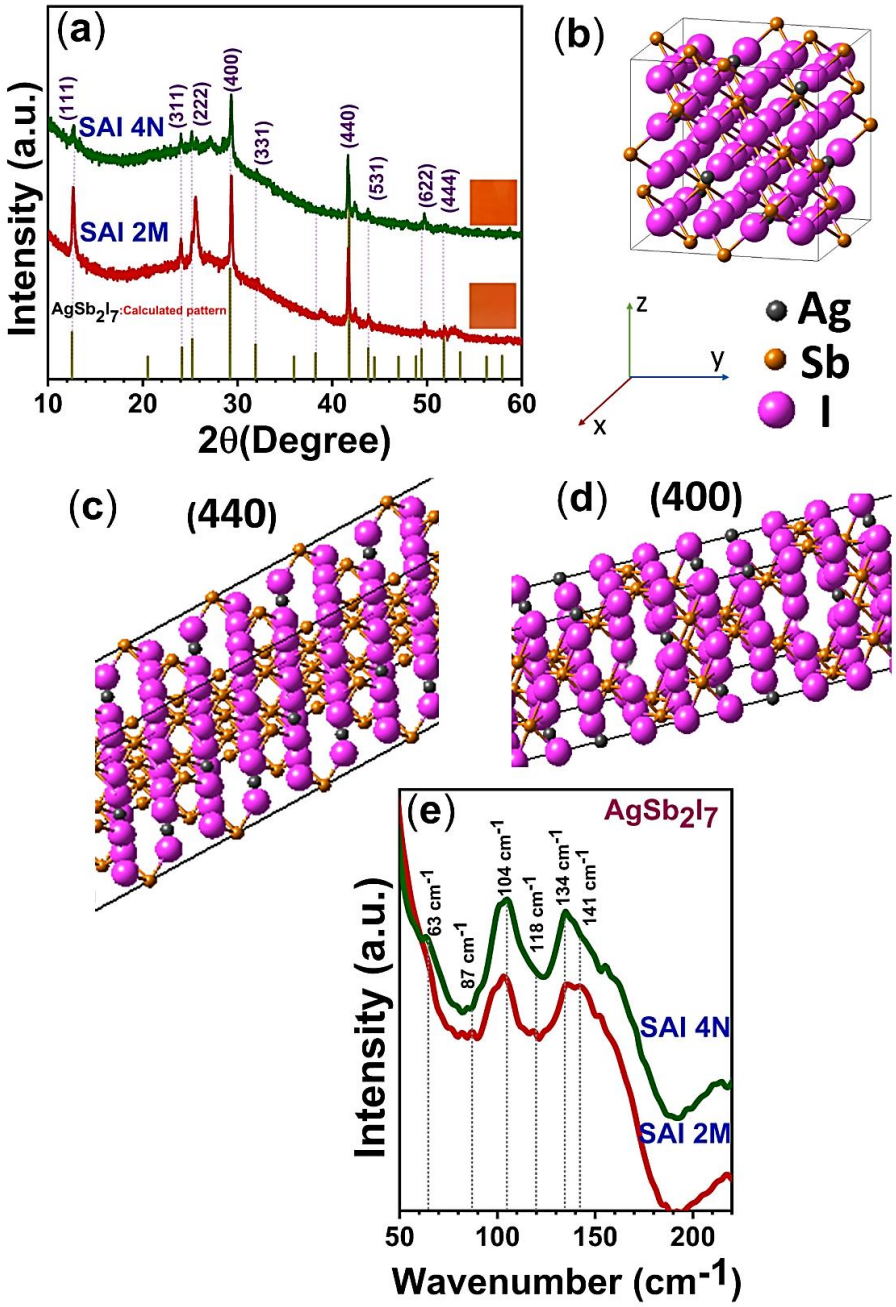

Figure 4.2. (a) XRD patterns of optimized $AgSb_2I_7$ thin films, comparing SAI 4N (thermal iodized) and SAI 2M (microwave iodized) (sample photos are also included). (b) Cubic $AgSb_2I_7$ structural model generated using MedeA software. (c) $AgSb_2I_7$ structure with (440) orientation. (d) $AgSb_2I_7$ structure with (400) orientation. (e) Raman spectra of $AgSb_2I_7$ thin films for both normal and microwave iodized samples [141].

Figure 4.2 (a) shows the XRD patterns of the optimized SAI 4N and SAI 2M thin films along with the photographs of the respective films. The diffraction patterns correlate with the presence of a cubic crystal structured silver antimony iodide ($AgSb_2I_7$) with a space group of *Fd3m* by comparing with the standard lines calculated using MedeA software (MedeA® 3.9, Materials Design, Inc., San Diego, CA, USA, 2024) as given in the figure. The calculated peak positions, interplanar distance (d) values and the respective (hkl) planes are given in Table 4.1. Based on these values, experimentally observed diffraction peaks at 12.54°, 24.15°, 25.24°, 29.22°, 31.91°, 41.8°, 43.82°, 49.46°, and 51.82° are indexed to the (111), (311), (222), (400), (331), (440), (531), (622), and (444) planes, of cubic $AgSb_2I_7$ in both cases. The thermally iodized thin films (SAI 4N) exhibit a preferential orientation along the (440) and (400) planes as seen in the figure, which is critical for achieving the desired crystal structure with minimal defects and thereby leading to better charge transport properties. In a study of $AgBi_{2-x}Sb_xI_7$ thin films, similar pattern was reported by analyzing the systematic shift in the diffraction peaks observed for the films formed by varying Bi/Sb ratio [64], without giving any reference for standard lines corresponding to phase pure $AgSb_2I_7$ [141].

Figure 4.3 depicts the optimization of silver thickness (30, 50, 70 and 100 nm) to achieve $AgSb_2I_7$ (SAI) formation during a consistent 4-minute thermal iodization. The XRD patterns show the phase-pure $AgSb_2I_7$ in SAI 30 thin films. Furthermore, the iodization time was adjusted for the films with 30 nm Ag, both thermal and microwave assisted iodization processes. Figures 4.4(a, b) present the diffraction patterns of the thin films formed by varying iodization from 4 to 10 minutes for thermal iodization and from 2 to 5 minutes for microwave iodization. Both thermal and microwave-iodized samples display $AgSb_2I_7$ phase. Longer duration of thermal iodization correlates with increased peak intensities. Additionally, a mixture of the SAI phase and AgI emerges after 2 minutes of iodization (SAIS02N) (Figure 4.5). In the case of microwave-treated samples, the peak intensities reduced for 5 min iodization which may be due to loss of material by the instantaneous heating during the iodization. The comparative analysis indicates that microwave iodization requires only half of the time for SAI phase formation compared to thermal iodization, showcasing the former's efficiency and energy-saving advantages [153]. In the hotplate heating, thermal conduction transfers heat from the hot surface to iodine kept in the Petri and the iodine vaporizes to react with the precursor layer of Ag/Sb_2S_3 to form silver antimony iodide as a result of sulfur replacement and diffusion

associated reaction [50]. This can often lead to uneven temperature distribution. In microwave heating, both iodine and the precursor Ag/Sb_2S_3 undergo instantaneous heating by electromagnetic waves due to localized microwave absorption resulting rapid and uniform internal heating, and thereby electromagnetic simulated modifications are possible during iodization. This efficient heating process enhances crystallization and grain growth, making it particularly effective for producing high-quality perovskite films with fewer defects [154]. Improved crystallinity and air-stability films due to microwave heat treatment of spin coated Ag_2BiI_5 perovskite was reported [155]. In our case, the high crystallinity of $AgSb_2I_7$ thin films with additional growth orientation along (111) planes can be attributed to this type of electromagnetically simulated growth during iodization. However, fine control of microwave power, frequency along with the substrate geometry and electrical characteristics are to be controlled to form highly oriented thin film growth without material loss [141,154,156].

Figures 4.2(b), (c), and (d) illustrate the unit cell, growth of (400) and (440) surfaces of cubic structured silver antimony iodide ($AgSb_2I_7$), generated using MedeA software. This structure was modelled by substituting Ag, Sb, and I atoms in place of Th, Zr, and H from the $ThZr_2H_7$ structure[63]. The lattice parameter, approximately a=b=c=12.233 Å, closely matches the experimental XRD data.

Further, the refinement of the crystal structure of silver antimony iodide ($AgSb_2I_7$) was performed using GSAS-II software and the data from Argonne National Laboratory [157]. The refined structure confirmed a centrosymmetric, face centered cubic lattice within the *Fd3m* space group. The unit cell dimensions were a=12.248 Å, with a unit cell volume of 1837.387 $Å^3$. Positional parameters for Ag, Sb, and I atoms were identified, along with their isotropic displacement parameters. The weighted residual (wR) was 4.18% and the goodness of fit (GOF) 1.83. Preferred orientation effects were analyzed using spherical harmonics up to order 8, yielding a texture index J of 2.4. Peak refinement yielded an average crystallite size of approximately 120 nm, nearly the same value for both cases. This large crystallite size indicates high crystallinity, which is advantageous for device performance due to improved charge transport and reduced defect density [141].

Table 4.1. Standard XRD lines calculated for $AgSb_2I_7$ thin films [141].

$AgSb_2I_7$				
Powder diffraction for Cu radiation, lambda = 1.54060				
h	**k**	**l**	**2Theta**	**I**
1	**1**	**1**	12.53	14.3
2	**2**	**0**	20.53	0.3
3	**1**	**1**	24.13	5.5
2	**2**	**2**	25.22	10.3
4	**0**	**0**	29.2	50.5
3	**3**	**1**	31.89	7.2
4	**2**	**2**	35.96	0.3
5	**1**	**1**	38.23	2
3	**3**	**3**	38.23	0.3
4	**4**	**0**	41.77	100
5	**3**	**1**	43.78	5.1
6	**2**	**0**	46.98	0.2
5	**3**	**3**	48.82	0.6
6	**2**	**2**	49.42	4.6
4	**4**	**4**	51.77	11.7
5	**5**	**1**	53.49	1.1
7	**1**	**1**	53.49	1.7
6	**4**	**2**	56.27	0.3
5	**5**	**3**	57.9	0.4
7	**3**	**1**	57.9	0.4
8	**0**	**0**	60.55	13.8
7	**3**	**3**	62.11	1.2
6	**6**	**0**	64.65	0.1
8	**2**	**2**	64.65	0.1
7	**5**	**1**	66.15	0.3
5	**5**	**5**	66.15	0.1
6	**6**	**2**	66.65	1.5
8	**4**	**0**	68.62	11.9
7	**5**	**3**	70.08	1.3
9	**1**	**1**	70.08	0.4
6	**6**	**4**	72.48	0.1
9	**3**	**1**	73.91	0.3
8	**4**	**4**	76.26	22
9	**3**	**3**	77.66	0.4
7	**7**	**1**	77.66	0.6
7	**5**	**5**	77.66	0.4
10	**2**	**0**	79.98	0.1
8	**6**	**2**	79.98	0.1
9	**5**	**1**	81.36	0.3
7	**7**	**3**	81.36	0
10	**2**	**2**	81.82	0.7

6	**6**	**6**	81.82	0.2
9	**5**	**3**	85.03	0.5
10	**4**	**2**	87.31	0.1
7	**7**	**5**	88.68	0
11	**1**	**1**	88.68	0
8	**8**	**0**	90.95	5.7
9	**5**	**5**	92.32	0.1
11	**3**	**1**	92.32	0.6
9	**7**	**1**	92.32	0.4
10	**6**	**0**	94.6	0
8	**6**	**6**	94.6	0
11	**3**	**3**	95.97	0
9	**7**	**3**	95.97	0.1
10	**6**	**2**	96.43	0.8
12	**0**	**0**	98.26	0.8
8	**8**	**4**	98.26	3.1
11	**5**	**1**	99.65	0.4
7	**7**	**7**	99.65	0.1
12	**2**	**2**	101.96	0
10	**6**	**4**	101.96	0.1
9	**7**	**5**	103.36	0.1
11	**5**	**3**	103.36	0
12	**4**	**0**	105.71	7.3
9	**9**	**1**	107.14	0.1
10	**8**	**2**	109.53	0.1
11	**7**	**1**	110.99	0
11	**5**	**5**	110.99	0
9	**9**	**3**	110.99	0
13	**1**	**1**	110.99	0
10	**6**	**6**	111.48	0.3
12	**4**	**4**	113.45	2.2
11	**7**	**3**	114.94	0.4
13	**3**	**1**	114.94	0.2
9	**7**	**7**	114.94	0.2
12	**6**	**2**	117.48	0.1
13	**3**	**3**	119.03	0
9	**9**	**5**	119.03	0.1
8	**8**	**8**	121.67	1.9
13	**5**	**1**	123.28	0.2
11	**7**	**5**	123.28	0.3
14	**2**	**0**	126.05	0
10	**10**	**0**	126.05	0
10	**8**	**6**	126.05	0.1
13	**5**	**3**	127.76	0.1
11	**9**	**1**	127.76	0
14	**2**	**2**	128.34	0.2

10	**10**	**2**	128.34	0.2
12	**8**	**0**	130.7	1.9
9	**9**	**7**	132.52	0.1
11	**9**	**3**	132.52	0.3
10	**10**	**4**	135.69	0
14	**4**	**2**	135.69	0.1
12	**6**	**6**	135.69	0
11	**7**	**7**	137.68	0
13	**7**	**1**	137.68	0
13	**5**	**5**	137.68	0.1
12	**8**	**4**	141.18	11.9
11	**9**	**5**	143.41	0.3
15	**1**	**1**	143.41	0.2
13	**7**	**3**	143.41	0.3
14	**6**	**0**	147.42	0

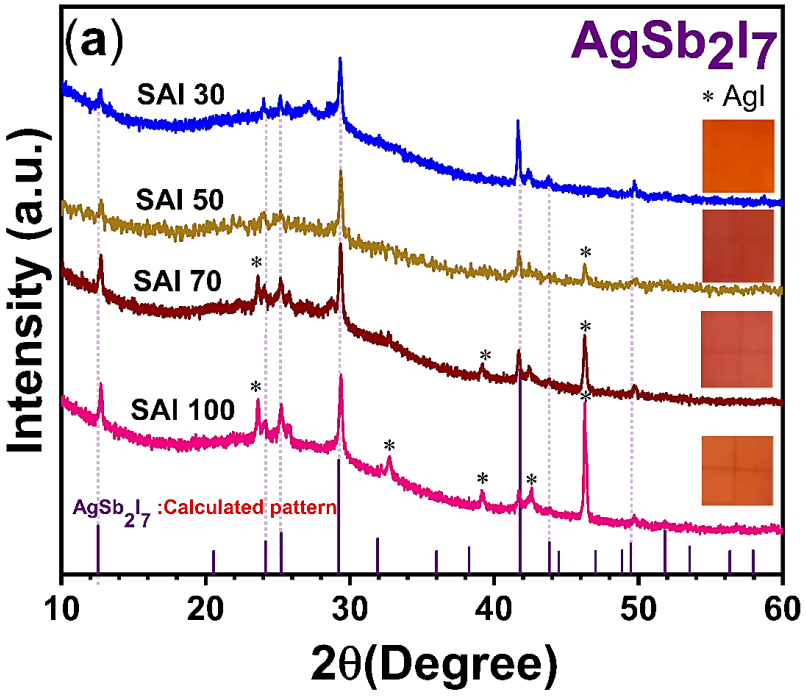

Figure 4.3. XRD patterns of $AgSb_2I_7$ thin films formed by varying Ag thickness [141].

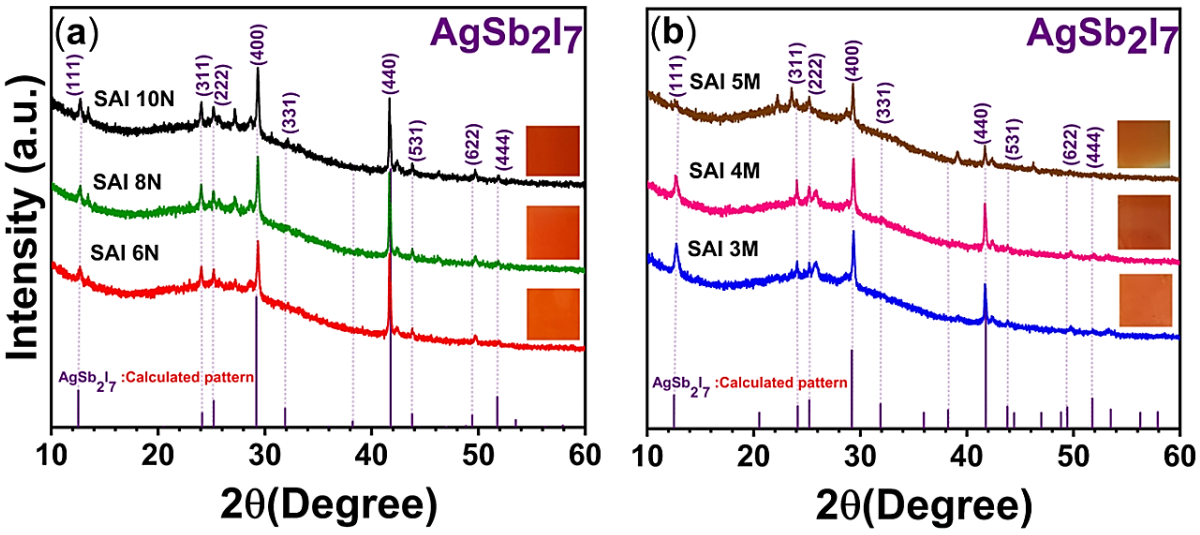

Figure 4.4. $AgSb_2I_7$ thin films XRD pattern by varying Iodization time (a) thermal iodized (b) microwave iodized [141].

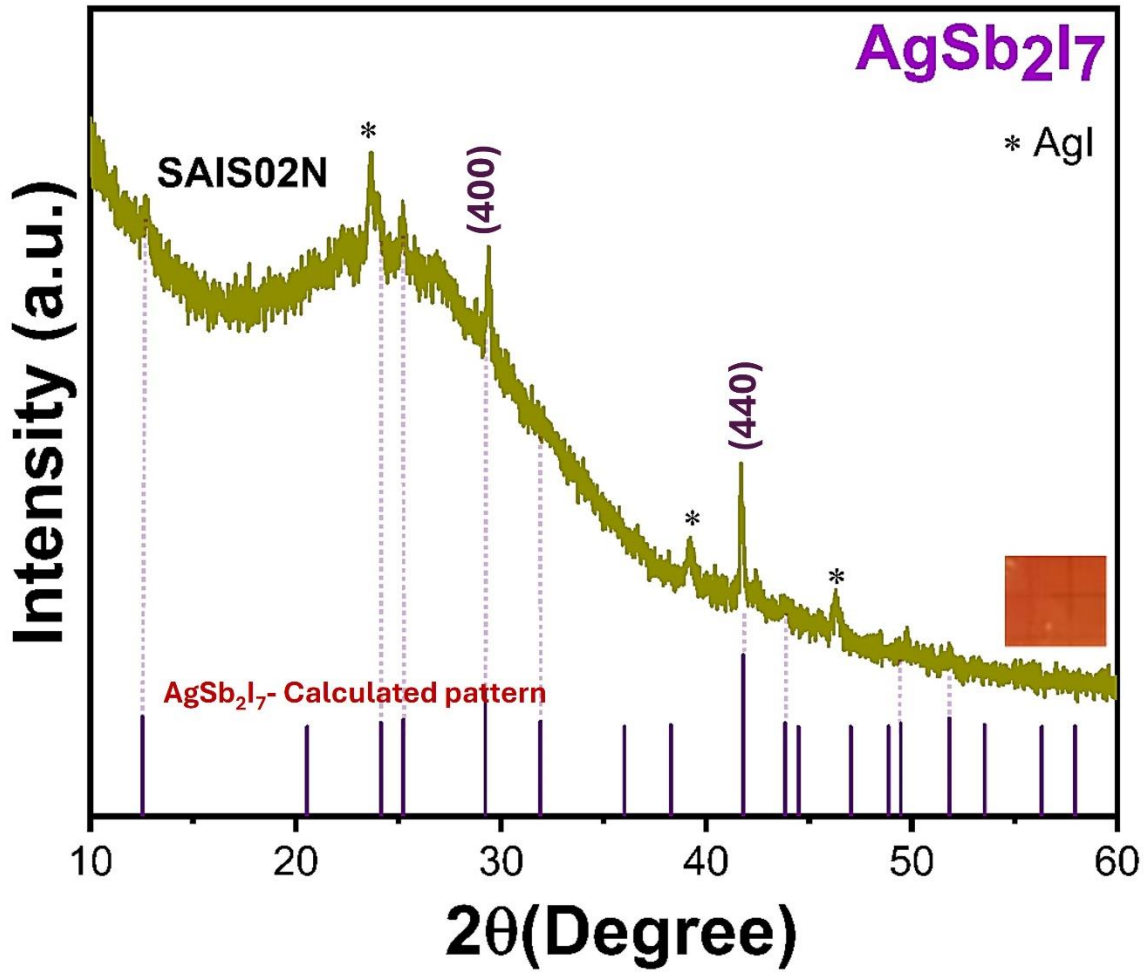

Figure 4.5. XRD pattern of SAI thin films at lower iodization time [141].

Raman spectroscopy was employed to investigate the vibrational energy modes of SAI ($AgSb_2I_7$) thin films, providing the first Raman analysis of $AgSb_2I_7$ thin films. In Figure 4.2(e) the Raman spectra of the SAI thin films, prepared using both thermal and microwave iodization are illustrated. Characteristic SAI peaks, near 63, 87, 104, 118, 134 and 141 cm^{-1} were observed, likely associated with the positions of SbI_3 and AgI peaks. In SbI_3, Raman peaks were found at 44, 65, 137, 159 cm^{-1} [67], while AgI exhibited peaks at 44 and 110 cm^{-1} [158]. The 63 cm^{-1} Raman line likely arises from the coupling of asymmetric stretching vibrations of iodine atoms shared between Ag–I and Sb–I bonds in the AgI and SbI_3 subunits. This line, observed with lower intensity, resembles the 68 cm^{-1} peak in the spectra of silver bismuth iodide (Ag_2BiI_5) [159], suggesting a left shift in the $AgSb_2I_7$ spectrum due to the lighter atomic mass of Sb compared to Bi. Additionally, a Raman line near 87 cm^{-1} observed in $AgSb_2I_7$ may correspond to intrinsic vibrational modes, potentially analogous to the E^g mode reported for BiI_3 in Ag_2BiI_5 [159]. This similarity could arise from shared structural motifs or comparable vibrational dynamics within the metal-halide framework, despite the compositional differences between the two materials. The absence of a broad Sb_2S_3 peak, typically linked to Sb–S bond vibrations [67] further confirms the formation of the ternary $AgSb_2I_7$ compound, as evidenced by distinct vibrational modes corresponding to Ag–I and Sb–I [141].

Theoretical studies on similar compounds, such as $AgBiI_4$ [160], have demonstrated that cation substitution can influence vibrational modes, particularly with respect to the size and charge of cations. The calculations showed larger cations induces strain in the crystal lattice, altering symmetry and affecting vibrational frequencies. Moreover, in this theoretical analysis, Zhai et al [160], explained that cation type, whether monovalent, divalent, or trivalent, also influences crystal symmetry and bonding environment, leading to changes in vibrational properties. These insights are relevant to silver antimony iodide, where similar effects may occur, as indicated by shifts in Raman peaks and characteristic lines observed in $AgSb_2I_7$ spectra [141].

4.5 Composition

Figure 4.6 presents the XPS survey spectra obtained after a 10-second argon ion etching of both SAI 4N and SAI 4M thin films. The spectra exhibit clear peaks corresponding to Ag, Sb, and I, with no detectable contamination or residual sulfur from the precursor,

underscoring the high purity of the films. For a detailed elemental analysis, high-resolution core-level XPS spectra of $AgSb_2I_7$ (SAI) thin films deposited on glass substrates were acquired. Figure 4.7(a-f) shows the core-level spectra of both SAI 4N and SAI 4M samples, measured under identical conditions following a single 10-second etching cycle using an argon ion beam. A monochromatic Al Kα X-ray source with a 400 µm spot size, energy step size of 0.2 eV, and a pass energy of 50 eV was employed for the analysis. All high-resolution peaks were fitted using a Gaussian-Lorentzian sum function, with a Shirley-type background correction applied for accurate peak deconvolution [141].

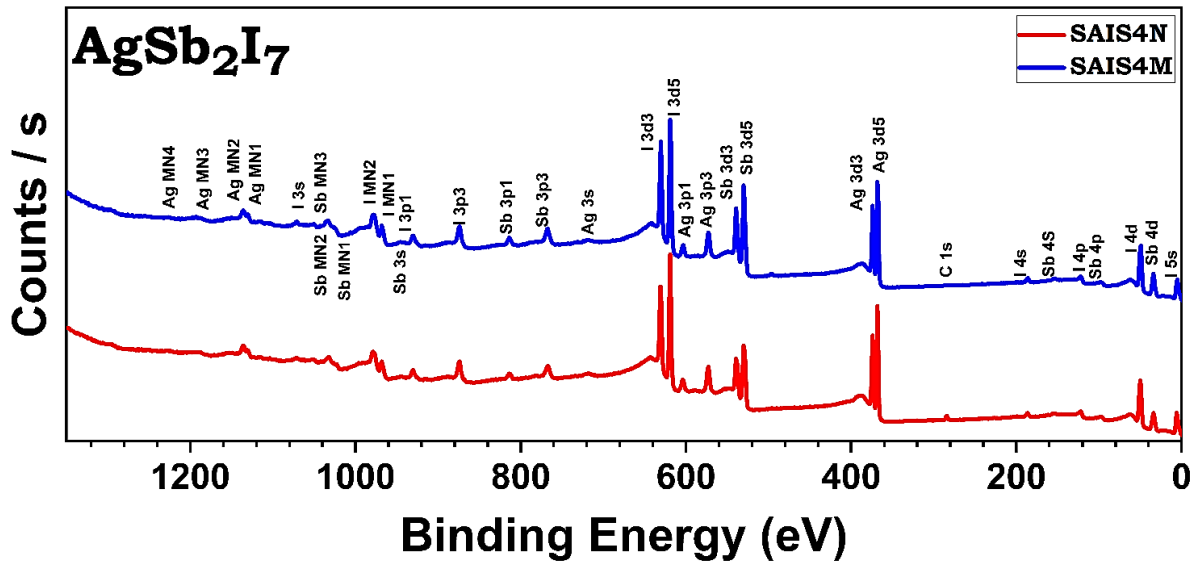

Figure 4.6. XPS survey spectrum of silver antimony iodide ($AgSb_2I_7$) thin film [141].

For SAI 4N, the Ag 3d spectrum (Figure 4.7(a)) displays two prominent peaks at binding energies of 368.5 eV ($3d_{5/2}$) and 374.5 eV ($3d_{3/2}$), with a spin-orbit splitting (ΔE) of 6 eV. These binding energies are characteristic of the +1 oxidation state [159] of silver (Ag^+) in $AgSb_2I_7$. The sharp and symmetrical nature of these peaks reflects the chemical uniformity of silver within the film, indicating the stable and homogenous incorporation of Ag^+ into the crystalline lattice of $AgSb_2I_7$. Unlike metallic silver (Ag^0), which typically exhibits plasmonic loss features as satellite peaks at higher binding energies due to free-electron density, no such plasmonic peaks were detected in the Ag 3d spectrum of SAI 4N, implying purely ionic nature of silver in the sample [141,161].

The Sb 3d spectrum for SAI 4N (Figure 4.7(b)) displays two doublets corresponding to different oxidation states of antimony. The primary doublet with higher intensity, observed

at binding energies of 530.7 eV ($3d_{5/2}$) and 540.0 eV ($3d_{3/2}$), is assigned to Sb^{3+} [50,67,162], which is the expected oxidation state of antimony in $AgSb_2I_7$. A secondary, lower-intensity doublet with binding energies of 528.8 eV ($3d_{5/2}$) and 538.2 eV ($3d_{3/2}$), can be attributed to metallic antimony (Sb^0) [50], This Sb^0 doublet may be the result of sputter-induced reduction during the XPS analysis [50,109].

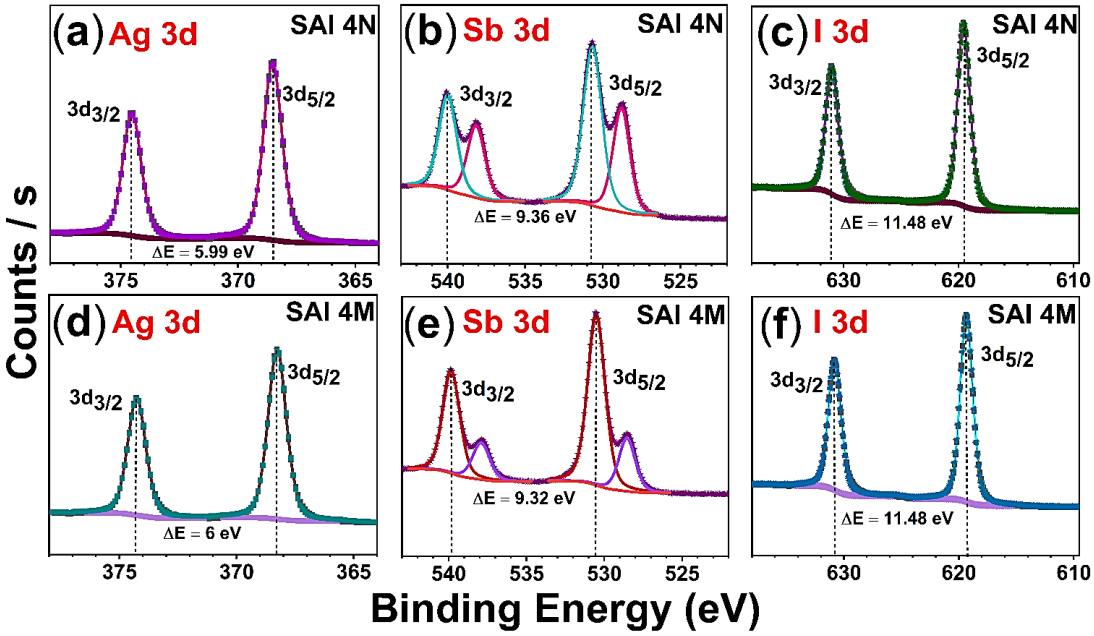

Figure 4.7. High-resolution core-level XPS spectra of silver antimony iodide ($AgSb_2I_7$) thin films: (a, b, c) represent Ag 3d, Sb 3d, and I 3d for sample SAI 4N (thermally iodized), while (d, e, f) correspond to Ag 3d, Sb 3d, and I 3d for sample SAI 4M (microwave-iodized) [141].

The I 3d spectrum for SAI 4N (Figure 4.7(c)) constitutes spin-orbit coupled 3d peaks at binding energies of 619.6 eV ($3d_{5/2}$) and 631 eV ($3d_{3/2}$), with a separation of 11.4 eV, corresponding to iodide ions (I^-) [50,67,159] in the $AgSb_2I_7$ structure.

The XPS spectra for SAI 4M (Figure 4.7(d), (e) and (f)) demonstrate similar results, indicating that the iodization method no influence on the chemical state of the elements. The Ag 3d peaks shift slightly to lower binding energies, 368.3 eV and 374.3 eV, while maintaining a ΔE of 6 eV, consistent with the +1 oxidation state. The Sb 3d spectrum retains similar features, with a primary doublet for Sb^{3+} and a lower-intensity doublet for Sb^0, reflecting comparable sputter-induced reduction behavior. Similarly, the I 3d peaks remain consistent, confirming the stable incorporation of iodide ions in samples.

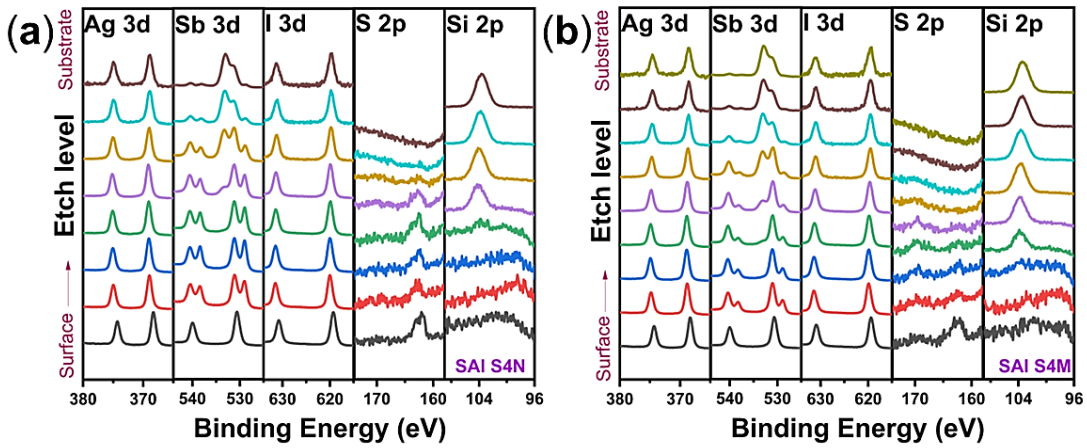

Figure 4.8. Depth profile of silver antimony iodide thin film a) SAI S4N, b)SAI S4M [141].

Depth profiles (Figure 4.8 (a, b)) reveal a uniform distribution of Ag, Sb, and I throughout from the film surfaces to the substrates. At the substrate/film interface, silicon and oxygen atoms are detected, with no sulfur indicating complete conversion to $AgSb_2I_7$. The quantitative analysis of the high-resolution spectroscopy (HRS) data reveals relative atomic concentrations of sulfur (0.22%), carbon (1.05%), silver (23.6%), antimony (30.0%), and iodine (44.4%), with integrated peak areas and signal intensities corroborating the presence and potential oxidation states of these elements in the sample, consistent with the phase of $AgSb_2I_7$, as further verified by additional EDX analysis.

Further, the total atomic composition of SAI 4N and SAI 2M thin films is estimated by EDX as given in Figure 4.9 (a, b). The thermally iodized sample shows an atomic composition of 10.3% Ag, 22.4% Sb, and 67.3% I, where as the microwave-iodized sample contains 14.4% Ag, 22.3% Sb, and 63.2% I. The thermally iodized sample shows Ag/Sb ratio of 0.46 and that of microwave-iodized sample, a slightly higher Ag/Sb ratio of 0.65 is detected. However, the formula stoichiometry ($AgSb_2I_7$), ratio of I/(Ag+Sb) of 1.72 is maintained in the microwaves films and a higher value of 2.05 in thermally iodized films. Thus, despite this variation, the microwave-iodized sample maintains the overall composition of $AgSb_2I_7$, demonstrating that microwave iodization is an effective method for achieving similar stoichiometry as thermal iodization. Notably, the XPS and EDX characterizations presented in this study provide the first comprehensive documentation of silver antimony iodide ($AgSb_2I_7$), highlighting the novel contributions to understanding its composition [141].

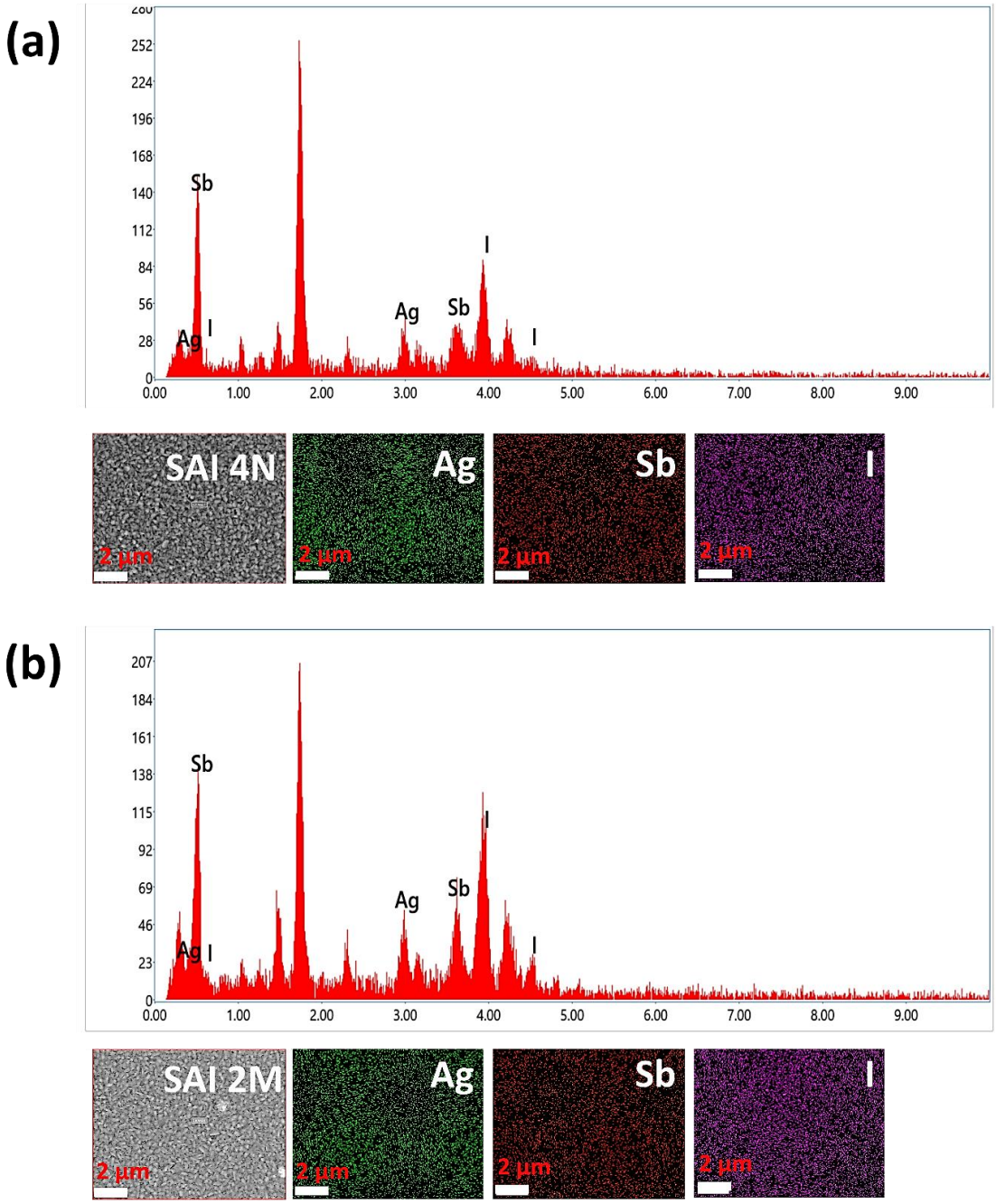

Element	Atomic%	
	SAI 4N	SAI 2M
Ag	10.3	14.4
Sb	22.4	22.3
I	67.3	63.2

Figure 4.9. EDX spectra and elemental mapping of silver antimony iodide thin films: (a) SAI 4N and (b) SAI 2M, where the additional peaks correspond to elements from the underlying FTO substrate [141].

4.6 Morphology

The surface morphology of the films (Figure 4.10) illustrates the distinct surface features of the silver antimony iodide (SAI) thin films prepared through thermal and microwave iodization methods. Both samples have a uniform and homogeneous morphology. However, distinct surface features emerge upon closer examination. The thermally iodized samples displayed a prominent interlocked rod-like structures distributed randomly, indicating a less surface coverage compared to that of microwave-iodized samples. The microwave treated samples demonstrate a coalescence effect resulting more compact morphology, where the rod-like structures expand to horizontally interlocked finger forms, creating a complete surface coverage of the film. Thus, morphology difference suggests that the microwave treatment not only influences the arrangement of the rods but also enhances the surface coverage by more compact and widened finger like features.

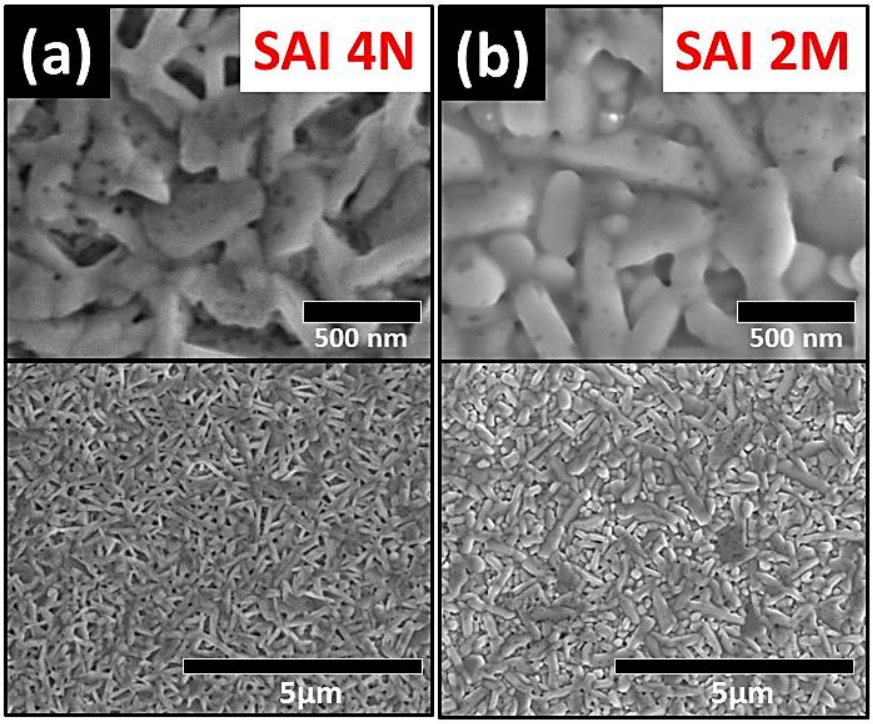

Figure 4.10. SEM images of silver antimony iodide thermal and microwave iodized thin films (a) SAI 4N (b) SAI 2M [141].

An increase in thermal iodization time further enhanced the melted rod-like morphology, as evident in the SEM images in Figure 4.11. In contrast, prolonging the microwave iodization time led to films with surface morphology composed of molten-like grains with irregular shapes and no distinct edges.

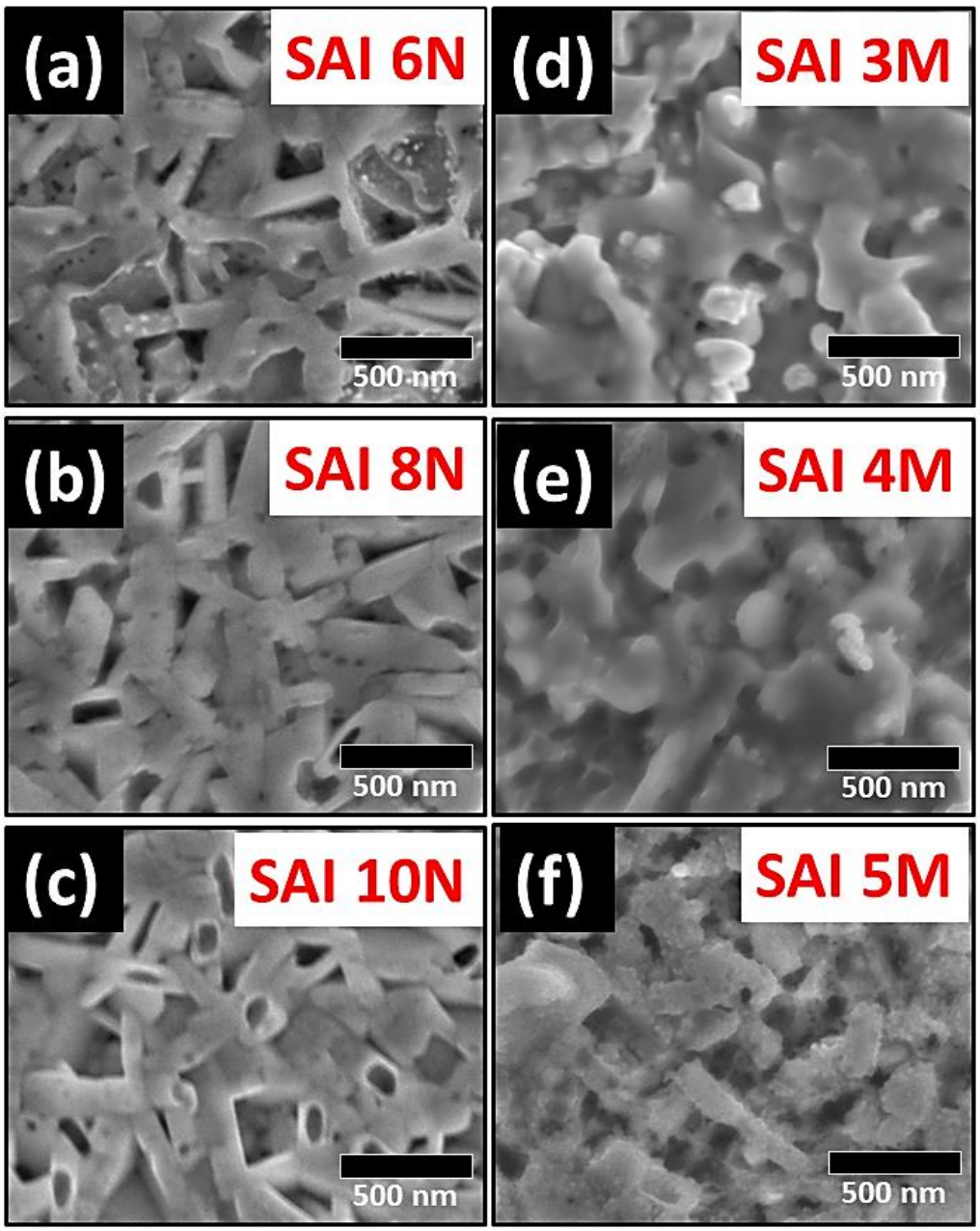

Figure 4.11. Higher magnification SEM images of silver antimony iodide thermal and microwave iodized thin films (a) SAI 6N (b) SAI 8N (c) SAI 10N (d) SAI 3M (e) SAI 4M (f) SAI 5M [141].

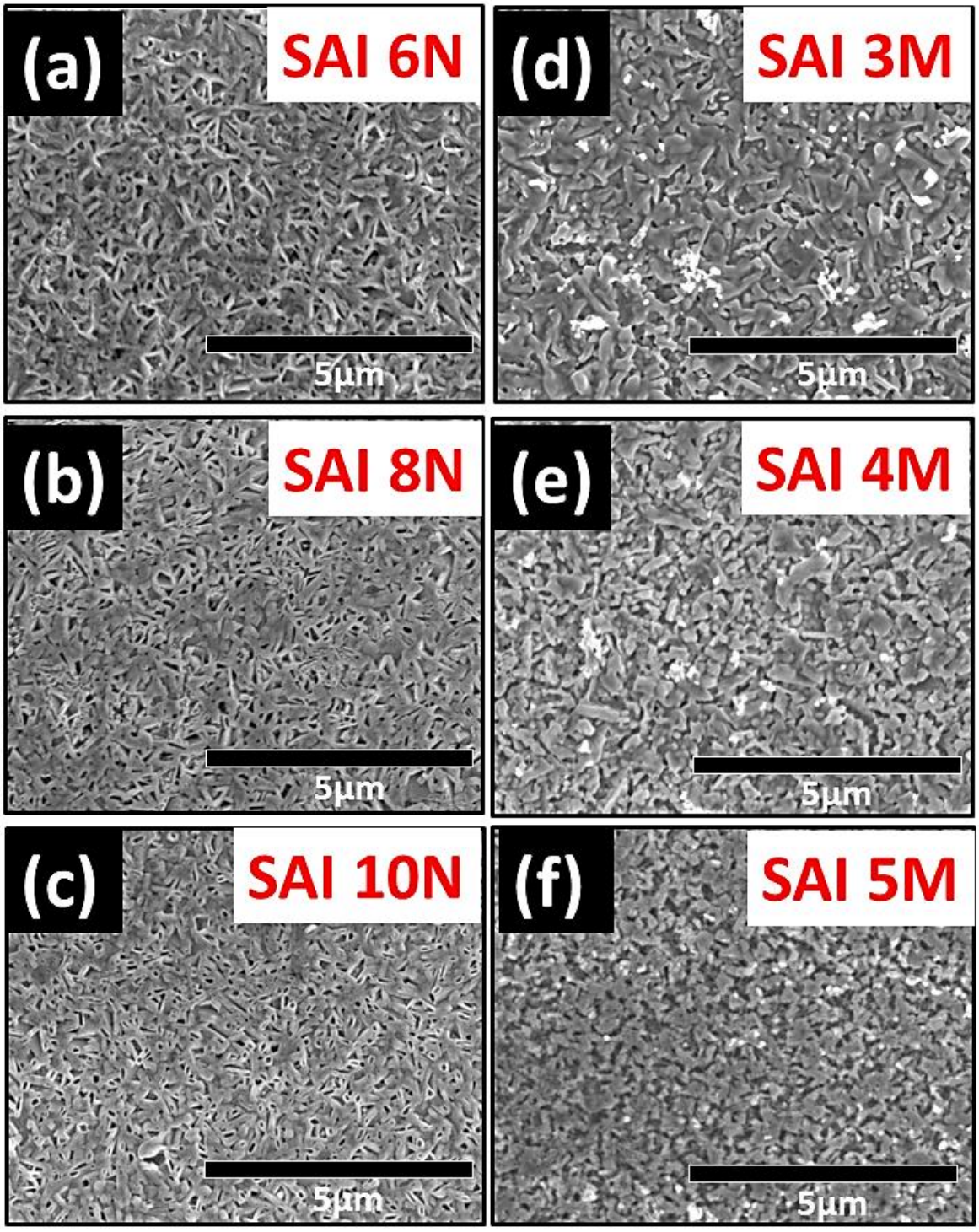

Figure 4.12. Lower magnification SEM images of silver antimony iodide thermal and microwave iodized thin films (a) SAI 6N (b) SAI 8N (c) SAI 10N (d) SAI 3M (e) SAI 4M (f) SAI 5M [141].

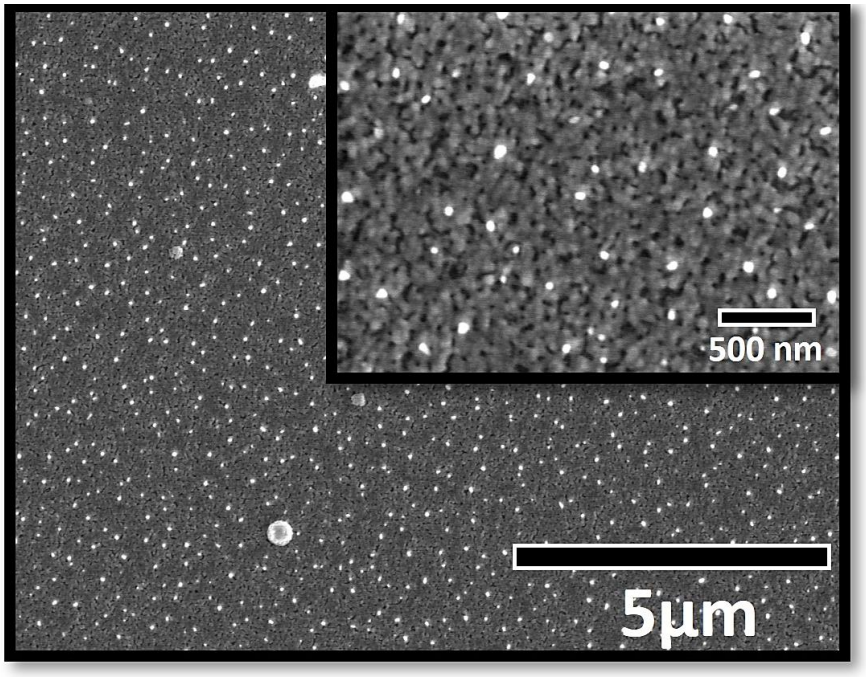

Figure 4.13. SEM images of Sb_2S_3/Ag as prepared thin films [141].

Figure 4.12 provides lower magnification SEM images of both thermally and microwave-iodized silver antimony iodide thin films, allowing for a broader assessment of the surface morphology across different magnifications. Figure 4.13 depicts the SEM images of the as-prepared Sb_2S_3/Ag thin-film surfaces, which initially exhibited a uniform silver surface morphology. Upon iodization, morphological changes were observed, with iodized films forming distinct hollow rods and faceted particles, signalling the formation of the ternary silver-antimony iodide compound as explained above. This transformation is attributed to the strong iodine affinity of antimony and silver [50,159], which aids in effective iodization and promotes the formation of well-defined crystalline structures. The interaction between antimony and iodine likely stabilizes grain boundaries, reducing structural discontinuities and leading to a more compact morphology. Additionally, microwave processing enhances diffusion by uniformly distributing thermal energy, facilitating homogeneous iodine incorporation and promoting uniform grain growth [141,163,164].

Formation of Sb_2S_3 from an aqueous chemical bath containing $SbCl_3$ and $Na_2S_2O_3$ [108,165] involves the formation of an intermediate complex, $Sb_2(S_2O_3)_3$ followed by its hydrolysis resulting deposition of Sb_2S_3. The reaction formulas can be written as:

$2SbCl_3+3Na_2S_2O_3 \rightarrow Sb_2(S_2O_3)_3+6NaCl$ ……(4.1)

$Sb_2(S_2O_3)_3+6H_2O \rightarrow Sb_2S_3+3HSO_4^-+3H_3O^+$ ……(4.2)

The controlled reactions take place on the substrate immersed in the chemical bath resulting Sb_2S_3 thin film deposition. Following this, a thin Ag layer of required thickness was thermally evaporated onto the Sb_2S_3 film forming Sb_2S_3/Ag precursor. Due to the iodization of the precursor, iodine simultaneously reacts with Ag and diffuses into Sb_2S_3 replacing sulfur [50,67,137]. Initially, silver reacts with iodine to form AgI which enhances the diffusion of iodine into Sb_2S_3 to form SbI_3 which in turn reacts with AgI producing $AgSb_2I_7$ [50,165]. Lower iodization can result in mixed faces of AgI and $AgSb_2I_7$ + S_2, forming a mixed phase as in Figure S3. As the process continues, the complete conversion to $AgSb_2I_7$ occurs via the thermodynamically favorable reaction.

$2Ag + I_2 \rightarrow 2AgI$ ……(4.3)

$Sb_2S_3 + 3I_2 \rightarrow 2SbI_3$ ……(4.4)

$2SbI_3 + AgI \rightarrow AgSb_2I_7 + S_2\uparrow$ ……(4.5)

The formation of $AgSb_2I_7$ is governed by both thermodynamic and kinetic factors, particularly the enthalpy of formation and the electronegativity of the elements involved. Iodine with higher electronegativity (2.66) than sulfur (2.58) exhibits a stronger tendency to attract electrons, which stabilizes Sb–I bonds and drives the substitution of sulfur by iodine [166]. Moreover, the enthalpy of formation plays a crucial role in directing this transformation. Sb_2S_3 has a formation enthalpy of approximately -141.8 ± 4.1 kJ/mol whereas $AgSb_2I_7$ exhibits a significantly lower enthalpy -260.6 kJ/mol, making the reaction thermodynamically favorable by reducing the Gibbs free energy [50,167]. In addition, the catalytic property of Ag [168] and the amorphous nature of chemical bath deposited Sb_2S_3 [108] can facilitate the diffusion and sulfur replacement reaction to form $AgSb_2I_7$ [141].

Prior studies have demonstrated that subtle modifications in composition and synthesis conditions can enhance crystallinity and promote uniform grain growth, leading to denser and defect-reduced morphologies [64,157]. In particular, tuning the elemental composition, such as partial substitution of bismuth with antimony or other additives, were shown to improve crystallinity, reduce surface defects, and promote well-defined grain formation in silver-antimony iodide-based materials [65,66]. Similarly, microwave irradiation has been reported to enhance grain growth and minimize defects in perovskite such as methylammonium lead iodide ($MAPbI_3$) through rapid and uniform heating [164]. In the present study, $AgSb_2I_7$ thin films also exhibited compact surface features with fewer pinholes [141].

4.7 Optical properties

Optical properties of the SAI thin films were evaluated from the transmittance and reflectance spectra given in Figure 4.14(a). The phase-pure films, specifically SAI 2M (microwave-iodized) and SAI 4N (thermally iodized), showed onset of absorptions in the visible region, around ~ 600 nm. From the figure, the sum of transmittance and reflectance values approached nearly 100% in the non-absorbing regions (wavelengths > 600 nm), and this implies $AgSb_2I_7$ thin films formed are uniform and specularly reflective. From the spectra, the absorption coefficient (α) [50] was calculated using equation (2.5).

$$\alpha = \frac{1}{d}\ln\left[\frac{(1-R)^2}{T}\right] \tag{2.5}$$

In this equation, T represents transmittance, R is reflectance, and d denotes the average film thickness (200 nm). Knowing absorption (α), the optical band gap (E_g) is evaluated from Tauc plots obtained using the equation (2.4).

$$(\alpha h\nu)^n = A\left(h\nu - E_g\right) \tag{2.4}$$

Here A is a constant, h is Plank's constant, and ν is the incident photon frequency. The value of n can vary based on the type of optical transition, n =1/2, 2 and 2/3 corresponds to direct allowed, indirect allowed and direct forbidden bandgap transitions.

In the present case, the band gap values evaluated from Tauc plots by extrapolating the respective linear part as given in Figure 4.14(b), direct bandgaps of 2.2 eV for SAI 2M and 2.1 eV for SAI 4N samples. This bandgap range aligns well with the values of 2.23 eV for the direct bandgap and 1.98 eV for the indirect bandgap reported for partially antimony substituted silver bismuth iodide thin films, which were prepared using a one-step spin-coating method with DMSO/DMF as solvents [64]. The films obtained by thermal and microwave iodization exhibit the band gap values that are consistent with the color of the films as seen in Figure 4.2 [141].

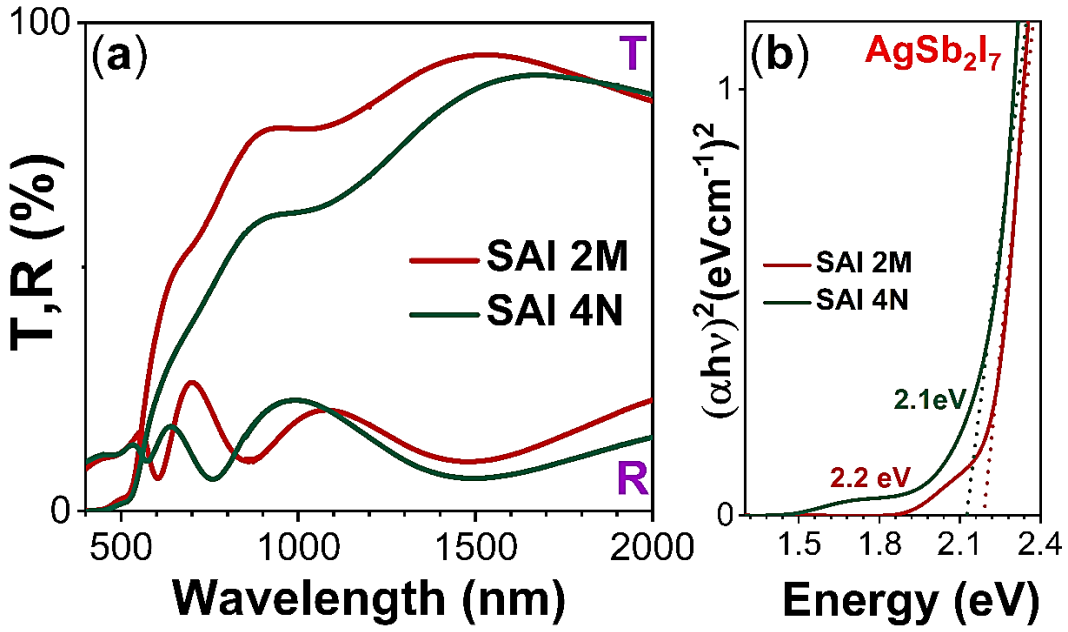

Figure 4.14. (a) Transmittance and reflectance spectra of silver antimony iodide (SAI) thin films, comparing SAI 2M (microwave-iodized) and SAI 4N (thermally iodized) samples. (b) Tauc plots showing the direct bandgaps of the SAI thin films [141].

In Figure 4.15, the transmittance and reflectance spectra, along with the corresponding Tauc plots, are shown for the SAI thin films prepared by varying iodization times. The graphs further indicate no noticeable change in the band gap values (2.1–2.2 eV). However, the band gap values of microwave treated samples (~2.2 eV) tend to be slightly higher than that of the thermally treated samples (~2.1 eV). This variation may be due to differences in the mechanisms involved in the synthesis methods. Additionally, slight variations in stoichiometry, grain size, and the presence of secondary phases can further influence the electronic structure and bandgap of the material [64,169].

The optical absorption properties of silver antimony iodide ($AgSb_2I_7$) make it a promising candidate for optoelectronic applications, characterized by a bandgap ranging from 2 to 2.2 eV. This bandgap facilitates effective absorption of visible light, positioning $AgSb_2I_7$ for potential use in solar cells and photodetectors. Similar trends can be seen in other rudorffite compound like $AgBiI_4$, which exhibit comparable bandgaps around 1.9 to 2.0 eV [44,170].

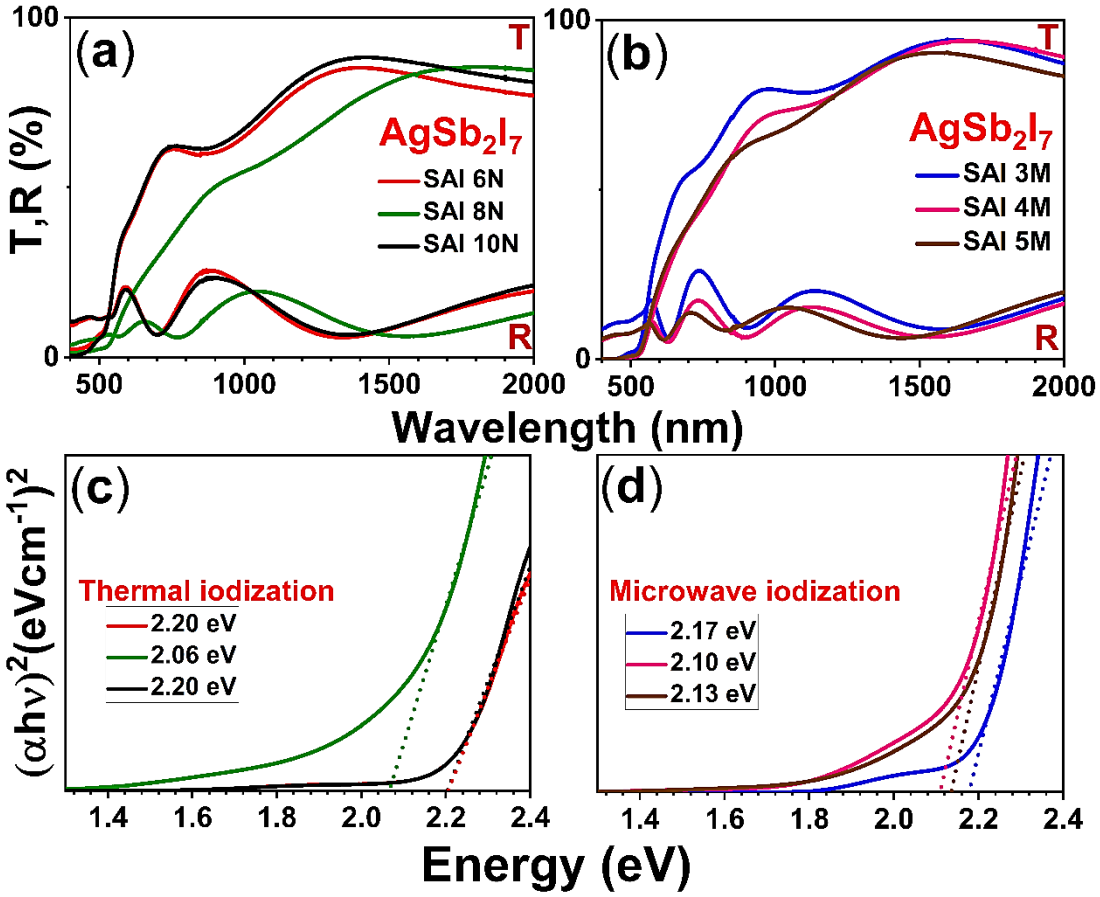

Figure 4.15. Transmittance, reflectance, and Tauc plots of silver antimony iodide thin films; (a,c) thermal iodization (b,d) microwave iodization [141].

4.8 Self-driven photoconduction of $AgSb_2I_7$ thin film

Silver antimony iodide ($AgSb_2I_7$) thin films fabricated on glass substrates and tested with Ag/C/$AgSb_2I_7$/C/Ag electrode (symmetric contacts) configurations exhibit photoconductive behavior even under zero-biased conditions. As shown in Figure 4.16, these films generate a photocurrent in the range of 10^{-10} A when exposed to a halogen lamp (white light) and LEDs of different wavelengths. Figure 4.16(a) highlights the material's repeatable photo-switching response and photoconductive nature under white light, implying its ability to operate as a self-powered photoconductor. Likewise, Figure 4.16(b) displays its broad spectral sensitivity (UV-Vis) with a comparable photocurrent under LED illumination without requiring an external bias.

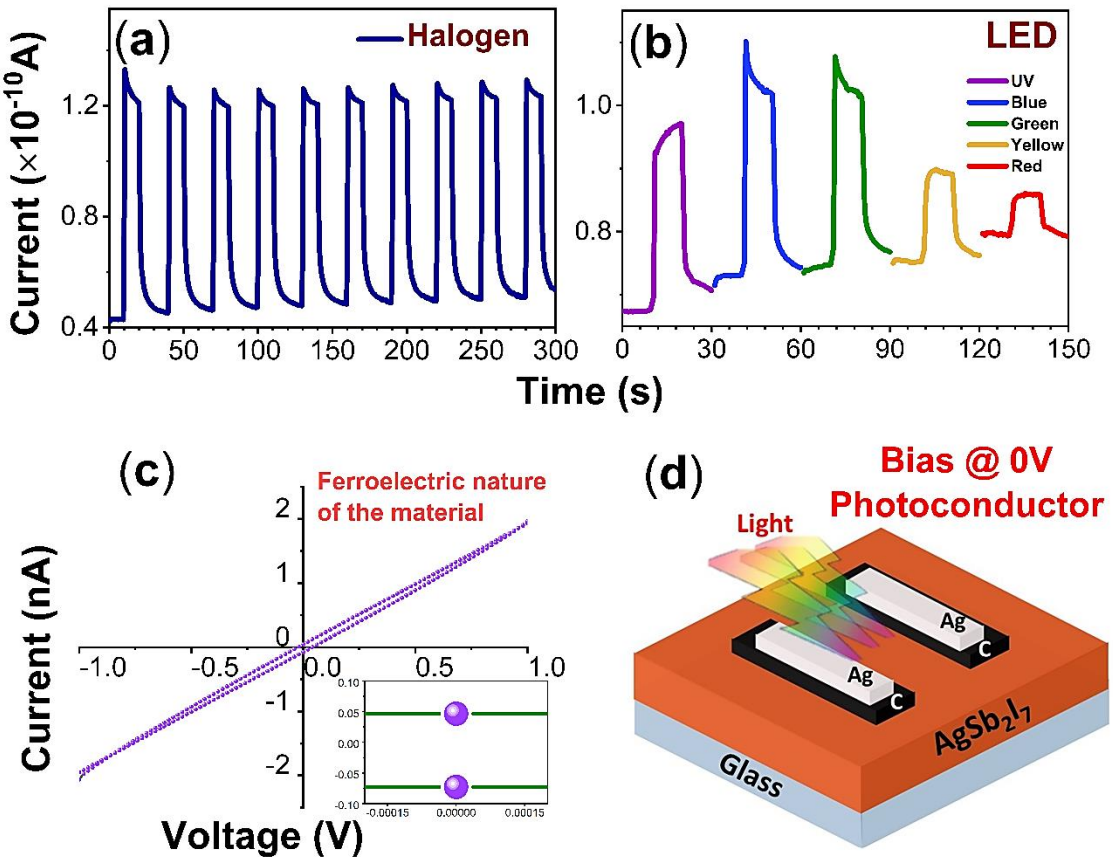

Figure 4.16. Self-powered photoresponse of $AgSb_2I_7$ thin films on a glass substrate: (a) photoresponse under halogen illumination, (b) LED illumination, (c) a weak ferroelectric hysteresis behavior, and (d) device schematic of Ag/C/$AgSb_2I_7$/Ag/C photoconductor structure [141].

Self-driven photoconductive behavior in semiconductor materials is often attributed to the formation of a Schottky barrier at the metal-semiconductor interfaces [171]. This occurs when there is a difference in work function between the metal electrode and the semiconductor, leading to the formation of an electric field that can drive carrier transport when illuminated, using asymmetric electrical contacts using different metal electrodes [171]. However, in our device configuration with symmetric Ag/C/$AgSb_2I_7$/C/Ag electrodes, the effect of a Schottky barrier is not expected, as the symmetry of the contacts negates any potential difference in work function that would create such a barrier. Instead, the observed photoconduction can be attributed to the ferroelectric properties of $AgSb_2I_7$, a material belonging to the emerging class of Polar-Active Semiconductors (PAS) [50,169,172–176]. These ferroelectric properties stem from the non-centrosymmetric

crystal structure, which enables spontaneous electric polarization. This polarization can be retained or reversed under an external electric field, resulting in internal electric fields that aid in charge separation and transport, even without applied bias. Such behavior is characteristic of Polar-Active Semiconductors and plays a crucial role in facilitating self-driven photoconduction in devices with symmetric contacts[50,141,169,172–176].

The ferroelectric behavior of PAS materials, including $AgSb_2I_7$, arises from their non-centrosymmetric crystal structure, which originates from ionic migrations [177]. In the present case, evidence of this ferroelectric nature is supported by a weak electrical hysteresis given in Figure 4.16(c) in which I-V curve is not retraced by reversing measurement. This may be an indication of polarization retention like behaviour, even the films were deposited on non-polar glass substrates. The inset in Figure 4.16(c) (zoomed version) further makes it clear that the current measured is differ in retraced curve. To ensure the stability of electrical measurement, the use of carbon electrodes is essential, as they act as a buffer to prevent silver migration and the formation of silver iodide at the interface with $AgSb_2I_7$. Thus, the mechanism behind the self-powered photoconduction in silver antimony iodide ($AgSb_2I_7$) thin films can be attributed to the materials ferroelectric properties, similar to those observed in other perovskites like $Cs_3Sb_2I_9$ [50], $MPSnI_3$ [174], and Sn-based hybrids [175]. Ferroelectricity in these materials arises from stereochemically active lone-pair electrons of metal cations (e.g., Ge Sn, Sb), which induce structural distortions and polarization. This polarization generates an internal electric field that drives the separation of photoexcited electron-hole pairs, eliminating the need for an external bias to produce a photocurrent [50,169,172–176]. In $AgSb_2I_7$, the spatial arrangement of Ag^+, Sb^{3+}, and I^- ions within the crystal lattice and halide ion migration induces lattice strain and localized structural irregularities. These processes disrupt crystal symmetry, creating polarization that enhances the internal electric field and facilitates carrier separation [119,121,124,178]. The lone pair electrons on Sb^{3+} ions within the $[Sb_2I_7]$ octahedra further contribute to the materials ferroelectric properties, making $AgSb_2I_7$ a promising PAS candidate for self-powered optoelectronic applications [125]. The I-V graph of SAI 4N, presented in Figure 4.17, supports the mechanism of self-powered photoconduction, as it clearly demonstrates a non-zero current at 0 V. However, further in-depth research is essential to understand the exact mechanism behind the self-driven photoconduction in these types of materials [141].

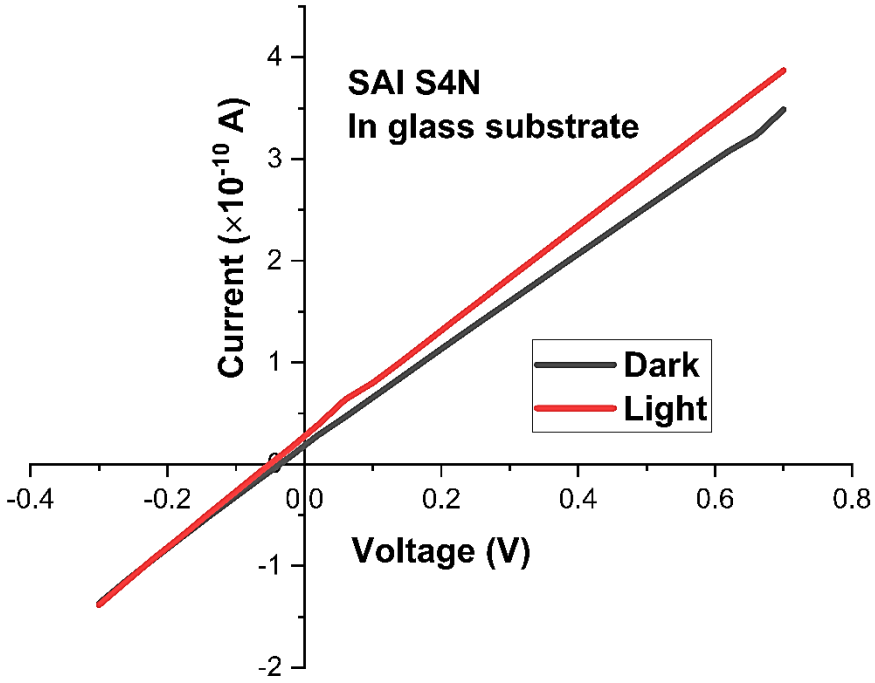

Figure 4.17. IV characteristics of S4N self-powered photodetector on glass substrate [141].

4.9 Photodiodes of $AgSb_2I_7$ thin film

Photodiodes with an FTO/n-CdS/$AgSb_2I_7$/C/Ag configuration were fabricated, as shown in Figure 4.18(a) and the device performance was evaluated. Photocurrent measurements at different wavelengths using LEDs are depicted in Figure 4.18(b) and (c), while Figure 4.18(d) and (e) illustrate the response to a 532 nm laser at various power levels. Sensitivity and responsivity, as the key parameters for assessing a photodetector performance, were calculated and the results are displayed in Figure 4.18(f) and (g) (sensitivity vs wavelength) and Figure 4.18(h) and (i) (responsivity vs laser power). Sensitivity (S), calculated using Equation 3, represents the percentage change in current under illumination compared to dark conditions:

$$S\ (\%) = [(I_l - I_d)/I_d] \times 100 \qquad (1.1)$$

where I_l is the current under illumination and I_d is the dark current.

Responsivity (R) measuring the photocurrent generated per unit of incident light power is calculated as,

$$R = I_{ph}/(A' P) \qquad (1.2)$$

where I_{ph}= (I_l - I_d), A is the effective area (0.09 cm^2) and P is the light intensity. External quantum efficiency (EQE) is calculated using Equation 5, represents the efficiency with which a photodetector converts incident photons into collected charge carriers:

$$\text{EQE (\%)} = [(hcR)/q\lambda] \times 100 \quad (1.3)$$

where h is the Planck's constant (6.626×10^{-34} J·s), c is the speed of light (3×10^8 m/s), q is the elementary charge (1.602×10^{-19} C) and λ is the wavelength of the incident light. Detectivity (D) is calculated using Equation 6, gives a measure of the photodetector's ability to detect weak signals:

$$D = (R\sqrt{A})/\sqrt{2qI_d} \quad (1.4)$$

The rise and decay times are calculated as the time taken for the photocurrent to reach 90% and 10% of its maximum value, respectively, the device's temporal response. The noise-equivalent power (NEP) is calculated using the formula [179]:

$$\text{NEP}= \frac{\sigma_{I_{dark}}}{R\sqrt{\Delta f}} \quad (1.5)$$

Where $\sigma_{I_{dark}}$ represents the standard deviation of the dark current, R is the responsivity of the device, and Δf is the bandwidth, set to 1 Hz. This method provides a measure of the noise level associated with the dark current, relative to the signal, and is a key parameter for evaluating the photodetector's performance.

The results in Table 4.2 indicate that SAI 4N demonstrates greater responsivity and sensitivity compared to the microwave-iodized SAI 2M samples, both showing similar photocurrent performance. Interestingly, less iodization in the microwave-iodized samples yielded equivalent performance to that of the double-time thermally iodized samples. This indicates that the iodization process significantly influences photodetection performance. Insights gained from this study highlight the intricate relationship between synthesis methods and material properties, ultimately affecting the efficiency of self-powered photodetectors. Figure 4.19 further demonstrates the photodetection capabilities under 395 nm laser illumination, adding another layer of understanding to the material's performance under different light sources. Figure 4.20 presents the zero-biased photoresponse and stability of FTO/n-CdS/i-$AgSb_2I_7$/C/Ag photodiode at different iodization times. The initial study focused on the pure material. The photocurrent decay under light exposure was influenced by iodization time, with longer iodization resulting in faster decay (Figure 4.20 (a)). However, the overall current level did not vary significantly with increased iodization. The thermal iodized SAI 4N samples showed

consistent performance during continuous self-powered operation (Figure 4.20 (b)). The crystalline structure, morphology, and composition directly influence the optical and electrical properties of materials, influencing their photodetection performance. Specifically, these factors govern charge carrier transport, diffusion, defect states, and band alignment, while optical absorption coefficient and band gap determine the photocurrent generation. In general, these electrical and optical characteristics of semiconductors determine the photodetector performance which involves mainly photocarrier generation and their transport [141,180,181].

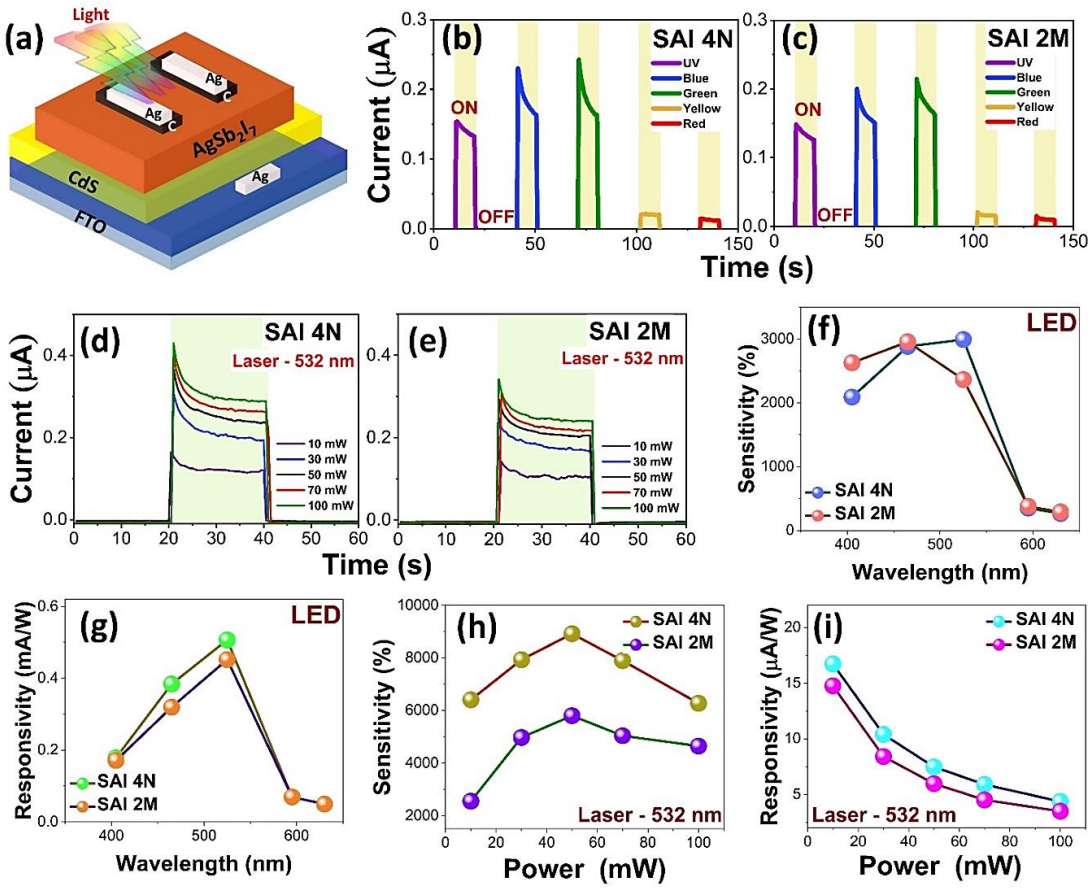

Figure 4.18. (a) Schematic representations of FTO/n-CdS/i-$AgSb_2I_7$/C/Ag photodiode measurement setups for characterizing the photodetection capabilities of silver antimony iodide thin films,: (b, c) photodetection measurements of SAI 4N (thermal iodized) and SAI 2M (microwave iodized) thin films using LEDs across different wavelengths, (d, e) response to a 532 nm laser at varying power levels, (f, g) sensitivity and responsivity variations with wavelength, and (h, i) with laser power [141].

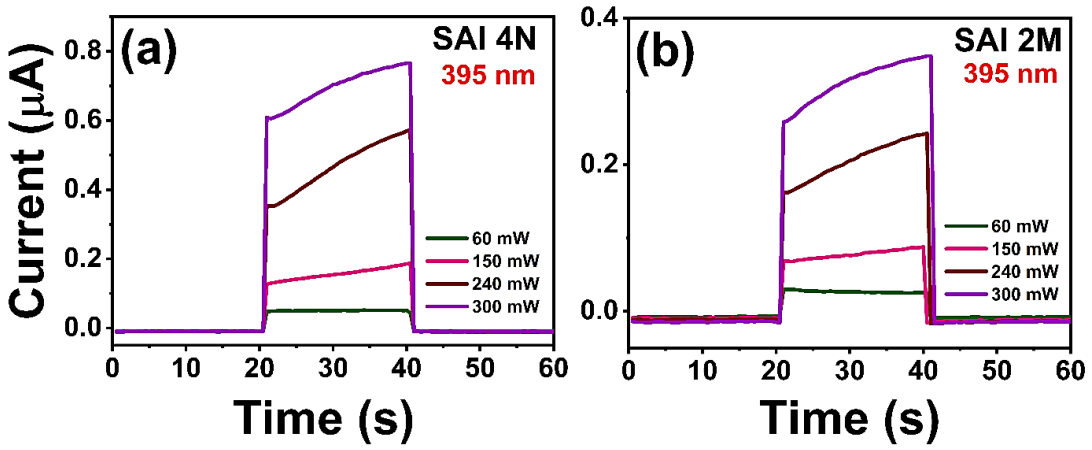

Figure 4.19. of silver antimony iodide thin films; (a,c) thermal iodization (b,d) microwave iodization [141].

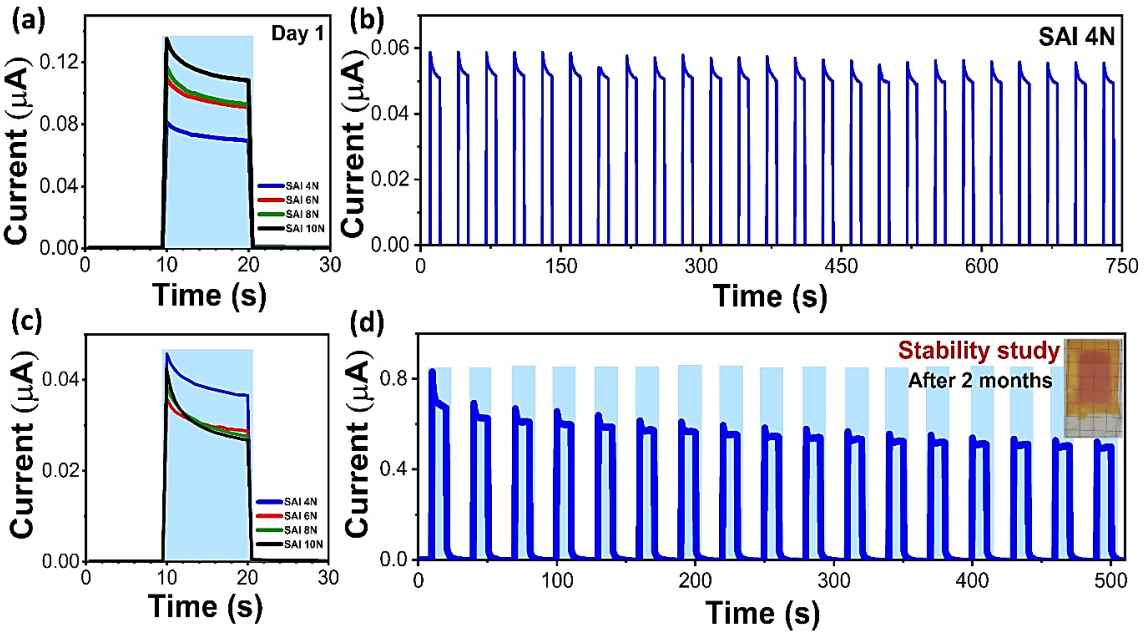

Figure 4.20. Zero-biased photoresponse and stability studies on SAI N photoconductors formed by varying iodization time and heterostructure (FTO/n-CdS/i-$AgSb_2I_7$/C/A photodiodes fabricated using SAI 4N (a) Photostability decreases with increased iodization time. (b) Photostability of the heterostructure device during continuous self-powered operation. (c) Environmental stability measurements of SAI N samples with varying iodization. (d) Stable photocurrent of the device after two months of storage. The illumination source was halogen light [141].

The environmental stability of these samples was evaluated after a few weeks (Figure 4.20 (c)), revealing that the SAI 4N film incorporated device exhibited greater stability compared to those with longer iodization times. These results imply shorter iodization times produce more photostable films. Iodine migration plays a significant role in the performance of these perovskites, with higher iodine content causing faster degradation [50].

After two months of storage, SAI 4N based device demonstrated stable photocurrent under halogen light (Figure 4.20 (d)), highlighting the environmental stability of silver antimony iodide thin films. The increase in current with respect to the day one measurement can be due to surface defect passivation and reduced iodine migration over time, both of which stabilize charge transport within the film [182]. These improvements in the material and interfaces lead to more effective charge collection, contributing to the sustained performance and increased photocurrent over time [141,183].

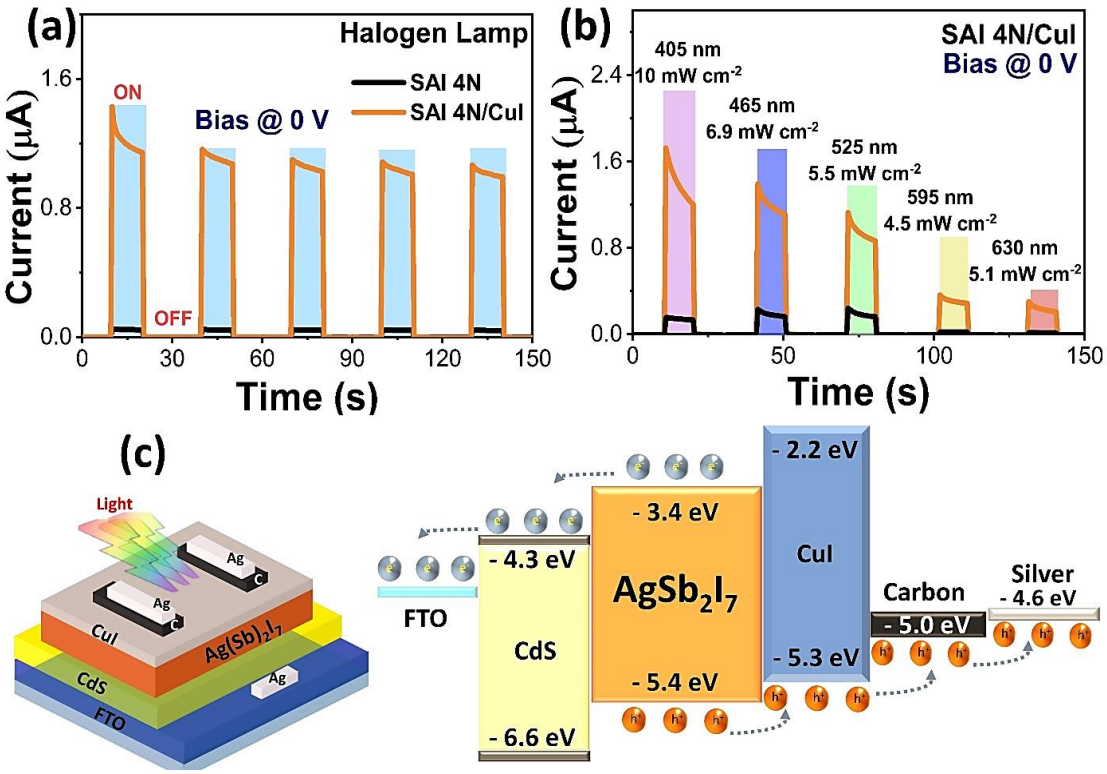

Figure 4.21. Photocurrent measurements for the heterostructure photodiode fabricated by incorporating a p-CuI layer (FTO/n-CdS/i-$AgSb_2I_7$/p-CuI configuration), showing performance under different light sources. (a) Halogen lamp, (b) LED, (c) Energy levels of the layers in the photodetector stack, along with the device configuration [141].

Table 4.2. Performance comparison of silver antimony iodide self-powered photodetectors [141].

Detector configuration	**Wavelength (nm)**	**On/off ratio**	**Rise Time**	**Decay time**	**NEP ($x10^{-7}$ $W/HZ^{1/2}$)**	**Sensitivity (%)**	**Responsivity (mA/W)**	**Detectivity ($x10^9$Jones)**	**EQE (%)**	**Reference**
FTO/n-CdS/i-$AgSb_2I_7$/C/Ag (SAI 4N)	405	19.9	0.37	0.43	14	2091	0.18	1.08	5.5	This work
	465	27.8	0.33	0.43	6.5	2882	0.38	2.24	11.8	
	525	28.9	0.31	0.43	5.2	2992	0.51	2.94	15.5	
	595	2.5	0.42	0.42	32	352	0.07	0.41	2.1	
	630	1.7	0.36	0.90	44	267	0.05	0.29	1.5	
FTO/n-CdS/i-$AgSb_2I_7$/C/Ag (SAI 2M)	405	25.3	0.37	0.41	20	2627	0.17	1.19	5.3	This work
	465	28.6	0.34	0.41	14	2955	0.32	2.07	9.8	
	525	22.6	0.34	0.40	17	2365	0.45	2.46	13.8	
	595	2.8	0.34	0.42	39	379	0.07	0.43	2.1	
	630	1.9	0.33	0.40	99	292	0.05	0.3	1.5	
FTO/n-CdS/i-$AgSb_2I_7$/p-CuI	405	467	0.32	0.40	1.8	46812	1.92	16.8	58.8	This work
	465	367	0.35	0.41	2.1	36754	2.25	19.3	68.8	
	525	220	0.34	0.40	1.8	22056	2.29	16.9	70	
	595	64.5	0.35	0.41	3.3	6545	0.912	6.44	27.9	
	630	34.4	0.32	0.40	16	3537	0.675	3.83	20.7	

FTO/$Cs_3Bi_2I_9$/Ag	450-950	1.4× 10^4	0.06	0.09	0.0013	-	0.00059	12	-	[135]
FTO/$Cs_3Bi_2I_9$/C-Ag	405	100	1.52	2.29	-	157	0.0051	0.593	-	[113]
***Note: No prior reports exist on self-powered photodetectors utilizing silver antimony iodide ($AgSb_2I_7$)**										

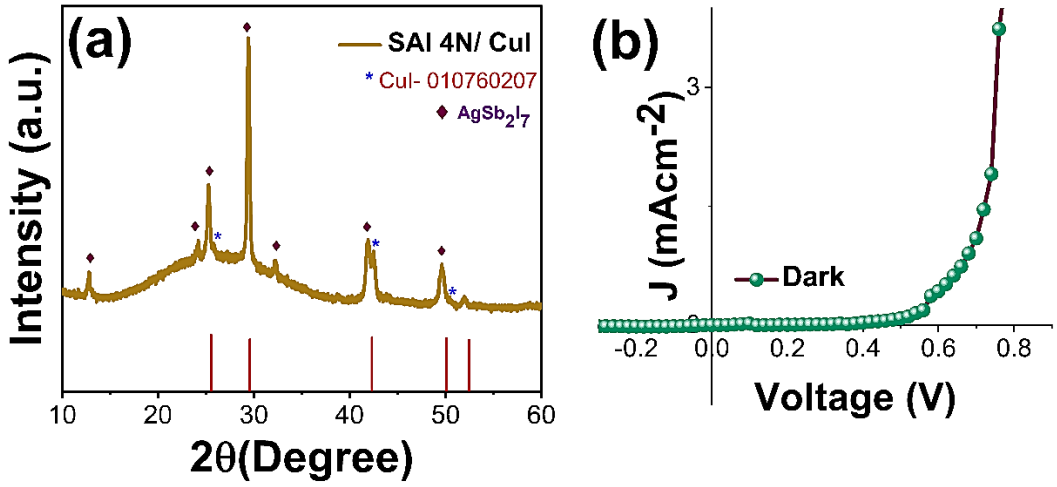

Figure 4.22. (a) XRD pattern of the SAI 4N/CuI sample, showing distinct peaks corresponding to CuI and $AgSb_2I_7$ phases, confirming the formation of both materials. (b) J-V characteristics in the dark, confirming the formation of a p-n junction. The device structure is FTO/n-CdS/i-$AgSb_2I_7$/p-CuI [141].

The performance of photodiode of FTO/n-CdS/i-$AgSb_2I_7$/p-CuI was as shown in Figure 4.21(a, b). Figure 4.22 (a) shows the XRD pattern of the SAI 4N/CuI sample formed by thermal iodization of Sb_2S_3/Ag/Cu precursor. Distinct peaks corresponding to both CuI and $AgSb_2I_7$ are observed. The CuI peaks appear at the following planes: (111), (200), (220), and (311) (ICSD No. 010760207). The $AgSb_2I_7$ peaks are present at the following planes: (111), (311), (222), (400), (331), (440), (531), and (622), as marked in the figure. J-V measurements of the heterostructure photodiode in the dark is given in Figure 4.22 (b) showing a good diode rectification. Under halogen lamp illumination (Figure 4.21(a)), the FTO/n-CdS/i-$AgSb_2I_7$/p-CuI device achieved a photocurrent of approximately 1.2 µA at zero bias, which is an order of magnitude higher than the 0.1 µA observed for the device without the CuI layer (SAI 4N). Similarly, under LED lamp illumination (Figure 4.21(b)), the maximum photocurrent recorded for the CuI-incorporated device was 1.6 µA at 405 nm, significantly surpassing the 0.1 µA obtained for the device without CuI. These results of the experiments indicated a clear trend: photodiodes that included CuI exhibit a higher current response for visible wavelengths (405–630 nm) compared to those without CuI. The improved carrier dynamics, driven by the CuI hole transport layer, directly contribute to the enhanced sensitivity (4.6×10^4 %) at 405 nm, responsivity (2.29 mA/W) at 525 nm, external quantum efficiency (EQE) of 70% at 525 nm, detectivity (D) (1.93×10^{10} Jones) at 465 nm, and overall performance under various light conditions (Table 4.2). This indicates that the CuI layer acts as a hole transport layer

(HTL), important role in enhancing photodetector performance. By facilitating efficient charge transport and enhancing the separation of photogenerated carriers, CuI boosts carrier dynamics within the device [141,184].

The schematic and energy band alignment of the devices is displayed in Figure 4.21(c) and (d) respectively. The FTO layer, with a conduction band minimum (CBM) around -4.5 eV [185], creates a favorable interface with the n-CdS layer, which has a conduction band at approximately -4.3 eV and a valence band maximum (VBM) at -6.6 eV [185]. This alignment facilitates efficient electron transfer from the i-$AgSb_2I_7$ layer to CdS layer, which has a conduction band edge at -3.4 eV [64,186] and a bandgap of -2.2 eV [187], serving as the light-absorbing material. When illuminated, the i-$AgSb_2I_7$ layer generates electron-hole pairs, which are efficiently transported to the CuI layer. The carbon layer, with a valence band edge around -5.0 eV [185], and it facilitates transport of photogenerated holes to the Ag electrode with work function of approximately -4.6 eV [187]. This alignment shows effective charge separation and collection at the electrodes. Studies have shown that CuI, with its high electrical conductivity, stability, and wide bandgap (~3.1 eV), serves as an effective HTL in optoelectronic devices, promoting efficient hole conduction while minimizing electron recombination [184]. It enhances charge transport and stability in perovskite solar cells, leading to improved device efficiency [188]. Additionally, CuI has been documented to improve charge extraction and overall performance in photodetectors [141,189].

To estimate the conduction band minimum (CBM) and valence band maximum (VBM) of $AgSb_2I_7$ with an experimentally determined bandgap of 2.0–2.2 eV, the Mulliken Electronegativity Method can be employed [190]. This method approximates the band edge positions using the following relations:

$$CBM = \chi - 4.5 - (Eg/2)$$

$$\chi\,(A_xB_yX_z) = (\,(\chi(A))^x + (\chi(B))^y + (\chi\,(X))^z)^{1/x+y+z}$$

$$VBM = CBM - Eg$$

Here, χ is the absolute electronegativity of the compound, 4.5 eV is the energy reference of the vacuum level, and Eg is the optical bandgap. The absolute electronegativity χ is calculated using the geometric mean of the electronegativities of the constituent elements: Ag (1.93), Sb (2.05), and I (2.66), yielding χ=2.45 eV. For an Eg of 2.0 eV, the CBM and VBM are calculated as -3.55 eV and -5.55 eV, respectively. For an Eg of 2.2 eV, the CBM and VBM are -3.65 eV and -5.85 eV, respectively. The reported values of CBM = -3.4 eV and VBM = -5.4 eV [64,186] are in reasonable agreement with the theoretical estimates, demonstrating the validity of the band edge positions derived from this empirical method.

Further analysis is required to fully elucidate the mechanisms behind CuI's influence, as it appears to not only enhance charge transport but also improve junction properties. This understanding will aid in optimizing future photodiode designs for higher efficiency. Even though we analysed only CuI incorporated devices by thermal iodization, microwave iodization for similar photodiodes is a promising avenue for future research. Fine power and frequency-controlled microwave processing is essential for the fabrication materials and devices with optimum performance and thus to achieve energy-efficient systems.

In this work, the formation of $AgSb_2I_7$ films is achieved through iodization and a sulfur-replacement diffusion reaction in Sb_2S_3/Ag precursor, where precise control over iodization parameters is crucial in determining the films' crystallinity, morphology, and optoelectronic characteristics.

In thermal heating using a hotplate, heat transfer is usually through a medium by conduction or convection generating thermal gradients resulting in a nonuniform reaction or product formation. In microwave-assisted processes, microwave radiation interacts with the materials and generates heat instantly without creating a thermal slope leading to uniform and faster heat transfer [191] resulting in high-pure and high-yield products. In the case of silver antimony iodide, the thermal heating transfers heat from the hot surface to iodine kept in the Petri, and the iodine vaporizes onto Ag/Sb_2S_3 precursor to form silver antimony iodide (Ag_2SbI_7) by sulfur replacement and diffusion-associated reaction [50] in 4 min. In microwave treatment, instantaneous heating due to direct microwave absorption results in faster and uniform heating of both iodine and the precursor Ag/Sb_2S_3 to form Ag_2SbI_7 in 2 min without secondary phases. Crystal structure and morphology analysis show that microwave heating results in highly oriented thin film growth with more compact and coalescent grains. However, the photodetectors fabricated by both rapid thermal and microwave iodization processes yield comparable performance parameters, including response time, sensitivity, detectivity, and responsivity. Based on the present method, a microwave-assisted process can be chosen to fabricate an FTO/CdS/Ag_2SbI_7 single junction self-powered photodetector as it is faster than rapid thermal heating. In the case of the FTO/CdS/Ag_2SbI_7/CuI device type, the rapid thermal iodization process may be preferred, as very precise control of power and time is crucial in microwave heating.

$AgSb_2I_7$ films belong to the emerging class of halide perovskites with contradictory properties of ferroelectricity and semiconductivity [192,193]. The synergy between material properties and $AgSb_2I_7$-based device structures encompasses their potential applications in

ferroelectric photovoltaics, self-powered photodetection, and X-ray detection, advancing the development of lead-free photodetectors [141].

4.10 Conclusions

- **Synthesis Achieved**: $AgSb_2I_7$ thin films were successfully synthesized using thermal and microwave iodization methods applied to sequentially deposited Sb_2S_3/Ag layers.
- **Structural Characteristics**: The films crystallized in a cubic rudorffite structure with near-stoichiometric elemental composition.
- **Morphological and Optical Properties**: Distinct morphologies and direct optical band gaps ranging from 2.0 to 2.2 eV were observed.
- **Photoconductive Nature**: The films demonstrated self-driven photoconduction attributed to their weak ferroelectric characteristics.
- **Photodiode Integration**: When integrated into FTO/n-CdS/i-$AgSb_2I_7$ heterostructures, the films functioned as self-powered photodiodes.
- **CuI Doping Effect**: In situ incorporation of CuI via single-step iodization of Ag and Cu on Sb_2S_3 enabled enhanced device performance.
- **Enhanced Light Detection**: The resulting FTO/n-CdS/i-$AgSb_2I_7$/p-CuI photodiodes showed strong self-powered response in the visible range (405–630 nm).
- **Device Performance Metrics**: The best-performing devices achieved:
- **Responsivity**: 2.29 mA/W
- **EQE**: 70%
- **Detectivity**: 1.69×10^{10} Jones
- **Sensitivity**: 2.2×10^4 % at 525 nm
- **Application Potential**: These findings highlight $AgSb_2I_7$ thin films as a viable material for zero-power-consuming visible light optoelectronic applications.

Chapter 5: Synthesis and characterization of mixed- alloy rudorffite ($Ag(Bi,Sb)_2I_7$) for photodetector applications

In this chapter, a novel synthesis route is presented for the fabrication of advanced lead-free ternary halide perovskite materials. The methodology is based on a multi-step process comprising the chemical bath deposition (CBD) of antimony sulfide (Sb_2S_3) or bismuth sulfide (Bi_2S_3) precursor layers, followed by the incorporation of silver via thermal evaporation, and a subsequent rapid iodization step to promote the formation of complex iodide compounds. This approach enables the controlled synthesis of silver antimony iodides ($AgSb_2I_7$ and Ag_2SbI_5), silver bismuth iodides ($AgBi_2I_7$), and the alloyed composition $Ag(Bi,Sb)_2I_7$. The process allows precise control over stoichiometry and phase formation, facilitating the tuning of structural and optoelectronic properties. The resulting materials exhibit promising characteristics for broad-spectrum photodetection, thereby offering a versatile platform for next-generation optoelectronic devices.

5.1 Introduction

Silver-based ternary halide compounds, particularly silver antimony iodide ($AgSb_2I_7$) and silver bismuth iodide ($AgBi_2I_7$), have recently emerged as potential lead-free alternatives for optoelectronic applications owing to their non-toxic constituents and promising optical properties [1]. These materials crystallize in perovskite-inspired or Rudorffite-type frameworks with corner- or face-sharing $[MI_6]^{3-}$ octahedra ($M = Sb^{3+}$, Bi^{3+}) that form three-dimensional structures with Ag^+ and I^- ions. They exhibit relatively wide bandgaps ranging from 1.9 to 2.1 eV, offering strong absorption in the visible range and potential for use in solar energy harvesting and photodetectors [2]. In contrast to lead halide perovskites, Ag-Sb/Bi-I compounds demonstrate better moisture resistance and chemical stability, making them attractive for long-term environmental deployment [3].

Various synthetic techniques have been reported for these compounds, including solid-state reactions, dual-source evaporation, chemical vapor deposition, and spin-coating using antisolvent methods [4–6]. While solution-based approaches using DMSO/HI or DMF/DMSO solvent mixtures followed by thermal annealing have led to highly

crystalline $AgBi_2I_7$ thin films, the complex processing steps and sensitivity to stoichiometry pose reproducibility challenges [5]. Additionally, $AgSb_2I_7$ films synthesized by iodization of Sb_2S_3–Ag films have shown potential, but achieving phase purity and dense morphologies remains difficult [7]. To address these limitations, alloying strategies involving cation substitution between Bi and Sb have been proposed to fine-tune optoelectronic properties, modulate bandgaps, and stabilize crystal phases [8]. However, such studies have mostly involved bulk powders or complex multistep protocols with limited control over thin film quality and device integration [9].

In this work, we introduce a controlled alloying strategy to fabricate thin films of $Ag(Bi_xSb_{1-x})_2I_7$ using a sequential deposition approach involving chemical bath deposition of Sb_2S_3 and/or Bi_2S_3, followed by silver evaporation and a rapid iodization step. This method enables uniform mixing of Bi and Sb within the octahedral framework and supports the formation of phase-pure cubic Rudorffite structures. By gradually varying the Bi:Sb ratio (Appendix A), we achieved systematic bandgap tuning from 2.02 eV (Sb-rich) to 1.93 eV (Bi-rich), alongside lattice expansion and improved phase stability. The alloyed films displayed intrinsic ferroelectric properties, allowing for switchable polarization-driven photocurrent generation under both visible and near-infrared light. This ferroelectric-assisted photodetection mechanism enhances self-powered operation, reducing the need for external bias and improving energy efficiency. Photodiode devices based on FTO/n-CdS/i-$Ag(Bi,Sb)_2I_7$/p-CuI heterojunctions demonstrated stable and reproducible photoresponse with enhanced responsivity and detectivity across compositions. Our results highlight the advantage of the mixed-cation design in simultaneously improving structural resilience, optical tunability, and device-level performance, offering a pathway toward sustainable and efficient lead-free optoelectronic materials.

5.2 Experimental

Materials

$SbCl_3$ (Antimony chloride, Fermont, 99.7%), $BiCl_3$ (Bismuth chloride), $(CH_3)_2CO$ (Acetone, Fermont, 99.6%), and $Na_2S_2O_3{\cdot}5H_2O$ (sodium thiosulfate, Fermont, 99.9%), Ag wire and iodine powder were all purchased and utilized without further purification.

Synthesis

Chemical bath deposition of Bi-alloyed Sb_2S_3 thin films

0.0014 M (449 mg-$BiCl_3$ and 325 mg-$SbCl_3$ in 100% Bi_2S_3 and Sb_2S_3) with changing ratios of Bi and Sb was fixed to prepare the chemical bath for Bi-alloyed Sb_2S_3 thin films. A calculated amount of $BiCl_3$ and $SbCl_3$ was dissolved in 2.4 ml $(CH_3)_2CO$ to prepare the bath. Then, 12.5 ml of 1 M $Na_2S_2O_3 \cdot 5H_2O$ and 65 ml of deionized water were added and mixed to create the bath, which had a final volume of 100 ml [108]. Prior to being positioned vertically in the bath, the premium glass substrates were carefully cleaned. The deposition process was conducted at room temperature for approximately two hours. Following this, the films were rinsed with deionized water and dried (*Appendix A*). For double-layer deposition (DLD), the same films were immersed in a similar bath for an additional two hours under ambient conditions.

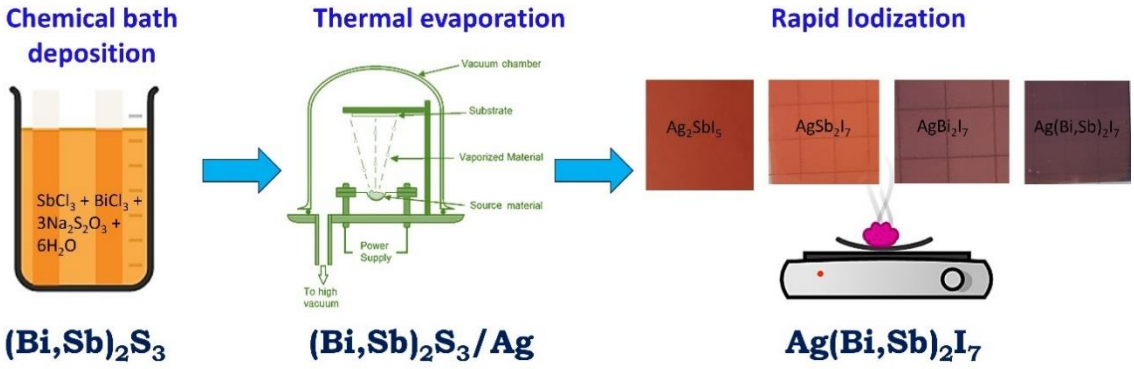

Figure 5.1. schematic diagram of mixed alloy rudorffite $Ag(Bi,Sb)_2I_7$ thin film synthesis.

Silver Deposition

(i) Thermal evaporation

A thermal evaporation system (Torr International, Model No: THE2-2.5 kW-TP) was used to evaporate silver onto the chemically deposited $(Bi,Sb)_2S_3$ thin film. The evaporation source was made of 99.9% pure silver wire. It was performed at a high vacuum of 10^{-6} Torr, with the substrate rotating at 20 rpm and a film deposition rate of 1.2 Å/s. As monitored by a quartz crystal thickness monitor, Ag of various thickness were deposited.

Rapid Iodization

Ag/$(Bi,Sb)_2S_3$ thin films were rapid iodized for different time durations. 50 mg of iodine powder was heated at 100°C in a petri dish for the formation of silver bismuth antimony iodide (SBAI). Figure 5.1 represents the schematic diagram of the whole process and the sample images. The DLD/Thermal evaporated Ag (30 nm)/iodized films (Ag_2SbI_5) were labelled as SAID4N (4 min), SAID6N (6 min), SAID8N (8 min), and SAID10N (10 min). The single layer Bi-alloyed Sb_2S_3 (Appendix A)/Thermal evaporated Ag (30 nm)/4 min iodized films were labelled as PAS ($AgSb_2I_7$), P25 ($Ag(Bi_{0.3},Sb_{0.7})_2I_7$), P50 ($(Ag(Bi_{0.4},Sb_{0.6})_2I_7)$), P75 ($(Ag(Bi_{0.5},Sb_{0.5})_2I_7)$), and PBS ($(AgBi_2I_7)$).

5.3 Results and discussions

5.4 Crystalline structure

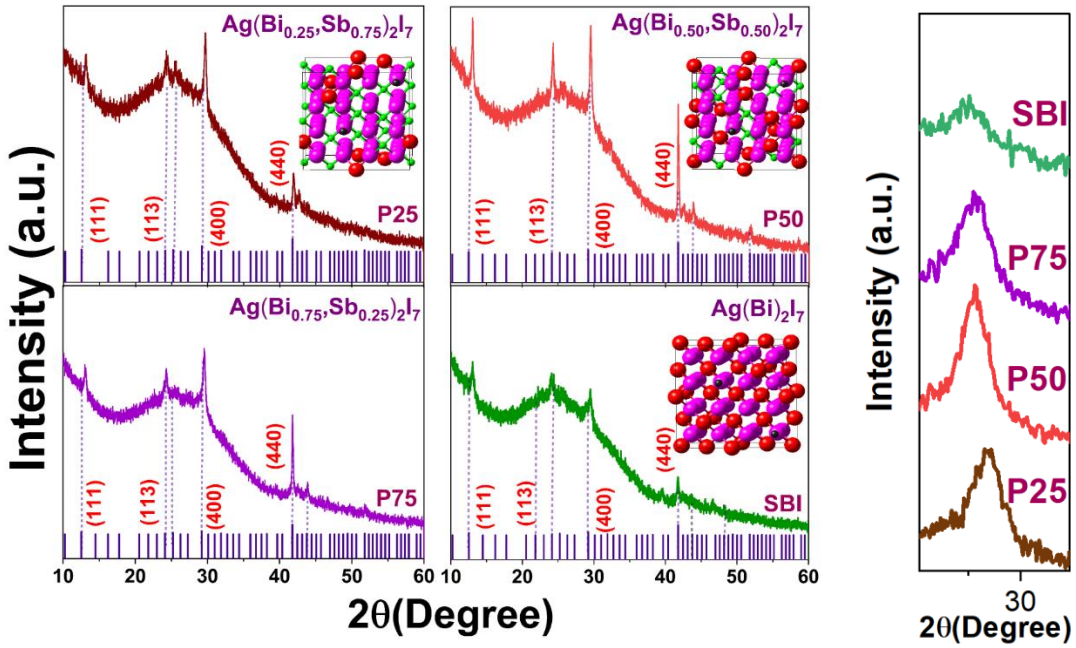

Figure 5.2. Simulated crystal structure and XRD patterns of $Ag(Bi,Sb)_2I_7$ thin films at varying Bi and Sb ratio. Peaks match the cubic $AgSb_2I_7$ phase, confirming phase purity. Crystallinity decreases with increasing Bi content.

The structural modeling of silver antimony iodide ($AgSb_2I_7$) using MedeA® software, as discussed in Chapter 4, served as the foundation for designing the mixed-composition $Ag(Bi,Sb)_2I_7$ system. The initial model was based on a cubic structure with *Fd*3*m* symmetry, wherein thorium (Th), zirconium (Zr), and hydrogen (H) atoms from the

$ThZr_2H_7$ prototype were replaced by silver (Ag), antimony (Sb), and iodine (I), respectively. To construct the mixed-cation structure, a fraction of Sb atoms was substituted with bismuth (Bi), preserving the overall stoichiometry of $Ag(Bi,Sb)_2I_7$.

To experimentally validate this structure, $Ag(Bi,Sb)_2I_7$ thin films were synthesized via thermal evaporation of Ag onto single-layer Sb_2S_3 substrates with varying Bi content (0–100%), followed by rapid iodization. X-ray diffraction (XRD) analysis revealed diffraction peaks at 12.54°, 24.15°, 25.24°, 29.22°, 31.91°, 41.80°, 43.82°, 49.46°, and 51.82°, which correspond to the (111), (113), (400), and (440) planes of the cubic $AgSb_2I_7$ structure (see Chapter 4).

Notably, the diffraction patterns (Figure 5.2) of the mixed Bi–Sb samples remained in good agreement with the simulated pattern for the *Fd*3*m* phase, indicating that partial substitution of Sb with Bi does not induce a phase transition. However, a progressive reduction in peak intensity and broadening was observed with increasing Bi content, pointing to a decrease in crystallinity and potential lattice strain due to ionic size mismatch between Bi^{3+} and Sb^{3+}. This trend suggests a partial disruption of long-range order in the crystal lattice, which may influence the optoelectronic behavior of the resulting films.

The absence of secondary phases across all compositions confirms the phase-pure formation of the $Ag(Bi,Sb)_2I_7$ system. These results validate the computationally predicted cubic structure and demonstrate that the incorporation of Bi into the $AgSb_2I_7$ framework is structurally feasible, albeit with diminishing crystallinity at higher Bi concentrations. This trade-off between compositional tuning and structural order must be considered in the context of device performance and material optimization.

A comparative study using a double-layer Sb_2S_3 structure was conducted to investigate the formation of additional perovskite phases, particularly Ag_2SbI_5. For thermally evaporated Ag, diffraction peaks were observed at 12.75°, 25.3°, 38.7°, and 52.3° (Figure 5.3 (a,b)). A variation in Ag thickness (100 nm, 60 nm, and 30 nm) revealed that 30 nm resulted in the most crystalline structure. Further optimization of iodization time confirmed that all samples exhibited high crystallinity (Figure 5.3(b)). The formation of Ag_2SbI_5 was successfully optimized using a 30 nm Ag layer in the thermal evaporation process, whereas Ag_2BiI_5 has yet to be achieved via this method.

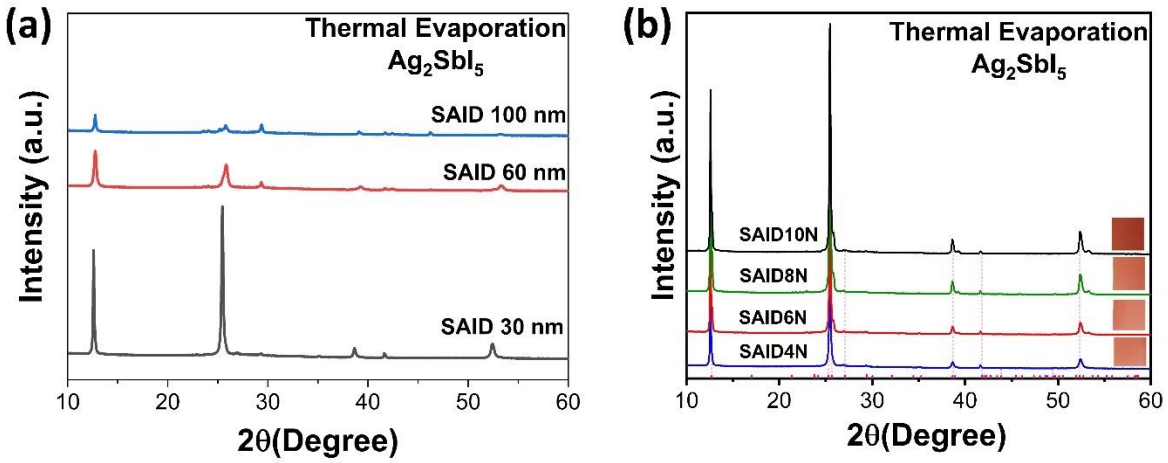

Figure 5.3: XRD optimization of silver aqntimony iodide thin films, showcasing the distinct peak patterns for Ag_2SbI_5 synthesized at varying silver molarities

For subsequent analysis, $Ag(Bi,Sb)_2I_7$ was synthesized via thermal evaporation onto a single-layer Sb_2S_3. The formation of $Ag_2(Bi,Sb)I_5$, however, requires optimization of a double-layer $(Bi,Sb)_2S_3$ structure. Since Appendix A has already established the optimal Bi/Sb ratio via EDX analysis, the following sections will focus on the single-layer formation of mixed-alloy Rudorffite thin films.

5.5 chemical structure

Raman spectroscopy was performed on the synthesized $Ag(Bi,Sb)_2I_7$ perovskite thin films to investigate their vibrational properties and structural characteristics (Figure 5.4). The Raman spectrum revealed distinct peaks at 48 cm^{-1}, 67 cm^{-1}, 103 cm^{-1}, 137 cm^{-1}, 160 cm^{-1}, 228 cm^{-1}, 270 cm^{-1}, 313 cm^{-1}, and 403 cm^{-1}, which are attributed to specific vibrational modes within the material. These peaks are indicative of the fundamental lattice vibrations and molecular interactions in the $Ag(Bi,Sb)_2I_7$ perovskite structure.

The variation in the intensities of these Raman peaks suggests the presence of different bonding configurations and interatomic interactions in the material. The observed intensity differences can be linked to the varying symmetry of the vibrational modes, which in turn reflect changes in the bonding environment as a result of the incorporation of bismuth into the structure.

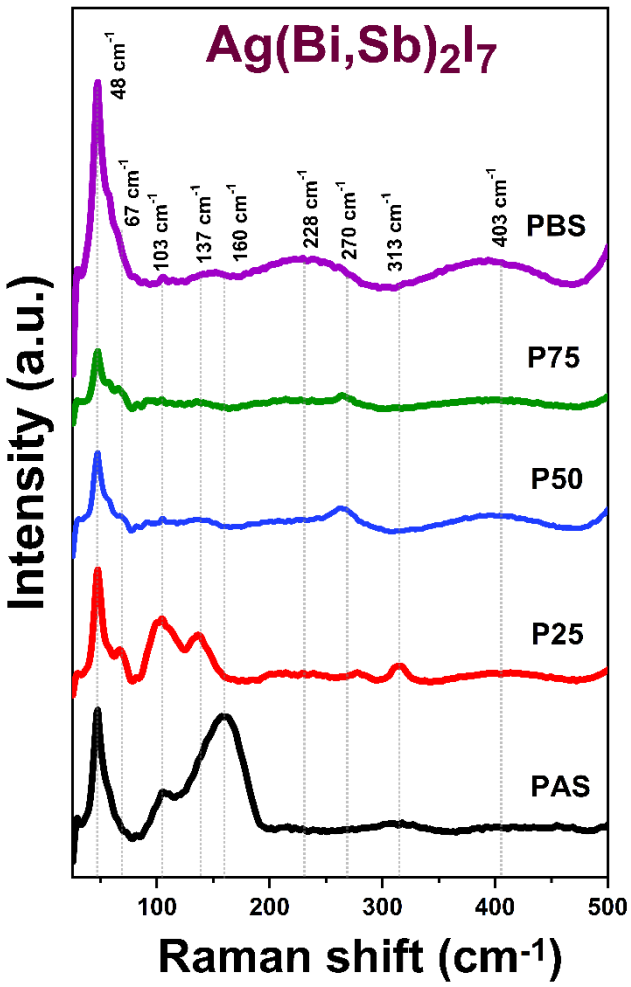

Figure 5.4. Raman spectra of $Ag(Bi,Sb)_2I_7$ thin films at varying Bi and Sb ratio

The Raman shifts and intensity variations observed in the spectrum provide valuable information about the vibrational characteristics of the $Ag(Bi,Sb)_2I_7$ perovskite thin films. These findings offer insights into how bismuth incorporation influences the material's structural stability and vibrational modes, complementing the X-ray diffraction (XRD) results. Taken together, the Raman and XRD data provide a comprehensive understanding of the structural properties of the synthesized perovskite thin films, which is essential for evaluating their potential in photodetection applications.

5.6 Elemental composition and their chemical state

X-ray Photoelectron Spectroscopy (XPS) was employed to investigate the elemental composition, chemical states, and surface chemistry of the $Ag(Bi,Sb)_2I_7$ perovskite thin films. This surface-sensitive technique was critical for understanding the chemical

environment and oxidation states of the key constituent elements- silver (Ag), bismuth (Bi), antimony (Sb), and iodine (I), which directly influence the film's optoelectronic properties and long-term stability.

The initial survey spectra (Figure 5.5) revealed the presence of all intended elements, with prominent signals corresponding to Ag, Bi, Sb, and I. This confirmed the successful incorporation of the cations and halide into the film matrix and verified the absence of significant contamination from extraneous species. No unexpected peaks associated with surface oxides, carbonates, or metallic states were observed, indicating the films were chemically clean and retained the intended perovskite phase at the surface.

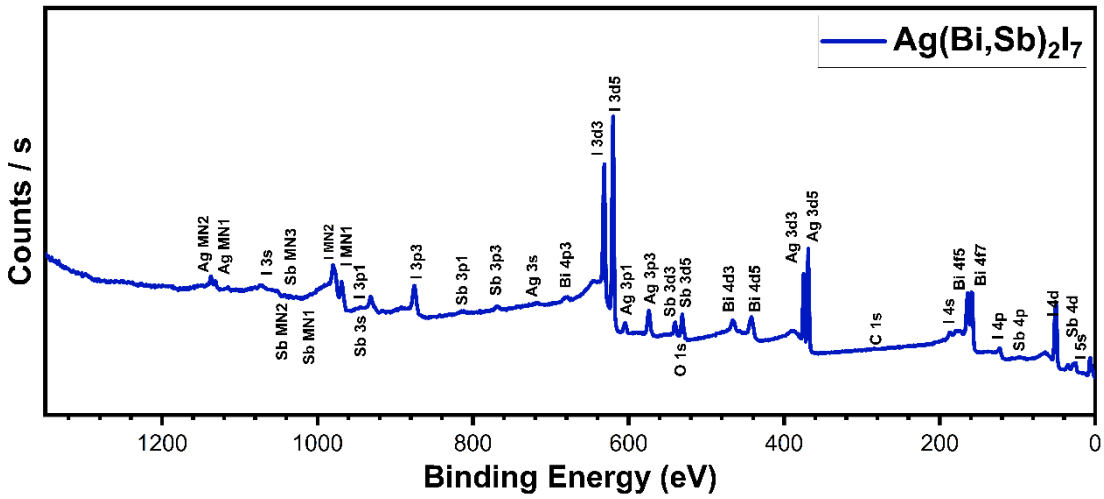

Figure 5.5. XPS survey spectrum of $Ag(Bi,Sb)_2I_7$ thin film showing the presence of Ag, Bi, Sb, and I without detectable impurities or surface contaminants. The absence of additional peaks confirms surface chemical purity and compositional integrity.

High-resolution core-level scans were performed to further elucidate the chemical states of the individual elements (Figure 5.6). The Ag 3d region displayed two well-defined peaks at binding energies of 368.8 eV and 374.8 eV, attributed to Ag $3d_{5/2}$ and Ag $3d_{3/2}$, respectively. The observed spin-orbit splitting of 6.0 eV is characteristic of silver in the +1 oxidation state (Ag^+), suggesting that silver is incorporated into the perovskite lattice in a chemically stable and oxidized form, likely coordinated within edge- or face-sharing halide octahedra.

The Sb 3d spectrum showed two major peaks at 531.1 eV and 540.4 eV, corresponding to Sb $3d_{5/2}$ and Sb $3d_{3/2}$, respectively. These binding energies are consistent with the presence of Sb^{3+}, which is typically found in halide perovskite environments and participates in octahedral coordination with iodine atoms. The sharpness and symmetry of these peaks suggest a well-defined chemical environment with minimal variation in the local bonding of Sb.

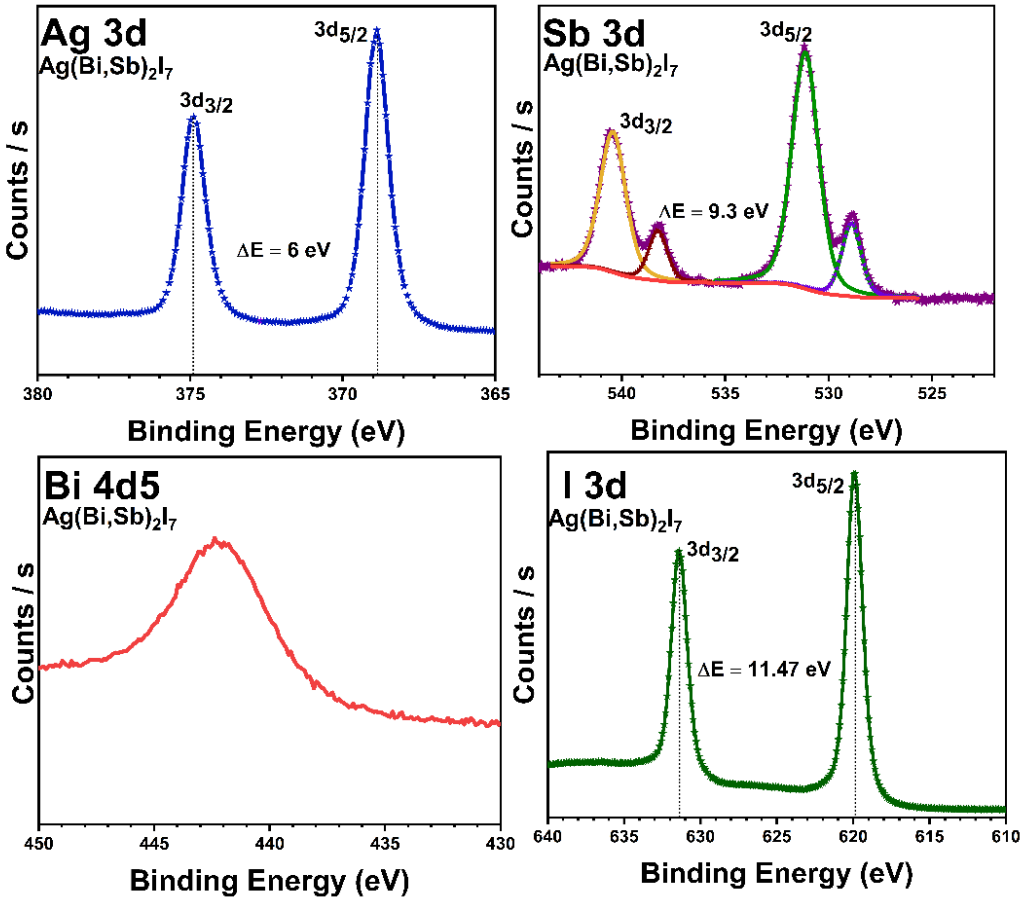

Figure 5.6. High-resolution XPS spectra of core-level regions: Ag 3d, Sb 3d, Bi 4d, and I 3d. The binding energies confirm the +1 oxidation state for Ag, +3 for Sb and Bi, and -1 for I, validating the chemical structure of the alloyed perovskite.

For bismuth, the Bi $4d_5$ peak was detected at 441.97 eV, consistent with the Bi^{3+} oxidation state. The lack of additional satellite features or shifted peaks confirmed that bismuth was uniformly incorporated into the perovskite lattice without signs of disproportionation or mixed valency. The Bi^{3+} state complements the Sb^{3+} configuration in the alloy, supporting

the idea of an isovalent substitution mechanism between Bi and Sb in the octahedral sites of the Rudorffite structure.

The iodine environment was examined through the I 3d core levels, with the $3d_{5/2}$ and $3d_{3/2}$ peaks appearing at 619.89 eV and 631.36 eV, respectively. The spin-orbit splitting of 11.47 eV is characteristic of iodide anions (I^-), indicating that iodine is present in the -1 oxidation state and strongly bonded to the surrounding cationic framework. The absence of shoulders or additional peaks in this region ruled out the presence of molecular iodine (I_2) or oxidized iodine species on the surface.

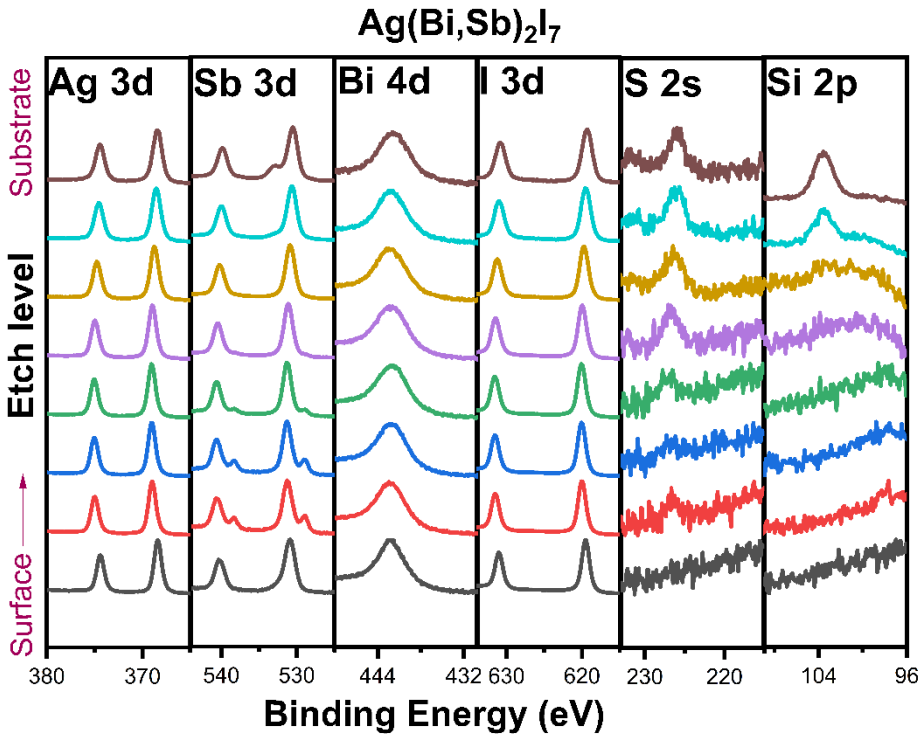

Figure 5.7. XPS depth profiling of $Ag(Bi,Sb)_2I_7$ thin film, showing consistent presence of Ag, Bi, Sb, and I across the film depth. The uniform elemental distribution indicates compositional homogeneity throughout the film thickness.

To assess the chemical uniformity of the films throughout their thickness, XPS depth profiling was performed via argon ion sputtering (Figure 5.7). This analysis confirmed that all constituent elements- Ag, Bi, Sb, and I, were consistently detected at successive depths, revealing a uniform distribution throughout the film. No significant elemental segregation or interfacial layering was observed during sputtering, indicating that the sequential

deposition and iodization process effectively produced a compositionally homogeneous perovskite thin film. Collectively, the XPS results validate the formation of a chemically stable, homogeneously alloyed $Ag(Bi,Sb)_2I_7$ phase, with all cations and anions occupying well-defined oxidation states appropriate for the Rudorffite structure. These findings provide important insight into the surface integrity and chemical configuration of the thin films, laying a solid foundation for their application in photodetection technologies where interfacial stability and reproducible chemical environments are critical to performance.

5.7 Optical properties

UV-VIS spectroscopy analysis was conducted to investigate the optical properties of the $Ag(Bi,Sb)_2I_7$ perovskite thin films, focusing on absorption, transmittance, and reflectance measurements. The band gap energy of the materials was determined based on these spectral analyses. In the case of pure silver antimony iodide ($AgSb_2I_7$), the band gap was observed to be 2.09 eV (Figure 5.8).

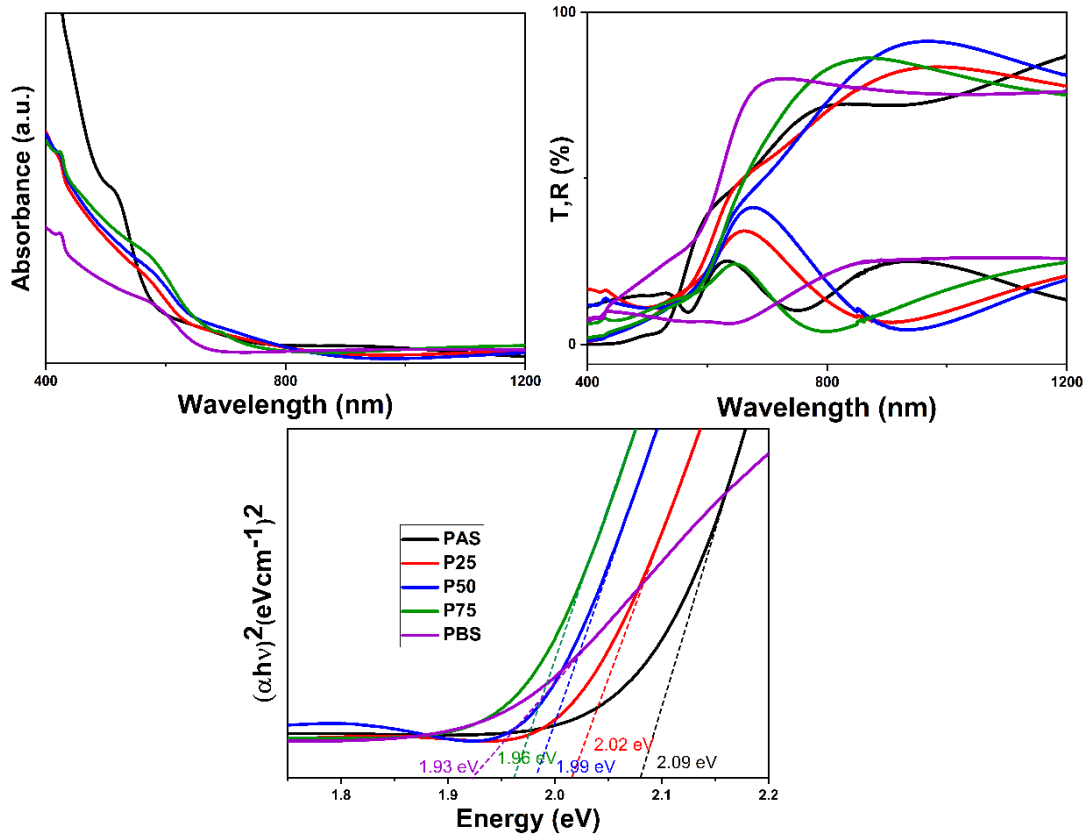

Figure 5.8. The absorbance, transmittance, reflectance spectra and Tauc plot of $Ag(Bi,Sb)_2I_7$ double perovskite thin films.

Subsequently, variations in the band gap energy were observed with different levels of bismuth (Bi) inclusion in the perovskite thin films. When 25% Bi was included, the band gap decreased to 2.02 eV, while with an equal ratio of 50% Bi and 50% Sb, the band gap further decreased to 1.99 eV. As the percentage of bismuth increased to 75%, the band gap decreased to 1.96 eV. Notably, in the case of pure silver bismuth iodide ($AgBi_2I_7$) with 100% Bi and 0% Sb, the band gap was measured at 1.93 eV.

Comparing these band gap values to the previously studied perovskite materials, it is evident that the inclusion of bismuth induces a systematic decrease in the band gap energy of the $Ag(Bi,Sb)_2I_7$ perovskite thin films. This trend suggests that the electronic structure and optical properties of the perovskite materials are influenced by the presence of bismuth and the variation in its concentration within the lattice. The decrease in band gap energy with increasing bismuth content can be attributed to the change in the electronic structure and band alignment caused by the substitution of bismuth for antimony in the perovskite structure.

The optical properties of the $Ag(Bi,Sb)_2I_7$ perovskite thin films, highlighting the tunability of the band gap energy through controlled variations in the bismuth content. This understanding is crucial for the optimization of the perovskite thin films for potential photodetection applications, allowing for the customization of optical properties and enhancing the overall performance of the photodetectors.

5.8 Ferroelectric Self-driven Photoconduction

The photodetection characteristics of $Ag(Bi,Sb)_2I_7$ perovskite thin films were evaluated under broadband and wavelength-specific illumination using a halogen lamp and light-emitting diodes (LEDs) of varying wavelengths, including ultraviolet (UV), visible (blue, green, yellow, red), and infrared (IR) regions (Figure 5.9). The objective was to assess the photoresponse and spectral responsivity of the thin films with varying Bi:Sb ratios.

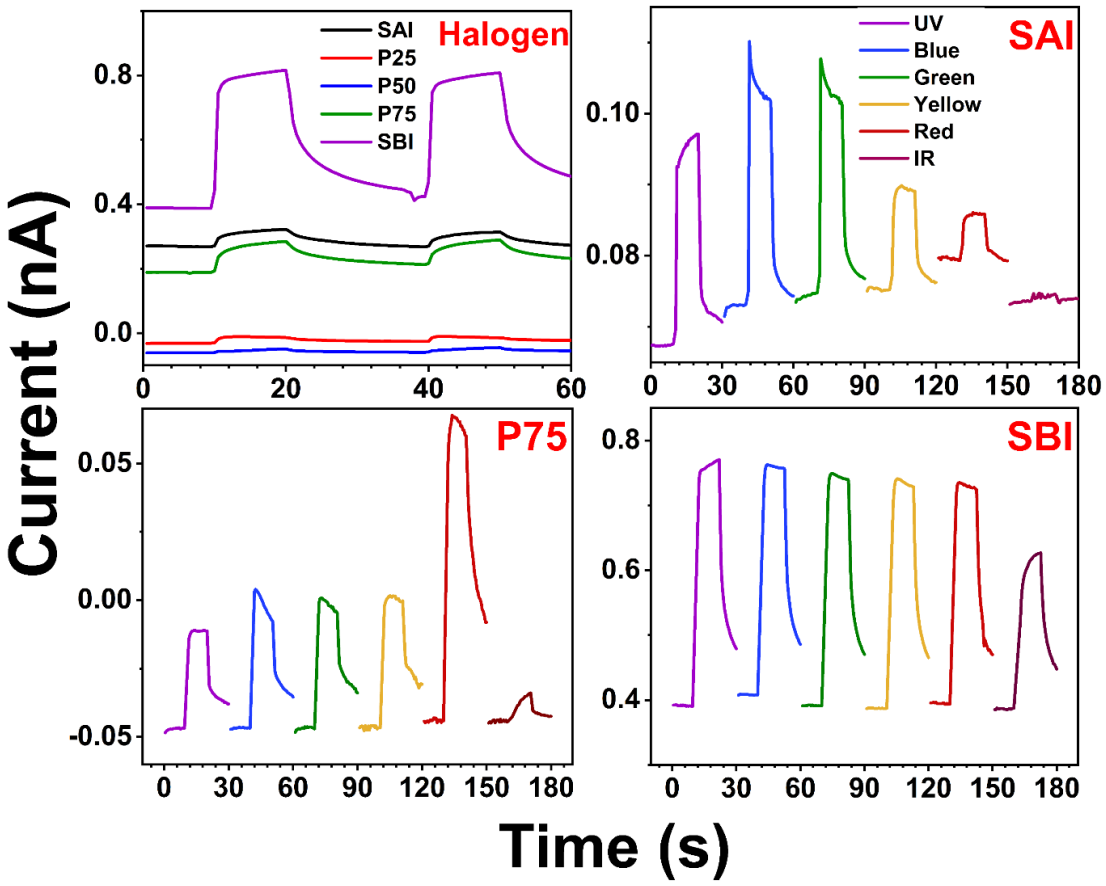

Figure 5.9. Self-powered photodetector measurements of $Ag(Bi,Sb)_2I_7$ perovskite thin films on glass substrate using different light sources.

Among the tested compositions, the phase-pure $AgSb_2I_7$ and $AgBi_2I_7$ thin films exhibited a pronounced photocurrent under halogen lamp illumination. Notably, the mixed-composition sample containing 75% Bi and 25% Sb (hereafter referred to as P75) demonstrated not only enhanced photocurrent levels comparable to the phase-pure samples but also superior temporal stability under continuous illumination. This enhanced performance without noticeable degradation suggests improved charge carrier dynamics and structural stability in the mixed-cation system.

Remarkably, the photodetector response was recorded on glass substrates without the incorporation of traditional device architectures such as p–n or Schottky junctions. The measurable photocurrent in the absence of engineered interfaces indicates the intrinsic ability of the $Ag(Bi,Sb)_2I_7$ thin films to generate and separate charge carriers upon illumination. This behavior is suggestive of spontaneous polarization effects, possibly

arising from ferroelectric properties within the perovskite structure, which may facilitate internal electric fields aiding in charge separation (see Chapter 4).

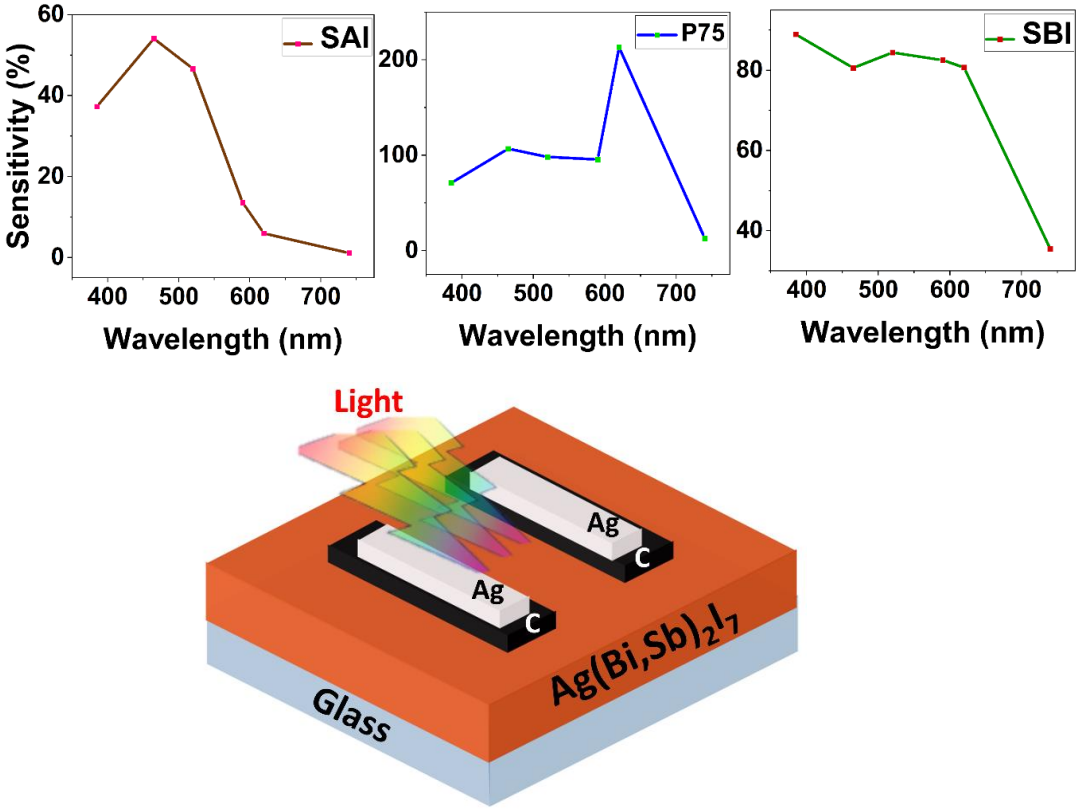

Figure 5.10. Self-powered photodetector Sensitivity comparison of $Ag(Bi,Sb)_2I_7$ perovskite thin films on glass substrate using different light sources.

To quantify the spectral response, three representative samples- $AgSb_2I_7$ (SAI), the P75 composition, and $AgBi_2I_7$- were exposed to discrete LED light sources across the spectral range. All samples exhibited measurable photoresponse over the full range of tested wavelengths (Figure 5.10), demonstrating their broadband photodetection capability. The calculated responsivity values indicated a significant enhancement in the P75 sample (3.49×10^{-11} A/W) compared to SAI (1.43×10^{-11} A/W) and $AgBi_2I_7$ (1.29×10^{-10} A/W), suggesting a synergistic effect of Bi and Sb incorporation on optimizing light absorption and charge transport properties.

These results underscore the tunable and versatile optoelectronic behavior of $Ag(Bi,Sb)_2I_7$ thin films. The ability to achieve high photoresponse across a broad spectral range, even on

non-junctional platforms, positions these materials as promising candidates for next-generation, low-cost, and flexible photodetectors.

5.9 Photodiodes of $Ag(Bi,Sb)_2I_7$ thin film

The incorporation of $Ag(Bi,Sb)_2I_7$ perovskite thin films into a structured junction device has led to a significant enhancement in photodetection performance, as evidenced by a marked increase in current response from the nanoampere to microampere range under illumination (Figure 5.11). The device architecture was constructed by sequentially depositing cadmium sulfide (CdS) on a fluorine-doped tin oxide (FTO) substrate, followed by $Ag(Bi,Sb)_2I_7$ as the intrinsic absorber layer, cuprous iodide (CuI) as the hole transport layer, and a carbon electrode. The structure was finalized by the deposition of an Ag top contact, forming a functional heterojunction photodetector.

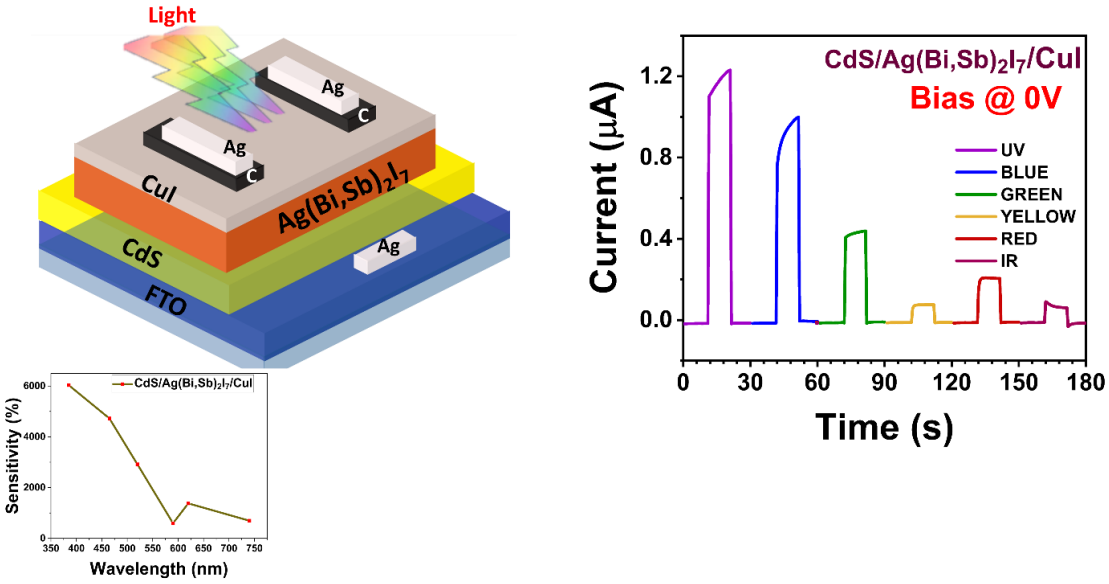

Figure 5.11. $Ag(Bi,Sb)_2I_7$-based photodetector device under illumination, demonstrating enhanced photocurrent response in the microampere range. The device architecture comprises FTO/CdS/$Ag(Bi,Sb)_2I_7$/CuI/Carbon/Ag, showcasing the improved charge transport and light-harvesting efficiency achieved through junction integration.

This multilayer configuration was designed to optimize light absorption and charge separation while leveraging the favorable electronic properties of the perovskite layer. The enhanced performance aligns with prior findings (see Chapter 4) demonstrating the

inherently high charge mobility, low trap density, and effective carrier lifetimes associated with Ag-based halide perovskites. The broad-spectrum light detection observed in the device is consistent with the previously reported broadband photoresponse characteristics of perovskite materials [11,194].

A responsivity of 4.14×10^{-7} A/W was recorded for the junction device, representing a substantial improvement over non-junction-based photodetector. This high responsivity indicates efficient photocarrier generation, separation, and collection, which can be attributed to the optimized energy band alignment and interfacial properties engineered through the combination of CdS, CuI, and $Ag(Bi,Sb)_2I_7$ layers. The synergistic role of these materials facilitates improved charge extraction and reduces recombination losses, thereby enhancing the photodetection efficiency.

The demonstrated performance highlights the viability of $Ag(Bi,Sb)_2I_7$-based heterojunction devices for next-generation optoelectronic applications. Their ability to achieve high responsivity without compromising stability makes them attractive for use in broadband photodetectors, imaging sensors, and light-harvesting technologies.

5.10 Conclusions

- **New Alloy Design Strategy**: Successfully synthesized cubic-phase $Ag(Bi,Sb)_2I_7$ thin films with tunable cationic substitution using a sequential deposition and iodization method.
- **Octahedral Network Tuning**: Substitution of Sb by Bi in the octahedral framework allowed precise control over structural and optoelectronic properties.
- **Phase Stability Enhancement**: Bi incorporation improved phase stability and promoted broader vibrational stability across the alloy system.
- **Bandgap Tunability**: A gradual bandgap narrowing from 2.02 eV (Sb-rich) to 1.93 eV (Bi-rich) was observed, indicating smooth electronic transitions across compositions.
- **Ferroelectric-Assisted Photodetection**: The alloyed $Ag(Bi,Sb)_2I_7$ films exhibited intrinsic ferroelectric behavior, supporting self-powered photoconduction under visible and NIR illumination.

- **Composition-Dependent Performance**: Tunable photodetection characteristics were achieved by varying Bi/Sb ratios, optimizing responsivity, EQE, and detectivity.
- **Stability in Heterojunctions**: $Ag(Bi,Sb)_2I_7$ films integrated into FTO/n-CdS/i-$Ag(Bi,Sb)_2I_7$/p-CuI heterostructures demonstrated more stable and reliable performance compared to the end-member compositions.

Chapter 6: Synthesis and characterization of copper antimony iodide (Cu_2SbI_5) perovskite thin films for photodetector application

The ever-evolving landscape of photonic and electronic devices necessitates the continuous exploration of novel materials and technologies. As researchers endeavor to push the boundaries of material science, the focus has increasingly shifted towards sustainable, high-performance compounds. This chapter delves into the realm of copper antimony iodide (Cu_2SbI_5) perovskite thin films, a material poised to revolutionize photodetector applications with its remarkable properties and eco-friendly profile.

6.1 Introduction

In recent years, the urgent need for non-toxic, sustainable alternatives to lead-based halide perovskites has driven the exploration of novel materials with comparable optoelectronic performance. Among these, copper-based halide perovskites have gained increasing attention due to copper's abundance, environmental safety, and its inherently high charge carrier mobility, making it a suitable replacement for toxic lead in perovskite optoelectronics [44,143].

The copper–bismuth–iodide (Cu–Bi–I) family has been the subject of foundational research in this field. Early work by Fourcroy et al. reported the synthesis of $CuBiI_4$ with a cubic *Fd3m* structure via a solid-state reaction route [69]. This was followed by Bahari et al., who refined the synthesis of $CuBiI_4$ through melt-crystallization and also reported the formation of Cu_2BiI_5 with a rhombohedral *R3m* symmetry under similar conditions [44]. Further structural tuning within this system was demonstrated by Baranwal et al., who developed Cu_3BiI_6 films via a conventional one-step spin-coating route using DMSO as the solvent [44] [70]. Ramachandran et al. later introduced a two-step method combining spin-coating and thermal evaporation (using DMF for BiI_3), leading to improved crystallinity and phase purity of Cu_2BiI_5 [71]. Sansom et al. revisited the $CuBiI_4$ system, confirming the R3m phase obtained through melt-crystallization [195].

Despite these significant contributions to the Cu–Bi–I system, research on its antimony counterpart remains limited. The isoelectronic substitution of Bi^{3+} with Sb^{3+} in halide lattices offers a promising pathway to tune the electronic structure, reduce toxicity further, and potentially enhance material stability. Notably, Jia et al. synthesized Cu_3SbI_6 using a conventional one-step spin-coating method, revealing a stable *R3m* structure and suitable optoelectronic properties for device applications [48].

Building on these prior developments, our work introduces a novel synthesis pathway for Cu–Sb–I compounds by employing a bilayer approach: chemical bath deposition (CBD) of Sb_2S_3 followed by thermal evaporation of Cu. This bilayer was then subjected to a rapid iodization process, resulting in the formation of phase-pure hexagonal Cu_2SbI_5. This method offers precise control over film composition and crystallinity while maintaining compatibility with low-temperature, scalable processing techniques. The synthesized phase was confirmed by comparing the experimental X-ray diffraction pattern with a simulated pattern generated from a calculated structure file, validating the formation of the hexagonal Cu_2SbI_5 phase.

Comprehensive characterization was performed to evaluate its structural, optical, and electronic properties. Raman spectroscopy revealed vibrational modes characteristic of the hexagonal Cu_2SbI_5 lattice. X-ray photoelectron spectroscopy (XPS) confirmed the expected oxidation states of Cu^{+} and Sb^{3+}, along with proper iodide coordination, supporting successful phase formation. UV–Visible spectroscopy showed strong absorption in the visible region, indicating its suitability for optoelectronic applications. Furthermore, low-bias photodetector measurements demonstrated a measurable photocurrent under illumination, suggesting the promise of hexagonal Cu_2SbI_5 as an active layer in lead-free photodetectors.

6.2 Crystalline structure

The crystalline structure analysis and optimization of Cu_2SbI_5 using XRD revealed promising findings. Three variations of copper molarity (30 nm, 50 nm, and 70 nm) were investigated, with phase-pure Cu_2SbI_5 observed in the 30 nm copper sample, showcasing high crystallinity. In contrast, the 50 nm and 70 nm copper samples exhibited copper iodide peaks. The crystal system of Cu_2SbI_5 was determined to be hexagonal, with peaks observed at 12.9, 25.7, 38.8, 42.4, 50.1, and 52.6 degrees, corresponding to the (003),

(102), (107), (108), (116), and (204) planes, where (003) and (102) were highly oriented. Figure 6.1 (a) illustrates these XRD findings, showcasing the peaks and crystallographic planes identified. Notably, the XRD analysis also depicted the presence of copper peaks before iodization, representing the initial film state before forming the ternary Cu_2SbI_5 compound.

Comparing these experimental results with reported articles, the literature suggests that the optimized crystalline structure obtained in the 30 nm copper sample aligns with the observed phase-pure Cu_2SbI_5 and high crystallinity. This finding underscores the significance of copper molarity in influencing the crystallographic properties of the synthesized material. The reaction mechanism leading to the formation of Cu_2SbI_5 involves multi-layer deposition steps: initially depositing Sb_2S_3 via chemical bath deposition, followed by the thermal evaporation of copper as the second layer. These two layers do not interact initially; however, upon iodization, a ternary compound of Cu_2SbI_5 is formed as the final product through a chemical reaction process.

The balanced chemical reaction predicted for the formation of Cu_2SbI_5 from Sb_2S_3, Cu, and iodine during the iodization process can be expressed as follows:

$$2Sb_2S_3+8Cu+7I_2 \rightarrow 4Cu_2SbI_5+6S\uparrow \qquad (6.1)$$

This reaction encapsulates the transformation of the precursor layers into the desired Cu_2SbI_5 ternary compound, highlighting the intricate chemical processes involved in the synthesis of the material.

Figure 6.1 (b) depicts the variation of iodization time on the crystallinity of the Cu_2SbI_5 thin films. The XRD analysis reveals that at 6 minutes of iodization time, high crystallinity is observed in the material. However, as the iodization time is extended to 8 and 10 minutes, a decrease in crystallinity is noted.

The decrease in crystallinity observed at 8 and 10 minutes of iodization time can be attributed to excessive iodization leading to the formation of secondary phases or defects within the Cu_2SbI_5 crystal lattice. Prolonged exposure to iodine may introduce impurities or disruptions in the crystal structure, affecting the overall crystallinity of the material. This loss in crystallinity may result in reduced peak intensities and broader peaks in the XRD pattern, indicating a decrease in the material's structural order and quality.

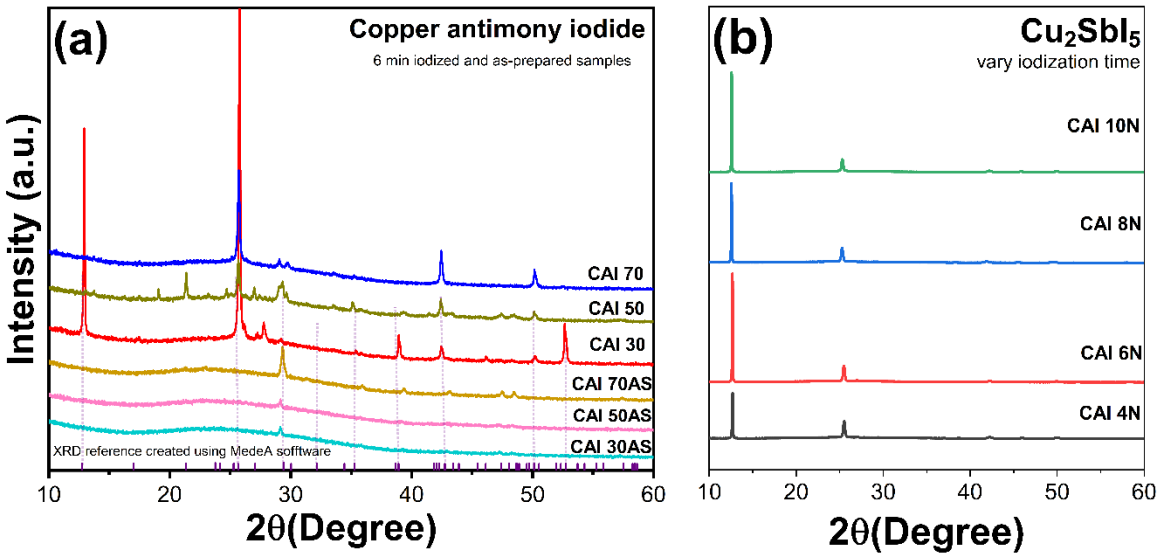

Figure 6.1. (a) illustrates the optimization of copper in Cu_2SbI_5 thin films with varying copper thickness, while (b) demonstrates the impact of varying iodization time on the material properties.

6.3 Raman spectroscopy

Figure 6.2 displays the Raman spectra of Cu_2SbI_5 thin films, highlighting distinct vibrational modes observed at 50, 84, 110, 150, and 218 cm^{-1}. The peak at 150 cm^{-1} is believed to stem from the second-order Raman line of SbI_3, aligning well with XRD results and reinforcing consistency in structural analysis. A systematic shift in peak positions by one or two wavenumbers between precursor and Cu_2SbI_5 perovskite thin films suggests the formation of the ternary phase. These shifts indicate structural changes, potentially reflecting alterations in bond lengths, angles, and molecular interactions during Cu_2SbI_5 formation. The cohesiveness between XRD and Raman spectroscopy findings underscores a robust understanding of the material's crystal structure and phase evolution, with specific Raman peaks offering key insights into vibrational modes and the crystalline properties of Cu_2SbI_5.

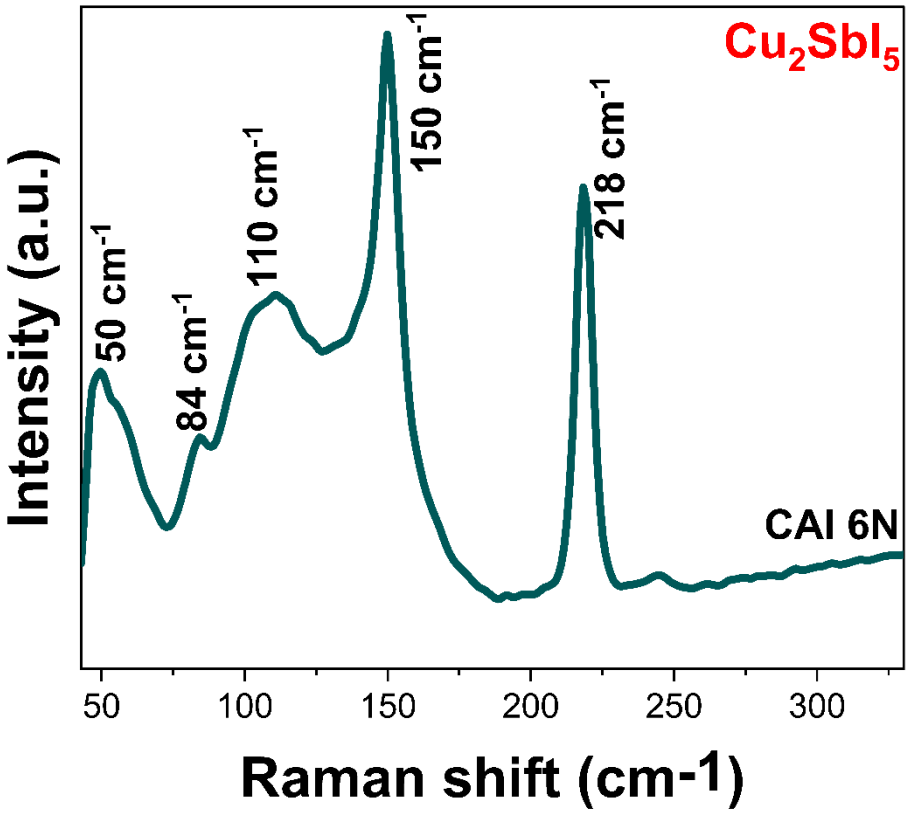

Figure 6.2. Raman spectra of Cu_2SbI_5 thin films showing peaks at 50, 84, 110, 150, and 218 cm^{-1}, highlighting structural characteristics and phase transitions within the material.

6.4 X-ray photoelectron spectroscopy (XPS)

Figure 6.3 presents the XPS survey spectra of the Cu_2SbI_5 thin films, confirming the presence of all expected constituent elements—copper (Cu), antimony (Sb), and iodine (I). The presence of only these elements in the survey scan supports the purity of the film and the successful formation of the Cu_2SbI_5 phase. No significant peaks corresponding to extrinsic impurities such as oxygen, carbon, or other metals were detected, suggesting that the film's surface is relatively free from contamination or unintentional doping.

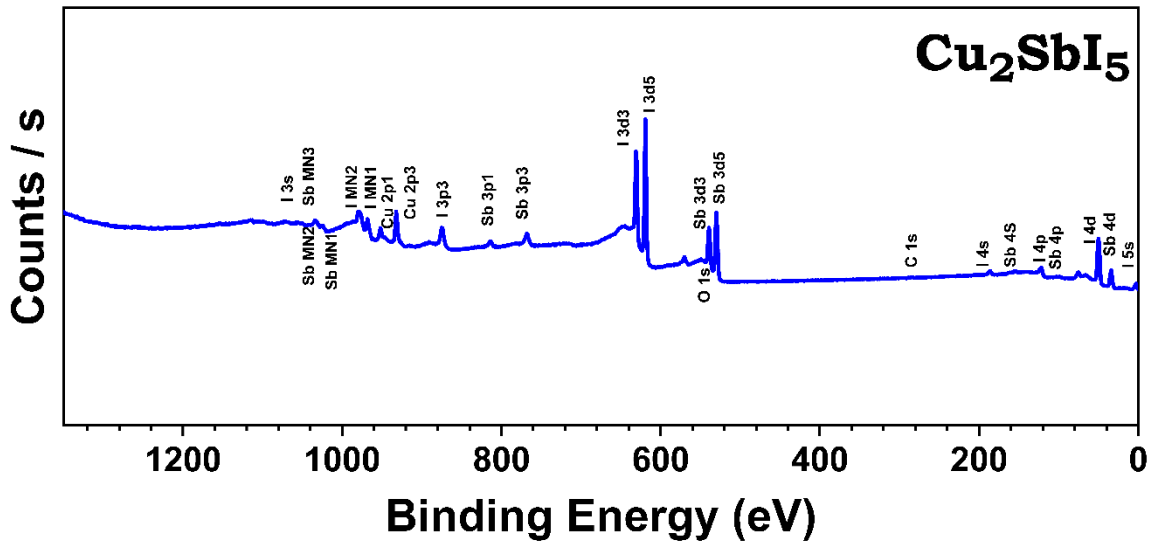

Figure 6.3. XPS survey spectra of Cu_2SbI_5 thin films showcasing the identification of all constituent elements, including copper (Cu), antimony (Sb), and iodine (I).

Figure 6.4(a) shows the high-resolution XPS spectra of the Cu 2p orbital. The spectra exhibit a primary feature at 932.25 eV, attributed to the Cu $2p_{3/2}$ peak, and a second peak at 952.0 eV, corresponding to the Cu $2p_{1/2}$ spin-orbit component. These values are consistent with the binding energies typically reported for Cu(I) species (Cu^{+}), as observed in copper(I) iodide (CuI) and related compounds. Notably, there is no significant satellite peak around 940–945 eV, which is characteristic of Cu(II) (Cu^{2+}) species, indicating that copper in Cu_2SbI_5 is predominantly in the +1 oxidation state.

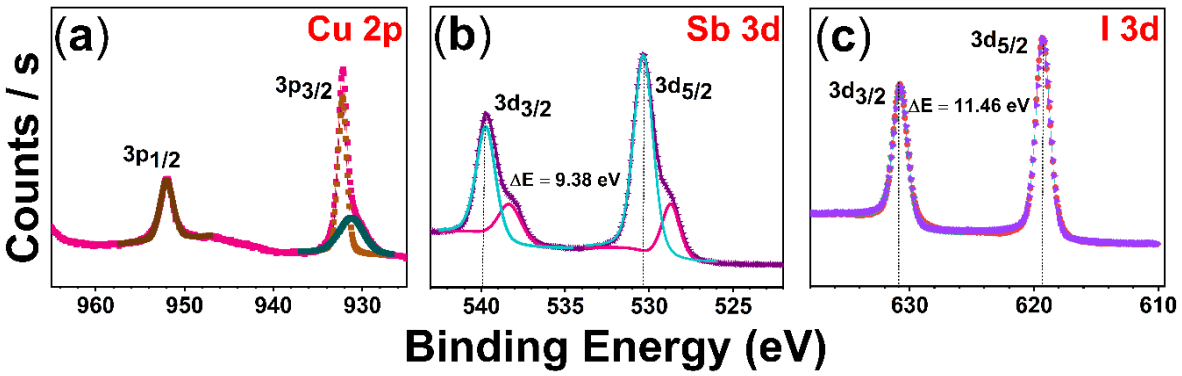

Figure 6.4. (a), (b), and (c): High-resolution XPS analyses of Cu, Sb, and I orbitals in Cu_2SbI_5 films reveal distinct peak structures and energy differences, offering insights into electronic structures and oxidation states.

Upon deconvolution, a single dominant peak is observed in the Cu 2p region with minimal separation between $2p_{3/2}$ and $2p_{1/2}$, which may be attributed to the relatively small spin-orbit splitting of Cu(I) and the overlap or broadening of the peaks. This can arise due to final-state effects or the specific chemical environment of copper in the Cu–Sb–I lattice. The lack of clear splitting does not necessarily imply the presence of elemental Cu (Cu^0), but instead suggests a stable Cu^+ state with a symmetric coordination environment, possibly due to strong Cu–I interactions that affect the spin-orbit splitting resolution.

Figure 6.4(b) shows the high-resolution spectra for the Sb 3d orbital. The deconvoluted peaks at approximately 530.3 eV and 539.7 eV correspond to Sb $3d_{5/2}$ and Sb $3d_{3/2}$, respectively, with a spin-orbit splitting of about 9.4 eV, which is in good agreement with reported values for Sb(III) species. These binding energy positions are consistent with antimony bonded to halides (e.g., in SbI_3 or Sb-based chalcohalides).

Additionally, a smaller feature around 528.7 eV could suggest a minor contribution from elemental antimony (Sb^0). However, this may also result from slight reduction during sputtering or local variation in bonding environments at the film surface. No strong evidence of Sb(V) (which typically exhibits a $3d_{5/2}$ binding energy above 531 eV) was observed, suggesting that antimony is primarily in the +3 oxidation state in this compound. The chemical state analysis therefore confirms the presence of Sb^{3+}, coherent with the stoichiometry and expected bonding in Cu_2SbI_5.

The high-resolution XPS spectra for iodine in Figure 6.4(c) display two well-defined peaks at 619.2 eV (I $3d_{5/2}$) and 630.7 eV (I $3d_{3/2}$), corresponding to the spin-orbit components of iodine. The energy separation of ~11.5 eV is characteristic of I^- species, as seen in metal iodides such as CuI and SbI_3. These values align with the iodide anion (I^-) in a halide lattice, confirming that iodine is in the –1 oxidation state throughout the Cu_2SbI_5 film.

There is no indication of iodine in higher oxidation states (such as I(V), which would shift the binding energy to higher values), nor is there evidence of significant iodine deficiency or oxidation. The sharpness and intensity of the peaks suggest strong bonding between iodine and the metal centers, particularly within the edge-sharing polyhedra typical of SbI_6 and CuI_4 structural units in mixed-metal halides.

In Figure 6.5, the XPS depth profile of the Cu_2SbI_5 thin films demonstrates the presence of copper (Cu), antimony (Sb), and iodine (I) throughout the depth of the film. This observation suggests that the elemental composition remains consistent across the thickness of the film, indicating uniform distribution and stability of the constituent elements within the material. The XPS depth profile analysis offers valuable insights into the compositional integrity and homogeneity of the Cu_2SbI_5 thin films, providing essential information for understanding the material's structure and properties.

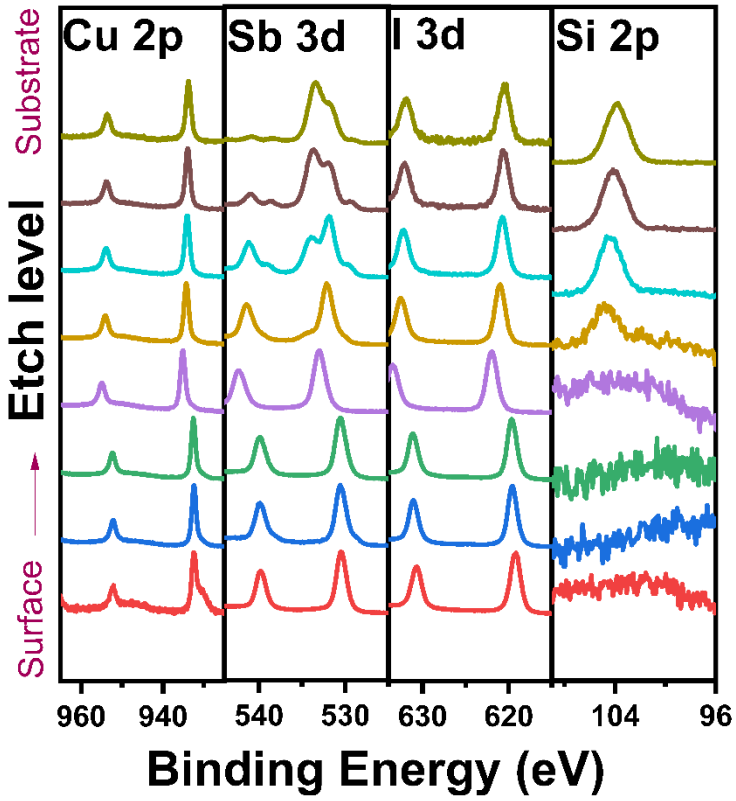

Figure 6.5. XPS depth profile analysis of Cu_2SbI_5 thin films revealing the consistent presence of copper, antimony, and iodine across the film's depth, indicating uniform distribution and compositional stability within the material.

6.5 UV-Vis/NIR spectroscopy

In Figure 6.6(a), the UV–vis absorbance spectra of Cu_2SbI_5 thin films subjected to different iodization conditions reveal distinct variations in optical behavior across the 400–1200 nm wavelength range. The films exhibit strong absorption in the visible region, with an absorption onset corresponding to a direct optical bandgap of approximately 2.2 eV, in agreement with earlier studies on iodide-rich copper-antimony halides, where

direct bandgaps in the range of 2.0–2.3 eV have been reported depending on composition and synthesis route [196,197]. The observed spectral differences among the samples suggest that iodization plays a crucial role, who showed that iodide content directly affects the Cu/Sb ratio and optical transitions in related compounds [54].

The increase in absorbance intensity, particularly in the 500–800 nm region, along with shifts in the absorption edge, can be attributed to improved crystallinity and enhanced iodide incorporation, leading to reduced trap states and better light-harvesting efficiency. The manipulation of iodine content effectively tunes the electronic band structure and enhances light–matter interaction, which is essential for optoelectronic device performance [198].

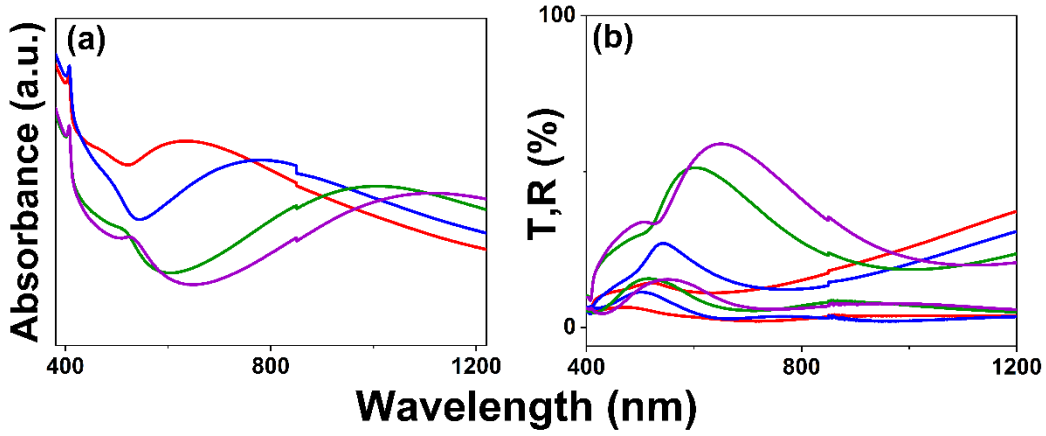

Figure 6.6. UV-vis spectroscopy analysis of Cu_2SbI_5 thin films, showcasing (a) absorbance variations with iodization levels and (b) transmittance and reflectance profiles, providing insights into the material's optical properties and light interactions across the spectrum.

Figure 6.6(b) presents the corresponding transmittance (T) and reflectance (R) spectra of the films. As expected, samples exhibiting higher absorbance show lower transmittance in the 400–800 nm region, confirming improved photon absorption and indicating that the films are more optically dense. This inverse relation between absorbance and transmittance has been previously reported for copper-antimony-based absorbers, where iodine-rich films exhibit dense and uniform morphologies with minimal pinholes, thus reducing light leakage [199]. Additionally, reflectance values across the spectrum exhibit variation, especially in the near-infrared region, where higher iodine incorporation appears to increase surface roughness or alter microstructure- leading to light scattering

and increased R values. These optical signatures correlate well with studies from previous literature, which have linked iodine-rich growth to textured morphologies with enhanced light-trapping capabilities [200]. The optical bandgap of 2.2 eV makes this material suitable for visible-light applications such as photodetectors and solar absorbers, particularly in tandem architectures where wider bandgap absorbers are required. These findings reinforce the importance of compositional engineering, as also emphasized by Maughan et al. and others, in achieving functional optoelectronic behavior in lead-free metal halides [201].

6.6 Photocurrent response measurement

The photodetection behavior of Cu_2SbI_5-based photodetectors synthesized under different iodization durations was systematically evaluated under monochromatic illumination at a fixed low bias of 0.05 V. The time-resolved photocurrent responses for samples iodized for 4 minutes (CAI 4N), 6 minutes (CAI 6N), and 10 minutes (CAI 10N) are presented in Figure 6.7. These measurements were performed under sequential exposure to light of different wavelengths - ultraviolet (UV), blue, green, yellow, red, and infrared (IR)- to investigate the wavelength-dependent photoresponse characteristics.

As shown in Figure 6.7, all devices exhibit a rapid and reversible switching behavior upon exposure to different wavelengths, indicative of efficient and stable photodetection. Notably, the photocurrent magnitude and spectral sensitivity vary with iodization time, suggesting a strong dependence of optoelectronic performance on film morphology and phase purity influenced by iodization duration.

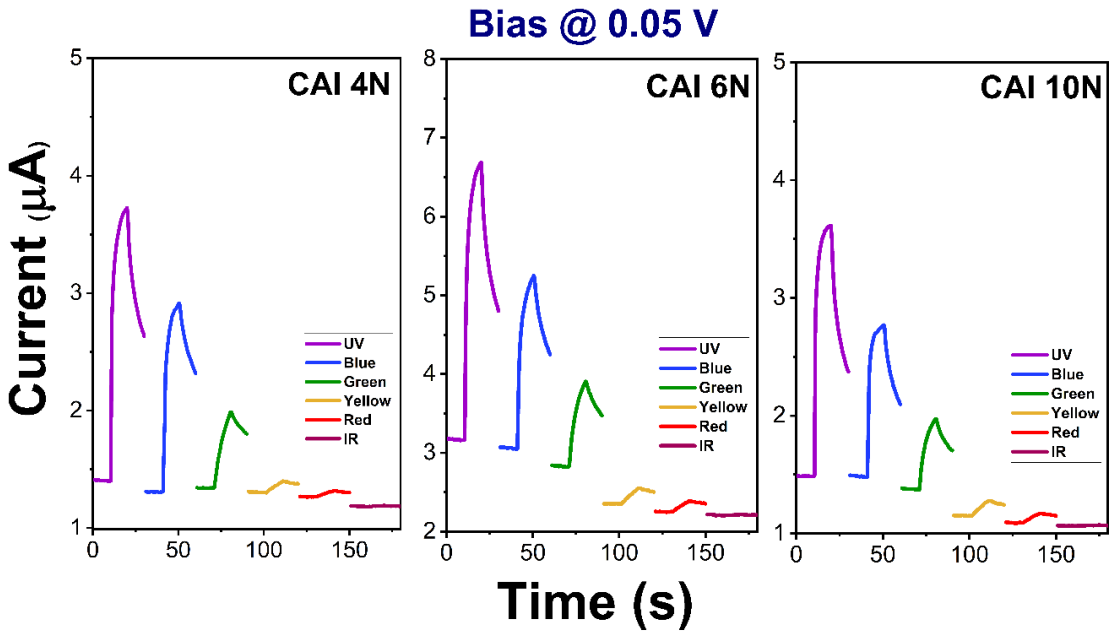

Figure 6.7. Investigation of Cu_2SbI_5 thin film photodetector response under different light sources and processing durations, showing enhanced performance in CAI 6N sample due to improved crystallinity and UV sensitivity at a low bias voltage.

Among the three samples, CAI 6N demonstrates the highest photocurrent response, achieving a peak value of approximately 7.0 µA under UV illumination. In comparison, CAI 4N and CAI 10N exhibit lower UV-induced photocurrents, peaking at 4.3 µA and 4.2 µA, respectively. This superior performance of the CAI 6N device is maintained across other wavelengths as well. For instance, under blue and green light, CAI 6N reaches peak currents of 5.2 µA and 3.4 µA, respectively, while CAI 4N and CAI 10N yield lower responses in these regions. The yellow, red, and IR regions also follow this trend, with CAI 6N consistently outperforming the other two samples.

The enhanced photoresponse of CAI 6N can be attributed to improved film quality, including better crystallinity, optimal iodide incorporation, and reduced surface and grain boundary defects. These improvements likely enhance charge carrier mobility and suppress recombination, thereby facilitating more efficient photogeneration and extraction of charge carriers.

To quantify the signal quality, the photo-to-dark current ratio (PDCR) was estimated by comparing the photocurrent under UV illumination to the baseline dark current just before exposure. CAI 6N exhibited a PDCR of approximately 1.33, while CAI 10N, despite showing a lower photocurrent, had a slightly higher PDCR of 1.67 due to its lower

dark current baseline. CAI 4N showed the lowest PDCR of 1.25, consistent with its suboptimal film formation and possibly incomplete iodization, leading to higher recombination losses. These findings indicate that while PDCR is a useful metric for evaluating the signal-to-noise ratio, it should be interpreted alongside absolute photocurrent levels for a comprehensive assessment of device performance.

Importantly, all devices exhibited fast and stable switching behavior with rapid rise and decay times (0.3 s), confirming their suitability for dynamic and real-time photodetection applications. The sharp transitions in current upon light on/off cycling suggest minimal trapping/detrapping effects, which is critical for repeatable and reliable detection.

6.7 Conclusions

- **New Synthesis Method**: Cu_2SbI_5 thin films were successfully synthesized using a novel and efficient route, enabling controlled phase formation.
- **Phase-Pure Hexagonal Structure**: XRD and Raman analyses confirmed the formation of phase-pure Cu_2SbI_5 with a well-defined hexagonal crystal structure.
- **Strong Lattice Vibrations**: Raman spectroscopy revealed distinct Sb–I stretching modes and Cu–I vibrational contributions, indicating a robust lattice framework.
- **Optical Bandgap**: The films exhibited a direct bandgap of approximately 2.2 eV, making them suitable for visible light optoelectronic applications.
- **Low-Bias-Assisted Charge Extraction**: Electrical characterization showed efficient charge extraction even at low applied bias, highlighting their potential for low-power or self-powered devices.
- **Material Potential**: The combination of structural purity, strong lattice dynamics, and favorable electronic behavior positions Cu_2SbI_5 as a promising candidate for environmentally friendly, lead-free optoelectronic devices.

Chapter 7: Conclusions, Summary and Outlook

7.1 Conclusions and Summary of thesis contributions

This research focuses on the characterization of lead-free antimony-based semiconductors for photodetector applications, aiming to develop efficient, environmentally friendly alternatives to traditional lead-based materials. The study investigates material systems: $Cs_3Sb_2I_9$, $AgSb_2I_7$, $Ag(Bi,Sb)_2I_7$, and Cu_2SbI_5, all synthesized under ambient conditions using simple methods.

The research explores the synthesis and characterization of these materials, assessing their structural, optical, and electrical properties. Key objectives include improving photodetection performance, enhancing stability, and optimizing charge transport through interface engineering. The work also addresses critical research gaps, such as understanding the role of inherent ferroelectric material property, interface engineering in $AgSb_2I_7$, optimizing the Bi/Sb ratio in Sb_2S_3-based alloys, and investigating the low-bias photodetection capabilities of Cu_2SbI_5.

Table 7.1 Thesis Contribution

Material	Thesis Contribution
$Cs_3Sb_2I_9$	New synthesis method and film characterization, ferroelectric property evaluation, Illumination stability & spectral response
$AgSb_2I_7$	Thermal & microwave synthesis and film characterization, ferroelectricity study, heterojunction optimization, Role of CuI in interfacial recombination
$Ag(Bi,Sb)_2I_7$	Phase stability at varying Bi/Sb ratios, Composition-property vs self-powered photodetection study
Cu_2SbI_5	Low-bias photodetection study, synthesis under ambient conditions

7.2 Comparative Analysis of Thin Film Synthesis

Table 7.2 Comparative analysis of thin film synthesis

Material	Precursor Composition	Deposition Method	Iodization Method	Key Features
$Cs_3Sb_2I_9$	Sb_2S_3 + CsCl + I_2	CBD + Spin-coating/Drop-casting	Conventional heating	Simple process, phase-pure formation
$AgSb_2I_7$	Sb_2S_3 + Ag + I_2	CBD + Thermal evaporation	Conventional & microwave heating	Enhanced crystallinity, compact morphology
Mixed-Alloy Rudorffite $Ag(Bi,Sb)_2I_7$	$(Bi,Sb)_2S_3$ + Ag + I_2	CBD + Thermal evaporation/CBD	Conventional heating	Formation of ternary perovskite structures
Cu_2SbI_5	Sb_2S_3 + Cu + I_2	CBD + Thermal evaporation	Conventional heating	Alternative metal iodide compound

7.3 Comparative Structural Analysis of $Cs_3Sb_2I_9$, $AgSb_2I_7$, Mixed-Alloy Rudorffite, and Cu_2SbI_5 Thin Films

Understanding the structural properties of these materials is crucial for evaluating their potential applications in optoelectronics and energy conversion. This section presents a comparative analysis of the crystal structures, space groups, and internal arrangements of $Cs_3Sb_2I_9$, $AgSb_2I_7$, mixed-alloy Rudorffite, and Cu_2SbI_5 thin films.

1. $Cs_3Sb_2I_9$ – 0D Hexagonal Perovskite ($P6_3/mmc$)

$Cs_3Sb_2I_9$ adopts a hexagonal lattice with a zero-dimensional structure composed of isolated Sb_2I_9 bioctahedra. Cesium ions occupy interstitial sites without contributing to a connected octahedral network. This molecular configuration restricts charge mobility, distinguishing it from materials with extended frameworks like $AgSb_2I_7$ or Cu_2SbI_5.

2. $AgSb_2I_7$ – 3D Cubic Rudorffite (Fd3m)

$AgSb_2I_7$ features a fully connected three-dimensional metal-halide lattice characteristic of the Rudorffite family. Both Ag^+ and Sb^{3+} ions are octahedrally coordinated with iodine, enabling isotropic charge transport. Its continuous structure contrasts with the discrete bioctahedra in $Cs_3Sb_2I_9$ and the 1D chains in Sb_2S_3.

3. Mixed-Alloy Rudorffite – Cubic (Fd3m)

This category compositions $Ag(Bi_X,Sb_{1-X})_2I_7$ share the cubic Rudorffite framework with octahedral coordination and 3D connectivity. Cation substitution (Ag, Sb, Bi) tailors properties such as bandgap and lattice strain. Their tunability and structural integrity make them ideal for optoelectronics.

5. Cu_2SbI_5 – Layered Hexagonal Structure

Cu_2SbI_5 forms a layered hexagonal network of interconnected Cu and Sb octahedra. Its structure induces moderate anisotropy in charge transport, more extensive than 0D $Cs_3Sb_2I_9$ yet less isotropic than cubic systems. Compared to 1D Sb_2S_3 (Appendix A), it presents a more cohesive framework.

Table 7.3 Comparison Table of Crystal Structure

Material	Crystal System	Space Group	Structural Features	Advantages over others
$Cs_3Sb_2I_9$	Hexagonal	$P6_3/mmc$	Isolated $[SbI_6]^{3-}$ octahedra	High stability, low recombination losses, but limited transport
$AgSb_2I_7$	Cubic	Fd3m	Fully connected metal-halide network of $[SbI_6]^{3-}$ octahedra	Superior charge transport, lower recombination compared to $Cs_3Sb_2I_9$
Mixed-Alloy Rudorffite	Cubic	Fd3m	Tunable cationic substitution of octahedral network	Similar to $AgSb_2I_7$ but tunable optical properties, defect passivation for improved stability
Cu_2SbI_5	Hexagonal	-	Layered octahedral network	Intermediate anisotropy, Better hole transport, alternative conduction mechanisms to $AgSb_2I_7$

7.4 Comparative Raman Analysis

The Raman spectra of these halide and chalcogenide materials reveal distinct vibrational characteristics that provide insights into their structural and compositional differences. This section compares their Raman-active modes and molecular vibrations to highlight the variations in bonding and lattice dynamics.

$Cs_3Sb_2I_9$: Vibrational Modes and Structural Implications

The Raman spectrum of $Cs_3Sb_2I_9$ exhibits characteristic peaks at 52, 72, 93, 108, 129, 145, 165, and 320 cm^{-1}, consistent with its P63/mmc hexagonal phase. The bending modes at 52 and 73 cm^{-1} correspond to low-energy lattice vibrations, while the bridge Sb-I stretching modes at 93 and 108 cm^{-1} suggest significant octahedral connectivity. The terminal Sb-I stretching vibrations appear at higher wavenumbers (129, 145, and 165 cm^{-1}), indicating stronger bonding interactions along the axial direction of the octahedra. These modes contribute to its relatively stable structure but result in a higher exciton binding energy compared to 3D perovskites.

$AgSb_2I_7$: Vibrational Behavior and Iodine Incorporation

The Raman spectrum of $AgSb_2I_7$ reveals peaks at 63, 87, 104, 118, 134, and 141 cm^{-1}. These peaks are primarily influenced by the presence of SbI_3 and AgI vibrations, suggesting a partial retention of molecular Sb-I bonding characteristics even in the cubic phase. Unlike $Cs_3Sb_2I_9$, which has well-defined terminal and bridging vibrations, the peaks of $AgSb_2I_7$ indicate a more uniform lattice vibration distribution, attributed to its cubic crystal structure. This feature enhances charge transport compared to $Cs_3Sb_2I_9$ but may result in increased defect states.

Mixed-Alloy Rudorffite: Broad Vibrational Range

$Ag(Bi,Sb)_2I_7$ exhibits a diverse Raman spectrum with peaks at 48, 67, 103, 137, 160, 228, 270, 313, and 403 cm^{-1}. The wide range of vibrational modes suggests a complex interaction of multiple cations in the lattice, leading to tunable optical and electronic properties. The presence of high-frequency peaks (228 cm^{-1} and above) implies stronger bonding interactions compared to $Cs_3Sb_2I_9$ and $AgSb_2I_7$. This broad spectrum indicates improved vibrational stability, which can contribute to enhanced defect passivation and longer carrier lifetimes.

Cu_2SbI_5: Distinct Molecular Vibrations

Cu_2SbI_5 thin films exhibit Raman peaks at 50, 84, 110, 150, and 218 cm^{-1}. The presence of lower-wavenumber peaks suggests strong lattice vibrations, while the peak at 218 cm^{-1} is

indicative of Sb-I stretching in a more anisotropic environment. Compared to $AgSb_2I_7$, Cu_2SbI_5 has fewer Raman-active modes, likely due to the simpler coordination environment of Sb and Cu. The strong 50 cm^{-1} peak aligns closely with lattice vibrations seen in $Cs_3Sb_2I_9$, while the higher-frequency modes show similarities to mixed-alloy Rudorffite structures, indicating partial structural overlap.

Table 7.4 Raman Spectral Comparison

Material	Characteristic Raman Peaks (cm^{-1})	Vibrational Assignments	Structural Implications
$Cs_3Sb_2I_9$	52, 72, 93, 108, 129, 145, 165, 320	Bending modes, bridge Sb-I stretching, terminal Sb-I stretching	Well-defined octahedral vibrations, stable but high exciton binding energy
$AgSb_2I_7$	63, 87, 104, 118, 134, 141	SbI_3 and AgI contributions, lattice vibrations	Uniform lattice vibration, enhanced charge transport but potential defect states
Mixed-Alloy Rudorffite	48, 67, 103, 137, 160, 228, 270, 313, 403	Lattice and molecular vibrational interactions	Broad vibrational stability, tunable properties, improved defect passivation
Cu_2SbI_5	50, 84, 110, 150, 218	Strong lattice vibrations, Sb-I stretching	Fewer Raman-active modes, anisotropic structure, efficient charge transport

7.5 Comparison of bandgap

The band gaps of $Cs_3Sb_2I_9$, $AgSb_2I_7$, Bi-alloyed Sb_2S_3, $Ag(Bi,Sb)_2I_7$, and Cu_2SbI_5 exhibit a wide range, from 1.35 eV to 2.2 eV, offering distinct advantages for various optoelectronic applications. $Cs_3Sb_2I_9$ thin films, with band gaps of approximately 1.6–1.7 eV depending on the deposition method, demonstrate semiconducting behavior similar to that of hybrid perovskites, making them suitable for photovoltaic and photodetector applications. The variation in band gap between drop-casted and spin-coated films suggests a strong dependence on film morphology and crystallinity. In comparison, $AgSb_2I_7$ has a wider band gap of 2.0–2.2 eV, which is advantageous for high-energy photon detection, such as in ultraviolet photodetectors. This material's layered structure and strong ionic bonding contribute to its higher band gap and stability. The Bi-alloyed Sb_2S_3 system (Appendix A) presents a tunable band gap ranging from 1.35 eV (pure Bi_2S_3) to 1.87 eV (pure Sb_2S_3),

with intermediate alloys exhibiting values around 1.64–1.75 eV. The gradual reduction in band gap with increasing Bi content is attributed to changes in crystal symmetry and electronic structure, providing a level of control beneficial for solar cell optimization. Similarly, the mixed alloy rudorffite $Ag(Bi,Sb)_2I_7$ system exhibits a decreasing band gap trend with increasing Bi content, from 2.02 eV (25% Bi) to 1.93 eV (100% Bi), indicating that Bi incorporation systematically alters the material's optoelectronic properties. The ability to tune the band gap by adjusting Bi/Sb ratios enables greater versatility in device applications. Cu_2SbI_5, with a band gap of 2.2 eV, represents the widest among these materials and is particularly suited for high-energy applications such as radiation detection and UV-sensitive photodetectors. Despite differences in composition, these materials share key similarities, including their potential for lead-free, stable, and tunable electronic structures. The main advantage of Bi and Sb alloying lies in band gap modulation, allowing fine control over absorption characteristics. While $Cs_3Sb_2I_9$ and $Ag(Bi,Sb)_2I_7$ offer tunable band gaps for optimized solar absorption, $AgSb_2I_7$ and Cu_2SbI_5 stand out for their wider band gaps, favoring high-energy detection applications. The comparative study underscores the role of synthesis methods and alloying strategies in tailoring material properties, demonstrating that subtle changes in composition and processing can lead to significant modifications in optoelectronic performance.

Table 7.5 Comparison Table- bandgap

Material	**Band Gap (eV)**	**Internal Structure Overview**
$Cs_3Sb_2I_9$	1.6–1.7	Narrow band gap, variation in morphology due to different synthesis methods (spin-coating vs drop-casting). Semiconducting.
$AgSb_2I_7$ (Silver Antimony Iodide)	2.0–2.2	Wide band gap, layered structure with strong ionic bonds, suitable for optoelectronic devices like photodetectors.
Bi-alloyed Sb_2S_3 (Appendix A)	1.35–1.87	Alloying with Bi reduces the band gap; alloyed films offer tunability for solar cell applications.

$Ag(Bi,Sb)_2I_7$ (Mixed Alloy Rudorffite)	1.93–2.02	Gradual decrease in band gap as Bi content increases, shift toward more metallic behavior, tunable for optoelectronic applications.
Cu_2SbI_5 (Copper Antimony Iodide)	2.2	Simple crystal structure, wide band gap, useful for radiation detection and photodetectors.

7.6 Comparative Analysis of Lead-Free Halide and Chalcogenide Photodetectors: Structural Modifications, Charge Transport, and Performance Optimization

The systematic investigation of lead-free antimony- and bismuth-based halides and chalcogenides for photodetection applications has provided valuable insights into their structural, optical, and electronic properties. The motivation for this research stems from the urgent need to develop non-toxic, stable, and efficient alternatives to lead-based perovskites while optimizing self-powered photodetection. By studying multiple compositions, including $Cs_3Sb_2I_9$, $AgSb_2I_7$, Bi-alloyed Sb_2S_3, $Ag(Bi,Sb)_2I_7$, and Cu_2SbI_5, this work explores how structural modifications, cation substitution, and interface engineering influence charge transport mechanisms, bandgap tuning, and overall device performance.

One of the most significant findings of this study is the ability of certain antimony-based halides to exhibit intrinsic photoconduction at zero bias. The observation of self-powered photodetection in $Cs_3Sb_2I_9$ and $AgSb_2I_7$ suggests that these materials possess built-in electric fields or defect-assisted charge transport pathways that facilitate efficient carrier separation. This phenomenon is particularly advantageous for low-power photodetector applications, where eliminating the need for an external bias can significantly enhance energy efficiency. Furthermore, $AgSb_2I_7$ demonstrated improved device performance upon the incorporation of CuI as a hole transport layer, emphasizing the critical role of interfacial engineering in optimizing charge extraction and reducing recombination losses. These results align with the broader understanding in literature that modifying interfaces can enhance stability and efficiency, making halide-based photodetectors more viable for long-term applications.

In addition to halide-based materials, this research investigated the effects of Bi-Sb alloying (Appendix A) in Sb_2S_3-based chalcogenide thin films. By systematically varying the Bi/Sb ratio, a clear trend was observed, wherein Bi-rich compositions exhibited lower bandgaps, enhanced absorption, and improved detectivity. However, this enhancement came with certain trade-offs, particularly in terms of response stability, suggesting that an optimal Bi/Sb ratio must be maintained to balance absorption efficiency and charge carrier transport. Among the studied compositions, $(Bi_{0.5}Sb_{0.5})_2S_3$ demonstrated the most consistent photodetection performance, highlighting the importance of compositionally engineered semiconductors in optimizing photodetector response.

The exploration of mixed alloy rudorffites, particularly $Ag(Bi,Sb)_2I_7$, further demonstrated the tunability of electronic properties by varying the Bi content. The ability to modulate the bandgap and charge transport characteristics through controlled Bi incorporation suggests that mixed alloying strategies offer a promising pathway for improving material stability while maintaining favorable optoelectronic properties. This tunability is crucial for tailoring photodetector response across different wavelength ranges, making these materials adaptable for specific applications.

Unlike the other materials investigated, Cu_2SbI_5 required an external bias for effective charge extraction, indicating that its charge transport properties are less conducive to self-powered detection. However, its high absorption coefficient and strong optical response suggest potential utility in high-energy photon detection applications. The necessity of an applied bias in Cu_2SbI_5-based devices reinforces the idea that charge transport limitations must be addressed through either doping strategies or interfacial modifications to enhance carrier mobility.

Table 7.6 Comparative Table of Photodetector Performance

Material	Operating Condition	Advantage	Limitation	Comparison with Reported Works
$Cs_3Sb_2I_9$	0V	Self-powered photoconduction due to ferroelectricity	Limited spectral response range	Similar to other ferroelectric perovskite-like materials that enhance charge separation
$AgSb_2I_7$	0V	Photoconduction observed, enhanced by CuI HTL	Performance dependent on interface engineering	Matches reports where heterojunctions improve transport efficiency
Bi-alloyed Sb_2S_3 (Appendix A)	5V	Tunable properties for sensitivity and stability	Response stability varies with composition	Compared to Sb_2S_3/Bi_2S_3 devices, alloying balances absorption and charge transport
$Ag(Bi,Sb)_2I_7$	0V	Tunable photodetection based on composition	Requires precise control of Bi/Sb ratio	Similar trends reported in mixed halide perovskites where cation substitution modifies response
Cu_2SbI_5	Requires small bias (0.05 V)	Suitable for high-energy photon detection	Not completely self-powered	Matches reports on Cu-based iodides requiring bias-assisted charge extraction

Overall, this research provides a comprehensive comparative analysis of lead-free materials for photodetection, highlighting the key correlations between crystal structure, bandgap, charge transport efficiency, and device performance. The results demonstrate that self-powered photodetection is achievable in specific antimony-based halides, while alloying and interfacial engineering present effective strategies for optimizing both halide and chalcogenide systems. The insights gained from this study contribute to the fundamental understanding of structure-property relationships in emerging optoelectronic materials and offer valuable design principles for the next generation of lead-free photodetectors.

7.7 Outlook

This research paves the way for the development of lead-free antimony-based photodetectors with enhanced efficiency, stability, and environmental sustainability. Future work will build upon the findings of this study by focusing on several key areas:

1. **Material Optimization and Scalability**: While the materials investigated in this study show promising photodetection properties, further optimization in terms of their synthesis and processing conditions is essential for large-scale production. Investigating alternative processing techniques, such as low-temperature deposition methods, could lead to better control over material morphology and performance.

2. **Advanced Device Fabrication**: Beyond material synthesis, further exploration into device architecture, including the optimization of electrode interfaces, will be crucial for improving the overall device efficiency and response time. Hybrid device configurations incorporating these antimony-based materials with complementary materials could enable broader applications, such as multi-spectral detection or high-speed photodetection.

3. **Exploration of Other Lead-Free Systems**: The scope of this research could be expanded by incorporating other lead-free semiconductors that exhibit promising optoelectronic properties, such as tin-based perovskites or other antimony alloys. These materials may further push the boundaries of photodetector performance, especially in terms of spectral range and sensitivity.

4. **Real-World Application Testing**: To demonstrate the practical viability of these materials, long-term stability and performance under real-world conditions must be tested. This includes exposure to various environmental factors, such as humidity, temperature, and UV light, to ensure reliable operation over extended periods.

5. **Integration with Emerging Technologies**: As the demand for self-powered and energy-efficient devices increases, these lead-free materials could find applications in fields beyond photodetection, such as wearable electronics, environmental monitoring, and smart sensors. Investigating their potential in these emerging technologies will help to maximize their impact.

References

[1] T. Haggren, H.H. Tan, C. Jagadish, III-V Thin Films for Flexible, Cost-Effective, and Emerging Applications in Optoelectronics and Photonics, Accounts Mater. Res. 4 (2023) 1046–1056. https://doi.org/10.1021/accountsmr.3c00138.

[2] F. Xia, T. Mueller, Y.M. Lin, A. Valdes-Garcia, P. Avouris, Ultrafast graphene photodetector, Nat. Nanotechnol. 4 (2009) 839–843. https://doi.org/10.1038/nnano.2009.292.

[3] F. Cao, X. Deng, X. Liu, L. Su, E. Hong, L. Wu, X. Fang, Photoimaging with Color-Sensing Abilities by Tuning the Band Gap of a Single-Crystal Lead-Free Perovskite, ACS Appl. Mater. Interfaces. 15 (2023) 28158–28165. https://doi.org/10.1021/acsami.3c03454.

[4] C.Z.N. Peidong Yang, L. Dou, P. Yang, Bandgap engineering in semiconductor alloy nanomaterials with widely tunable compositions, Nat. Rev. Mater. 2 (2017) 1–15. https://doi.org/10.1038/natrevmats.2017.70.

[5] H.J. Snaith, R. Humphry-Baker, P. Chen, I. Cesar, S.M. Zakeeruddin, M. Grätzel, Charge collection and pore filling in solid-state dye-sensitized solar cells, Nanotechnology. 19 (2008). https://doi.org/10.1088/0957-4484/19/42/424003.

[6] T.M. Schmidt, T.T. Larsen-Olsen, J.E. Carlé, D. Angmo, F.C. Krebs, Upscaling of Perovskite Solar Cells: Fully Ambient Roll Processing of Flexible Perovskite Solar Cells with Printed Back Electrodes, Adv. Energy Mater. 5 (2015) 1–9. https://doi.org/10.1002/aenm.201500569.

[7] K. Domanski, W. Tress, T. Moehl, M. Saliba, M.K. Nazeeruddin, M. Grätzel, Working Principles of Perovskite Photodetectors: Analyzing the Interplay between Photoconductivity and Voltage-Driven Energy-Level Alignment, Adv. Funct. Mater. 25 (2015) 6936–6947. https://doi.org/10.1002/adfm.201503188.

[8] S. Klassen, The Photoelectric Effect: Reconstructing the Story for the Physics Classroom, Sci. Educ. 20 (2011) 719–731. https://doi.org/10.1007/s11191-009-9214-6.

[9] S. Few, J.M. Frost, J. Nelson, Models of charge pair generation in organic solar cells, Phys. Chem. Chem. Phys. 17 (2015) 2311–2325. https://doi.org/10.1039/c4cp03663h.

[10] P. Tyagi, S.M. Arveson, W.A. Tisdale, Colloidal Organohalide Perovskite Nanoplatelets Exhibiting Quantum Confinement, J. Phys. Chem. Lett. 6 (2015) 1911–1916. https://doi.org/10.1021/acs.jpclett.5b00664.

[11] L. Dou, Y.M. Yang, J. You, Z. Hong, W.H. Chang, G. Li, Y. Yang, Solution-processed hybrid perovskite photodetectors with high detectivity, Nat. Commun. 5 (2014). https://doi.org/10.1038/ncomms6404.

[12] D. Li, G. Dong, W. Li, L. Wang, High performance organic-inorganic perovskite-optocoupler based on low-voltage and fast response perovskite compound photodetector, Sci. Rep. 5 (2015) 1–6. https://doi.org/10.1038/srep07902.

[13] Y. Fang, Q. Dong, Y. Shao, Y. Yuan, J. Huang, Highly narrowband perovskite single-crystal photodetectors enabled by surface-charge recombination, Nat. Photonics. 9 (2015) 679–686. https://doi.org/10.1038/nphoton.2015.156.

[14] Y. Fang, J. Huang, Resolving weak light of sub-picowatt per square centimeter by hybrid perovskite photodetectors enabled by noise reduction, Adv. Mater. 27 (2015) 2804–2810. https://doi.org/10.1002/adma.201500099.

[15] Z. Wang, R. Yu, C. Pan, Z. Li, J. Yang, F. Yi, Z.L. Wang, Light-induced pyroelectric effect as an

effective approach for ultrafast ultraviolet nanosensing, Nat. Commun. 6 (2015) 1–7. https://doi.org/10.1038/ncomms9401.

[16] E. Shi, H. Li, L. Yang, L. Zhang, Z. Li, P. Li, Y. Shang, S. Wu, X. Li, J. Wei, K. Wang, H. Zhu, D. Wu, Y. Fang, A. Cao, Colloidal Antire fl ection Coating Improves Graphene − Silicon Solar Cells, (2013) 0–5.

[17] W. Cao, J. Xue, Recent progress in organic photovoltaics: Device architecture and optical design, Energy Environ. Sci. 7 (2014) 2123–2144. https://doi.org/10.1039/c4ee00260a.

[18] R. Dewan, D. Knipp, Light trapping in thin-film silicon solar cells with integrated diffraction grating, J. Appl. Phys. 106 (2009) 23058–23065. https://doi.org/10.1063/1.3232236.

[19] D. Luo, X. Li, A. Dumont, H. Yu, Z.H. Lu, Recent Progress on Perovskite Surfaces and Interfaces in Optoelectronic Devices, Adv. Mater. 33 (2021) 1–24. https://doi.org/10.1002/adma.202006004.

[20] T.H. Han, S. Tan, J. Xue, L. Meng, J.W. Lee, Y. Yang, Interface and Defect Engineering for Metal Halide Perovskite Optoelectronic Devices, Adv. Mater. 31 (2019) 1–35. https://doi.org/10.1002/adma.201803515.

[21] Q. Lu, Z. Yang, X. Meng, Y. Yue, M.A. Ahmad, W. Zhang, S. Zhang, Y. Zhang, Z. Liu, W. Chen, A Review on Encapsulation Technology from Organic Light Emitting Diodes to Organic and Perovskite Solar Cells, Adv. Funct. Mater. 31 (2021) 1–41. https://doi.org/10.1002/adfm.202100151.

[22] P. Gao, D. Konrad, S. Aghazada, M.K. Nazeeruddin, Molecular engineering of functional materials for energy and opto-electronic applications, Chimia (Aarau). 69 (2015) 253–263. https://doi.org/10.2533/chimia.2015.253.

[23] G. Li, Y. Wang, L. Huang, W. Sun, Research Progress of High-Sensitivity Perovskite Photodetectors: A Review of Photodetectors: Noise, Structure, and Materials, ACS Appl. Electron. Mater. 4 (2022) 1485–1505. https://doi.org/10.1021/acsaelm.1c01349.

[24] L.B. Luo, G.A. Wu, Y. Gao, L. Liang, C. Xie, Z.X. Zhang, X.W. Tong, T. Wang, F.X. Liang, A Highly Sensitive Perovskite/Organic Semiconductor Heterojunction Phototransistor and Its Device Optimization Utilizing the Selective Electron Trapping Effect, Adv. Opt. Mater. 7 (2019) 1–11. https://doi.org/10.1002/adom.201900272.

[25] L.D. Yuan, H.X. Deng, S.S. Li, S.H. Wei, J.W. Luo, Unified theory of direct or indirect band-gap nature of conventional semiconductors, Phys. Rev. B. 98 (2018) 1–10. https://doi.org/10.1103/PhysRevB.98.245203.

[26] P.K. Samanta, Band gap engineering, quantum confinement, defect mediated broadband visible photoluminescence and associated quantum States of size tuned zinc oxide nanostructures, Optik (Stuttg). 221 (2020) 165337. https://doi.org/10.1016/j.ijleo.2020.165337.

[27] L. Tao, Z. Chen, Z. Li, J. Wang, X. Xu, J. Bin Xu, Enhancing light-matter interaction in 2D materials by optical micro/nano architectures for high-performance optoelectronic devices, InfoMat. 3 (2021) 36–60. https://doi.org/10.1002/inf2.12148.

[28] Y. Chen, H. Liu, G. Yu, C. Ma, Z. Xu, J. Zhang, C. Zhang, M. Chen, D. Li, W. Zheng, Z. Luo, X. Yang, K. Li, C. Yao, D. Zhang, B. Xu, J. Yi, C. Yi, B. Li, H. Zhang, Z. Zhang, X. Zhu, S. Li, S. Chen, Y. Jiang, A. Pan, Defect Engineering of 2D Semiconductors for Dual Control of Emission and Carrier Polarity, Adv. Mater. 36 (2024) 22–26. https://doi.org/10.1002/adma.202312425.

[29] P.E. Janolin, A.S. Anokhin, Z. Gui, V.M. Mukhortov, Y.I. Golovko, N. Guiblin, S. Ravy, M. El Marssi, Y.I. Yuzyuk, L. Bellaiche, B. Dkhil, Strain engineering of perovskite thin films using a single substrate, J. Phys. Condens. Matter. 26 (2014). https://doi.org/10.1088/0953-8984/26/29/292201.

[30] Y.C. Choi, K.W. Jung, Recent progress in fabrication of antimony/bismuth chalcohalides for lead-free solar cell applications, Nanomaterials. 10 (2020) 1–15. https://doi.org/10.3390/nano10112284.

[31] J. Zhou, F. Zhao, J. Shen, Y. Zhou, Y. Wu, Y. Guo, J. Jiang, J. Chu, Inorganic lead-free antimony-based perovskite-inspired solar cells with a carbon electrode and green anti-solvent regulation, J. Mater. Chem. C. 9 (2021) 15301–15308. https://doi.org/10.1039/d1tc03885k.

[32] S. Perera, H. Hui, C. Zhao, H. Xue, F. Sun, C. Deng, N. Gross, C. Milleville, X. Xu, D.F. Watson, B. Weinstein, Y.Y. Sun, S. Zhang, H. Zeng, Chalcogenide perovskites - an emerging class of ionic semiconductors, Nano Energy. 22 (2016) 129–135. https://doi.org/10.1016/j.nanoen.2016.02.020.

[33] S.F. Hoefler, G. Trimmel, T. Rath, Progress on lead-free metal halide perovskites for photovoltaic applications: a review, Monatshefte Fur Chemie. 148 (2017) 795–826. https://doi.org/10.1007/s00706-017-1933-9.

[34] M.G. Ju, J. Dai, L. Ma, X.C. Zeng, Lead-Free Mixed Tin and Germanium Perovskites for Photovoltaic Application, J. Am. Chem. Soc. 139 (2017) 8038–8043. https://doi.org/10.1021/jacs.7b04219.

[35] C.C. Stoumpos, M.G. Kanatzidis, Halide Perovskites: Poor Man's High-Performance Semiconductors, Adv. Mater. 28 (2016) 5778–5793. https://doi.org/10.1002/adma.201600265.

[36] B. Chen, R. Chen, B. Huang, Strong Electron–Phonon Coupling Induced Self-Trapped Excitons in Double Halide Perovskites, Adv. Energy Sustain. Res. 4 (2023). https://doi.org/10.1002/aesr.202300018.

[37] M. Lyu, J.H. Yun, P. Chen, M. Hao, L. Wang, Addressing Toxicity of Lead: Progress and Applications of Low-Toxic Metal Halide Perovskites and Their Derivatives, Adv. Energy Mater. 7 (2017). https://doi.org/10.1002/aenm.201602512.

[38] G. Volonakis, M.R. Filip, A.A. Haghighirad, N. Sakai, B. Wenger, H.J. Snaith, F. Giustino, Lead-Free Halide Double Perovskites via Heterovalent Substitution of Noble Metals, J. Phys. Chem. Lett. 7 (2016) 1254–1259. https://doi.org/10.1021/acs.jpclett.6b00376.

[39] A.H. Slavney, T. Hu, A.M. Lindenberg, H.I. Karunadasa, A Bismuth-Halide Double Perovskite with Long Carrier Recombination Lifetime for Photovoltaic Applications, J. Am. Chem. Soc. 138 (2016) 2138–2141. https://doi.org/10.1021/jacs.5b13294.

[40] R. Nie, R.R. Sumukam, S.H. Reddy, M. Banavoth, S. Il Seok, Lead-free perovskite solar cells enabled by hetero-valent substitutes, Energy Environ. Sci. 13 (2020) 2363–2385. https://doi.org/10.1039/d0ee01153c.

[41] Y. Bekenstein, B.A. Koscher, S.W. Eaton, P. Yang, A.P. Alivisatos, Highly Luminescent Colloidal Nanoplates of Perovskite Cesium Lead Halide and Their Oriented Assemblies, J. Am. Chem. Soc. 137 (2015) 16008–16011. https://doi.org/10.1021/jacs.5b11199.

[42] S. Tao, I. Schmidt, G. Brocks, J. Jiang, I. Tranca, K. Meerholz, S. Olthof, Absolute energy level positions in tin- and lead-based halide perovskites, Nat. Commun. 10 (2019) 1–10. https://doi.org/10.1038/s41467-019-10468-7.

[43] Z. Jin, Z. Zhang, J. Xiu, H. Song, T. Gatti, Z. He, A critical review on bismuth and antimony halide based perovskites and their derivatives for photovoltaic applications: Recent advances and challenges, J. Mater. Chem. A. 8 (2020) 16166–16188. https://doi.org/10.1039/d0ta05433j.

[44] A. Chakraborty, N. Pai, J. Zhao, B.R. Tuttle, A.N. Simonov, V. Pecunia, Rudorffites and Beyond : Perovskite-Inspired Silver / Copper Pnictohalides for Next-Generation Environmentally Friendly Photovoltaics and Optoelectronics, Adv. Funct. Mater. 32 (2022) 2203300. https://doi.org/10.1002/adfm.202203300.

[45] A. Okada, K. Keil, Caswellsilverite, NaCrS2: a new mineral in the Norton County enstatite achondrite., Am. Mineral. 67 (1982) 132–136.

[46] I. Ganesh, A review on magnesium aluminate (MgAl2O4) spinel: Synthesis, processing and applications, Int. Mater. Rev. 58 (2013) 63–112. https://doi.org/10.1179/1743280412Y.0000000001.

[47] B. Saparov, F. Hong, J.P. Sun, H.S. Duan, W. Meng, S. Cameron, I.G. Hill, Y. Yan, D.B. Mitzi, Thin-Film Preparation and Characterization of Cs3Sb2I9: A Lead-Free Layered Perovskite Semiconductor, Chem. Mater. 27 (2015) 5622–5632. https://doi.org/10.1021/acs.chemmater.5b01989.

[48] X. Jia, L. Ding, A low-temperature solution-processed copper antimony iodide rudorffite for solar cells, Sci. China Mater. 62 (2019) 54–58. https://doi.org/10.1007/s40843-018-9300-6.

[49] Y.N. Ivanov, a a Sukhovskii, V. V Lisin, I.P. Aleksandrova, Phase Transitions of Cs 3 Sb 2 I 9 , Cs 3 Bi 2 I 9 , and Cs 3 Bi 2 Br 9 Crystals, Inorg. Mater. 37 (2001) 739–743.

[50] V.P.V. Sasidharan, M.U.R. Hernandez, S. Shaji, D.A. Avellaneda, S.K. Chandran, M.G. Méndez, B. Krishnan, Cesium antimony iodide perovskite thin films by rapid iodization of Sb2S3-CsCl precursor under ambient conditions, J. Alloys Compd. 972 (2024) 172870. https://doi.org/10.1016/j.jallcom.2023.172870.

[51] Z. Jin, Z. Zhang, J. Xiu, H. Song, T. Gatti, Z. He, A critical review on bismuth and antimony halide based perovskites and their derivatives for photovoltaic applications: Recent advances and challenges, J. Mater. Chem. A. 8 (2020) 16166–16188. https://doi.org/10.1039/d0ta05433j.

[52] S. Berri, Theoretical analysis of the structural, electronic, optical and thermodynamic properties of trigonal and hexagonal Cs3Sb2I9 compound, Eur. Phys. J. B. 93 (2020) 1–12. https://doi.org/10.1140/epjb/e2020-10143-1.

[53] Y. Peng, F. Li, Y. Wang, Y. Li, R.L.Z. Hoye, L. Feng, K. Xia, V. Pecunia, Enhanced photoconversion efficiency in cesium-antimony-halide perovskite derivatives by tuning crystallographic dimensionality, Appl. Mater. Today. 19 (2020) 21–23. https://doi.org/10.1016/j.apmt.2020.100637.

[54] M. Wang, W. Wang, B. Ma, W. Shen, L. Liu, K. Cao, S. Chen, W. Huang, Lead-Free Perovskite Materials for Solar Cells, Springer Singapore, 2021. https://doi.org/10.1007/s40820-020-00578-z.

[55] N.K. Vishnoi, A review on perovskite solar cells, Asian J. Multidimens. Res. 10 (2021) 365–370. https://doi.org/10.5958/2278-4853.2021.01106.x.

[56] F. Umar, J. Zhang, Z. Jin, I. Muhammad, X. Yang, H. Deng, K. Jahangeer, Q. Hu, H. Song, J. Tang, Dimensionality Controlling of Cs 3 Sb 2 I 9 for Efficient All-Inorganic Planar Thin Film Solar Cells by HCl-Assisted Solution Method, Adv. Opt. Mater. 7 (2019) 1–9.

https://doi.org/10.1002/adom.201801368.

[57] S.K. Shil, F. Wang, Z. Lai, Y. Meng, Y. Wang, D. Zhao, M.K. Hossain, K.O. Egbo, Y. Wang, K.M. Yu, J.C. Ho, Crystalline all-inorganic lead-free Cs3Sb2I9 perovskite microplates with ultra-fast photoconductive response and robust thermal stability, Nano Res. 14 (2021) 4116–4124. https://doi.org/10.1007/s12274-021-3351-x.

[58] J. Pal, S. Manna, A. Mondal, S. Das, K. V. Adarsh, A. Nag, Colloidal Synthesis and Photophysics of M 3 Sb 2 I 9 (M=Cs and Rb) Nanocrystals: Lead-Free Perovskites , Angew. Chemie. 129 (2017) 14375–14379. https://doi.org/10.1002/ange.201709040.

[59] T.D. Chonamada, A.B. Dey, P.K. Santra, Degradation Studies of Cs3Sb2I9: A Lead-Free Perovskite, ACS Appl. Energy Mater. 3 (2020) 47–55. https://doi.org/10.1021/acsaem.9b01899.

[60] S. Paramanik, A. Maiti, S. Chatterjee, A.J. Pal, Large Resistive Switching and Artificial Synaptic Behaviors in Layered Cs3Sb2I9 Lead-Free Perovskite Memory Devices, Adv. Electron. Mater. 8 (2022) 1–10. https://doi.org/10.1002/aelm.202100237.

[61] A. Singh, N.C. Chiu, K.M. Boopathi, Y.J. Lu, A. Mohapatra, G. Li, Y.F. Chen, T.F. Guo, C.W. Chu, Lead-Free Antimony-Based Light-Emitting Diodes through the Vapor-Anion-Exchange Method, ACS Appl. Mater. Interfaces. 11 (2019) 35088–35094. https://doi.org/10.1021/acsami.9b10602.

[62] Z. Lai, Y. Meng, F. Wang, X. Bu, D. Chen, P. Xie, W. Wang, D. Li, Y. Zhang, W. Wang, C. Liu, S.P. Yip, J.C. Ho, PDMS-Assisted Low-Temperature Synthesis of Submillimeter All-Inorganic Halide Perovskite Microcrystals for High-Performance Photodetectors, Adv. Opt. Mater. 10 (2022) 2201127. https://doi.org/10.1002/ADOM.202201127.

[63] Z. Xiao, W. Meng, D.B. Mitzi, Y. Yan, Crystal Structure of AgBi2I7 Thin Films, J. Phys. Chem. Lett. 7 (2016) 3903–3907. https://doi.org/10.1021/acs.jpclett.6b01834.

[64] H. Zhu, A. Erbing, H. Wu, G.J. Man, S. Mukherjee, C. Kamal, M.B. Johansson, H. Rensmo, M. Odelius, E.M.J. Johansson, Tuning the Bandgap in Silver Bismuth Iodide Materials by Partly Substituting Bismuth with Antimony for Improved Solar Cell Performance, ACS Appl. Energy Mater. 3 (2020) 7372–7382. https://doi.org/10.1021/acsaem.0c00712.

[65] M.B. Gray, E.T. McClure, N.P. Holzapfel, F.P. Evaristo, W. Windl, P.M. Woodward, Exploring the AgSb1−xBixI4 phase diagram: Thermochromism in layered CdCl2-type semiconductors, J. Solid State Chem. 297 (2021) 1–7. https://doi.org/10.1016/j.jssc.2021.121997.

[66] F. Iyoda, R. Nishikubo, A. Wakamiya, A. Saeki, Ag-(Bi, Sb, In, Ga)-I Solar Cells: Impacts of Elemental Composition and Additives on the Charge Carrier Dynamics and Crystal Structures, ACS Appl. Energy Mater. 3 (2020) 8224–8232. https://doi.org/10.1021/acsaem.0c00628.

[67] A.A. Ramachandran, B. Krishnan, S. Devasia, D.A. Avellaneda, M.I. Mendivil Palma, J.A. Aguilar Martinez, S. Shaji, Photosensitive antimony triiodide thin films by rapid iodization of chemically deposited antimony sulfide, Mater. Res. Bull. 142 (2021) 111382. https://doi.org/10.1016/j.materresbull.2021.111382.

[68] M.D. Prasad, M.G. Krishna, S.K. Batabyal, Silver Bismuth Iodide Nanomaterials as Lead-Free Perovskite for Visible Light Photodetection, ACS Appl. Nano Mater. 4 (2021) 1252–1259. https://doi.org/10.1021/acsanm.0c02857.

[69] P.H. Fourcroy, D. Carré, F. Thévet, J. Rivet, Structure du tétraiodure de cuivre(I) et de bismuth(III), CuBiI4, Acta Crystallogr. Sect. C Cryst. Struct. Commun. 47 (1991) 2023–2025. https://doi.org/10.1107/s0108270191005309.

[70] A.K. Baranwal, H. Masutani, H. Sugita, H. Kanda, S. Kanaya, N. Shibayama, Y. Sanehira, M. Ikegami, Y. Numata, K. Yamada, T. Miyasaka, T. Umeyama, H. Imahori, S. Ito, Lead-free perovskite solar cells using Sb and Bi-based A3B2X9 and A3BX6 crystals with normal and inverse cell structures, Nano Converg. 4 (2017). https://doi.org/10.1186/s40580-017-0120-3.

[71] A. Adappattu Ramachandran, B. Krishnan, D. Avellaneda Avellaneda, M. Isabel Mendivil Palma, J. Amilcar Aguilar Martinez, S. Shaji, Development of lead-free Cu2BiI5 rudorffite thin films for visible light photodetector application, Appl. Surf. Sci. 564 (2021) 150438. https://doi.org/10.1016/j.apsusc.2021.150438.

[72] R.S. Mane, C.D. Lokhande, Chemical deposition method for metal chalcogenide thin films, Mater. Chem. Phys. 65 (2000) 1–31. https://doi.org/10.1016/S0254-0584(00)00217-0.

[73] H. Ilchuk, P. Shapoval, V. Kusnezh, Chemical Surface Deposition of CdS Ultra Thin Films from Aqueous Solutions, Sol. Cells - Thin-Film Technol. (2011). https://doi.org/10.5772/23495.

[74] S. Gorer, G. Hodes, Quantum size effects in the study of chemical solution deposition mechanisms of semiconductor films, J. Phys. Chem. 98 (1994) 5338–5346. https://doi.org/10.1021/j100071a026.

[75] D.E. Bornside, C.W. Macosko, L.E. Scriven, Spin coating: One - dimensional model □, 5193 (1989) 5185–5193.

[76] D. Meyerhofer, Characteristics of resist films produced by spinning, J. Appl. Phys. 49 (1978) 3993–3997. https://doi.org/10.1063/1.325357.

[77] A.G. Emslie, F.T. Bonner, L.G. Peck, Flow of a viscous liquid on a rotating disk, J. Appl. Phys. 29 (1958) 858–862. https://doi.org/10.1063/1.1723300.

[78] M. Ohring, Thin-Film Evaporation Processes, Mater. Sci. Thin Film. (2002) 95–144. https://doi.org/10.1016/b978-012524975-1/50006-9.

[79] D.M. Mattox, Vacuum Evaporation and Vacuum Deposition, 2010. https://doi.org/10.1016/b978-0-8155-2037-5.00006-x.

[80] D.L. Smith, Thin-film deposition: principles and practice, 1996. https://doi.org/10.5860/choice.33-3347.

[81] E. Atkins, Elements of X-ray Diffraction, 1978. https://doi.org/10.1088/0031-9112/29/12/034.

[82] A.L. Patterson, The scherrer formula for X-ray particle size determination, Phys. Rev. 56 (1939) 978–982. https://doi.org/10.1103/PhysRev.56.978.

[83] C. V. Raman, K.S. Krishnan, A new type of secondary radiation [11], Nature. 121 (1928) 501–502. https://doi.org/10.1038/121501c0.

[84] The Raman effect, 1932.

[85] A. Kochubei, Y. Luchko, J.A.T. Machado, Basic theory, 2019. https://doi.org/10.1515/9783110571622.

[86] E. Smith, G. Dent, Resonance Raman Scattering A pratical Approach, 2019.

[87] M.S. Ummah, Physical Principles of Electron Microscopy, 2019. http://scioteca.caf.com/bitstream/handle/123456789/1091/RED2017-Eng-8ene.pdf?sequence=12&isAllowed=y%0Ahttp://dx.doi.org/10.1016/j.regsciurbeco.2008.06.005%0Ahttps://www.researchgate.net/publication/305320484_SISTEM_PEMBETUNGAN_TERPUSAT_STRATEGI_MELESTARI.

[88] P. Echlin, Handbook of Sample Preparation for Scanning Electron Microscopy and X-Ray Microanalysis, 2009. https://doi.org/10.1007/978-0-387-85731-2.

[89] J.I. Goldstein, D.E. Newbury, J.R. Michael, N.W.M. Ritchie, J.H.J. Scott, D.C. Joy, Trace Analysis by SEM/EDS, 2018. https://doi.org/10.1007/978-1-4939-6676-9_21.

[90] R.K. Vempati, T.R. Hess, D.L. Cocke, X-Ray photoelectron spectroscopy, 2018. https://doi.org/10.2136/sssabookser5.3.c12.

[91] S.A. Chambers, X-ray photoelectron spectroscopy of epitaxial films and heterostructures, Surf. Sci. Rep. 79 (2024) 100638. https://doi.org/10.1016/j.surfrep.2024.100638.

[92] F.A. Stevie, C.L. Donley, Introduction to x-ray photoelectron spectroscopy, J. Vac. Sci. Technol. A Vacuum, Surfaces, Film. 38 (2020). https://doi.org/10.1116/6.0000412.

[93] J.F. Moulder, W.F. Stickle, P.E. Sobol, K.D. Bomben, Handbook of X-ray photoelectron spectroscopy, Perkin-Elmer Corp. (1992) 1–261. https://doi.org/10.1002/0470014229.ch22.

[94] M.S. Ummah, An introduction to surface analysis by XPS and AES, 2019. http://scioteca.caf.com/bitstream/handle/123456789/1091/RED2017-Eng-8ene.pdf?sequence=12&isAllowed=y%0Ahttp://dx.doi.org/10.1016/j.regsciurbeco.2008.06.005%0Ahttps://www.researchgate.net/publication/305320484_SISTEM_PEMBETUNGAN_TERPUSAT_STRATEGI_MELESTARI.

[95] M.Y.P.Y. Cardona, Fundamentals of Semiconductors: Physics and Materials, 2010.

[96] J. Tauc, OPTICAL PROPERTIES AND ELECTRONIC STRUCTURE OF AMORPHOUS Ge AND Si, 34 (1968) 78–86.

[97] B.A. Prew, Physics of Semiconductor Devices, 1975. https://doi.org/10.1088/0031-9112/26/9/031.

[98] MATERIAL AND DEVICE SEMICONDUCTOR MATERIAL AND DEVICE Third Edition, n.d.

[99] G.S. Nolas, H.J. Goldsmid, J. Sharp, J. Goldsmid, Thermoelectrics : basic principles and new materials developments, 2001. http://books.google.com/books?id=ZmnQYgEACAAJ%0Ahttp://swb.bsz-bw.de/DB=2.1/PPN?PPN=322033969%0Ainhaltsverzeichnis: http://swbplus.bsz-bw.de/bsz089954297inh.htm%0Acover: http://swbplus.bsz-bw.de/bsz089954297cov.htm%0Ainhaltstext: https://zbmath.org/?q=an:

[100] S. Devasia, S. Shaji, D.A. Avellaneda, J.A.A. Martinez, B. Krishnan, In situ crystallization of 0D perovskite derivative Cs3Bi2I9 thin films via ultrasonic spray, J. Alloys Compd. 893 (2022) 162294. https://doi.org/10.1016/j.jallcom.2021.162294.

[101] S.T. Thornton, G. Abdelmageed, R.F. Kahwagi, G.I. Koleilat, Progress towards lead-free, efficient, and stable perovskite solar cells, J. Chem. Technol. Biotechnol. 97 (2022) 810–829. https://doi.org/10.1002/jctb.6830.

[102] Y. Hai, W. Huang, Z. Li, D. Wu, Q. Huang, X. Tang, Morphology Regulation and Photocatalytic CO2Reduction of Lead-Free Perovskite Cs3Sb2I9Microcrystals, ACS Appl. Energy Mater. 4 (2021) 5913–5917. https://doi.org/10.1021/acsaem.1c00722.

[103] C. Song, L. Tong, F. Liu, L. Ye, G.J. Cheng, Addressing the Reliability and Electron Transport Kinetics in Halide Perovskite Film via Pulsed Laser Engineering, Adv. Funct. Mater. 30 (2020) 1–10. https://doi.org/10.1002/adfm.201906781.

[104] L. Wu, Z. Dong, L. Zhang, C. Liu, K. Wang, B. Zou, High-Pressure Band-Gap Engineering and

Metallization in the Perovskite Derivative Cs3Sb2I9, ChemSusChem. 12 (2019) 3971–3976. https://doi.org/10.1002/cssc.201901388.

[105] B.W.W. Kyle M. McCall,†‡ Constantinos C. Stoumpos,† Svetlana S. Kostina,‡ Mercouri G. Kanatzidis, Strong Electron–Phonon Coupling and Self-Trapped Excitons in the Defect Halide Perovskites A3M2I9 (A = Cs, Rb; M = Bi, Sb), Chem. Mater. 2017, 29, 9, 4129–4145 Publ. DateApril 26, 2017 Https//Doi.Org/10.1021/Acs.Chemmater.7b01184. 9 (n.d.) 14.

[106] H. Shimizu, Y. Ohbayashi, K. Yamamoto, K. Abe, M. Midorikawa, Y. Ishibashi, Y. Takagi, Second-order Raman spectra of CsCl single crystals, J. Phys. Chem. Solids. 37 (1976) 411–415. https://doi.org/10.1016/0022-3697(76)90022-6.

[107] S. Ullah, P. Yang, J. Wang, L. Liu, Y.Q. Li, F. Zafar, S.E. Yang, T. Xia, H. Guo, Y. Chen, The Fabrication of Lead-Free Cs2SnI6 Perovskite Films Using Iodine-Rich Strategy for Optoelectronic Applications, Phys. Status Solidi Appl. Mater. Sci. 218 (2021) 2100271. https://doi.org/10.1002/pssa.202100271.

[108] B. Krishnan, A. Arato, E. Cardenas, T.K.D. Roy, G.A. Castillo, On the structure, morphology, and optical properties of chemical bath deposited Sb 2 S 3 thin films, Appl. Surf. Sci. 254 (2008) 3200–3206. https://doi.org/10.1016/j.apsusc.2007.10.098.

[109] T.A. Chowdhury, Depth Profile Study of Electroless Deposited Sb 2 S 3 Thin Films Using XPS for Photovoltaic Applications, Mater. Sci. Appl. 14 (2023) 397–406. https://doi.org/10.4236/msa.2023.147025.

[110] A. Singh, K.M. Boopathi, A. Mohapatra, Y.F. Chen, G. Li, C.W. Chu, Photovoltaic Performance of Vapor-Assisted Solution-Processed Layer Polymorph of Cs3Sb2I9, ACS Appl. Mater. Interfaces. 10 (2018) 2566–2573. https://doi.org/10.1021/acsami.7b16349.

[111] J. Tong, Q. Jiang, F. Zhang, S.B. Kang, D.H. Kim, K. Zhu, Wide-Bandgap Metal Halide Perovskites for Tandem Solar Cells, ACS Energy Lett. 6 (2021) 232–248. https://doi.org/10.1021/acsenergylett.0c02105.

[112] J. Mei, M. Liu, P. Vivo, V. Pecunia, Two-Dimensional Antimony-Based Perovskite-Inspired Materials for High-Performance Self-Powered Photodetectors, Adv. Funct. Mater. 31 (2021). https://doi.org/10.1002/adfm.202106295.

[113] S. Devasia, S. Shaji, D.A. Avellaneda, J.A. Aguilar Martinez, B. Krishnan, Ultrasonically sprayed Cs3Bi2I9 thin film based self-powered photodetector, Mater. Chem. Phys. 296 (2023) 127295. https://doi.org/10.1016/j.matchemphys.2023.127295.

[114] Y. Liu, Y. Gao, J. Zhi, R. Huang, W. Li, X. Huang, G. Yan, Z. Ji, All-inorganic lead-free NiO x / Cs 3 Bi 2 Br 9 perovskite heterojunction photodetectors for ultraviolet multispectral imaging, Nano Res. 12 (2021). https://doi.org/https://doi.org/10.1007/s12274-021-3608-4.

[115] D. Liu, B. Bin Yu, M. Liao, Z. Jin, L. Zhou, X. Zhang, F. Wang, H. He, T. Gatti, Z. He, Self-Powered and Broadband Lead-Free Inorganic Perovskite Photodetector with High Stability, ACS Appl. Mater. Interfaces. 12 (2020) 30530–30537. https://doi.org/10.1021/acsami.0c05636.

[116] D. Hao, D. Liu, Y. Shen, Q. Shi, J. Huang, Air-Stable Self-Powered Photodetectors Based on Lead-Free CsBi3I10/SnO2 Heterojunction for Weak Light Detection, Adv. Funct. Mater. 31 (2021) 1–9. https://doi.org/10.1002/adfm.202100773.

[117] C. Perumal Veeramalai, S. Feng, X. Zhang, S.V.N. Pammi, V. Pecunia, C. Li, Lead–halide perovskites for next-generation self-powered photodetectors: a comprehensive review, Photonics Res. 9 (2021) 968. https://doi.org/10.1364/prj.418450.

[118] W. Tian, Y. Wang, L. Chen, L. Li, Self-Powered Nanoscale Photodetectors, Small. 13 (2017) 1–22. https://doi.org/10.1002/smll.201701848.

[119] J.K. Li, C. Ge, K.J. Jin, J.Y. Du, J.T. Yang, H. Bin Lu, G.Z. Yang, Self-driven visible-blind photodetector based on ferroelectric perovskite oxides, Appl. Phys. Lett. 110 (2017) 142901. https://doi.org/10.1063/1.4979587.

[120] M. Chen, X. Shen, C. Zhou, D. Cao, W. Xue, High-performance self-powered visible-blind ultraviolet photodetection achieved by ferroelectric PbZr0.52Ti0.48O3 thin films, J. Alloys Compd. 897 (2022) 163208. https://doi.org/https://doi.org/10.1016/j.jallcom.2021.163208.

[121] N.F. Montcada, M. Méndez, K.T. Cho, M.K. Nazeeruddin, E. Palomares, Photo-induced dynamic processes in perovskite solar cells: The influence of perovskite composition in the charge extraction and the carrier recombination, Nanoscale. 10 (2018) 6155–6158. https://doi.org/10.1039/c8nr00180d.

[122] B. Yang, D. Bogachuk, J. Suo, L. Wagner, H. Kim, J. Lim, A. Hinsch, G. Boschloo, M.K. Nazeeruddin, A. Hagfeldt, Strain effects on halide perovskite solar cells, Chem. Soc. Rev. 51 (2022) 7509–7530. https://doi.org/10.1039/d2cs00278g.

[123] R. Wen, Y. Wang, X. Ma, Y. Yan, Q. Ma, J. Gao, H. Sun, H. Huang, Z. Gao, Reversible Thermochromic Bismuth Iodide Enabled by Self-Adjustment, Adv. Opt. Mater. 11 (2023). https://doi.org/10.1002/adom.202203148.

[124] N.K. Tailor, S. Satapathi, Structural Disorder and Spin Dynamics Study in Millimeter-Sized All-Inorganic Lead-Free Cesium Bismuth Halide Perovskite Single Crystals, ACS Appl. Energy Mater. 3 (2020) 11732–11740. https://doi.org/10.1021/acsaem.0c01849.

[125] I. Caracelli, I. Haiduc, J. Zukerman-Schpector, E.R.T. Tiekink, Delocalised antimony(lone pair)- and bismuth-(lone pair)...π(arene) interactions: Supramolecular assembly and other considerations, Coord. Chem. Rev. 257 (2013) 2863–2879. https://doi.org/10.1016/j.ccr.2013.05.022.

[126] M.T. Islam, M.R. Jani, K.M. Shorowordi, Z. Hoque, A.M. Gokcek, V. Vattipally, S.S. Nishat, S. Ahmed, Numerical simulation studies of Cs3Bi2I9 perovskite solar device with optimal selection of electron and hole transport layers, Optik (Stuttg). 231 (2021) 166417. https://doi.org/10.1016/j.ijleo.2021.166417.

[127] E. Yoo, S.V.N. Pammi, K.Y. Kim, T. Van Dang, J.H. Eom, Y.J. Choi, S.G. Yoon, Strategic extended air stability of organolead halide perovskite nonvolatile memory devices, J. Alloys Compd. 811 (2019) 151999. https://doi.org/10.1016/j.jallcom.2019.151999.

[128] J. Lim, M. Kim, H.H. Park, H. Jung, S. Lim, X. Hao, E. Choi, S. Park, M. Lee, Z. Liu, M.A. Green, J. Seo, J. Park, J.S. Yun, Kinetics of light-induced degradation in semi-transparent perovskite solar cells, Sol. Energy Mater. Sol. Cells. 219 (2021) 110776. https://doi.org/https://doi.org/10.1016/j.solmat.2020.110776.

[129] H. Wang, D.H. Kim, Perovskite-based photodetectors: Materials and devices, Chem. Soc. Rev. 46 (2017) 5204–5236. https://doi.org/10.1039/c6cs00896h.

[130] R. Zhao, K. Zhang, J. Zhu, S. Xiao, W. Xiong, J. Wang, T. Liu, G. Xing, K. Wang, S. Yang, X. Wang, Surface passivation of organometal halide perovskites by atomic layer deposition: An investigation of the mechanism of efficient inverted planar solar cells, Nanoscale Adv. 3 (2021) 2305–2315. https://doi.org/10.1039/d1na00075f.

[131] J. Ye, M.M. Byranvand, C.O. Martínez, R.L.Z. Hoye, M. Saliba, L. Polavarapu, Defect Passivation in Lead-Halide Perovskite Nanocrystals and Thin Films: Toward Efficient LEDs and

Solar Cells, Angew. Chemie - Int. Ed. 60 (2021) 21636–21660. https://doi.org/10.1002/anie.202102360.

[132] E.L. Unger, A.R. Bowring, C.J. Tassone, V.L. Pool, A. Gold-Parker, R. Cheacharoen, K.H. Stone, E.T. Hoke, M.F. Toney, M.D. McGehee, Chloride in Lead Chloride-Derived Organo-Metal Halides for Perovskite-Absorber Solar Cells, Chem. Mater. 26 (2014) 7158–7165. https://doi.org/10.1021/cm503828b.

[133] Y. Zhao, S. Jiao, S. Liu, Y. Jin, S. Yang, X. Wang, T. Liu, H. Jin, D. Wang, S. Gao, J. Wang, Surface passivation of CsPbBr3 films by interface engineering in efficient and stable self-powered perovskite photodetector, J. Alloys Compd. 965 (2023) 171434. https://doi.org/https://doi.org/10.1016/j.jallcom.2023.171434.

[134] Z. Wang, A.K. Baranwal, M.A. Kamarudin, chi huey Ng, M. Pandey, T. Ma, S. Hayase, Xanthate-induced sulfur doped all-inorganic perovskite with superior phase stability and enhanced performance, Nano Energy. 59 (2019) 258–267. https://doi.org/10.1016/j.nanoen.2019.02.049.

[135] A.A. Hussain, Constructing Caesium-Based Lead-Free Perovskite Photodetector Enabling Self-Powered Operation with Extended Spectral Response, ACS Appl. Mater. Interfaces. 12 (2020) 46317–46329. https://doi.org/10.1021/acsami.0c14083.

[136] Y. Zhao, C. Li, L. Shen, Recent advances on organic-inorganic hybrid perovskite photodetectors with fast response, InfoMat. 1 (2019) 164–182. https://doi.org/10.1002/inf2.12010.

[137] A. Paul, S. Shaji, B. Krishnan, D.A. Avellaneda, Novel low-cost synthesis of crystalline SnI4 thin films via anionic replacement: Effect of iodization time on properties, Opt. Mater. (Amst). 133 (2022) 112982. https://doi.org/10.1016/j.optmat.2022.112982.

[138] T. L. Cottrell, The Strengths ofChemical Bonds, 2d ed., Butterworth, London, 1958; B. deB. Darwent, National Standard Reference Data Series, NationalBureau of Standards, no. 31, Washington, 1970; S. W. Benson, J. Chem. Educ. 42:502 (1965), (n.d.).

[139] K. Sandeep, K. Padmakumar, K.U. Ambili, P. Jishnu, K.H. Fousia, A.R. Ramesh, J.P. Rappai, V. Santhi, M. Shanthil, Anion Exchange in Lead Halide Perovskites: An Overview, Phys. Status Solidi Basic Res. 259 (2022) 1–8. https://doi.org/10.1002/pssb.202100600.

[140] J. Yang, Composition and dimension dependent static and dynamic stabilities of inorganic mixed halide antimony perovskites, J. Mater. Chem. C. 9 (2021) 8891–8901. https://doi.org/10.1039/d1tc01223a.

[141] Varshika Puthan Veedu Sasidharan, Sadasivan Shaji, David Avellaneda Avellaneda, Manuel Garcia Mendez, Bindu Krishnan, Rudorffite silver antimony iodide (AgSb 2 I 7) thin films by thermal and microwave-assisted synthesis for self-powered visible light detection, J. Alloys Compd. 1035 (2025). https://doi.org/10.1016/j.jallcom.2025.181479.

[142] H.C. Sansom, G.F.S. Whitehead, M.S. Dyer, M. Zanella, T.D. Manning, M.J. Pitcher, T.J. Whittles, V.R. Dhanak, J. Alaria, J.B. Claridge, M.J. Rosseinsky, AgBiI4 as a Lead-Free Solar Absorber with Potential Application in Photovoltaics, Chem. Mater. 29 (2017) 1538–1549. https://doi.org/10.1021/acs.chemmater.6b04135.

[143] A. Bera, S. Paramanik, A. Maiti, A.J. Pal, Energy landscape in silver-bismuth-iodide rudorffites: Combining scanning tunneling spectroscopy and Kelvin probe force microscopy, Phys. Rev. Mater. 5 (2021) 095404. https://doi.org/10.1103/PhysRevMaterials.5.095404.

[144] H. Zhu, M. Pan, M.B. Johansson, E.M.J. Johansson, High Photon-to-Current Conversion in

Solar Cells Based on Light-Absorbing Silver Bismuth Iodide, ChemSusChem. 10 (2017) 2592–2596. https://doi.org/10.1002/cssc.201700634.

[145] I. Turkevych, S. Kazaoui, N. Shirakawa, N. Fukuda, Potential of AgBiI4rudorffites for indoor photovoltaic energy harvesters in autonomous environmental nanosensors, Jpn. J. Appl. Phys. 60 (2021) 2–7. https://doi.org/10.35848/1347-4065/abf2a5.

[146] H. Zhu, M. Pan, M.B. Johansson, E.M.J. Johansson, Superior Performance of Silver Bismuth Iodide Photovoltaics Fabricated via Dynamic Hot-Casting Method under Ambient Conditions Biplab, ChemSusChem. 10 (2017) 2592–2596. https://doi.org/10.1002/cssc.201700634.

[147] H. Ye, B. Sun, Z. Wang, Z. Liu, X. Zhang, X. Tan, T. Shi, Z. Tang, G. Liao, High performance flexible memristors based on a lead free AgBiI4perovskite with an ultralow operating voltage, J. Mater. Chem. C. 8 (2020) 14155–14163. https://doi.org/10.1039/d0tc03287e.

[148] X. Geng, Y.A. Chen, Y.Y. Li, J. Ren, G.H. Dun, K. Qin, Z. Lin, J. Peng, H. Tian, Y. Yang, D. Xie, T.L. Ren, Lead-Free Halide Perovskites for Direct X-Ray Detectors, Adv. Sci. 2300256 (2023) 1–26. https://doi.org/10.1002/advs.202300256.

[149] V. Pecunia, Y. Yuan, J. Zhao, K. Xia, Y. Wang, S. Duhm, L. Portilla, F. Li, Perovskite-Inspired Lead-Free Ag2BiI5 for Self-Powered NIR-Blind Visible Light Photodetection, Nano-Micro Lett. 12 (2020) 1–12. https://doi.org/10.1007/s40820-020-0371-0.

[150] S. Premkumar, T. Thrupthika, M. Palanivel, D. Liu, D. Nataraj, W. Lei, J. Gui, Preparation of nano dumbbell-shaped silver bismuth iodide perovskite hybrids and their enhanced photocurrent properties, New J. Chem. 47 (2023) 11669–11674. https://doi.org/10.1039/d3nj01064c.

[151] H. Zhu, I. Turkevych, H. Lohan, P. Liu, R.W. Martin, F.C.P. Massabuau, R.L.Z. Hoye, Progress and applications of (Cu–)Ag–Bi–I semiconductors, and their derivatives, as next-generation lead-free materials for photovoltaics, detectors and memristors, Int. Mater. Rev. 69 (2024) 19–62. https://doi.org/10.1177/09506608231213065.

[152] F.J. Amaya Suazo, S. Shaji, D.A. Avellaneda, J.A. Aguilar-Martínez, B. Krishnan, Solar cell using spray casted Cs2SnI6 perovskite thin films on chemical bath deposited CdS yielding high open circuit voltage, Sol. Energy. 207 (2020) 486–495. https://doi.org/10.1016/j.solener.2020.06.101.

[153] J. Xu, Z. Hu, X. Jia, L. Huang, X. Huang, L. Wang, P. Wang, H. Zhang, J. Zhang, J. Zhang, Y. Zhu, A rapid annealing technique for efficient perovskite solar cells fabricated in air condition under high humidity, Org. Electron. 34 (2016) 84–90. https://doi.org/10.1016/j.orgel.2016.04.012.

[154] B. Reeja-Jayan, K.L. Harrison, K. Yang, C.L. Wang, A.E. Yilmaz, A. Manthiram, Microwave-assisted low-temperature growth of thin films in solution, Sci. Rep. 2 (2012) 1–8. https://doi.org/10.1038/srep01003.

[155] S.S. Hosseini, M. Adelifard, M. Ataei, An investigation on physical properties of Ag 2 BiI 5 absorber layers synthesized by microwave assisted spin coating technique, J. Mater. Sci. Mater. Electron. 30 (2019) 5021–5029. https://doi.org/10.1007/s10854-019-00799-y.

[156] L. Qiu, J. Xu, W. Cai, Z. Xie, Y. Yang, Fabrication of Cu 2 ZnSnS 4 thin films by microwave assisted sol-gel method, Superlattices Microstruct. 126 (2019) 83–88. https://doi.org/10.1016/j.spmi.2018.12.020.

[157] B.H. Toby, R.B. Von Dreele, GSAS-II: The genesis of a modern open-source all purpose crystallography software package, J. Appl. Crystallogr. 46 (2013) 544–549.

https://doi.org/10.1107/S0021889813003531.

[158] D. Palles, I. Konidakis, C.P.E. Varsamis, E.I. Kamitsos, Vibrational spectroscopic and bond valence study of structure and bonding in Al2O3-containing AgI-AgPO3 glasses, RSC Adv. 6 (2016) 16697–16710. https://doi.org/10.1039/c6ra00162a.

[159] A.A. Ramachandran, B. Krishnan, D.A.A. Leal, E.G. Martinez, J.A.A. Martinez, D.A. Avellaneda, S. Shaji, Ag2BiI5 perovskite thin films: Studies on structure, morphology, composition and optoelectronic properties for visible photodetector application, Mater. Today Commun. 24 (2020) 101092. https://doi.org/10.1016/j.mtcomm.2020.101092.

[160] W. Zhai, L. Huang, X. Cui, G. Li, Z. Zhang, P. Chen, Y. Li, Y. Tang, L. Lin, Z. Yan, J.M. Liu, Tuning the morphology and optoelectronic properties of AgBiI4 film through isopropanol treatment, J. Mater. Chem. C. 10 (2022) 5321–5327. https://doi.org/10.1039/d1tc05445g.

[161] Y. Tachibana, K. Kusunoki, T. Watanabe, K. Hashimoto, H. Ohsaki, Optical properties of multilayers composed of silver and dielectric materials, Thin Solid Films. 442 (2003) 212–216. https://doi.org/10.1016/S0040-6090(03)00984-2.

[162] V.B. Ghanwat, S.S. Mali, R.M. Mane, P.S. Patil, C.K. Hong, P.N. Bhosale, Thermoelectric properties of nanocrystalline Cu3SbSe4 thin films deposited by a self-organized arrested precipitation technique, New J. Chem. 39 (2015) 5661–5668. https://doi.org/10.1039/c5nj00686d.

[163] J. Cai, Z. Wu, S. Wang, J. Guo, M. Fan, W. Xu, H. Jin, J. Wan, Exploring advanced microwave strategy for the synthesis of two-dimensional energy materials, Appl. Phys. Rev. 11 (2024) 041320. https://doi.org/10.1063/5.0231081.

[164] Q. Cao, S. Yang, Q. Gao, L. Lei, Y. Yu, J. Shao, Y. Liu, Fast and Controllable Crystallization of Perovskite Films by Microwave Irradiation Process, ACS Appl. Mater. Interfaces. 8 (2016) 7854–7861. https://doi.org/10.1021/acsami.6b01558.

[165] A. Nadukkandy, S. Devasia, P. Abraham, S. Shaji, D.A. Avellaneda, J.A. Aguilar-Martínez, E.G. Martinez, R.F. Cienfuegos-Pelaes, B. Krishnan, Monoclinic AgSbS2 thin films for photovoltaic applications: Computation, growth and characterization approaches, Mater. Sci. Semicond. Process. 135 (2021) 106074. https://doi.org/10.1016/j.mssp.2021.106074.

[166] H. Stiller, The nature of Chemical bond of Magnetite, F. Frolich H Stiller. (1963).

[167] J.J. Reed, Digitizing “The NBS tables of chemical thermodynamic properties: Selected values for inorganic and c1 and c2 organic substances in SI Units”1, J. Res. Natl. Inst. Stand. Technol. 125 (2020). https://doi.org/10.6028/JRES.125.007.

[168] T.G. Truong, B. Rotonnelli, M. Rieu, J.P. Viricelle, I. Kalaitzidou, D. Marinha, L. Burel, A. Caravaca, P. Vernoux, H. Kaper, Catalytic and electrochemical properties of ag infiltrated perovskite coatings for propene deep oxidation, Catalysts. 10 (2020). https://doi.org/10.3390/catal10070729.

[169] Y. Shi, W. Chu, L. Zhang, B. Wang, W.A. Saidi, J. Zhao, O. V Prezhdo, Band Gap Narrowing in Lead-Halide Perovskites by Dynamic Defect Self-Doping for Enhanced Light Absorption and Energy Upconversion, ACS Chem. Mater. x (2025) xxx–xxx. https://doi.org/https://doi.org/10.1021/acs.chemmater.4c02530.

[170] N.J. Podraza, W. Qiu, B.B. Hinojosa, H. Xu, M.A. Motyka, S.R. Phillpot, J.E. Baciak, S. Trolier-Mckinstry, J.C. Nino, Band gap and structure of single crystal BiI3: Resolving discrepancies in literature, J. Appl. Phys. 114 (2013) 033110. https://doi.org/10.1063/1.4813486.

[171] Y.J. Kim, M.R. Kumar, G.M. Kumar, M. Kim, Self-powered silicon metal-semiconductor-metal photodetector based on asymmetric Schottky barrier heights, Appl. Phys. Lett. 123 (2023) 252111. https://doi.org/10.1063/5.0178740.

[172] Y. Zhang, E. Parsonnet, A. Fernandez, S.M. Griffin, H. Huyan, C.K. Lin, T. Lei, J. Jin, E.S. Barnard, A. Raja, P. Behera, X. Pan, R. Ramesh, P. Yang, Ferroelectricity in a semiconducting all-inorganic halide perovskite, Sci. Adv. 8 (2022) 6, 1–10. https://doi.org/10.1126/sciadv.abj5881.

[173] M. Si, A.K. Saha, S. Gao, G. Qiu, J. Qin, Y. Duan, J. Jian, C. Niu, H. Wang, W. Wu, S.K. Gupta, P.D. Ye, A ferroelectric semiconductor field-effect transistor, Nat. Electron. 2 (2019) 580–586. https://doi.org/10.1038/s41928-019-0338-7.

[174] H.Y. Zhang, R.G. Xiong, Three-dimensional narrow-bandgap perovskite semiconductor ferroelectric methylphosphonium tin triiodide for potential photovoltaic application, Chem. Commun. 59 (2022) 920–923. https://doi.org/10.1039/d2cc06408a.

[175] L. Li, X. Liu, C. He, S. Wang, C. Ji, X. Zhang, Z. Sun, S. Zhao, M. Hong, J. Luo, A Potential Sn-Based Hybrid Perovskite Ferroelectric Semiconductor, J. Am. Chem. Soc. 142 (2020) 1159–1163. https://doi.org/10.1021/jacs.9b11341.

[176] J. Liao, W. Wen, J. Wu, Y. Zhou, S. Hussain, H. Hu, J. Li, A. Liaqat, H. Zhu, L. Jiao, Q. Zheng, L. Xie, Van der Waals Ferroelectric Semiconductor Field Effect Transistor for In-Memory Computing, ACS Nano. 17 (2023) 6095–6102. https://doi.org/10.1021/acsnano.3c01198.

[177] H. Wang, M. Zhou, H. Luo, Electric-Field-Induced Dynamic Electronic Junctions in Hybrid Organic-Inorganic Perovskites for Optoelectronic Applications, ACS Omega. 3 (2018) 1445–1450. https://doi.org/10.1021/acsomega.7b02009.

[178] H.Y. Liu, H.Y. Zhang, X.G. Chen, R.G. Xiong, Molecular Design Principles for Ferroelectrics: Ferroelectrochemistry, J. Am. Chem. Soc. 142 (2020) 15205–15218. https://doi.org/10.1021/jacs.0c07055.

[179] C.H. Ji, K.T. Kim, S.Y. Oh, RSC Advances using a Zr-doped TiO x cathode interlayer †, (2018) 8302–8309. https://doi.org/10.1039/c8ra00730f.

[180] J.L. Pura, Optical and Electrical Properties of Low-Dimensional Crystalline Materials: A Review, Crystals. 13 (2023). https://doi.org/10.3390/cryst13010108.

[181] S. Joishy, A. Antony, P. Poornesh, R.J. Choudhary, R. B.V, Influence of Cd on structure, surface morphology, optical and electrical properties of nano crystalline ZnS films, Sensors Actuators, A Phys. 303 (2020) 111719. https://doi.org/10.1016/j.sna.2019.111719.

[182] M.M. Byranvand, M. Saliba, Defect Passivation of Perovskite Films for Highly Efficient and Stable Solar Cells, Sol. RRL. 5 (2021) 2100295. https://doi.org/10.1002/solr.202100295.

[183] G. Niu, X. Guo, L. Wang, Review of recent progress in chemical stability of perovskite solar cells, J. Mater. Chem. A. 3 (2015) 8970–8980. https://doi.org/10.1039/c4ta04994b.

[184] K. Takahashi, Y. Suzuki, Perovskite solar cells with CuI inorganic hole conductor, Jpn. J. Appl. Phys. 56 (2017) 4–9. https://doi.org/10.7567/JJAP.56.08MC04.

[185] X. Liu, H. Andersen, Y. Lu, B. Wen, I.P. Parkin, M. De Volder, B.D. Boruah, Porous Carbon Coated on Cadmium Sulfide-Decorated Zinc Oxide Nanorod Photocathodes for Photo-accelerated Zinc Ion Capacitors, ACS Appl. Mater. Interfaces. 15 (2023) 6963–6969. https://doi.org/10.1021/acsami.2c20995.

[186] V. Jovovic, J.P. Heremans, Measurements of the energy band gap and valence band structure

of AgSbTe2, Phys. Rev. B - Condens. Matter Mater. Phys. 77 (2008) 1–8. https://doi.org/10.1103/PhysRevB.77.245204.

[187] F. Kherrat, L. Dehimi, H. Bencherif, M.M.A. Moon, M.K. Hossain, N.A. Sonmez, T. Ataser, Z. Messai, S. Özçelik, Performance enhancement of eco-friendly Cs3Sb2I9-based perovskite solar cell employing Nb2O5 and CuI as efficient charge transport layers, Micro and Nanostructures. 183 (2023) 2773–0123. https://doi.org/10.1016/j.micrna.2023.207676.

[188] F. Meng, P. Jia, X. Li, Y. Tang, B. Song, J. Guo, L. Qin, Y. Hu, F. Teng, Z. Lou, Y. Hou, Efficient Perovskite Solar Cells with a CuI-Modified Polymer Hole-Transport Layer, ACS Appl. Energy Mater. 5 (2022) 11034–11041. https://doi.org/10.1021/acsaem.2c01681.

[189] Y.-J. Chen, M.-H. Li, J.-Y. Liu, C.-W. Chong, J.-C.-A. Huang, P. Chen, Double-side operable perovskite photodetector using Cu/Cu 2 O as a hole transport layer , Opt. Express. 27 (2019) 24900. https://doi.org/10.1364/oe.27.024900.

[190] J. Gao, W. Zeng, R. Luo, Z. Liu, Q.J. Liu, The Applicable Guideline for the Three Criteria in Identifying p/n-Type Characteristics, Cryst. Growth Des. 24 (2024) 3777–3785. https://doi.org/10.1021/acs.cgd.4c00108.

[191] A. Kumar, Y. Kuang, Z. Liang, X. Sun, Microwave chemistry, recent advancements, and eco-friendly microwave-assisted synthesis of nanoarchitectures and their applications: a review, Mater. Today Nano. 11 (2020) 100076. https://doi.org/10.1016/j.mtnano.2020.100076.

[192] W. Zheng, X. Wang, X. Zhang, B. Chen, H. Suo, Z. Xing, Y. Wang, H.L. Wei, J. Chen, Y. Guo, F. Wang, Emerging Halide Perovskite Ferroelectrics, Adv. Mater. 35 (2023) 1–21. https://doi.org/10.1002/adma.202205410.

[193] J. Zhang, K. Ji, J. He, Y. Xie, Two-dimensional ferroelectricity in all-inorganic halide perovskite monolayer Cs2PbX4 (X= F, Cl, Br, I), Phys. Rev. B. 110 (2024) 1–9. https://doi.org/10.1103/PhysRevB.110.195428.

[194] H. Röhm, T. Leonhard, M.J. Hoffmann, A. Colsmann, Ferroelectric domains in methylammonium lead iodide perovskite thin-films, Energy Environ. Sci. 10 (2017) 950–955. https://doi.org/10.1039/c7ee00420f.

[195] H.C. Sansom, G. Longo, A.D. Wright, L.R.V. Buizza, S. Mahesh, B. Wenger, M. Zanella, M. Abdi-Jalebi, M.J. Pitcher, M.S. Dyer, T.D. Manning, R.H. Friend, L.M. Herz, H.J. Snaith, J.B. Claridge, M.J. Rosseinsky, Highly Absorbing Lead-Free Semiconductor Cu2AgBiI6for Photovoltaic Applications from the Quaternary CuI-AgI-BiI3Phase Space, J. Am. Chem. Soc. 143 (2021) 3983–3992. https://doi.org/10.1021/jacs.1c00495.

[196] B. Vargas, E. Ramos, E. Pérez-Gutiérrez, J.C. Alonso, D. Solis-Ibarra, A Direct Bandgap Copper-Antimony Halide Perovskite, J. Am. Chem. Soc. 139 (2017) 9116–9119. https://doi.org/10.1021/jacs.7b04119.

[197] J. Xu, L.A. Castriotta, A. Di Carlo, T.M. Brown, Air-Stable Lead-Free Antimony-Based Perovskite Inspired Solar Cells and Modules, ACS Energy Lett. 9 (2024) 671–678. https://doi.org/10.1021/acsenergylett.3c02409.

[198] R.J. Sutton, G.E. Eperon, L. Miranda, E.S. Parrott, B.A. Kamino, J.B. Patel, M.T. Hörantner, M.B. Johnston, A.A. Haghighirad, D.T. Moore, H.J. Snaith, Bandgap-Tunable Cesium Lead Halide Perovskites with High Thermal Stability for Efficient Solar Cells, Adv. Energy Mater. 6 (2016) 1–6. https://doi.org/10.1002/aenm.201502458.

[199] V. Vinayakumar, S. Shaji, D. Avellaneda, J.A. Aguilar-Martínez, B. Krishnan, Copper antimony sulfide thin films for visible to near infrared photodetector applications, RSC Adv. 8 (2018)

31055–31065. https://doi.org/10.1039/C8RA05662E.

[200] N. Yamada, R. Ino, Y. Ninomiya, Truly Transparent p-Type γ-CuI Thin Films with High Hole Mobility, Chem. Mater. 28 (2016) 4971–4981. https://doi.org/10.1021/acs.chemmater.6b01358.

[201] A.E. Maughan, A.M. Ganose, M.M. Bordelon, E.M. Miller, D.O. Scanlon, J.R. Neilson, Defect Tolerance to Intolerance in the Vacancy-Ordered Double Perovskite Semiconductors Cs2SnI6 and Cs2TeI6, J. Am. Chem. Soc. 138 (2016) 8453–8464. https://doi.org/10.1021/jacs.6b03207.

[202] J. Kumar, Y. Dror, E. Edri, (BixSb1−x)2Se3 thin films for short wavelength infrared region solar cells, J. Mater. Chem. C. 10 (2022) 8702–8710. https://doi.org/10.1039/d2tc01300b.

[203] M.T.S. Nair, Y. Peña, J. Campos, V.M. García, P.K. Nair, Chemically Deposited Sb2 S 3 and Sb2 S 3 - CuS Thin Films, J. Electrochem. Soc. 145 (1998) 2113–2120. https://doi.org/10.1149/1.1838605.

[204] S. Mahanty, J.M. Merino, M. León, Preparation and optical studies on flash evaporated Sb2S3 thin films, J. Vac. Sci. Technol. A Vacuum, Surfaces, Film. 15 (1997) 3060–3064. https://doi.org/10.1116/1.580847.

[205] M.P. Deshpande, K. Chauhan, K.N. Patel, P. Rajput, H.R. Bhoi, S.H. Chaki, Study of Sb2S3 thin films deposited by SILAR method, Mater. Res. Express. 5 (2018) 0–7. https://doi.org/10.1088/2053-1591/aac4ef.

[206] D.B. Khadka, M.A. Islam, S. Kato, T. Soga, Fabrication and Properties of Bi2S3 Nanowire Thin Film Solar Cells by Spin Coating with Varying Sulfur Concentrations in the Precursor, J. Electron. Mater. 53 (2024) 4224–4235. https://doi.org/10.1007/s11664-024-11129-2.

[207] F. Ding, Q. Wang, S. Zhou, G. Zhao, Y. Ye, R. Ghomashchi, Synthesis of Bi 2 S 3 thin films based on pulse-plating bismuth nanocrystallines and its photoelectrochemical properties: Green Synthesis of Bi2S3 thin films, R. Soc. Open Sci. 7 (2020). https://doi.org/10.1098/rsos.200479.

[208] C.J. Tang, G.Z. Wang, H.Q. Wang, Y.X. Zhang, G.H. Li, Facile synthesis of Bi2S3 nanowire arrays, Mater. Lett. 62 (2008) 3663–3665. https://doi.org/10.1016/j.matlet.2008.04.021.

[209] Y.X.N. Afiq Radzwan, Rashid Ahmed, Amiruddin Shaari, Abdullahi Lawal, First-principles calculations of antimony sulphide Sb2S3, J. Guangxi Univ. Sci. Technol. 35 (2024) 285–289.

[210] N. Huo, A. Figueroba, Y. Yang, S. Christodoulou, A. Stavrinadis, C. Magén, G. Konstantatos, Engineering Vacancies in Bi2S3 yielding Sub-Bandgap Photoresponse and Highly Sensitive Short-Wave Infrared Photodetectors, Adv. Opt. Mater. 7 (2019) 1–7. https://doi.org/10.1002/adom.201900258.

[211] H. Zhang, J. Diao, M. Ouyang, H. Yadegari, M. Mao, J. Wang, G. Henkelman, F. Xie, D.J. Riley, Enhancing the Performance of Bi2S3 in Electrocatalytic and Supercapacitor Applications by Controlling Lattice Strain, Adv. Funct. Mater. 32 (2022). https://doi.org/10.1002/adfm.202205974.

[212] M.H. Shang, J. Zhang, S. Wei, Y. Zhu, L. Wang, H. Hou, Y. Wu, T. Fujikawa, N. Ueno, Bi-doped Sb2S3 for low effective mass and optimized optical properties, J. Mater. Chem. C. 4 (2016) 5081–5090. https://doi.org/10.1039/c6tc00513f.

[213] P. Baláž, E. Guilmeau, M. Achimovičová, M. Baláž, N. Daneu, O. Dobrozhan, M. Kaňuchová, Bismuth doping in nanostructured tetrahedrite: Scalable synthesis and thermoelectric performance, Nanomaterials. 11 (2021). https://doi.org/10.3390/nano11061386.

[214] H. Omer, Sulfur 15.1, 1 (1988). https://doi.org/10.1016/B978-0-7506-3365-9.50021-3.

[215] H. Ben Abdallah, W. Ouerghui, Spin–orbit coupling effect on electronic, linear and nonlinear optical properties of Bi2S3 and the ternary bismuth sulfide Bi2S2.75Se0.25: Ab-initio calculations, Opt. Quantum Electron. 54 (2022) 1–18. https://doi.org/10.1007/s11082-021-03411-y.

[216] A. Bafekry, B. Mortazavi, M. Faraji, M. Shahrokhi, A. Shafique, H.R. Jappor, C. Nguyen, M. Ghergherehchi, S.A.H. Feghhi, Ab initio prediction of semiconductivity in a novel two-dimensional Sb2X3 (X= S, Se, Te) monolayers with orthorhombic structure, Sci. Rep. 11 (2021) 1–10. https://doi.org/10.1038/s41598-021-89944-4.

[217] A. Walsh, Y. Yan, M.N. Huda, M.M. Al-Jassim, S.H. Wei, Band edge electronic structure of BiVO 4: Elucidating the role of the Bi s and V d orbitals, Chem. Mater. 21 (2009) 547–551. https://doi.org/10.1021/cm802894z.

[218] R. Gao, X. He, C. Chen, X. Bao, F. Yang, X. Yang, J. He, C. Dong, C. Li, S. Chen, G. Liang, S. Jiang, J. Tang, G. Zhang, K. Li, (Bi,Sb)2Se3 Alloy Thin Film for Short-Wavelength Infrared Photodetector and TFT Monolithic-Integrated Matrix Imaging, Small. 20 (2024) 1–9. https://doi.org/10.1002/smll.202308070.

[219] H. Song, X. Zhan, D. Li, Y. Zhou, B. Yang, K. Zeng, J. Zhong, X. Miao, J. Tang, Rapid thermal evaporation of Bi2S3 layer for thin film photovoltaics, Sol. Energy Mater. Sol. Cells. 146 (2016) 1–7. https://doi.org/10.1016/j.solmat.2015.11.019.

[220] P.K. Panigrahi, A. Pathak, The Growth of Bismuth Sulfide Nanorods from Spherical-Shaped Amorphous Precursor Particles under Hydrothermal Condition, J. Nanoparticles. 2013 (2013) 1–11. https://doi.org/10.1155/2013/367812.

[221] M.I. Medina-Montes, Z. Montiel-González, F. Paraguay-Delgado, N.R. Mathews, X. Mathew, Structural, morphological and spectroscopic ellipsometry studies on sputter deposited Sb2S3 thin films, J. Mater. Sci. Mater. Electron. 27 (2016) 9710–9719. https://doi.org/10.1007/s10854-016-5033-0.

[222] P.A. Chate, S.D. Lakde, Electrical, optical and structural properties of rod shaped Bi2S3 thin films deposited by dip technique, J. Mater. Sci. Mater. Electron. 26 (2015) 5847–5851. https://doi.org/10.1007/s10854-015-3145-6.

[223] T.O. Ajiboye, D.C. Onwudiwe, Bismuth sulfide based compounds: Properties, synthesis and applications, Results Chem. 3 (2021) 100151. https://doi.org/10.1016/j.rechem.2021.100151.

[224] S.R.Y. Daniel N. Congreve, Jiye Lee, Nicholas J. Thompson, Eric Hontz, M.A.B. Philip D. Reusswig, Matthias E. Bahlke, Sebastian Reineke, Troy Van Voorhis, External Quantum Efficiency Above 100% in a Singlet-Exciton-Fission–Based Organic Photovoltaic Cell, (2013) 334–337. https://doi.org/10.1126/science.1232994.

[225] G. Konstantatos, I. Howard, A. Fischer, S. Hoogland, J. Clifford, E. Klem, L. Levina, E.H. Sargent, Ultrasensitive solution-cast quantum dot photodetectors, Nature. 442 (2006) 180–183. https://doi.org/10.1038/nature04855.

Appendix A. Synthesis and characterization of Chemical bath deposited Bi alloyed Sb_2S_3 thin films for photodetector application

A.1 Introduction

Semiconductor materials have been pivotal in driving advancements in optoelectronic technologies, enabling precise control over their structural, electronic, and optical properties. Among these materials, bismuth-alloyed antimony sulfide (Bi-alloyed Sb_2S_3) has gained significant attention due to its promising applications in photovoltaics, photodetectors, and photocatalysis. The ability to fine-tune the bismuth content in Sb_2S_3 thin films presents a unique opportunity to optimize their optoelectronic properties, particularly by enhancing carrier transport and light absorption—two key factors in improving device efficiency [202]. However, despite its potential, the full impact of Bi incorporation on the electronic structure, defect formation, and charge carrier dynamics in Sb_2S_3 remains an open question. A systematic experimental and theoretical investigation is thus required to understand and optimize its performance for next-generation optoelectronic devices.

Extensive research has been conducted on the synthesis and characterization of Sb_2S_3 and Bi_2S_3 thin films, focusing on achieving high-quality films with controlled morphological, optical, and electrical properties [108]. Several deposition techniques have been explored to enhance crystallinity and film uniformity. Chemical bath deposition (CBD), widely used for Sb_2S_3 films, allows for precise control over thickness and stoichiometry by adjusting precursor concentrations and deposition conditions [108,203]. Flash evaporation has proven effective in producing high-purity Sb_2S_3 thin films suitable for optical applications [204], whereas successive ionic layer adsorption and reaction (SILAR) has been employed for precise thickness modulation [205]. For Bi_2S_3, spin-coating techniques have demonstrated tunable optical and photovoltaic properties by varying sulfur precursor concentrations [206]. Additionally, alternative deposition methods such as pulse-plating and dip-coating with

malonic acid ligands have been explored to enhance film crystallinity and morphology [207,208].

Theoretical studies based on Density Functional Theory (DFT) have provided deeper insights into the electronic and structural properties of these materials. First-principles calculations using the Full-Potential Linearized Augmented Plane Wave (FP-LAPW) method have been instrumental in analyzing the band structure, charge transport mechanisms, and phase transitions in Sb_2S_3, highlighting its potential for photovoltaic applications [209]. Furthermore, DFT-based investigations have revealed that sulfur vacancies in Sb_2S_3 introduce mid-gap defect states, significantly affecting its optoelectronic properties [208]. Similarly, Bi_2S_3 has been studied using DFT to understand the role of sulfur vacancies in modifying mid-gap states, which is crucial for improving infrared photodetection capabilities [210]. In addition, lattice strain engineering has emerged as an effective strategy to modify the electronic structure of Bi_2S_3, enhancing its electrocatalytic and supercapacitor performance and broadening its applicability in energy-related fields [211].

While considerable progress has been made in understanding the fundamental properties of Sb_2S_3 and Bi_2S_3, the impact of Bi doping in Sb_2S_3 remains underexplored. Recent studies indicate that Bi doping reduces the effective mass of charge carriers in Sb_2S_3, leading to improved charge transport and enhanced optical absorption, thereby making it a promising candidate for photovoltaic and photodetector applications [212]. Additionally, investigations into $(BixSb_{1-x})_2Se_3$ thin films for short-wavelength infrared solar cells have demonstrated tunable bandgaps and enhanced optoelectronic properties with increasing Bi content [202]. Experimental synthesis of Bi-doped Sb_2S_3 has been achieved through high-energy milling of elemental precursors followed by spark plasma sintering, yielding $Cu_{12}Sb_{4-x}Bi_xS_{13}$ solid solutions with reduced thermal conductivity—an essential feature for thermoelectric applications [213]. Meanwhile, DFT calculations suggest that Bi incorporation modifies the band structure and introduces mid-gap states, influencing charge carrier mobility and necessitating optimization of doping concentrations to achieve a balance between optical and electronic performance [212].

Despite these advances, the potential of Bi alloying in Sb_2S_3 for broadband photodetection remains largely unexplored. This presents a critical research gap that must be addressed through scalable synthesis techniques and advanced theoretical modeling to enhance the material's optoelectronic properties while maintaining its structural integrity.

In this study, we present a comprehensive investigation into the optoelectronic properties of Bi-alloyed Sb_2S_3 thin films, systematically examining the effects of varying Bi concentrations on their structural, electronic, and optical characteristics. Using Density Functional Theory (DFT) calculations via the Vienna Ab initio Simulation Package (VASP), we analyze the electronic structure, defect formation, and stability of these films, correlating theoretical predictions with experimental observations. A holistic characterization approach integrating X-ray diffraction (XRD), Raman spectroscopy, X-ray photoelectron spectroscopy (XPS), energy-dispersive X-ray spectroscopy (EDX), and photodetection analyses provides valuable insights into bandgap tunability and charge carrier dynamics. The findings from this work contribute to the development of Bi-alloyed Sb_2S_3 as a next-generation material for broadband photodetection and advanced optoelectronic applications.

A.2 Experimental

A.2.1. Materials

$SbCl_3$ (Antimony chloride, Fermont, 99.7%), $BiCl_3$ (Bismuth chloride), $(CH_3)_2CO$ (Acetone, Fermont, 99.6%), and $Na_2S_2O_3{\cdot}5H_2O$ (sodium thiosulfate, Fermont, 99.9%) were all purchased and utilized without further purification.

A.2.2. Synthesis

A.2.2.1. Chemical bath deposition of Bi-alloyed Sb_2S_3 thin films

Figure A.1 depicts a schematic representation of the synthesis process. 0.0014 M (449 mg-$BiCl_3$ and 325 mg-$SbCl_3$ in 100% Bi_2S_3 and Sb_2S_3) with changing ratios of Bi, while Sb was fixed to prepare the chemical bath to produce Bi-alloyed Sb_2S_3 thin films. A calculated amount of $BiCl_3$ and $SbCl_3$ was dissolved in 2.4 ml $(CH_3)_2CO$ to prepare the bath. Then, 12.5 ml of 1 M $Na_2S_2O_3{\cdot}5H_2O$ and 65 ml of deionized water were added and mixed to create the bath, which had a final volume of 100 ml [108]. The premium glass substrates were thoroughly cleaned with soap solution before being placed vertically in the bath. The deposition process continued for almost two hours at room temperature. Films were removed after 2 hours of deposition, washed with deionized water, and dried. At 380°C for 30 minutes, these films underwent vacuum annealing at a pressure of 10^{-3}.

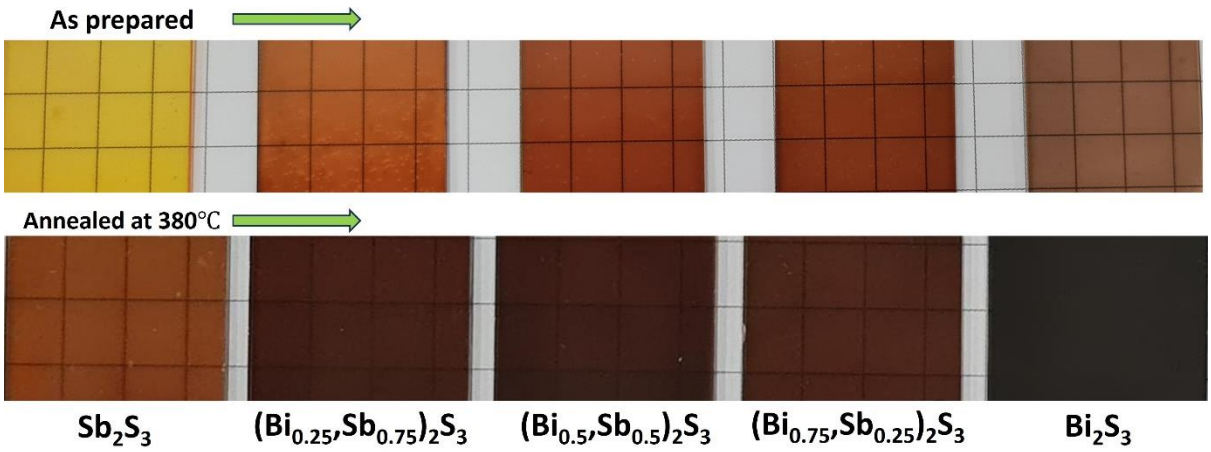

Figure A.1. sample images of Bi-alloyed Sb_2S_3 thin films.

A.2.2.2. Characterization

A comprehensive analysis of Bi-alloyed Sb_2S_3 thin films was conducted using various characterization techniques to investigate their crystal structure, chemical composition, morphology, optical, and optoelectronic properties. X-ray diffraction (XRD) patterns were recorded in the 2θ range of 10-60° with a step size of 0.001° using a PANalytical Empyrean diffractometer in normal mode, utilizing Cu-Kα radiation with a wavelength of 1.54056 Å to determine the crystalline structure and phases present. Raman spectroscopy was performed using a Thermo Scientific DXR Raman microscope with a 532 nm excitation laser to analyze vibrational modes. The chemical states and elemental composition were examined using a Thermo Scientific K-alpha X-ray photoelectron spectrometer (XPS). For elemental analysis and mapping, energy-dispersive X-ray spectroscopy (EDX) was carried out at 10 kV using a 6010LA system. Surface morphology was studied with a Hitachi SU 8020 scanning electron microscope (SEM). Optical transmittance and reflectance spectra were obtained using a Jasco V-770 UV-Vis-NIR spectrophotometer. Electrical measurements were conducted using a Keithley 6487 picoammeter/voltage source, with electrical contacts made using flash-dry silver paint (SPI supplies). Measurements were taken both in the dark and under illumination provided by a halogen lamp and LEDs to assess the films optoelectronic properties.

A.3 Composition analysis

Table A.1. Compositional analysis of bismuth-alloyed antimony sulfide ($(Bi,Sb)_2S_3$) thin films, as determined by EDX. The table shows the sulfur (S), antimony (Sb), and bismuth (Bi) weight percentages for various compositions, along with the corresponding sulfur-to-metal ratios and revised compositions based on increasing bismuth content.

Chemical bath composition (%)		**EDX composition (wt%)**			**Bi/(Sb+Bi)**	**Sb/(Sb+Bi)**	**S/(Sb+Bi)**	**Revised Composition (Based on EDX)**
Sb	**Bi**	**S**	**Sb**	**Bi**				
100	**0**	42	58	0	N/A	1	0.72	Sb_2S_3
75	**25**	38.8	44.5	16.7	0.27	0.73	0.70	**$(Bi_{0.3}, Sb_{0.7})_2S_3$**
50	**50**	38.6	35.8	25.6	0.42	0.58	0.79	**$(Bi_{0.4}, Sb_{0.6})_2S_3$**
25	**75**	33.4	33.2	33.5	0.5	0.5	0.5	**$(Bi_{0.5}, Sb_{0.5})_2S_3$**
0	**100**	41.5	0	58.5	1	N/A	0.71	Bi_2S_3

The chemical composition of the synthesized bismuth-alloyed antimony sulfide ($(Bi,Sb)_2S_3$) thin films was analyzed using EDX, providing essential insights into the sulfur (S), antimony (Sb), and bismuth (Bi) content. The results, summarized in Table A.1, highlight systematic variations in sulfur and metal ratios as bismuth content in the precursor solution increased.

In pure Sb_2S_3, the observed sulfur-to-antimony (S/Sb) ratio was 0.72, which is lower than the ideal stoichiometric ratio of 1.5. This sulfur deficiency, commonly seen in films prepared via chemical bath deposition (CBD), is likely due to factors such as precursor concentrations, deposition conditions, and the nature of the deposition process itself. Despite this deficiency, the films maintained the antimony sulfide phase, confirming successful film formation. At 25% Bi content, the EDX analysis showed a composition of S = 38.8 wt%, Sb = 44.5 wt%, and Bi = 16.7 wt%, yielding an S/Bi ratio of 2.324 and an S/(Sb+Bi) ratio of 0.70. These ratios suggest partial incorporation of bismuth into the Sb_2S_3 lattice, leading to a revised composition of $(Bi_{0.3},Sb_{0.7})_2S_3$. This indicates the onset of alloying, with bismuth beginning to substitute for antimony within the structure. For the 50% Bi sample, the composition was S = 38.6 wt%, Sb = 35.8 wt%, and Bi = 25.6 wt%, resulting in an S/Bi ratio of 1.508 and an S/(Sb+Bi) ratio of 0.79. This was revised to $(Bi_{0.4},Sb_{0.6})_2S_3$, reflecting a more balanced

incorporation of both elements. The sulfur content approached the stoichiometric ratio of Sb_2S_3, signaling a more homogeneous alloyed structure.

At 75% Bi substitution, the near-equal distribution of Sb and Bi (S = 33.4 wt%, Sb = 33.2 wt%, Bi = 33.5 wt%) resulted in an S/(Sb+Bi) ratio of 0.5, corresponding to the $(Bi_{0.5}Sb_{0.5})_2S_3$ phase. This well-balanced alloy structure enhances optoelectronic properties such as light absorption and charge transport. The lower sulfur ratio is attributed to sulfur sublimation [206,214] and spin-orbit coupling (SOC)-induced instability [215]. Sulfur's volatility at the annealing temperature of 380°C, its loss is more pronounced in Bi-rich samples due to weaker Bi–S bonds [206,214]. Increased Bi content also induces lattice distortions, promoting sulfur vacancies and further reducing sulfur content. Additionally, strong SOC effects weaken Bi–S interactions, exacerbating sulfur loss. The post-annealing lightening effect results from bandgap widening, sulfur deficiency, and phase segregation, all of which influence optical absorption.

In contrast, fully substituted Bi_2S_3 exhibited slight sulfur enrichment (S/Bi ratio of 0.710), as revealed by EDX analysis. This deviation likely arises from bismuth volatilization during deposition, leaving residual sulfur. The varying sulfur behavior at different Bi substitution levels underscores the role of Bi incorporation in phase stability and composition. The EDX-derived compositions were used as inputs for DFT simulations with VASP, providing deeper insights into the structural and electronic properties of Bi-alloyed Sb_2S_3 films for optimized optoelectronic applications.

A.4 Preliminary Theoretical Calculations

These preliminary Density Functional Theory (DFT) calculations were exploratory and did not fully adhere to the finalized computational protocols.

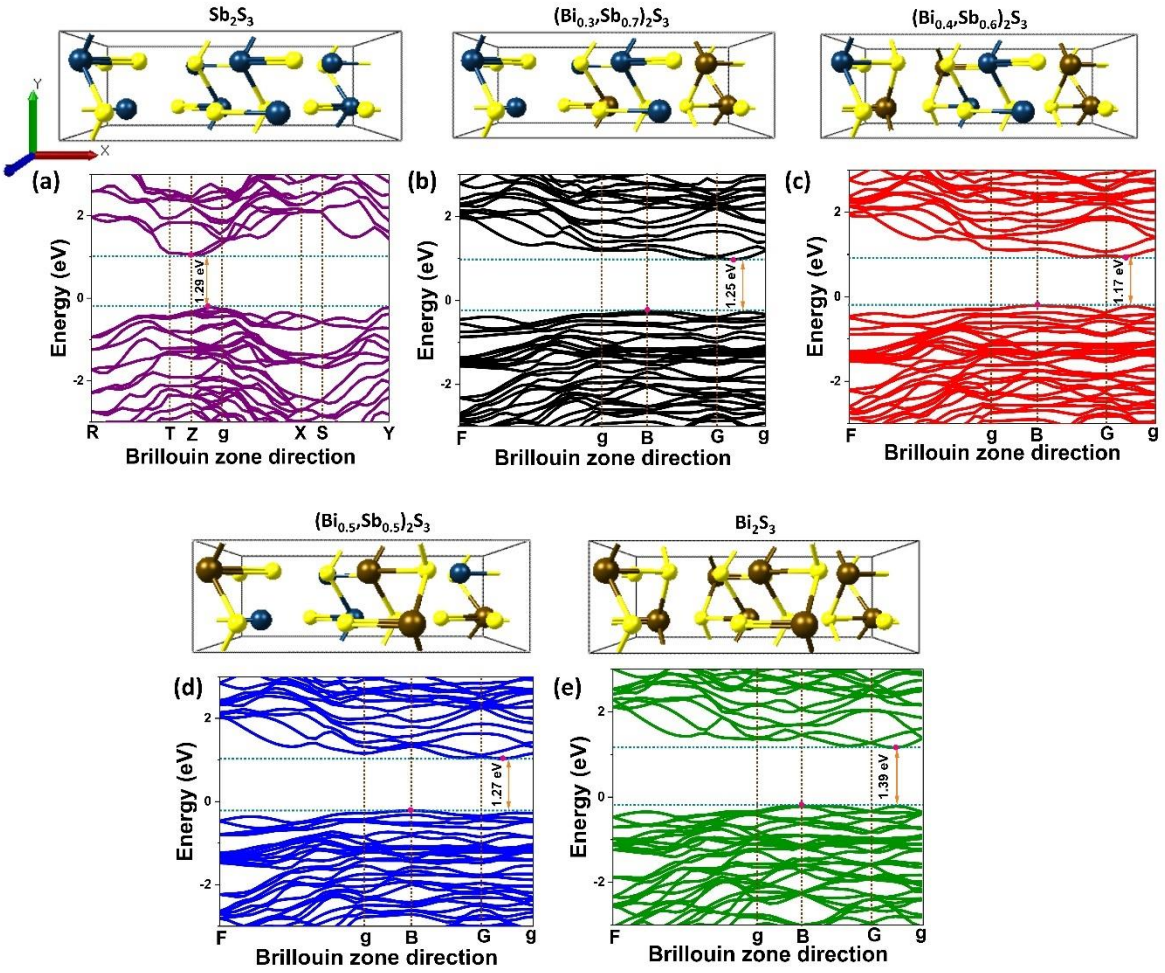

Figure A.2. (a-e) presents the calculated band structures and atomic configurations of Sb_2S_3 and its Bi-substituted variants, $(Bi_xSb_{1-x})_2S_3$ (x = 0 to 1), illustrating the evolution of the electronic properties and structural changes with increasing Bi content, including bandgap narrowing, band flattening, and lattice distortions, which suggest tunable optoelectronic characteristics for potential applications.

Figure A.2(a-e) illustrates the calculated band structures and corresponding atomic configurations of Sb_2S_3 and its Bi-substituted variants, $(Bi_xSb_{1-x})_2S_3$, where x ranges from 0 to 1. These plots highlight the evolution of the electronic properties and structural changes as Bi substitution increases. The pristine Sb_2S_3 structure, shown in Figure A.2(a), follows an orthorhombic Brillouin zone path R-T-Z-g (Γ)-X-S-Y. The calculated direct bandgap at the Γ point is 1.29 eV, with well-defined and sharp electronic bands. High symmetry points such as R and Γ show considerable band dispersions, suggesting favorable carrier transport properties [216]. The atomic model reveals a highly ordered lattice structure characteristic of pristine Sb_2S_3. Upon introducing 30% Bi substitution, as shown in Figure A.2(b), the Brillouin zone

path transitions to F-Γ-B-G-Γ, and the bandgap decreases slightly to 1.25 eV. The appearance of new electronic states and band crossings at F and G points indicates significant electronic interactions due to the Bi incorporation. The curvature of the conduction band near the Γ point becomes flatter, which implies a reduction in carrier mobility. The atomic structure shows slight lattice distortions, primarily reflected in changes in bond angles and lengths compared to pristine Sb_2S_3. At 40% Bi substitution, the bandgap narrows further to 1.17 eV, as shown in Figure A.2(c). The band structure reveals pronounced states near the B and G points, with flatter conduction band regions around F and Γ, indicating increased carrier localization, which may hinder charge transport. Structural analysis suggests that higher Bi incorporation induces lattice distortions, leading to increased instability and disorder. The significant reduction in bandgap arises from enhanced Sb–Bi orbital interactions, which delocalize the valence band. Additionally, lattice strain alters bond angles, potentially introducing mid-gap states or flattening the band structure. The presence of defect states, such as Bi or Sb vacancies, may further lower the optical gap. Moreover, the Bi 6s lone pair, which reduces band dispersion, likely stabilizes lower energy states, contributing to the observed bandgap narrowing [217].

In Figure A.2(d), with 50% Bi substitution, the bandgap slightly increases to 1.27 eV. The electronic bands exhibit complex behavior with significant flattening near the G and B points. Such flattening implies reduced electronic dispersion and the presence of localized electronic states. The atomic structure reveals substantial lattice rearrangement, with distorted Bi-S bond angles and increased unit cell complexity, indicating a transition toward a different structural phase. The shift in bandgap towards Sb_2S_3, rather than Bi_2S_3, is primarily due to crystal structure stabilization. At 50% substitution, the system adopts a configuration that aligns more closely with Sb_2S_3 in terms of lattice symmetry and bonding. The Bi 6s lone pair also plays a crucial role, as its asymmetric charge distribution typically induces local distortions [217]. However, at this composition, the balanced presence of Bi and Sb minimizes these distortions, making the band structure more similar to Sb_2S_3. Furthermore, unlike the 40% Bi substitution, which introduces structural disorder and narrows the bandgap, the 50% composition stabilizes a more ordered phase, reducing mid-gap states and preserving a bandgap close to that of Sb_2S_3.

Figure A.2(e) illustrates the fully substituted Bi_2S_3 structure with an increased bandgap of 1.39 eV. The band structure shows significant flattening near Γ and reduced dispersion at B, indicating stronger carrier localization and enhanced electronic interactions. The atomic model reveals a Bi-rich framework with distinct lattice coordination, marking a structural transition from Sb_2S_3. The bandgap difference between Sb_2S_3 (1.29 eV) and Bi_2S_3 (1.39 eV) arises from

their electronic structures. Sb_2S_3, with its higher covalency due to Sb's greater electronegativity, has a narrower bandgap. In contrast, Bi_2S_3's increased ionic character broadens the conduction band, slightly raising the bandgap. The conduction band minimum (CBM) in Sb_2S_3 is primarily derived from Sb 5p states, while the valence band maximum (VBM) originates from S 3p states. Weaker Sb–S hybridization leads to a lower bandgap, whereas Bi_2S_3's delocalized Bi 6p orbitals contribute to a wider gap. Moreover, stronger spin-orbit coupling (SOC) in Bi, which generally lowers the bandgap, is counteracted by robust Bi–S interactions, resulting in a slightly higher bandgap than Sb_2S_3 [215]. Progressive Bi substitution in Sb_2S_3 modulates the bandgap while introducing structural distortions. The emergence of new symmetry points and band flattening across the Brillouin zone highlight the influence of Bi-induced electronic interactions, making Bi-substituted Sb_2S_3 a viable candidate for tailored optoelectronic applications.

Table A.2: Structural and lattice parameters for different $(Bi,Sb)_2S_3$ compositions.

System	a (Å)	b (Å)	c (Å)	Volume (Å³)	Pressure (MPa)
Sb_2S_3	12.11	3.88	11.19	525.7	8
$(Bi_{0.3}, Sb_{0.7})_2S_3$	12	3.94	11.16	527.3	-38
$(Bi_{0.4}, Sb_{0.6})_2S_3$	12	3.94	11.14	529.7	-109
$(Bi_{0.5}, Sb_{0.5})_2S_3$	11.9	3.96	11.18	526.9	-113
Bi_2S_3	11.8	4.0	11.18	530.5	-236

Table A.3: Electronic properties of various $(Bi,Sb)_2S_3$ alloys, including bandgap and conduction band minimum (CBM).

System	Band Gap (eV)	CBM (eV)	VBM (eV)	Fermi Level (eV)	Behavior
Sb_2S_3	1.29	1.054	-0.240	0.407	Intrinsic SC
$(Bi_{0.3}, Sb_{0.7})_2S_3$	1.25	1.03	-0.22	0.405	Intrinsic SC
$(Bi_{0.4}, Sb_{0.6})_2S_3$	1.17	0.95	-0.22	0.360	Intrinsic SC
$(Bi_{0.5}, Sb_{0.5})_2S_3$	1.27	1.034	-0.231	0.401	Intrinsic SC
Bi_2S_3	1.39	1.173	-0.219	0.477	Intrinsic SC

Table A.4: Material behavior and density of $(Bi,Sb)_2S_3$ compositions with varying bismuth content.

System	Density (Mg/m^3)	Atomic Partial Charges	Notable Features
Sb_2S_3	4.29	Sb: ~2.57, S: ~3.21	Typical semiconductor properties
$(Bi_{0.3}, Sb_{0.7})_2S_3$	5.1	Bi/Sb: Mixed	Alloying increases density slightly
$(Bi_{0.4}, Sb_{0.6})_2S_3$	5.35	Bi/Sb: Mixed	Increased compression, density rises
$(Bi_{0.5}, Sb_{0.5})_2S_3$	5.38	Bi/Sb: Mixed	Stable alloy, close to Bi_2S_3
Bi_2S_3	6.4	Bi: ~12.4, S: ~3.20	High stability and consistent bandgap

Incorporating bismuth into antimony sulfide (Sb_2S_3) to form alloyed $(Bi,Sb)_2S_3$ materials leads to significant changes in the structural and electronic properties of the resulting films, as seen in Table A.2. The lattice constants of pure Sb_2S_3 are a = 12.11 Å, b = 3.88 Å, and c = 11.19 Å, with a material volume of 525.7 $Å^3$ at a pressure of 8 MPa. When bismuth is introduced, these parameters change subtly. For example, at 50% bismuth content, the lattice constant a decreases slightly to 11.9 Å, while b increases to 3.96 Å. These changes indicate a structural rearrangement at the atomic level, which could influence material stability and optoelectronic performance. The pressure associated with these alloys is consistently negative, with the pressure becoming more negative as the bismuth content increases, reaching -236 MPa for Bi_2S_3. This negative pressure suggests that bismuth incorporation leads to compression of the material's structure, which may affect its electronic and optical properties. When comparing to Bi-doped Sb_2S_3, the alloyed $(Bi,Sb)_2S_3$ system shows a more comprehensive impact on the

materials structure, with Bi atoms causing a broader rearrangement of the Sb–S bonds [212]. Unlike doping, where Bi atoms occupy specific Sb sites and create site-specific distortions, alloying results in a more uniform change in the bond lengths and angles, which can further influence the materials stability and electronic properties [212].

The electronic properties of the $(Bi,Sb)_2S_3$ alloys, as detailed in Table A.3, also exhibit clear trends with increasing bismuth content. Pure Sb_2S_3 has a bandgap of 1.29 eV, which narrows slightly to 1.25 eV for $(Bi_{0.3},Sb_{0.7})_2S_3$ and 1.17 eV for $(Bi_{0.4},Sb_{0.6})_2S_3$. However, at 50% bismuth content, $(Bi_{0.5},Sb_{0.5})_2S_3$ shows a slight increase in the bandgap to 1.27 eV, with Bi_2S_3 exhibiting the widest bandgap at 1.39 eV. These changes suggest that while bismuth incorporation initially enhances conductivity, higher bismuth concentrations stabilize the electronic structure, potentially reducing defects and enhancing material stability. The conduction band minimum (CBM) and valence band maximum (VBM) shift in response to the alloying process, but the Fermi level remains within the intrinsic semiconductor range across all compositions, indicating stable semiconductor behavior with tunable optoelectronic properties. The theoretical analysis of $(Bi,Sb)_2S_3$ alloys, showing bandgap narrowing followed by stabilization with increasing bismuth content, aligns with the observed complex density of states and enhanced delocalization in Bi-doped Sb_2S_3, indicating changes in electronic properties [212].

The material density of the alloys also increases as bismuth content rises, as shown in Table A.4. Pure Sb_2S_3 has a density of 4.29 Mg/m³, which increases to 5.1 Mg/m³ for $(Bi_{0.3},Sb_{0.7})_2S_3$, 5.35 Mg/m³ for $(Bi_{0.4},Sb_{0.6})_2S_3$, and 5.38 Mg/m³ for $(Bi_{0.5},Sb_{0.5})_2S_3$. The density of Bi_2S_3 is the highest, at 6.4 Mg/m³, reflecting the heaviest bismuth concentration. This increase in density corresponds to the higher atomic mass of bismuth and suggests that the alloys become more compact and stable as the bismuth content rises. Additionally, the atomic partial charges of the alloys show mixed charge distributions between Bi and Sb, with charge redistribution occurring as bismuth content increases. Bi_2S_3, in particular, exhibits a high density and stable charge distribution, contributing to its greater material stability, which is critical for device performance.

Substituting bismuth into Sb_2S_3 also induces crucial changes in the electronic structure, which are confirmed by density of states (DOS) calculations. Pure Sb_2S_3 has a bandgap of 1.29 eV, and the DOS reveals that the valence band is primarily composed of sulfur p-orbitals, while the conduction band is dominated by antimony contributions. As bismuth is substituted for antimony, the bandgap narrows, reaching a minimum of 1.17 eV for $(Bi_{0.4},Sb_{0.6})_2S_3$. However,

at higher bismuth concentrations, the bandgap increases again, with Bi_2S_3 exhibiting a bandgap of 1.39 eV. This narrowing and subsequent broadening indicate enhanced hybridization between Bi and Sb orbitals, improving electronic interactions and contributing to structural stability. The shift in electronic structure emphasizes the tunability of the material's semiconductor properties, particularly for $(Bi_{0.5},Sb_{0.5})_2S_3$, which represents an ideal compromise between structural stability and electronic performance.

The structural modifications resulting from bismuth substitution are further reflected in the lattice volume and axial elongation, particularly along the b-axis. Bismuth's larger atomic radius and higher mass compared to antimony lead to a slight elongation of the b-axis and an increase in lattice volume. Intermediate compositions, particularly $(Bi_{0.5},Sb_{0.5})_2S_3$, exhibit improved lattice symmetry and reduced defect density, suggesting optimized material properties for device applications. The substitution of bismuth not only leads to increased material density but also enhances the overall stability of the structure, contributing to the material's long-term performance in electronic devices. These changes in lattice symmetry, along with a more stable charge distribution, contribute to the alloy's enhanced performance and suggest it could be suitable for a wide range of optoelectronic applications.

The VASP results for the $(Bi_{0.5},Sb_{0.5})_2S_3$ thin film demonstrate its potential for photodetection across a broad wavelength range. The bandgap of 1.27 eV allows for enhanced light absorption in the UV-VIS-NIR spectrum, and the alloying of bismuth with antimony optimizes the electronic structure, improving charge transport properties. This results in reduced recombination losses and enhanced photogenerated carrier separation, leading to higher photodetector efficiency. The $(Bi_{0.5},Sb_{0.5})_2S_3$ sample also exhibits a stable lattice with fewer defects and reduced strain, owing to bismuth incorporation. This contributes to its material integrity, making it more resilient to environmental degradation. The higher density of this composition (5.38 Mg/m^3) further enhances its chemical stability, making it a promising candidate for photodetector applications. These factors collectively contribute to the material's excellent performance in optoelectronic devices, particularly for applications in photodetection.

The incorporation of bismuth into Sb_2S_3 results in an alloy system with tunable structural, electronic, and material properties, offering flexibility for various applications, especially in photodetectors. Among the different compositions, $(Bi_{0.5},Sb_{0.5})_2S_3$ emerges as the most promising candidate for future device applications due to its optimal balance of structural

stability, density, and electronic performance. The ability to modify the material's properties through bismuth alloying creates opportunities for improving the efficiency of optoelectronic devices. This versatility positions $(Bi,Sb)_2S_3$ alloys as a valuable material for further research and development in the field of optoelectronics.

A.5 Density of States Analysis

The Density of States (DOS) analysis provides critical insights into the electronic structure of materials, particularly in understanding band edge contributions from different atomic orbitals. The DOS of five different compositions: pure Sb_2S_3, Bi-substituted Sb_2S_3 ($(Bi_{0.3}Sb_{0.7})_2S_3$, $(Bi_{0.4}Sb_{0.6})_2S_3$, $(Bi_{0.5}Sb_{0.5})_2S_3$), and pure Bi_2S_3 are presented in Figure A.3 (a-e). The color-coded partial DOS helps to determine which atomic orbitals contribute to the valence and conduction band edges, influencing the material's optoelectronic properties. In the case of pure Sb_2S_3 (Figure A.3 (a)), the total DOS (black curve) shows a well-defined bandgap, with a sharp density of states at the conduction band minimum (CBM) and valence band maximum (VBM). The valence band edge is predominantly composed of Sb p-orbitals (blue) and S p-orbitals (orange), indicating strong hybridization between Sb and S. This is expected, as antimony in Sb_2S_3 exists in a 3+ oxidation state, forming covalent bonds with sulfur. The conduction band, on the other hand, is primarily dominated by Sb s-orbitals (light blue), suggesting that the lowest energy electronic transitions involve Sb-based conduction states. The presence of a high DOS at the CBM implies good electron transport properties, making Sb_2S_3 a promising material for optoelectronic applications.

The valence band is primarily dominated by Sb and Bi p-orbitals, while the conduction band exhibits contributions from Sb s-orbitals and Bi p-orbitals. The gradual shift in DOS indicates enhanced hybridization, influencing the electronic structure and optoelectronic properties.

With the introduction of 30% Bi substitution (Figure A.3 (b)), significant changes are observed in the DOS. The valence band remains largely dominated by Sb p-orbitals (blue) and S p-orbitals (orange); however, the contribution from Bi p-orbitals (brown) begins to emerge at the VBM. This suggests that Bi incorporation modifies the electronic structure by slightly perturbing the bonding interactions. The conduction band also sees contributions from Bi p-orbitals, which were absent in pure Sb_2S_3. This indicates that Bi plays a role in modifying the conduction band edge, potentially affecting the bandgap. Since Bi has a larger atomic radius and different electronegativity compared to Sb, this substitution could lead to localized states that slightly alter the electronic band structure. At 40% Bi substitution (Figure A.3 (c)), the

DOS follows a similar trend to the 30% case, but with enhanced Bi contributions. The Bi p-orbitals become more pronounced at both the valence and conduction bands, while Sb contributions decrease slightly. This signifies increased Bi-S bonding interactions, altering the band dispersion and possibly reducing the bandgap due to increased hybridization. The conduction band DOS shows a smoother distribution, indicating a potential change in carrier effective mass, which may improve charge transport properties. The band edges remain relatively sharp, implying that electronic transitions are still well-defined. For the 50% Bi-substituted composition (Figure A.3 (d)), a significant transformation occurs in the DOS. The valence band now shows almost equal contributions from Bi p-orbitals (brown) and Sb p-orbitals (blue), indicating strong Bi-Sb-S hybridization. This suggests that the material is transitioning towards a Bi-dominated electronic structure. In the conduction band, Bi p-orbitals and Sb s-orbitals contribute nearly equally, meaning that the electronic transitions are now influenced by both Sb and Bi states. The overall DOS distribution appears smoother, which may reduce electron-hole recombination and enhance carrier mobility. Such changes in DOS are critical for tuning the material's optical absorption properties, potentially benefiting photodetector applications.

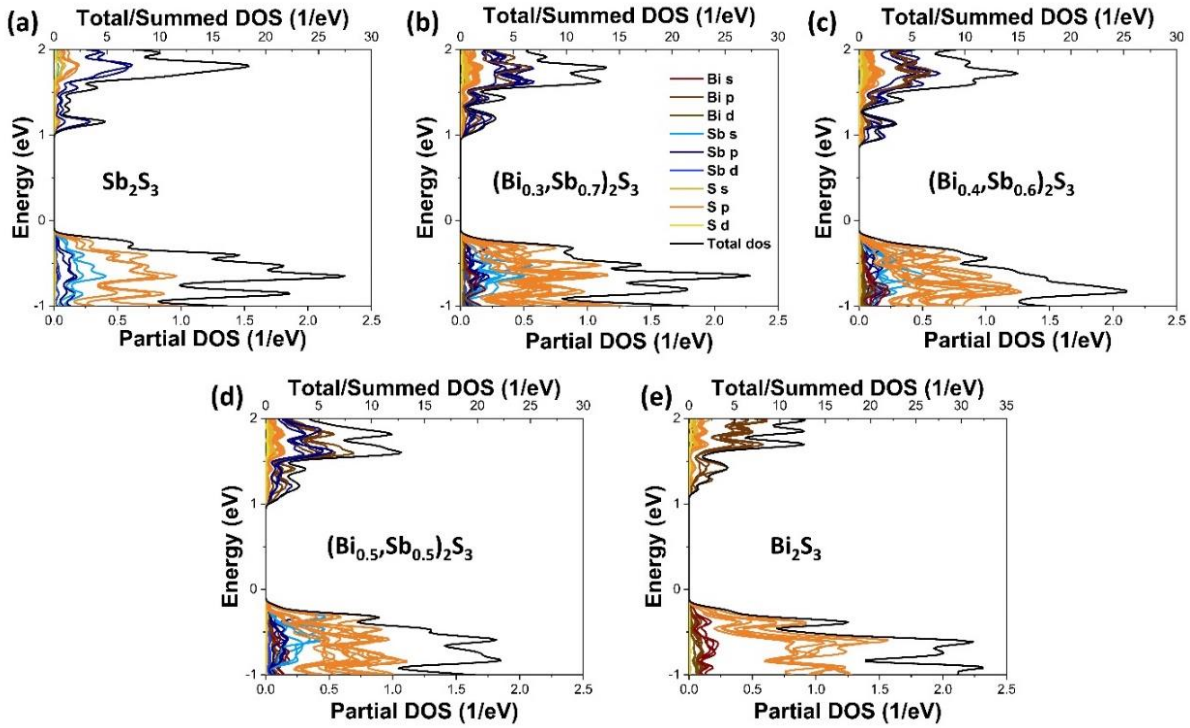

Figure A.3. Projected DOS plots for (a) Sb_2S_3, (b) $(Bi_{0.3}Sb_{0.7})_2S_3$, (c) $(Bi_{0.4}Sb_{0.6})_2S_3$, (d) $(Bi_{0.5}Sb_{0.5})_2S_3$, and (e) Bi_2S_3, showing the evolution of electronic states with increasing Bi substitution.

In pure Bi_2S_3 (Figure A.3 (e)), the DOS shows a drastically different profile compared to Sb_2S_3. The valence band is now almost entirely composed of Bi p-orbitals (brown) and S p-orbitals (orange), indicating that the electronic structure is dominated by Bi-S interactions. The conduction band also shifts towards Bi-based states, with significant contributions from Bi p-orbitals. Compared to Sb_2S_3, the conduction band DOS is broader, suggesting a more dispersed electronic structure. Across the five compositions, the gradual substitution of Sb with Bi leads to a progressive shift in the DOS characteristics. Initially dominated by Sb p-orbitals, the valence band progressively incorporates Bi p-orbitals, leading to a mixed Sb-Bi character. This suggests that Bi substitution enhances orbital hybridization, which may lower the bandgap. The pure Sb_2S_3 conduction band is primarily Sb s-based, but with increasing Bi content, Bi p-orbitals contribute significantly, altering the CBM and possibly affecting electron transport properties. The gradual increase in Bi content modifies the band dispersion, potentially influencing optical absorption, carrier lifetimes, and charge mobility. These changes are crucial for applications in photodetectors, thermoelectrics, and photovoltaics.

A.6 Phonon calculations

The phonon calculations obtained using VASP for Sb_2S_3 and Bi-Sb mixed chalcogenides are presented in Figure A.4(a-c), providing detailed insights into the thermodynamic properties of these materials. The plots illustrate key thermodynamic parameters, including total energy (E), entropy (S), heat capacity (Cv), Helmholtz free energy (A), and the temperature-scaled entropy (-TS) as functions of temperature. These parameters offer valuable information on the structural stability, vibrational states, and overall thermodynamic behavior of the materials under varying temperature conditions. In Figure A.4(a), the thermodynamic profile of pure Sb_2S_3 is shown. The total energy exhibits a continuous decrease with increasing temperature, indicating enhanced system stability as the temperature rises. This behavior can be attributed to the material's ability to accommodate thermal energy without undergoing structural instability. The entropy curve exhibits an exponential increase, a characteristic feature of crystalline materials where the number of accessible vibrational states increases with temperature. The heat capacity follows the Dulong-Petit limit, showing a saturation trend at higher temperatures, which aligns with the theoretical prediction for crystalline solids as all vibrational modes are fully excited. The Helmholtz free energy (A) demonstrates a consistent decline across the temperature range,

reflecting the increasing thermodynamic favorability of the material with temperature. The -TS component plays a pivotal role in this decline, contributing significantly to the reduction of Helmholtz free energy, particularly at elevated temperatures. This underscores the importance of entropy in stabilizing the system under thermal excitation.

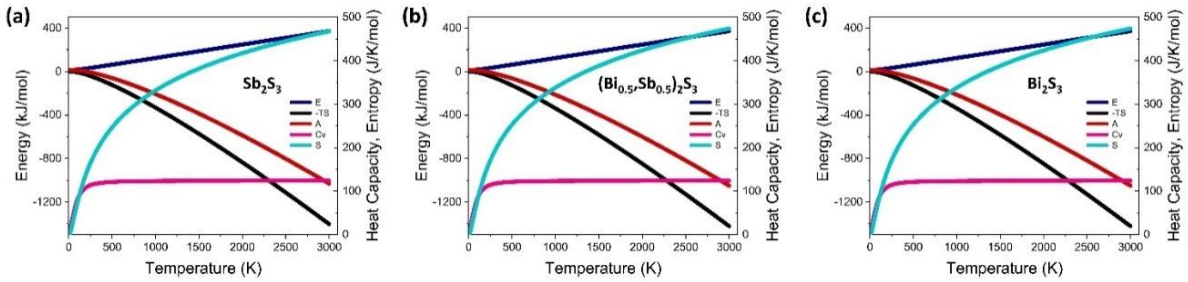

Figure A.4. Thermodynamic properties of a) Sb_2S_3, b) $(Bi_{0.5}Sb_{0.5})_2S_3$, and c) Bi_2S_3, showing phonon calculations and how Bi substitution enhances thermodynamic stability and vibrational characteristics with temperature.

In Figure A.4(b), corresponding to the $(Bi_{0.5},Sb_{0.5})_2S_3$ composition, a balanced substitution between Bi and Sb leads to more negative total energy values compared to pure Sb_2S_3, indicating enhanced thermodynamic stability. The substitution introduces more complex bonding interactions, which contribute to the observed increase in stability. The entropy remains high, consistent with the vibrational contributions from both Bi and Sb atoms, while the heat capacity saturates at higher temperatures. The Helmholtz free energy also shifts to more negative values, confirming a thermodynamically favorable state for this mixed composition. The combined contribution of entropy and energetic stabilization due to the Bi substitution enhances the system's overall stability. Figure A.4(c) presents the thermodynamic properties of Bi_2S_3. This sample shows the most negative total energy values among the compositions studied, indicating superior thermodynamic stability compared to Sb-rich samples. The entropy and heat capacity are the highest due to the heavier atomic mass of Bi and the more complex bonding nature of Bi_2S_3. These factors contribute to increased vibrational states and higher thermal energy absorption capabilities. The -TS component becomes dominant at elevated temperatures, driving the Helmholtz free energy to its most stable state. The increased entropic contribution underscores the material's capability to maintain stability under high-temperature conditions. The phonon calculations and thermodynamic analysis reveal a clear trend where increasing Bi content consistently improves system stability and introduces more complex vibrational states. These observations highlight the potential of Bi-Sb chalcogenides for applications that require high

thermal stability and robust structural properties. The enhanced thermodynamic stability observed for the mixed compositions, particularly $(Bi_{0.5},Sb_{0.5})_2S_3$ and Bi_2S_3, suggests that controlled Bi substitution can be a viable strategy for optimizing the thermodynamic and structural properties of chalcogenide materials.

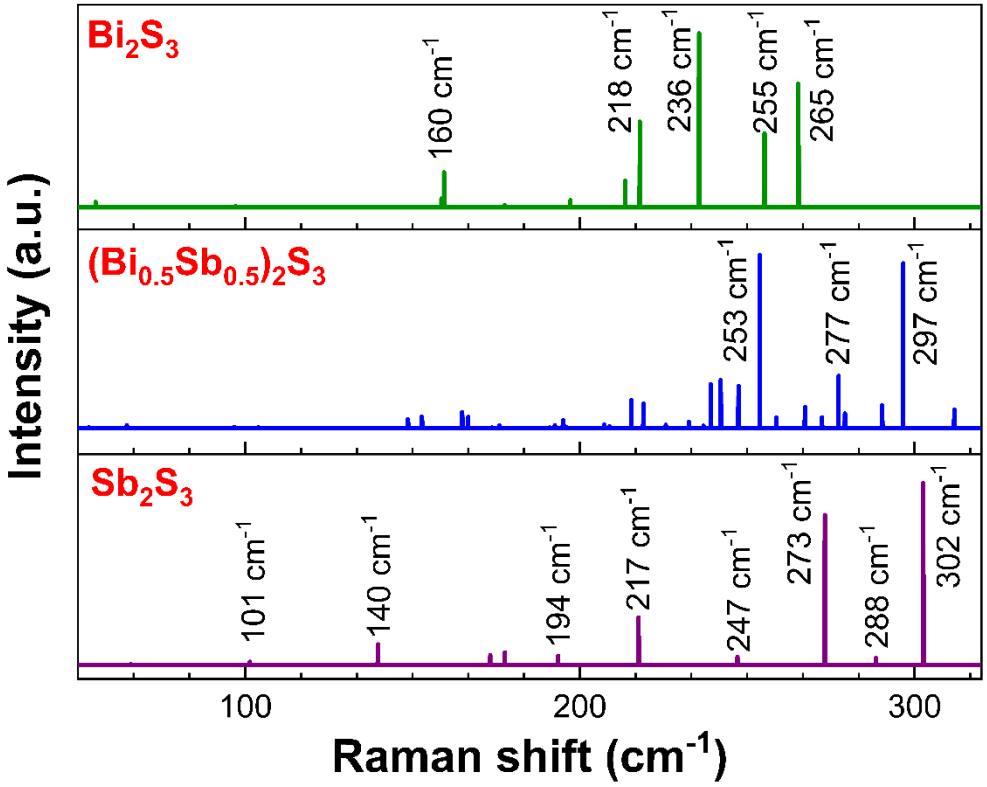

Figure A.5. shows the Raman phonon calculation illustrating the structural evolution and vibrational changes upon Bi substitution in Sb_2S_3.

The vibrational and symmetry analysis of Bi_2S_3, Sb_2S_3, and $(Bi_{0.5}Sb_{0.5})_2S_3$ reveals distinct structural characteristics that influence their optoelectronic and thermal transport properties(Table A.5). Bi_2S_3 and $(Bi_{0.5}Sb_{0.5})_2S_3$ exhibit low-symmetry structures associated with the C_1 (1) point group, where the only symmetry operation is identity. This absence of symmetry constraints results in a broad vibrational spectrum for Bi_2S_3, as there are no restrictions on its phonon modes. Alloying in $(Bi_{0.5}Sb_{0.5})_2S_3$ disrupts lattice symmetry, introducing complex phonon interactions due to the random distribution of Bi and Sb atoms. This disorder alters vibrational dynamics, enhancing light absorption and thermal transport, making the alloy a promising candidate for optoelectronic and thermoelectric applications. In contrast, Sb_2S_3 adopts an orthorhombic D_{2h} (mmm) point group, which incorporates multiple symmetry elements, including reflection and inversion operations. These structural symmetries impose order on its

vibrational modes, resulting in distinct classifications observed in both Raman and infrared (IR) spectra. The Raman-active Ag, B1g, B2g, and B3g modes in Sb_2S_3 contribute to its selective light-matter interactions, while B1u, B2u, and B3u modes are responsible for IR absorption, making Sb_2S_3 suitable for applications requiring precise spectral control.

Table A.5. compares the crystal symmetries, phonon frequencies, vibrational characteristics, and optical activities of Bi_2S_3, Sb_2S_3, and $(Bi_{0.5}Sb_{0.5})_2S_3$.

Parameter	**Bi_2S_3**	**Sb_2S_3**	**$(Bi_{0.5}Sb_{0.5})_2S_3$**
Crystal Point Group	C_1 (1)	D_2h (mmm)	C_1 (1)
Symmetry Elements	Identity only	8 elements (including inversion center)	Identity only
Irreducible Representations	A(RI) (exclusive)	Ag, B1g, B2g, B3g for Raman; B1u, B2u, B3u for IR	A(RI) (exclusive)
TO Phonon Frequency Range (THz)	-0.021 to 7.774	-0.340 to 9.073	-0.108 to 6.565
LO Phonon Frequency Range (THz)	-0.045 to 8.572	-0.340 to 9.892	-0.085 to 9.644
Negative Phonon Modes	Present (-0.021, -0.045 THz)	Present (-0.340, -0.020 THz)	Present (-0.108, -0.085 THz)
Vibrational Characteristics	Isotropic; all A(RI) modes	Complex; mixture of Ag, B modes	Complex with vibrational mode mixing
Raman Activity	Unpolarized scattering possible	Ag, B1g, B2g, B3g modes Raman active	Possible due to multiple A(RI) modes
IR Activity	None	B1u, B2u, B3u IR-active modes	No distinct separation
Anharmonicity Indicators	Negative frequencies	Negative frequencies	Negative frequencies

Raman spectra further confirm the structural evolution upon Bi substitution (Figure A.5). Sb_2S_3 exhibits peaks at 101 cm^{-1}, 140 cm^{-1}, 194 cm^{-1}, 217 cm^{-1}, 247 cm^{-1}, 273 cm^{-1}, 288 cm^{-1}, and 302 cm^{-1}, corresponding to Sb–S stretching and bending vibrations in the orthorhombic phase. Bi_2S_3, characterized by its rhombohedral phase, displays peaks at 160 cm^{-1}, 218 cm^{-1}, 236 cm^{-1}, 255 cm^{-1}, and 265 cm^{-1}, with lower vibrational frequencies due to the heavier Bi atoms that weaken bond stiffness. The alloy $(Bi_{0.5}Sb_{0.5})_2S_3$ presents a combination of these vibrational features, with peaks at 253 cm^{-1}, 277 cm^{-1}, and 297 cm^{-1}, along with additional weak modes. The observed shifts and broadened peaks indicate structural distortion, phonon confinement, and

increased disorder due to Bi incorporation, leading to inhomogeneous strain. The Bi–S and Sb–S interactions influence the sulfur bonding environment, affecting phonon scattering, charge transport, and overall optoelectronic properties.

Vibrational frequency analysis further distinguishes these materials. Bi_2S_3 exhibits simpler vibrational modes, with transverse optical (TO) frequencies ranging from -0.021 THz to 7.774 THz and longitudinal optical (LO) frequencies extending up to 8.572 THz. Negative frequencies, indicative of structural instability, anharmonic effects, or numerical artifacts in density functional theory (DFT) calculations, are present in all three materials. Sb_2S_3, with its stiffer Sb–S bonds, reaches higher frequencies of up to 9.892 THz, reflecting greater structural stability. The alloy $(Bi_{0.5}Sb_{0.5})_2S_3$ displays a broader vibrational spectrum with LO frequencies extending to 9.644 THz, highlighting significant phonon mixing and lattice distortions due to alloying. The vibrational mode analysis also underscores differences in scattering properties. The minimal symmetry constraints in Bi_2S_3 result in broader Raman peaks, whereas the well-ordered vibrational modes of Sb_2S_3 produce sharp and well-defined spectral features. The alloy, due to its disrupted symmetry and enhanced phonon interactions, presents more complex scattering behavior with broader Raman peaks, indicating increased phonon disorder. The incorporation of Sb into the Bi_2S_3 framework combines the structural flexibility of Bi_2S_3 with the enhanced stability conferred by Sb–S interactions, potentially improving phonon-mediated properties such as light absorption and charge transport. These findings highlight the structural and vibrational distinctions among the three materials and emphasize the alloy's potential for advanced applications where tunability of vibrational modes is critical for optimizing performance.

A.7 Crystalline structure

Figure A.6(a) displays the X-ray diffraction (XRD) patterns of Bi-alloyed Sb_2S_3 thin films synthesized via the chemical bath deposition method. A clear shift from antimony sulfide to bismuth sulfide phases is observed as the bismuth content in the alloy increases. The diffraction patterns reveal an orthorhombic crystal system with a Pbnm space group, consistent with phase-pure Sb_2S_3 (ICDD reference no: 000060474) and Bi_2S_3 (ICDD reference no: 000431471). For Sb_2S_3, the lattice parameters are determined to be a = 11.229 Å, b = 11.31 Å, and c = 3.839 Å, while for Bi_2S_3, the parameters are a = 11.15 Å, b = 11.3 Å, and c = 3.98 Å. The main reflection peaks for Sb_2S_3 lies at 15.6°, 17.5°, 25°, 28.5°, 35.6°, and 43.2°, corresponding to the (020), (120), (310), (230), (240), and (520) planes, respectively. About the Bi_2S_3 it exhibits peaks at

15.8°, 17.8°, 25°, 27.3°, 29°, 39.1°, 47.2°, and 48.2°, corresponding to the (200), (210), (130), (021), (211), (041), (530), and (060) planes, respectively (**Figure A.7**). Notably, the introduction of bismuth into the Sb_2S_3 matrix results in the disappearance of the peak at 35.6° and a shift of the 28.5° peak towards 29°, which is the main intense peak for Bi_2S_3. This shift, along with changes in peak intensity and the emergence of new phases, becomes more pronounced as the bismuth content increases. Specifically, the intensities of the (020), (120), and (310) planes of Sb_2S_3 decrease with higher Bi alloying, and new peaks appearing at 27.3°, 39.1°, and 48.2°, characteristic of phase-pure Bi_2S_3, emerge, as a result of significant alteration of the crystalline structure.

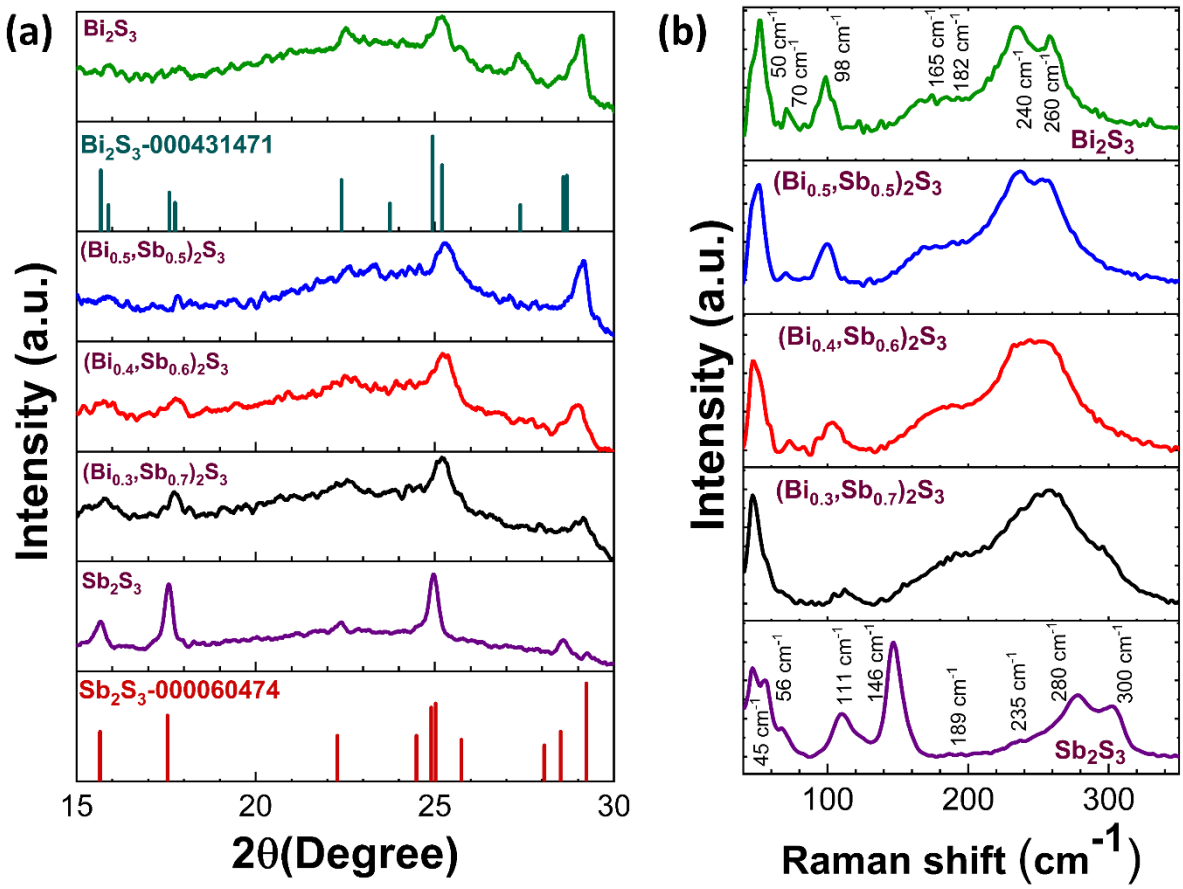

Figure A.6. Bi-alloyed Sb_2S_3 thin films at varying Bi and Sb ratio. (a) XRD pattern (JCPDS files are included as the reference pattern), (b) Raman spectra

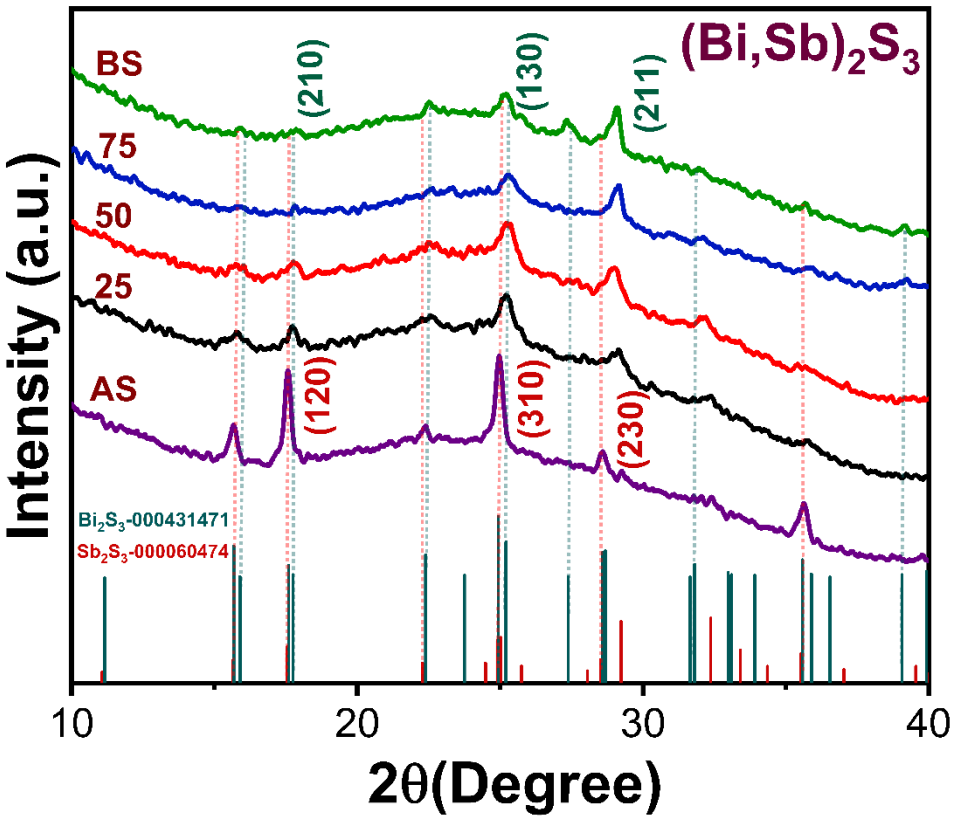

Figure A.7. Bi-alloyed Sb_2S_3 thin films XRD pattern from 10° to 40°.

Comparing our findings with other studies, the observed phase transition and peak shifts are consistent with reports on alloyed metal chalcogenides, where the introduction of a secondary metal leads to a gradual shift in diffraction peaks towards those of the alloying metal. For example, in similar alloy systems such as Bi-alloyed Sb_2Se_3, researchers have documented a shift in peak positions and the gradual disappearance of specific Sb_2Se_3 peaks as the Bi content increases, aligning with our observations in the Sb_2S_3 system[218][202]. Additionally, the reduction in intensity of Sb_2S_3 peaks and the emergence of new peaks unique to Bi_2S_3 are indicative of the formation of a solid solution, as seen in other Bi-alloyed systems. These findings are crucial as they demonstrate the tunability of the crystal structure through alloying, which can significantly influence the material's optoelectronic properties. This comparison underscores the potential for tailoring material properties by adjusting alloy compositions, a concept that has been successfully applied in various semiconductor systems to optimize performance for specific applications. The findings from this study contribute to a deeper understanding of the alloying effects in Sb_2S_3 and provide a foundation for further research into the development of high-performance materials for optoelectronic devices.

Figure A.6(b) shows the Raman spectra of Bi-alloyed Sb_2S_3 thin films. The Raman spectra of Bi_2S_3 thin films exhibit two distinct peaks at 54 and 100 cm^{-1} and one broad peak spanning 150 to 200 cm^{-1}. Furthermore, the strong and broad Raman peaks observed at 240 and 260 cm^{-1} are caused by the Bi_2S_3 A_g and B_{1g} vibrations [219][220]. In the case of Sb_2S_3, distinctive peaks of anti-symmetric Sb-S bending at 189 cm^{-1}, symmetric Sb-S bending at 235 cm^{-1}, and anti-symmetric Sb-S stretching at 280 and 300 cm^{-1} were noted[221]. In the instance of Bi-alloyed Sb_2S_3 thin films, we could see a shift in the Raman peak from pure Sb_2S_3 to pure Bi_2S_3 as the amount of Bi inclusion increased.

The Raman spectra of Bi-alloyed Sb_2S_3 thin films, showcases how the introduction of bismuth alters the vibrational modes characteristic of the parent compounds. The Raman spectra of pure Bi_2S_3 thin films are marked by two distinct peaks at 54 cm^{-1} and 100 cm^{-1}, along with a broad peak extending from 150 to 200 cm^{-1}. Additionally, strong and broad Raman peaks are observed at 240 cm^{-1} and 260 cm^{-1}, which correspond to the Ag and B1g vibrational modes of Bi_2S_3, as reported in previous studies [219,220]. On the other hand, the Raman spectra of pure Sb_2S_3 thin films exhibit characteristic peaks at 189 cm^{-1}, attributed to anti-symmetric Sb-S bending, 235 cm^{-1}, corresponding to symmetric Sb-S bending, and peaks at 280 cm^{-1} and 300 cm^{-1}, associated with anti-symmetric Sb-S stretching [221]. As bismuth is alloyed into Sb_2S_3, a noticeable shift in these Raman peaks is observed, transitioning from the distinctive features of Sb_2S_3 to those of Bi_2S_3, indicating a gradual alteration in the material's vibrational modes with increasing Bi content.

In studies of Bi-alloyed Sb_2Se_3, researchers have reported shifts in Raman peaks as the bismuth content increases, which align with the progressive substitution of antimony by bismuth in the crystal lattice[202]. These shifts in Raman spectra are indicative of changes in bond strength and lattice dynamics, which can be directly correlated with the material's alloy composition. Specifically, the broadening and shifting of peaks, such as those observed at 240 cm^{-1} and 260 cm^{-1} in Bi_2S_3, suggest a modification in the vibrational properties as the lattice accommodates the larger Bi atoms. Additionally, the disappearance or attenuation of specific Sb_2S_3 Raman peaks, including symmetric and anti-symmetric Sb-S bending and stretching modes, further supports the formation of a solid solution where Sb-S bonds are progressively replaced by Bi-S bonds. This phenomenon, observed in other alloyed Sb_2S_3 systems, underscores the tunability of Raman-active modes through alloying, with significant implications for the material's optoelectronic properties and potential device applications.

A.8 Elemental composition and chemical state

The XPS spectra presented here represent the core-level binding energy regions of Sb 3d and Bi 4f for samples with varying Bi:Sb ratios, ranging from pure Sb_2S_3 to Bi-doped systems, ultimately transitioning to pure Bi_2S_3. This detailed analysis sheds light on the effects of Bi alloying on the electronic structure of the alloyed $(Bi_xSb_{1-x})_2S_3$ samples. The analysis was conducted under controlled conditions following one cycle of 10-second argon ion beam etching, with acquisition parameters including a 400 μm spot size, 0.1 eV energy step size for high resolution, and a pass energy of 50 eV. All high-resolution peaks were fitted using a Gaussian-Lorentzian sum function with a Shirley-type background correction, ensuring accurate deconvolution of overlapping peaks.

In Figure A.8(a), which displays the Sb 3d core level, two prominent peaks corresponding to the Sb $3d_{5/2}$ and Sb $3d_{3/2}$ doublets are evident in all spectra. As the Bi content increases, transitioning from pure Sb_2S_3 to the alloy $(Bi_xSb_{1-x})_2S_3$, a slight shift is observed in the Sb $3d_{5/2}$ peak towards higher binding energy. This shift indicates a change in the local chemical environment of the Sb atoms due to the alloying with Bi. The increase in binding energy suggests that Bi incorporation alters the bonding interactions around Sb. As the Bi concentration increases, a progressive decrease in the intensity of the Sb peaks is observed. This can be attributed to the diminishing presence of Sb atoms as Bi is introduced into the alloy. The reduction in peak intensity is consistent with the decrease in Sb content as the Bi:Sb ratio shifts, which leads to a relative decrease in the number of Sb atoms contributing to the signal. Compared to pure Sb_2S_3, the Sb 3d peaks in the alloyed samples show slight broadening. This broadening reflects the presence of a mixed Sb and Bi environment, where subtle variations in the local bonding structures exist due to the coexistence of both elements in the lattice. The broader peaks indicate increased disorder or structural changes at the atomic level, which is typical in alloyed materials.

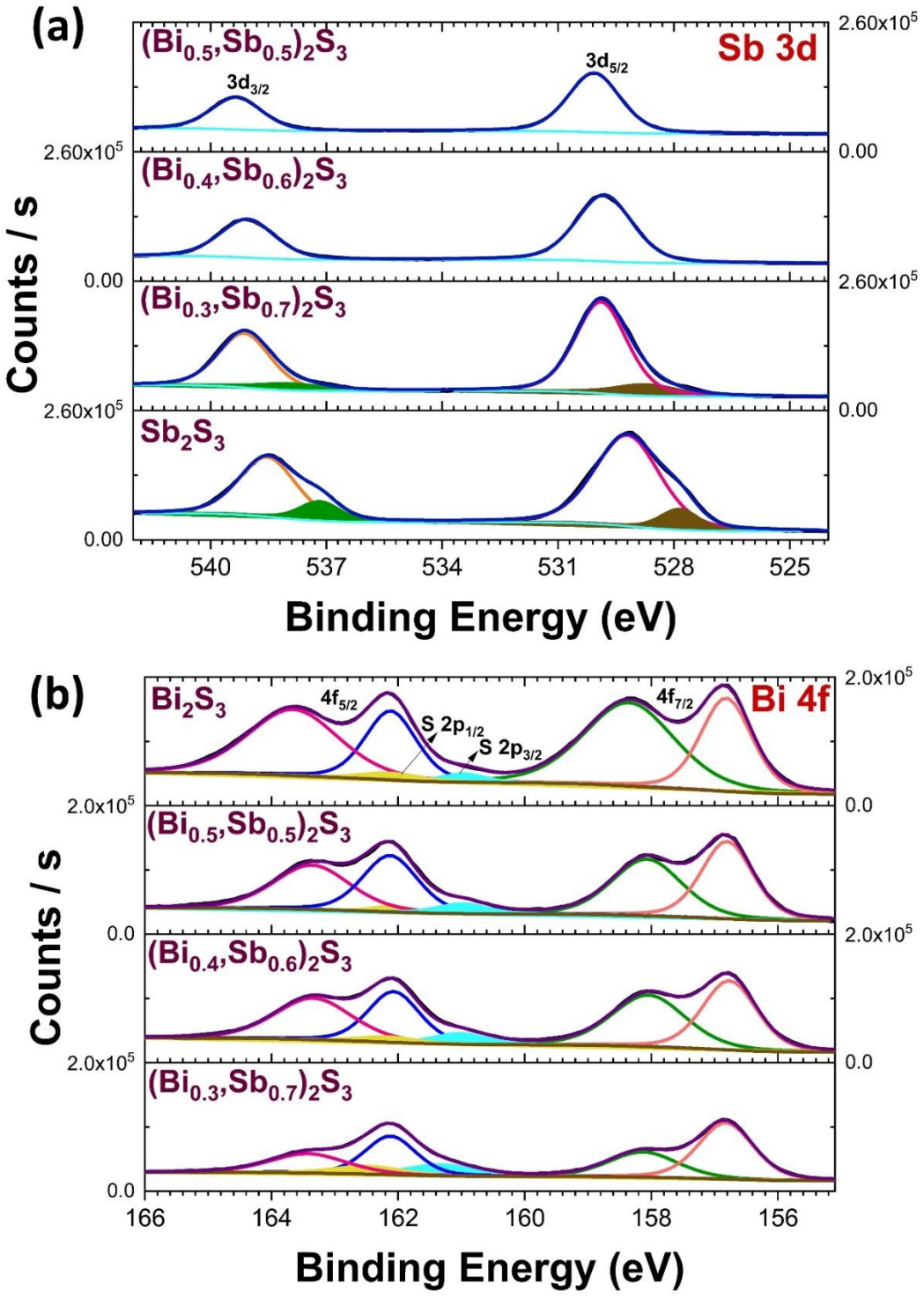

Figure A.8: XPS spectra of Sb 3d (a) and Bi 4f (b) core levels show binding energy shifts and changes in peak intensity and broadening with increasing Bi content, reflecting modifications in the chemical environment and bonding interactions between Sb and Bi in the alloys.

In Figure A.8(b), which shows the Bi 4f core level, two distinct peaks corresponding to the Bi $4f_{7/2}$ and Bi $4f_{5/2}$ doublets are evident in all Bi-containing samples. For pure Bi_2S_3, these peaks appear at characteristic binding energies. However, as Sb is introduced into the system, particularly in the $(Bi_{0.5}Sb_{0.5})_2S_3$ alloy, a shift towards lower binding energy is observed for the Bi peaks. This shift indicates a possible change in Bi's oxidation state or its interaction with the sulfur atoms, suggesting that Bi is more electropositive in the alloyed system compared to the pure Bi_2S_3 phase. The intensity of the Bi 4f peaks increases with the amount of Bi in the alloy, following the expected trend based on the stoichiometry of the samples. The highest peak intensity is observed in the pure Bi_2S_3 sample, where Bi content is maximal. As the Bi content decreases in the alloyed systems, the peak intensity of Bi also decreases proportionally, aligning with the Bi:Sb ratio. In the alloyed samples, the Bi peaks are slightly broader compared to pure Bi_2S_3. This broadening is likely due to a combination of factors, including mixed local environments around Bi atoms, potential minor variations in oxidation states, and possible strain effects induced by the incorporation of Sb into the lattice.

The observed shifts in the binding energies of both Sb and Bi peaks are indicative of changes in the local chemical environments caused by the alloying process. The introduction of Bi alters the Sb-S bonding characteristics, while Sb influences Bi-S interactions. This charge transfer between Bi and Sb atoms is a key feature of the alloying process, and it reflects the dynamic interactions between these two elements within the lattice.

In the S 2p region, small features for S $2p_{1/2}$ and S $2p_{3/2}$ are observed. These features remain largely unchanged across the various samples, suggesting that the sulfur environment is relatively stable during the alloying process. The lack of significant variation in the sulfur signals implies that sulfur's role in bonding is not heavily influenced by the Bi:Sb substitution.

The XPS analysis of the alloyed $(Bi_xSb_{1-x})_2S_3$ samples reveals several important trends: The Sb 3d peaks shift to higher binding energies with increased Bi content, while the Bi 4f peaks shift to lower binding energies. These shifts are indicative of changes in the local chemical environments and oxidation states of the elements involved. The intensity of the Sb 3d peaks decreases, while the intensity of the Bi 4f peaks increases, in line with the Bi:Sb ratio. The peaks for the alloyed samples are broader, indicating a more complex local bonding environment and potential structural strain. These findings confirm the successful incorporation of Bi into the Sb_2S_3 lattice and highlight the significant changes in the electronic structure and local bonding environment due to alloying.

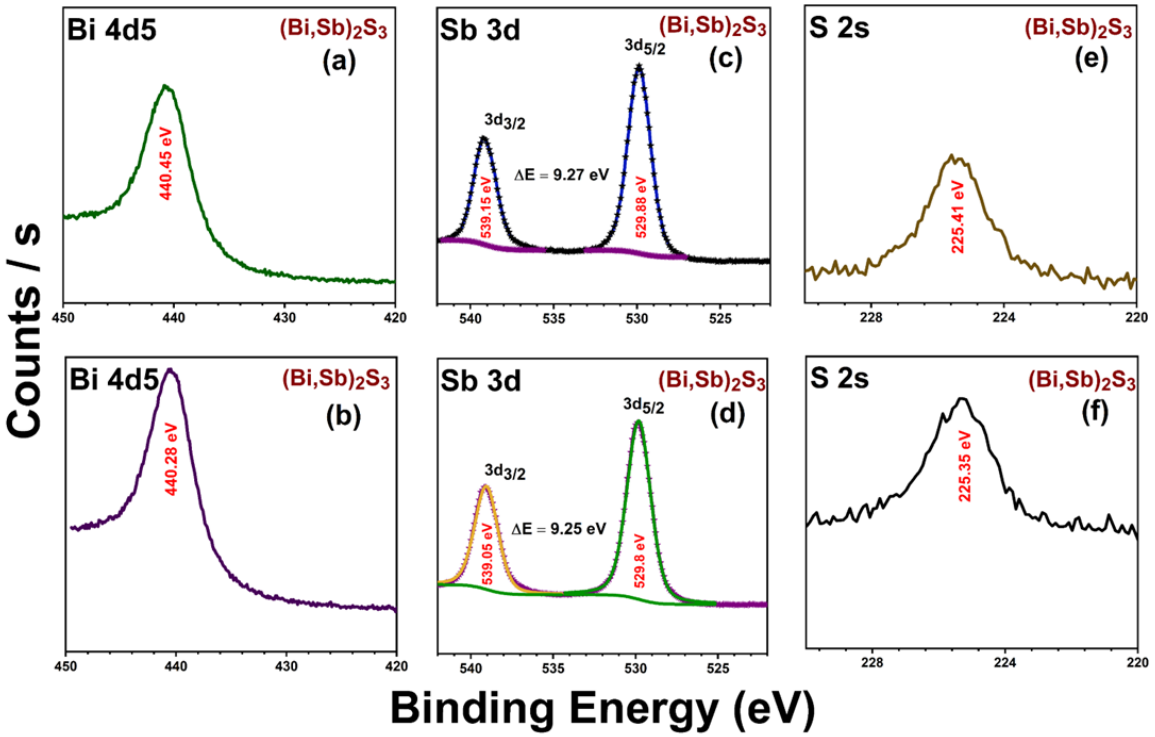

Figure A.9. High-resolution core-level XPS spectra of $(Bi_{0.5},Sb_{0.5})_2S_3$ as-prepared and 380°C annealed thin films a,b) Bi 4d5, c,d) Sb 3d, e,f) S 2s.

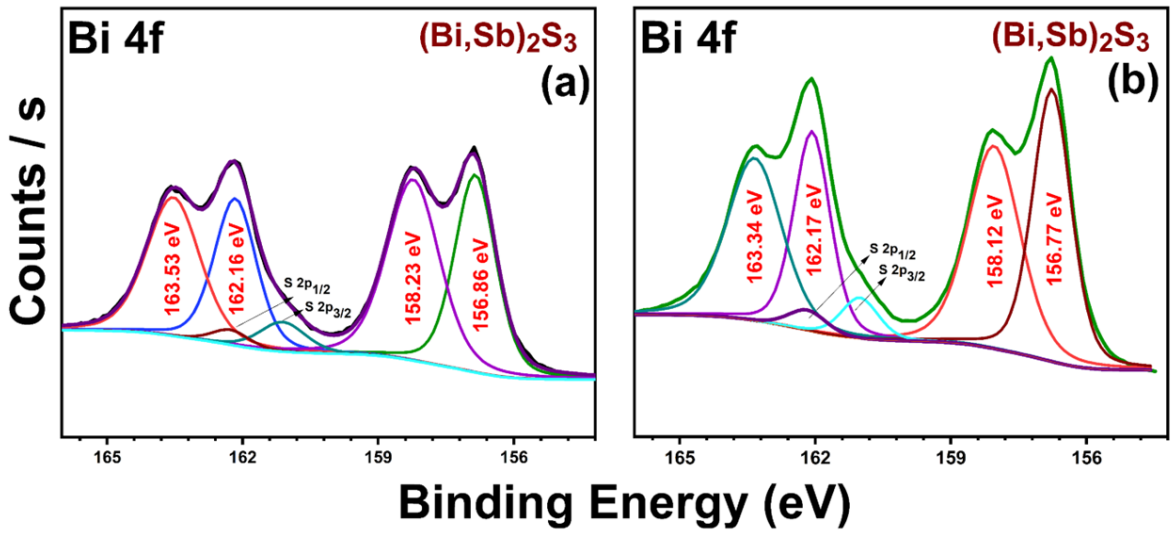

Figure A.10. High-resolution core-level XPS spectra of $(Bi_{0.5},Sb_{0.5})_2S_3$ as-prepared and 380°C annealed thin films a,b) Bi 4f.

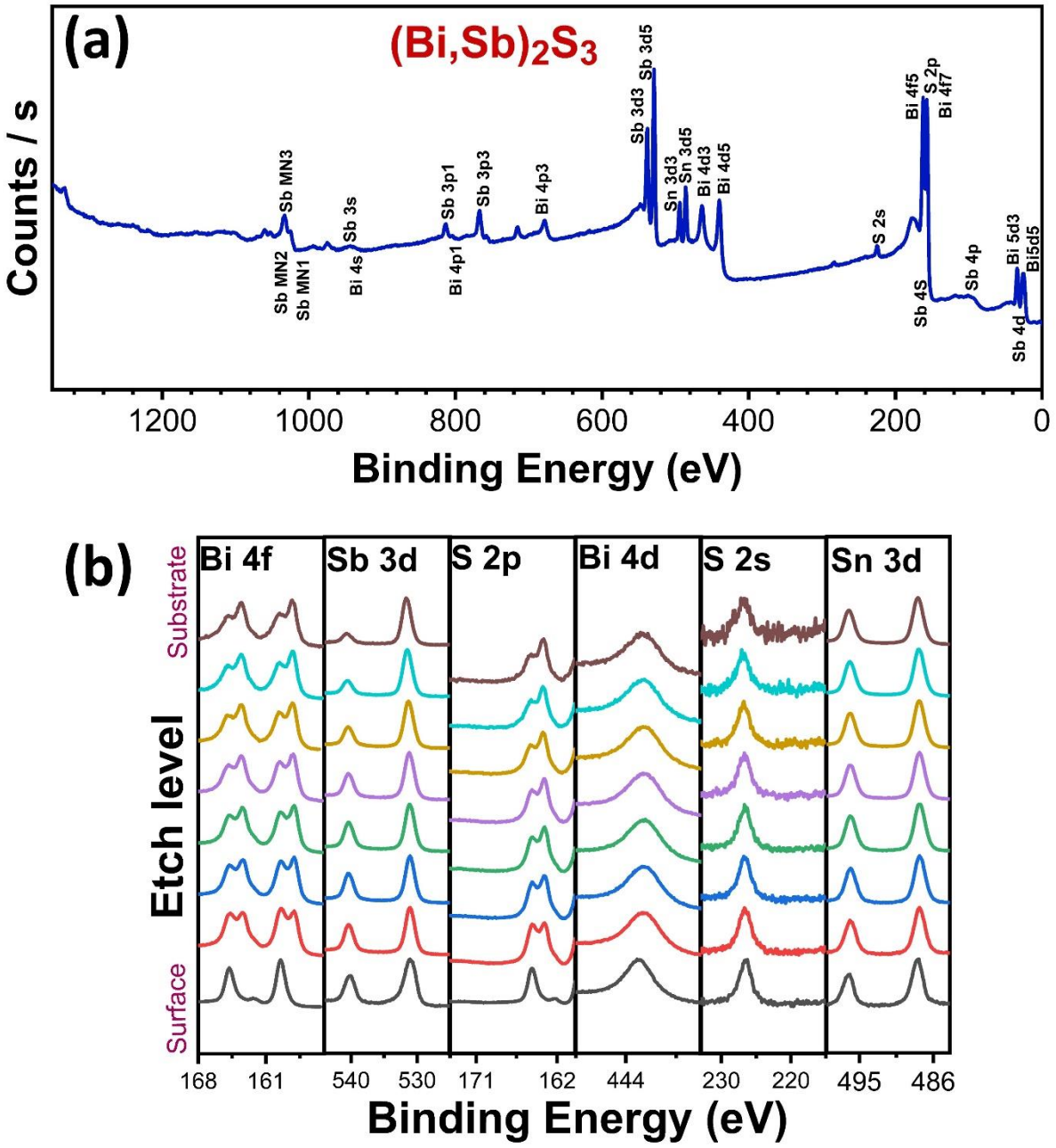

Figure A.11. a) Survey spectrum of Bi-alloyed Sb_2S_3 thin films at varying Bi and Sb ratio. High-resolution core-level XPS spectra of $(Bi_{0.5},Sb_{0.5})_2S_3$ 380°C annealed thin films b) $(Bi_{0.5},Sb_{0.5})_2S_3$ thin films depth profile on FTO substrate, with etch levels after an etch time of 15 seconds each.

Figure A.9 illustrates the high-resolution XPS spectra of Bi 4d, Sb 3d, and S 2s core levels for both as-prepared and annealed films. The Bi $4d_{5/2}$ peak was observed at a binding energy of 440.45 eV, while the S 2s peak appeared at 225.41 eV in the unannealed samples, with negligible shifts observed after annealing, indicating the stability of these elements' chemical states. The Sb 3d core level displayed peaks at binding energies of 529.88 eV and 539.15 eV,

characteristic of the Sb^{3+} oxidation state, with a spin-orbit splitting of 9.27 eV, further affirming the chemical identity of Sb in the films [50,67,162].

Figure A.10 presents the Bi 4f spectrum in Bi-alloyed Sb_2S_3 thin films, where the overlapping binding energies of S 2p and Bi 4f required deconvolution to resolve the peaks. The deconvoluted spectrum identified Bi $4f_{7/2}$ and Bi $4f_{5/2}$ peaks corresponding to the Bi^{3+} state at 158.23 eV and 163.53 eV, respectively. Additional peaks at 156.86 eV and 162.16 eV were assigned to metallic bismuth (Bi^0), with a spin-orbit splitting of 5.3 eV. The S 2p region revealed peaks for S^{2-} at 161.11 eV (S $2p_{3/2}$) and 162.27 eV (S $2p_{1/2}$), with a spin-orbit splitting of 1.16 eV, reflecting the stable bonding of sulfur in the films.

Figure A.11(a) shows the survey spectrum for 50% Bi-alloyed Sb_2S_3 films deposited on FTO glass, confirming the presence of Bi, Sb, and S elements without detectable contamination, indicative of the high purity of the samples. Figure A.11(b) displays the depth profile analysis, demonstrating the uniform distribution of Bi, Sb, and S throughout the thin films, further confirming the successful and consistent deposition of the alloyed material onto the FTO substrate.

The S2s XPS data (Figure A.12, Table A.6) for the $(Bi_x,Sb_{1-x})_2S_3$ systems reveal several important trends related to sulfur's chemical environment and composition. The binding energy (BE) values are consistent around 225.2–225.35 eV across all samples, indicating the presence of S^{2-} species typical of sulfides. However, a slight shift in BE is observed as the Bi content increases, likely due to the difference in electronegativity between Sb and Bi, which influences the chemical surroundings of sulfur. A clear trend is noted in peak height and area, which both decrease as Bi content increases, ranging from 11660 CPS in Sb_2S_3 to 4521 CPS in Bi_2S_3 and from 28,497 CPS·eV to 12,044 CPS·eV respectively. This suggests a decrease in sulfur concentration as Bi replaces Sb within the structure. Both normalized and peak areas also decrease, further indicating a reduction in sulfur content in Bi-rich samples. The atomic percentage and peak-to-peak atomic percentage show a decreasing trend with increasing Bi content, highlighting a reduction in sulfur incorporation or possible sulfur vacancy formation in Bi-rich samples. This trend aligns with the expected stoichiometry of the compounds. An interesting anomaly is observed in the $(Bi_{0.5},Sb_{0.5})_2S_3$ sample, which shows a lower sulfur atomic percentage compared to $(Bi_{0.4},Sb_{0.6})_2S_3$ despite a higher Bi content. This suggests non-stoichiometry or phase complexity possibly due to the competitive bonding environments of Bi and Sb. These XPS observations are consistent with EDX results, which also show lower sulfur

content in $(Bi_{0.5},Sb_{0.5})_2S_3$ compared to other compositions. This agreement between XPS and EDX indicates sulfur deficiency, likely due to vacancy formation. Despite compositional changes, the binding energies confirm that sulfur remains in the S^{2-} state across all samples. However, the variations suggest changes in the local bonding environment, especially in mixed Bi-Sb systems.

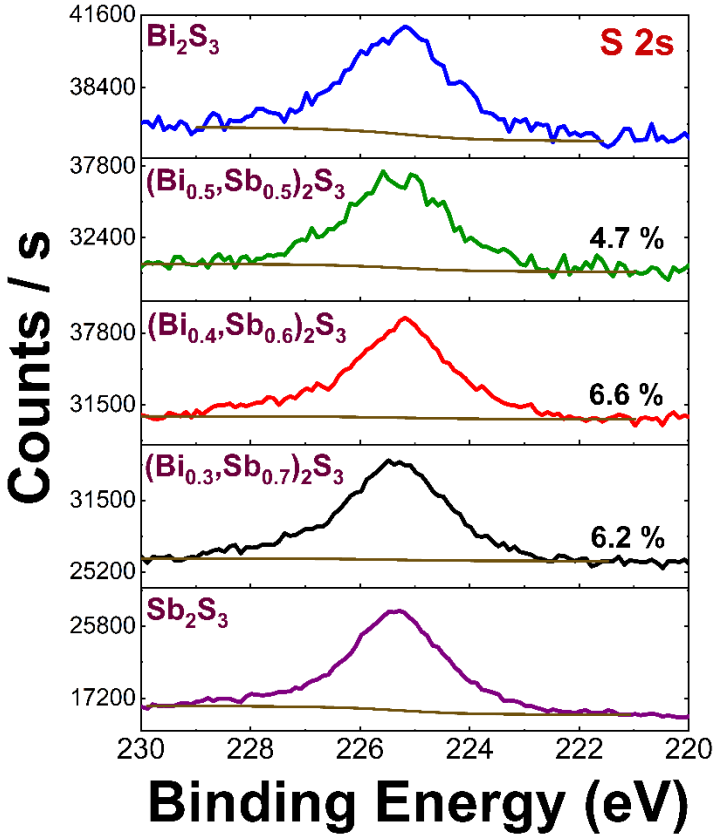

Figure A.12: XPS spectra of S 2s showing binding energy shifts, changes in peak intensity and atomic percentage with increasing Bi content.

Table A.6: S2s XPS parameters showing the effect of Bi content on binding energy, peak intensity, and sulfur composition in $(Bi_x,Sb_{1-x})_2S_3$ samples.

System	Peak BE	Height (CPS)	FWHM (eV)	Area (P) (CPS.eV)	Atomic %	PP At. %
Sb_2S_3	225.35	11660	1.9	28497	5.4	3.5
$(Bi_{0.3}, Sb_{0.7})_2S_3$	225.34	8538	2	21570	6.2	4.7
$(Bi_{0.4}, Sb_{0.6})_2S_3$	225.2	8337	1.9	21009	6.6	5.9
$(Bi_{0.5}, Sb_{0.5})_2S_3$	225.3	6740	1.9	17447	4.7	4.0
Bi_2S_3	225.22	4521	2.3	12044	2.4	1.6

A.9 Scanning electron microscopy (SEM)

The SEM analysis in Figure A.13 highlights the influence of bismuth incorporation on the morphology of antimony sulfide compounds. The pure Sb_2S_3 sample exhibits a spherical morphology, which is only subtly altered in the $(Bi_{0.3}, Sb_{0.7})_2S_3$ sample, where the spherical shape remains dominant, though minor changes in the surface texture are observed due to bismuth incorporation. As the bismuth content increases to $(Bi_{0.4}, Sb_{0.6})_2S_3$ and $(Bi_{0.5}, Sb_{0.5})_2S_3$, more significant morphological changes emerge. Small spikes develop around the spherical particles, suggesting that bismuth is progressively influencing the structural arrangement. This shift hints at a more complex growth behavior, where the interaction between bismuth and antimony modifies the particle surface, potentially increasing the surface area. At the Bi_2S_3 sample, the morphology undergoes a marked transformation, transitioning from spherical particles to a more compact structure with larger grains. This change indicates a significant shift in growth dynamics, with bismuth promoting more uniform and larger-scale growth, which is likely due to its unique crystallographic and electronic properties that alter growth kinetics.

These findings align with previous research, where bismuth incorporation in semiconductor matrices has been shown to induce distinct morphological changes [202]. Specifically, studies have reported that increasing bismuth content leads to the formation of rod-like and needle-like structures in bismuth-based compounds, a trend consistent with the transition observed in the 100% bismuth sample [222]. This transformation is attributed to the crystallographic and electronic properties of bismuth, which promote anisotropic growth.

The literature further suggests that these morphological changes are linked to the material's electronic and optical properties [223]. The transition from spherical to compact, larger grain structures can significantly affect charge transport and light absorption, key factors in optoelectronic applications. The spiked structures at intermediate bismuth concentrations may increase the surface area, improving catalytic and sensing efficiency. These structural modifications underscore the importance of bismuth content in tuning the material’s properties for specific applications, demonstrating that precise compositional control is crucial in optimizing semiconductor materials for desired functionalities.

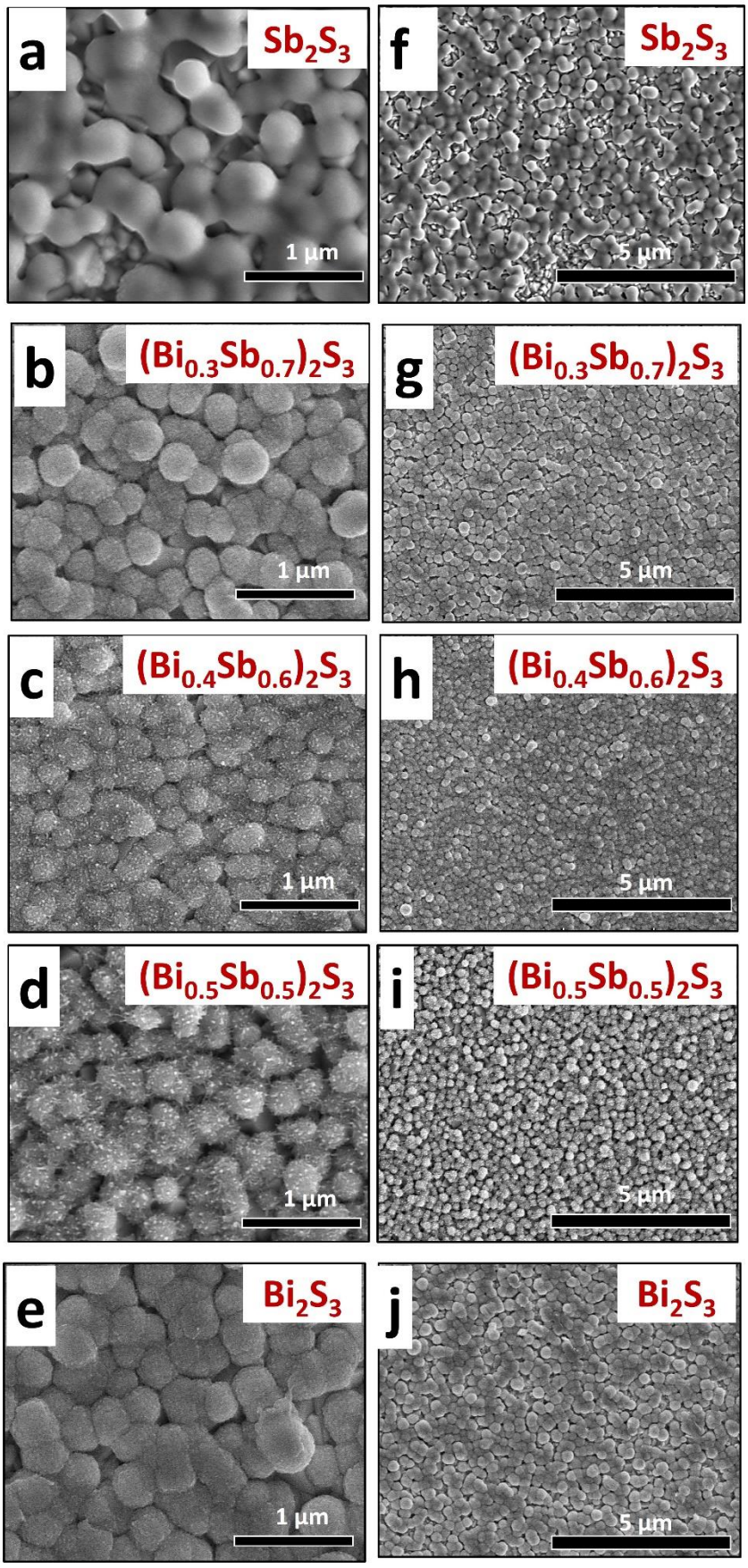

Figure A.13. SEM analysis of Bi-alloyed Sb_2S_3 thin films at varying Bi and Sb ratio.

A.10 Optical properties

UV-Vis-NIR spectroscopy

The optical properties of Sb_2S_3, Bi_2S_3, and their mixed compositions were analyzed using UV-Vis spectroscopy, as shown in Figure A.14. The absorbance spectra (Figure A.14(a)) reveal a systematic shift in the absorption edge with varying Bi and Sb ratios. Pure Sb_2S_3 exhibits the highest absorbance in the visible range, with an absorption edge around 600 nm, while Bi_2S_3 shows a shift toward longer wavelengths, extending into the near-infrared region. Intermediate compositions, such as $(Bi_{0.3}, Sb_{0.7})_2S_3$, $(Bi_{0.4}, Sb_{0.6})_2S_3$ and $(Bi_{0.5}, Sb_{0.5})_2S_3$, demonstrate absorbance trends between these two extremes, indicating the tunability of optical properties through alloying.

To quantify this behavior, Tauc plots ($(\alpha h\nu)^2$ vs. energy) were used to estimate the optical bandgaps of the compositions (Figure A.9(b)). The band-band transition (E_g) is determined using the empirical relation:

$$(\alpha h\nu)^n = A\left(h\nu - E_g\right) \quad (1)$$

A is a constant, h is the Planck's constant, and ν is the frequency of the incident photons. The value of n depends on the kind of optical transition, with n=2 signifying a direct allowed bandgap transition and n=2/3 signifying a direct forbidden bandgap transition. Pure Sb_2S_3 exhibited the widest bandgap of 1.87 eV, while Bi_2S_3 had the narrowest bandgap of 1.35 eV. The intermediate alloys displayed bandgap energies of 1.73 eV for $(Bi_{0.3}, Sb_{0.7})_2S_3$, 1.64 eV for $(Bi_{0.4}, Sb_{0.6})_2S_3$, and 1.75 eV for $(Bi_{0.5}, Sb_{0.5})_2S_3$. This progressive reduction in bandgap with increasing Bi content can be attributed to modifications in the electronic structure and lattice effects introduced by the alloying process. The observed trend highlights the potential for fine-tuning bandgap energies to suit specific application requirements.

The shift in optical properties from Sb-rich to Bi-rich compositions underscores the versatility of this material system for various optoelectronic applications. Wider bandgap materials, such as Sb_2S_3, are ideal for visible-light-based devices, including photodetectors and solar cells. Conversely, narrower bandgap compositions, such as Bi_2S_3, are more suitable for near-infrared applications. The intermediate alloys provide a balance, offering adjustable optical properties

to optimize performance across a broader spectrum. The systematic variation in optical absorbance and bandgap energies within the Bi-Sb-S system demonstrates the feasibility of tailoring material properties for specific functionalities. These findings open avenues for the development of efficient light-harvesting and sensing devices, with composition-dependent tunability as a significant advantage.

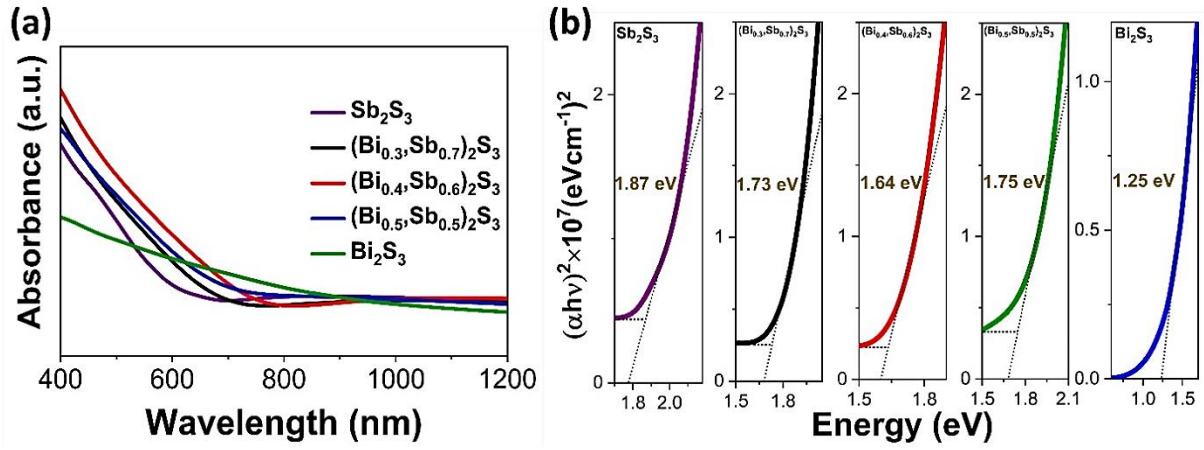

Figure A.14. (a) UV-Vis absorbance spectra of Sb_2S_3, Bi_2S_3, and their mixed compositions, showing a systematic shift in the absorption edge with varying Bi/Sb ratios. (b) Tauc plots for the corresponding compositions, highlighting the tunable bandgap energies ranging from 1.22 eV (Bi_2S_3) to 1.97 eV (Sb_2S_3).

The comparison of experimental and theoretical electronic properties of $(Bi,Sb)_2S_3$ alloys reveals notable differences and underlying trends. For pure Sb_2S_3, the experimental bandgap (1.87 eV) significantly exceeds the theoretical value (1.29 eV), reflecting the influence of structural imperfections, grain boundaries, and strain in real-world samples. These factors, combined with the distinction between optical (experimental) and electronic (theoretical) bandgaps, account for the observed discrepancies.

As bismuth content increases, experimental bandgaps for $(Bi_{0.3}, Sb_{0.7})_2S_3$ (1.73 eV) and $(Bi_{0.4}, Sb_{0.6})_2S_3$ (1.64 eV) follow a narrowing trend, consistent with theoretical predictions (1.25 eV and 1.17 eV, respectively). However, the higher experimental values suggest alloying-induced effects, such as strain or disorder, which are not fully captured by idealized theoretical models. These effects influence the local electronic structure, widening the optical bandgap while preserving the trend.

For $(Bi_{0.5}, Sb_{0.5})_2S_3$, experimental and theoretical results diverge further, with the bandgap measured at 1.75 eV compared to a predicted 1.27 eV. This discrepancy highlights the role of synthesis conditions, phase segregation, or defects in altering the optical bandgap. In contrast, Bi_2S_3 shows a reduced experimental bandgap of 1.25 eV, slightly lower than the theoretical 1.39 eV, likely due to defect-induced bandgap narrowing in the synthesized material.

Despite these differences, both experimental and theoretical data exhibit a clear trend: increasing bismuth content initially narrows the bandgap, stabilizing the electronic structure and enhancing optoelectronic properties. The shifts in conduction and valence band edges predicted by theory align qualitatively with experimental observations, confirming the alloys' intrinsic semiconductor behavior. Overall, this comparison highlights the influence of real-world synthesis conditions on material properties and the complementary roles of experimental and theoretical approaches in understanding and optimizing $(Bi,Sb)_2S_3$ alloys for optoelectronic applications. These findings demonstrate the potential of bismuth incorporation to fine-tune bandgap energies for devices such as photodetectors and solar cells.

A.11 Photocurrent response measurement

The photoresponse characteristics of the Sb_2S_3 alloy system were evaluated at an applied voltage of 5 V to investigate the impact of alloying on photodetection performance. Figure A.15(a) shows the performance of pure Sb_2S_3, which exhibited a weak photoresponse with current in the nanoampere range across the UV-VIS-IR spectrum. This poor performance is attributed to the material's limited absorption efficiency and suboptimal charge carrier transport properties, making it unsuitable for high-performance photodetectors.

Alloying with bismuth significantly improved the photoresponse, as shown in Figure A.15(b) for $(Bi_{0.3}, Sb_{0.7})_2S_3$. The photocurrent increased indicate enhanced light absorption and improved charge carrier mobility. The uniformity of the current spikes suggests better broadband sensitivity, although the response remained moderate and indicated room for further optimization.

The performance further improved with the composition $(Bi_{0.4}, Sb_{0.6})_2S_3$ (Figure A.15(c)), where the photocurrent showed greater enhancement in the UV-VIS regions due to reduced trap states and improved crystallinity. However, while the overall response was better

compared to $(Bi_{0.3}, Sb_{0.7})_2S_3$, it was not yet optimal for stable and efficient photodetection across the spectrum.

The optimal performance was observed with $(Bi_{0.5}, Sb_{0.5})_2S_3$, as shown in Figure A.15(d). This composition exhibited consistently high photocurrent across the UV, VIS, and IR regions, indicating excellent broadband sensitivity. The balanced alloy composition resulted in an optimized bandgap, which enhanced light absorption across a wide spectral range. Furthermore, the improved crystallinity reduced defect density and enhanced charge carrier transport, resulting in a higher on/off ratio and stable, repeatable photodetection. The superior structural integrity and consistent response confirmed $(Bi_{0.5}, Sb_{0.5})_2S_3$ as the most stable and efficient composition in the alloy series.

In comparison, pure Bi_2S_3 (Figure A.15(e)) demonstrated the highest absolute photocurrent, particularly in the UV and VIS regions, due to its excellent optical and electrical properties, including high light absorption and superior charge carrier mobility. However, its response was less uniform in the IR region, and the higher bismuth content could lead to structural instability, making it less suitable for long-term applications. While Bi_2S_3 achieved the highest current output, the balanced and stable performance of $(Bi_{0.5}, Sb_{0.5})_2S_3$ made it the most practical and reliable choice for real-world applications.

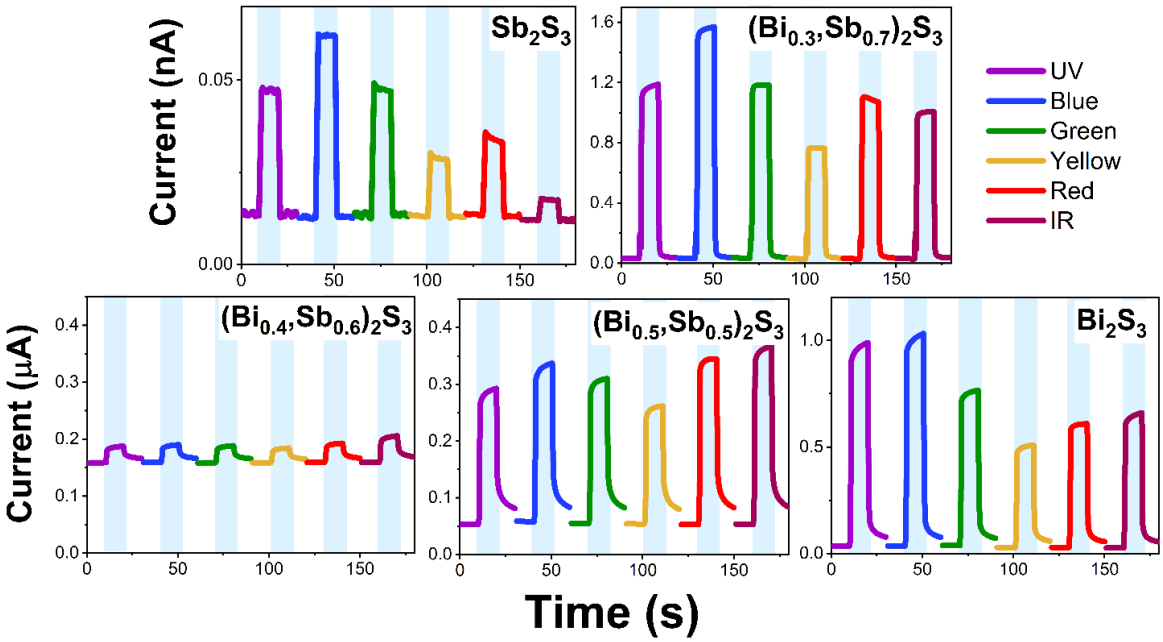

Figure A.15. photoresponse measurement of Bi-alloyed Sb_2S_3 thin films using different LED

The optoelectronic performance of Sb_2S_3-Bi_2S_3 alloys, summarized in Table A.5, highlights the critical influence of bandgap engineering. The sensitivity (S), calculated using Equation 2, represents the percentage change in current under illumination relative to the dark current conditions:

$$S\ (\%) = [(I_l - I_d)/I_d] \times 100 \quad (2)$$

where I_l is the current under illumination and I_d is the dark current. Responsivity (R), which measures the photocurrent generated per unit of incident light power, is given by:

$$R = I_{ph}/(A' P) \quad (3)$$

where $I_{ph} = (I_l - I_d)$, A is the effective area (0.25 cm^2), and P is the light intensity. External quantum efficiency (EQE), calculated using Equation 4, indicates the efficiency of a photodetector in converting incident photons into collected charge carriers:

$$EQE\ (\%) = [(hcR)/q\lambda] \times 100 \quad (4)$$

where h is Planck's constant (6.626×10^{-34} J·s), c is the speed of light (3×10^8 m/s), q is the elementary charge (1.602×10^{-19} C), and λ is the wavelength of the incident light. Detectivity (D), calculated using Equation 5, quantifies the photodetector's ability to detect weak signals:

$$D = (R\sqrt{A})/\sqrt{2qI_d} \quad (5)$$

Pure Sb_2S_3, with the widest bandgap of 1.87 eV, exhibited limited photodetection capabilities. At 465 nm, it achieved a maximum external quantum efficiency (EQE) of 0.008%, a detectivity of 7.18×10^9 Jones, and a responsivity of 0.03 mA/W. The poor performance of Sb_2S_3 is attributed to its relatively low light absorption and inefficient carrier generation, resulting in minimal responsivity across all measured wavelengths. The on/off ratio remained below 5.0, and sensitivity peaked at 395% at 465 nm, further confirming the material's limited ability to generate photocurrent. In contrast, Bi_2S_3, with the narrowest bandgap of 1.25 eV, demonstrated the highest photoresponse. At 465 nm, it achieved an EQE of 150%, a detectivity of 2.61×10^{12} Jones, and a responsivity of 562 mA/W. The EQE exceeding 100% in Bi_2S_3 is attributed to a photoconductive gain mechanism facilitated by trap-assisted carrier multiplication, where photogenerated charge carriers are efficiently transported and contribute to an amplified photocurrent [224][225]. Additionally, its high absorption coefficient enhances charge carrier generation, resulting in significantly higher detectivity and sensitivity compared to Sb_2S_3. The highest sensitivity of Bi_2S_3 was recorded at 465 nm, reaching 2676%, with a peak detectivity of

2.61×10^{12} Jones. However, its operational stability remains a challenge, as performance degradation over extended exposure was observed.

Among the alloy compositions, $(Bi_{0.3}Sb_{0.7})_2S_3$, with a bandgap of 1.73 eV, achieved the highest on/off ratio of 45.2 and a maximum sensitivity of 4419% at 465 nm. Its responsivity at this wavelength was 0.88 mA/W, and the detectivity reached 1.33×10^{11} Jones. While its EQE (24%) and detectivity were moderate compared to Bi_2S_3, its optimized bandgap allowed for a balance between photon absorption and charge carrier transport. However, the overall photocurrents remained in the nanoampere range, limiting further improvements in detectivity. $(Bi_{0.4}Sb_{0.6})_2S_3$, with a slightly narrower bandgap of 1.64 eV, exhibited intermediate performance. At 525 nm, it achieved a peak detectivity of 5.60×10^{10} Jones, a maximum EQE of 5%, and a responsivity of 25.3 mA/W at 630 nm. Despite its improved photoresponse compared to Sb_2S_3, its response stability remained inferior to other alloy compositions, as indicated by relatively low on/off ratios across all wavelengths.

$(Bi_{0.5}Sb_{0.5})_2S_3$, possessing a bandgap of 1.75 eV, demonstrated the most consistent photodetection performance. It exhibited a peak detectivity of 8.76×10^{11} Jones at 630 nm and a maximum EQE of 45% at 630 nm. The highest responsivity of 228 mA/W was observed at 630 nm, confirming efficient light absorption and charge carrier transport. Although its EQE and detectivity values did not surpass those of pure Bi_2S_3, its balanced performance across multiple wavelengths and enhanced stability make it a strong candidate for long-term photodetection applications. The trend from Sb-rich to Bi-rich alloys reveals a progressive increase in detectivity, EQE, and responsivity with decreasing bandgap, balanced by stability considerations. While Bi_2S_3 achieved the highest detectivity and EQE due to trap-assisted charge multiplication, $(Bi_{0.5}Sb_{0.5})_2S_3$ exhibited the most stable and efficient photodetection performance among the alloys. The detailed photoresponse metrics for all compositions at different wavelengths are presented in Table A.7.

Table A.7 Summary of the photoresponse parameters at different wavelengths for $(Bi,Sb)_2S_3$ thin films with varying bismuth content.

Sample	Wavelength (nm)	On/off ratio	Sensitivity (%)	Responsivity (mA/W)	Detectivity ($\times 10^9$Jones)	EQE (%)
Sb_2S_3	405	3.29	229	0.01	3.09	0.004
	465	4.94	395	0.03	7.18	0.008
	525	3.48	248	0.03	5.97	0.006
	595	2.18	118	0.01	3.41	0.003
	630	2.56	156	0.02	4.03	0.003
	740	1.48	48	0.002	0.440	0.0003
$(Bi_{0.3}, Sb_{0.7})_2S_3$	405	33.8	3284	0.45	68.2	0.14
	465	45.2	4419	0.88	133	0.24
	525	32.6	3160	0.83	122	0.2
	595	24.7	2373	0.65	104	0.14

	630	34.0	3304	0.83	130	0.16
	740	30.5	2950	0.29	44.6	0.05
$(Bi_{0.4}, Sb_{0.6})_2S_3$	405	1.17	17	10.9	24.2	3.3
	465	1.18	19	17.0	37.8	4.6
	525	1.18	18	20.6	45.8	4.9
	595	1.15	16	21.7	48.1	4.5
	630	1.20	20	25.3	56.0	5
	740	1.28	28	13.2	29.1	2.2
$(Bi_{0.5}, Sb_{0.5})_2S_3$	405	5.37	437	93.2	357	29
	465	5.62	462	157	574	42
	525	5.55	455	182	686	43
	595	4.78	378	182	691	38
	630	6.49	549	228	876	45
	740	6.73	573	91.8	350	15

Bi_2S_3	405	27.0	2604	372	1740	114
	465	27.8	2676	562	2610	150
	525	19.4	1840	520	2330	123
	595	17.3	1627	419	2180	87
	630	20.7	1972	452	2340	89
	740	24.2	2324	185	1000	31

These findings align with similar studies in the field, where bismuth incorporation in semiconductor materials has been shown to enhance photocurrent due to its influence on the material's electronic structure and defect states. Research on Bi-doped Sb_2Se_3 films reported an increase in photocurrent with higher bismuth content, attributing this to improved charge carrier mobility and reduced recombination rates [218]. Moreover, the observed enhancement in photocurrent at elevated annealing temperatures is consistent with studies that emphasize the role of thermal processing in optimizing grain size and crystallinity, thereby improving the material's photoconductive properties.

This research establishes a strong foundation for advancing bismuth-alloyed antimony sulfide ($(Bi,Sb)_2S_3$) thin films in diverse optoelectronic applications. The study highlights their superior photoresponse, particularly at higher bismuth concentrations and optimized annealing conditions, alongside their broad spectral sensitivity spanning UV to IR regions. Comprehensive analyses, including DFT studies, reveal insights into bandgap tunability, photocurrent enhancement, and the structural and electronic optimization of these materials. These findings pave the way for exploring new alloying strategies, innovative device designs, and practical applications, fostering the development of efficient and versatile optoelectronic technologies.

A.12 Photocatalytic Performance and Stability Analysis

The photocatalytic performance and stability of bismuth-alloyed antimony sulfide ($(Bi_xSb_{1-x})_2S_3$ compositions were evaluated through three degradation cycles, as shown in Figure A.16. The study involved pure Sb_2S_3 (AS), $(Bi_{0.3}, Sb_{0.7})_2S_3$ (25), $(Bi_{0.4}, Sb_{0.6})_2S_3$ (50), $(Bi_{0.5}, Sb_{0.5})_2S_3$ (75), and pure Bi_2S_3 (100). The degradation behavior was assessed using plots of ln(C0/C) versus time under continuous illumination, where C0 and C represent the initial and instantaneous concentrations of the target compound, respectively.

In the first cycle, all samples showed a linear degradation trend, indicating pseudo-first-order kinetics. The pure Sb_2S_3 (AS) sample exhibited the fastest degradation, which is attributed to its efficient light absorption and charge separation capabilities. However, its structural instability under light exposure led to rapid deterioration. The introduction of bismuth in $(Bi_{0.3}, Sb_{0.7})_2S_3$ (25) and $(Bi_{0.4}, Sb_{0.6})_2S_3$ (50) decreased the degradation rate compared to pure Sb_2S_3, highlighting the stabilizing effect of bismuth. Nevertheless, these compositions still showed limited stability. The $(Bi_{0.5}, Sb_{0.5})_2S_3$ (75) sample demonstrated a more moderate degradation

rate and enhanced stability, likely due to an optimized alloying ratio. Pure Bi_2S_3 (100) exhibited the lowest degradation rate but had limited photocatalytic efficiency due to its lower light absorption capacity.

The second and third cycles revealed significant differences in sample stability. By the second cycle, severe degradation was evident for AS and $(Bi_{0.3}, Sb_{0.7})_2S_3$ (25), rendering them ineffective for further photocatalytic cycles. The $(Bi_{0.4}, Sb_{0.6})_2S_3$ (50) sample also showed complete degradation after the second cycle, which can be attributed to structural instability caused by insufficient bismuth substitution. In contrast, the $(Bi_{0.5}, Sb_{0.5})_2S_3$ (75) composition maintained its photocatalytic activity throughout all three cycles, indicating superior stability. This can be explained by the balanced substitution ratio of bismuth and antimony, which likely enhances the structural robustness and prevents defect formation. Pure Bi_2S_3 (100) also remained stable across all cycles but continued to show limited efficiency.

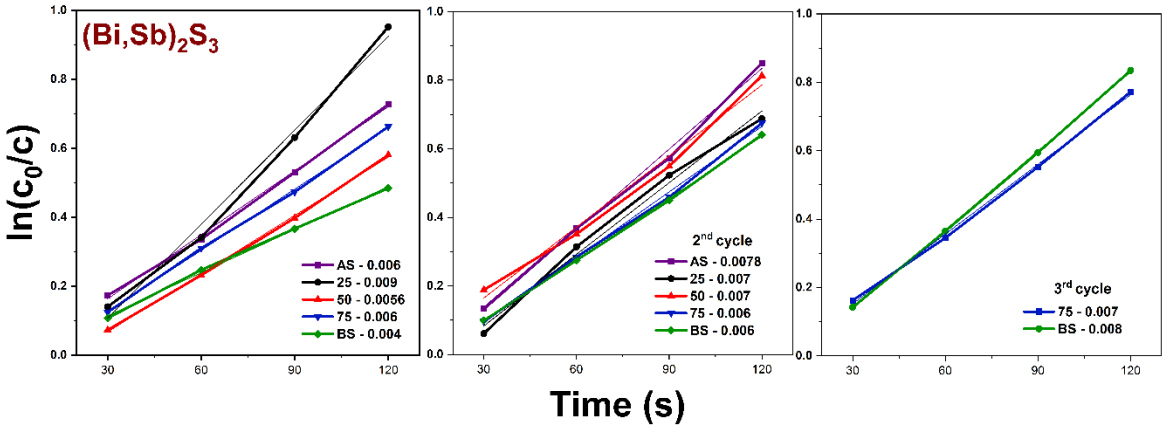

Figure A.16. Bi-alloyed Sb_2S_3 thin film photocatalytic dye degradation efficiency.

The enhanced stability and photocatalytic performance observed in the $(Bi_{0.5}Sb_{0.5})_2S_3$ sample during cycle 3, as shown in Figure A.16, are due to structural and electronic factors arising from the partial substitution of antimony by bismuth in the crystal lattice. Bismuth's larger ionic radius (1.03 Å vs. 0.76 Å for Sb^{3+}) induces lattice distortions that improve charge carrier dynamics by increasing electron-hole pair separation and reducing recombination, which enhances photocatalytic activity. However, an excess of bismuth, as seen in Bi_2S_3, reduces light absorption due to changes in band structure and optical properties. While Bi_2S_3 is more structurally stable, its photocatalytic efficiency is lower. The key benefit of the $(Bi_{0.5}Sb_{0.5})_2S_3$ composition lies in the balanced optimization of structural stability and light absorption.

In Sb-rich compositions such as $(Bi_{0.3}Sb_{0.7})_2S_3$ and $(Bi_{0.4}Sb_{0.6})_2S_3$, prolonged light exposure leads to sulfur loss, resulting in sulfur vacancies that act as charge carrier traps, disrupting the crystal structure and accelerating performance degradation. Incomplete bismuth substitution in these compositions can cause non-uniform lattice structures, making them more susceptible to degradation under illumination.

During cycle 3, $(Bi_{0.5}Sb_{0.5})_2S_3$ exhibited significant improvement in photocatalytic performance, which can be attributed to two key mechanisms: surface restructuring and defect state saturation. Prolonged light exposure and repeated cycles induce surface restructuring, forming a more stable and passivated surface that reduces defect density, enhancing charge separation and transport. Additionally, defect states such as sulfur vacancies, which initially act as recombination centers, become saturated with repeated exposure, reducing their impact on photocatalytic performance.

While Bi_2S_3 also showed a performance improvement in cycle 3, its limited optical absorption hindered its overall efficiency. The findings from Figure A.16 highlight the importance of compositional optimization in bismuth-antimony sulfides for photocatalytic applications. The superior performance of $(Bi_{0.5}Sb_{0.5})_2S_3$ in cycle 3 demonstrates the benefits of partial bismuth substitution, which enhances structural stability, reduces recombination losses, and maintains photocatalytic efficiency over multiple cycles. These results underscore the crucial role of material design in achieving durable and efficient photocatalysts.

A.13 Conclusions

- **Successful Synthesis**: $(Bi,Sb)_2S_3$ thin films were successfully synthesized using a room-temperature chemical bath deposition method followed by annealing at 380°C.
- **Structural Analysis**: XRD confirmed the formation of an orthorhombic crystal structure after annealing.
- **Lattice Dynamics**: Raman spectroscopy revealed significant shifts in vibrational modes with increasing bismuth content, indicating changes in lattice dynamics.
- **Morphological Evolution**: SEM showed a clear transition in grain morphology—from small spherical grains in Sb_2S_3 to larger grains in Bi_2S_3—highlighting the impact of bismuth incorporation on grain size.
- **Bandgap Tunability**: Optical measurements demonstrated a tunable bandgap ranging from 1.87 eV (pure Sb_2S_3) to 1.25 eV (pure Bi_2S_3), with the $(Bi_{0.5}Sb_{0.5})_2S_3$ composition showing an intermediate value of 1.75 eV.

- **Photodetection Performance**: The $(Bi_{0.5}Sb_{0.5})_2S_3$ alloy exhibited superior photodetection properties, achieving:
- **Detectivity**: 8.76×10^{11} Jones
- **EQE**: 45%
- **Balanced Photocurrent Response**
- **Theoretical Support**: Preliminary DFT calculations validated the enhanced electronic structure and thermodynamic stability of the $(Bi_{0.5}Sb_{0.5})_2S_3$ alloy.
- **Optoelectronic Potential**: The study demonstrated that $(Bi,Sb)_2S_3$ films offer tunable bandgaps, enhanced stability, and broad-spectrum photoresponse, making them strong candidates for next-generation optoelectronic devices.

Appendix B. International Research Experience and Knowledge Dissemination

B.1 Exchange Program NTU

As part of an academic exchange program at Nanyang Technological University (NTU), Singapore, I conducted research under the guidance of Prof. Nripan Mathews, focusing on the development of screen-printed carbon-based perovskite devices. My work involved the fabrication and optimization of both lead-based ($MAPbI_3$) and lead-free perovskite solar cells, with specific applications in solar energy harvesting and radiation detection. This experience enhanced my understanding of scalable fabrication techniques and the multifunctionality of perovskite materials in emerging optoelectronic applications.

This academic exchange was made possible with the generous support of **Fundación UANL**, which provided funding for travel expenses.

NANYANG TECHNOLOGICAL UNIVERSITY SINGAPORE

Reg no. 200604393R

31 July 2024

To Whom It May Concern

Letter of Certification

This is to certify that the person named below is a Non-Graduate Non-Exchange/Fee Paying student at School of Materials Science and Engineering, Nanyang Technological University, Singapore.

Name	: VARSHIKA PUTHAN VEEDU SASIDHARAN
Period of Research Attachment	: January 2024 to July 2024
School	: School of Materials Science and Engineering
NTU Supervisor	: Associate Professor Nripan Mathews

Yours faithfully

Professor Ng Kee Woei
Associate Chair (Research)
School of Materials Science and Engineering
Nanyang Technological University

School of Materials Science and Engineering

50 Nanyang Avenue, North Spine, Block N4.1, Singapore 639798, T: +65 6790 4142, F: +65 6790 9081, www.ntu.edu.sg

Figure B.1. Certificate of participation issued under the guidance of Prof. Nripan Mathews, Nanyang Technological University (NTU), Singapore.

B.2 Publications

1) V.P.V Sasidharan, M.U.R.Hernandez, S.Shaji, D.A.Avellaneda, S.K.Chandran, M.G.Méndez, B. Krishnan;"Cesium antimony iodide perovskite thin films by rapid iodization of Sb_2S_3-CsCl precursor under ambient conditions"
J. Alloys Compd., vol. 972, no. January 2024,
doi: https://doi.org/10.1016/j.jallcom.2023.172870

2) V.P.V Sasidharan, S.Shaji, D.A.Avellaneda, M.G.Méndez, B. Krishnan;" Rudorffite silver antimony iodide ($AgSb_2I_7$) thin films by thermal and microwave-assisted synthesis for self-powered visible light detection"
J. Alloys Compd., vol. 1035, June 2025, 181479
doi: https://doi.org/10.1016/j.jallcom.2025.181479

B.3 Conferences

1) **Conference FCFM 2022** Nuevo Leon, Mexico
   April. 2022
   Presented a talk titled Synthesis and characterization of antimony-based lead-free halide perovskites for zero biased photodetector applications.
2) **Smf Congreso Nacional de Fisica 2022** Zacatecas, Mexico
   Oct. 2022
   Presented a paper titled: Cesium Antimony Iodide thin films: A lead-free Perovskite as Zero-Biased Photodetectors.
3) **Conference FCFM 2023** Nuevo Leon, Mexico
   March. 2023
   Presented a talk titled *In-situ* synthesis of silver antimony iodide rudorffite for self-powered photodetection.
4) **International Conference on emerging trends in sustainable energy 2023**
   Palakkad, India
   July. 2023
   Presented a Paper (oral) titled Emerging trends in sustainable energy.